Molecular targeting of autophagy in glioblastoma

Dissertation

Zur Erlangung des Doktorgrades

der Naturwissenschaften

vorgelegt am Fachbereich 15

der Johann Wolfgang Goethe-Universität

in Frankfurt am Main

von

Nina Michelle Meyer

aus Gelnhausen

Frankfurt, 2019

(D 30)

vom Fachbereich 15 der

Johann Wolfgang Goethe-Universität als Dissertation angenommen.

Dekan: Prof. Dr. Sven Klimpel

Gutachter: Prof. Dr. Heinz D. Osiewacz

Prof. Dr. Donat Kögel

Datum der Disputation: 16.07.2019

Die Ergebnisse dieser Arbeit wurden bereits teilweise in folgenden Publikationen veröffentlicht:

Warnsmann V, Meyer N, Hamann A, Kögel D, Osiewacz HD (2018) A novel role of the mitochondrial permeability transition pore in (-)-gossypol-induced mitochondrial dysfunction. Mech Ageing Dev 170: 45-58.

Meyer N, Zielke S, Michaelis JB, Linder B, Warnsmann V, Rakel S, Osiewacz HD, Fulda S, Mittelbronn M, Münch C, et al (2018) AT 101 induces early mitochondrial dysfunction and HMOX1 (heme oxygenase 1) to trigger mitophagic cell death in glioma cells. Autophagy 14: 1693-1709

Zielke S, Meyer N, Mari M, Abou-El-Ardat K, Reggiori F, van Wijk SJL, Kögel D, Fulda S (2018) Loperamide, pimozide, and STF-62247 trigger autophagy-dependent cell death in glioblastoma cells. Cell Death Dis 9: 994.

Table of contents

1 Introduction 1

1.1 Glioblastoma 1
1.1.1 Genotypic and histological characteristics of glioblastomas 1
1.1.2 New therapeutic approaches 3
1.2 Autophagy 5
1.2.1 Molecular machinery 5
1.2.2 Signaling pathways that regulate autophagy 7
1.2.3 Selective autophagy of organelles 8
1.2.3.1 Mitophagy 8
1.2.3.2 Lysophagy 11
1.3 Mitochondria in health and disease 12
1.3.1 The respiratory chain 12
1.3.2 The mitochondrial network 13
1.3.3 Mitochondria and cell death 13
1.4 Programmed cell death 14
1.4.1 Intrinsic and extrinsic apoptosis 16
1.4.2 Regulated (necrotic) cell death forms 18
1.4.2.1 Necroptosis 18
1.4.2.2 Ferroptosis 18
1.4.3 Autophagy-dependent cell death 19
1.4.3.1 Autophagy-dependent cell death and cancer 19
1.4.3.2 Autophagy-dependent cell death and glioblastoma 20
1.4.4 Lysosome-dependent cell death 22

2 Objective 24

3 Material 27

3.1 Cell culture 27
3.2 Plasmids 28
3.3 Chemicals 29
3.4 Antibodies 33
3.5 Buffers and solutions 34
3.6 Commercial kits 36

3.7 siRNA oligonucleotides 37
3.8 Oligonucleotides for generation and detection of CRISPR/Cas9 KOs 37
3.9 Primers for qRT-PCR 38
3.10 Laboratory equipment 39
3.11 Software 42

4 Methods 43

4.1 Cell culture 43
4.1.1 Cultivation of cells 43
4.1.2 Determination of the cell number 43
4.1.3 Freezing cells 44
4.1.4 Thawing cells 44
4.2 Protein analysis 44
4.2.1 Whole cell lysates 44
4.2.2 Protein quantification 45
4.2.3 Sodium dodecyl sulfate polyacrylamide gel electrophoresis (SDS PAGE) 45
4.2.4 Western blot 46
4.3 siRNA transfection 46
4.4 Fluorescence microscopy 46
4.4.1 Determination of autophagic flux by microscopy with the ptfLC3 plasmid 47
4.4.2 Determination of lysosomal membrane permeabilization using the pmCherry-GAL3 Plasmid 48
4.4.3 Staining of cellular cholesterol with filipin III 48
4.5 Flow cytometry 48
4.5.1 Assessment of mitochondrial depolarization by TMRM measurements 49
4.5.2 Determination of mitochondrial mass by MTG measurements 50
4.5.3 Monitoring cell death by APC-annexin V-binding and PI uptake 50
4.5.4 Determination of autophagic flux with the pMRX-IP-GFP-LC3-RFP-LC3ΔG plasmid 51
4.5.5 Determination of reactive oxygen species with CM-H2DCFDA 52
4.5.6 Assessment of lipid peroxidation with BODIPY 581/591 C11 52
4.6 CRISPR/Cas9 knockout 53
4.6.1 Vector design for CRISPR/Cas9 knockout 53
4.6.2 Transformation 54
4.6.3 Colony-Screen PCR for determination of colonies that contain the appropriate vector. 55
4.6.4 Plasmid purification 56
4.6.5 Transfection of cas9 and guide RNA for CRISPR/Cas9 knockouts 56
4.6.6 Cell sorting 56

4.6.7 Single cell dilution 57
4.6.8 DNA extraction and PCR for detection of CRISPR/Cas9 knockout clones 57
4.7 Assessment of caspase activity 59
4.8 Determination of gene expression by quantitative real-time polymerase chain reaction (qRT-PCR) 60
4.9 Proteomics (TMT-labeled approach) 61
4.9.1 Cell lysis, reduction and alkylation 61
4.9.2 Methanol/chloroform precipitation 61
4.9.3 Dissolving the protein pellet 62
4.9.4 Digestion with lysyl endopeptidase and trypsin 62
4.9.5 Desalting and concentration of the peptides 62
4.9.6 TMT-labeling of protein digests 63
4.9.7 Fractionation of peptides 63
4.9.8 Proteome analysis 64
4.10 Fractionation of cytosol and membrane and immunoblot analysis 64
4.11 Cathepsin B assay 64
4.12 Acid sphingomyelinase activity assay 65
4.13 Sample preparation for targeted analysis of sphingolipids and ceramides 65
4.14 Statistics 66

5 Results 67

5.1 AT 101 induces mitochondrial dysfunction 67
5.2 AT 101 treatment decreases mitochondrial protein abundance and shows features of mitophagy induction 71
5.3 AT 101 triggers mitophagy induction that can be reduced by pharmacological and genetic autophagy inhibition 77
5.4 AT 101 induces an autophagic cell death in glioma cells 82
5.5 AT 101 induces lethal mitophagy that is dependent on the selective mitophagy receptors BNIP3 and BNIP3L 84
5.6 HMOX1 is involved in AT 101-induced mitophagy and cell death 87
5.7 Identification of new autophagic cell death inducers 90
5.8 Imipramine + ticlopidine, STF-62247, loperamide and pimozide increase the autophagic flux 97
5.9 Signaling pathways involved in imipramine + ticlopidine-, STF-62247-, loperamide- and pimozide-induced autophagy and cell death 102
5.10 The cellular lipid metabolism is altered in imipramine + ticlopidine-, STF-62247-, loperamide- and pimozide-treated cells 105

5.11 Loperamide and pimozide induce lysosomal membrane permeabilization 116

5.12 Loperamide- and pimozide-induced lysophagy promotes cell survival and is dependent on VCP 124

6 Discussion 128

6.1 AT 101-induced mitochondrial damage and mPTP opening in glioma cells 128

6.2 The role of ATG5-dependent mitophagy induced by AT 101 129

6.3 Hyperactivated autophagy following AT 101 treatment promotes cell death and may be beneficial for cancer treatment 130

6.4 The pro-death function of selective mitophagy induced by AT 101 131

6.5 The role of BNIP3 and BNIP3L in selective mitophagy and cell death 132

6.6 The role of HMOX1 in death induced by AT 101 133

6.7 Involvement of additional cell death mechanisms in AT 101-induced cell demise 134

6.8 Determination of ACD induction following loperamide, pimozide and STF-62247 treatment by using *ATG5* and *ATG7* knockout models 136

6.9 Implication of upstream autophagy regulators in loperamide-, pimozide- and STF-62247-induced autophagy and ACD 138

6.10 Pimozide-, but not loperamide-induced ACD is dependent on receptor-mediated signaling 138

6.11 Loperamide and pimozide impair cholesterol trafficking and induce lipotoxicity in glioma cells 139

6.12 Deregulated lipid homeostasis leads to autophagy-dependent LMP and subsequent lysosomal cell death that is partially rescued by selective lysophagy 141

6.13 Implications of impaired lipid trafficking and lysosomal damage for cancer therapy ... 144

6.14 Conclusion 145

7 Summary 149

8 Zusammenfassung 154

9 Literature 160

10 Supplemental information 175

11 Appendix 189

11.1 Abbreviations 189

11.2 Figures 195

11.3 Tables 197

12 Acknowledgements ..... Fehler! Textmarke nicht definiert.

13 Curriculum Vitae ..... Fehler! Textmarke nicht definiert.

1 Introduction

1.1 Glioblastoma

Gliomas are the most frequent primary central nervous system (CNS) tumors and derive from astrocytes and oligodendrocytes or their precursors. The classification of gliomas differentiates four tumor grades based on criteria like cell density, nuclear atypia, mitosis number, vascular hyperplasia and necrosis, with the glioblastoma (GBM; grade IV) being the most aggressive malignant primary brain tumor that accounts for 60% - 70% of all glial tumors (Gupta et al., 2005). GBM has an incidence of 3.19 cases per 100,000 people per year in the United States and a median survival time of 15 months despite the standard therapy options including maximal save surgical resection, followed by radiotherapy and chemotherapy with temozolomide (TMZ) (Thakkar et al., 2014). Complete resection is difficult due to the invasiveness of these tumors and their location, which is almost exclusively in the brain, and in 60% of the cases in the four lobes, controlling motor function, speech and senses. Furthermore, differentiating between normal tissue and tumor-infiltrated areas is one of the major challenges (Wilson et al., 2014). The methylation status of the O6-methylguanine methyltransferase (MGMT) has become a clinically significant marker, as the gene encodes a DNA repair protein that causes resistance against the alkylating agent TMZ. The MGMT gene is often silenced by hypermethylation of the promotor and is linked to prolonged overall survival (Krex et al., 2007). However, standard treatment extends the survival only a few months in most cases, as the GBM reoccurs quickly, and patients often dye due to cerebral edema, causing increased intracranial pressure (Krex et al., 2007). Glioblastomas can occur at all ages, but most patients are between 45 and 70 years old (Jawhari et al., 2016).

1.1.1 Genotypic and histological characteristics of glioblastomas

Over 90% of the GBMs are primary tumors that appear *de novo*, but the tumors can also develop as secondary GBMs from lower grade astrocytomas. Secondary GBMs often have a better prognosis and differ from primary GBMs by certain gene mutations. Beside the original histological classification, since 2016, the World Health Organization (WHO) categorizes the CNS tumors also by their molecular parameters (Louis et al., 2016).

While primary GBMs are mainly characterized by alterations of EGFR (epidermal growth factor receptor), CDKN2A (cyclin dependent kinase inhibitor 2A) and PTEN (phosphatase and tensin homolog), secondary GBMs often exhibit TP53 (tumor protein p53) and IDH1

(isocitrate dehydrogenase 1 $NADP^+$) mutations (Ohgaki and Kleihues, 2007; Jawhari et al., 2016). In addition, monosomy 10 is often observed in both, primary and secondary GBMs, which is characterized by diverse point mutations and gene deletions. The recent progress in molecular characterization, e.g. the DNA methylation-based classification of CNS tumors, has already improved the diagnostic accuracy and may support the determination of prognosis and treatment response (Louis et al., 2016; Capper et al., 2018).

The histological characteristics of GBM define two distinguishable tumor areas, including a high cell density area that mostly consists of tumor cells with atypical nuclei and newly formed blood vessels (bulk tumor) and an area with isolated cancer cells infiltrating the parenchyma (infiltration zone). In addition, necrotic areas and highly hypoxic regions are often found in the bulk tumor regions of GBM (Jawhari et al., 2016). Hypoxia is often detected in solid tumors and occurs due to uncontrolled cell proliferation or abnormal neovascularization. Hypoxia constitutes a metabolic stress condition and selection pressure for the tumor cells, promoting the formation of highly aggressive cells (Shchors and Evan, 2007; Jawhari et al., 2016). Moreover, GBMs are often characterized by a highly multiform genotypic and phenotypic character: one tumor cell population can consist of several subclones with genetic heterogeneity. The complexity and highly invasive nature of GBMs contributes to their treatment resistance (Holland, 2000). Another obstacle of GBM therapy is the existence of self-renewing, tumorigenic cancer stem-like cells (CSCs), which support tumor progression (Lathia et al., 2015).

A severe hallmark of GBMs are the defects in apoptotic signaling pathways and overexpression of antiapoptotic genes, leading to a high resistance against caspase-dependent apoptosis (Jiang et al., 2003; Kögel et al., 2010). Most GBMs display strongly upregulated XIAP (X-linked inhibitor of apoptosis) levels, thereby preventing caspase 3, 7 and 9 from the execution of apoptosis (Wagenknecht et al., 1999). In addition, overexpressed anti-apoptotic BCL2 (B-cell CLL/lymphoma 2) proteins inhibit the activation of BAX (BCL2 associated X) and BAK1 (BCL2 antagonist/killer 1) as well as BECN1 (beclin 1), thereby preventing apoptosis and autophagy. Given the fact that the established therapies to treat GBM have only limited success, many studies focused on the exploitation of alternative forms of cell death, such as autophagy-dependent cell death, to improve glioma therapy. Of note, it has been reported that both disrupted autophagy and excess autophagy can have a detrimental effect on cancer cells, and the induction of autophagic cell death (ACD) is an emerging concept to treat GBMs (Kögel et al., 2010).

1.1.2 New therapeutic approaches

The advances in understanding the molecular signaling and pathology of GBMs as well as their communication with the tumor microenvironment and improvements in surgical and preoperative mapping techniques raise hope to achieve prolonged survival of GBM patients. However, a variety of investigated techniques, e.g. radio-immunotherapy, stereotactic radiosurgery and hyperfractionation, did not result in significant survival advantages so far (Barani and Larson, 2015; Davis, 2016). Nevertheless, several clinical studies with pharmacological agents and virotherapies will give new insight about different treatment options in the next years. Table 1.1 lists the major ongoing clinical trials of malignant gliomas. Interestingly, the antimalarial agent and late-stage autophagy inhibitor chloroquine is also currently investigated for treatment of GBM in combination with radiotherapy and chemotherapy with TMZ in a small number of clinical trials. However, it is still unclear whether the autophagy-inhibiting-properties of chloroquine is responsible for its tumor-suppressing effects (Weyerhäuser et al., 2018).

In 2015, a device delivering tumor-treating fields named Optune was approved by the Food and Drug Administration (FDA) for GBM treatment. The technology delivers low intensity, intermediate frequency alternating electrical fields to the tumor cells, thereby causing interrupted cell division and cell death. Additional therapy with Optune together with TMZ resulted in longer progression free and overall survival compared to TMZ alone (Stupp et al., 2015). Moreover, immune checkpoint blockade by targeting PD1 (programmed cell death 1), PDL1 (programmed cell death 1 ligand 1) or CTLA4 (cytotoxic T-lymphocyte associated protein 4) showed anti-tumor activity in melanoma and non-small-cell lung cancer and might be a promising strategy in recurrent GBM (Lieberman, 2017). Furthermore, manipulation of the blood-brain-barrier with nanoparticles to enhance targeted delivery of drugs is currently studied (Davis, 2016). In addition, an even more defined molecular subtyping of GBMs might be a promising approach to identify tumor abnormalities and to target these tumor cells with tailored therapies.

Table 1.1. Major ongoing clinical trials of malignant gliomas (Paolillo et al., 2018).

Drug(s)	Phase	Conditions	Estimated Completion Date	NCT Number
[1] Bevacizumab	1,2	Glioblastoma Multiform	January 2018	NCT01811498
[1] Bevacizumab	2	Glioblastoma	May 2018	NCT02157103
[1] Bevacizumab [2] Temozolomide Dietary Supplement Vitamin C	1,2	Malignant Glioma	March 2020	NCT01891747
[1] Bevacizumab [2] Temozolomide	2	Glioblastoma	January 2019	NCT01149850
[1] Bevacizumab [2] Temozolomide	3	Recurrent Glioblastoma	July 2023	NCT02761070
[3] Cetuximab	1,2	Glioblastoma	June 2019	NCT02861898
Cerebraca Wafer [2] *n*-butylidenephthalide (BP)	1,2	Recurrent High Grade Glioma	August 2019	NCT03234595
[2] TH-302 [1] Bevacizumab	2	Glioblastoma	July 2018	NCT02342379
[2] Temozolomide Metformin	2	Glioblastoma	December 2018	NCT03243851
[2] VAL-083 (Dianhydrogalactitol) [2] Temozolomide or [2] Lomustine or [2] Carboplatin	3	Glioblastoma Multiform	August 2019	NCT03149575
[4] Capecitabine [2] Temozolomide	1,2	Glioblastoma Multiform Glioblastoma	June 2021	NCT03213002
[6] Cisplatin [2] Temozolomide	2	High-grade Gliomas	December 2017	NCT02263105
[7] SGT-53 [2] Temozolomide	2	Recurrent Glioblastoma	December 2019	NCT02340156
[8] Cediranib Maleate [9] Olaparib [1] Bevacizumab	2	Recurrent Glioblastoma	October 2019	NCT02974621
[10] Neratinib [3] CC-115 [11] Abemaciclib [2] Temozolomide	2	Glioblastoma	May 2021	NCT02977780
[12] Nivolumab [1] Bevacizumab [13] Ipilimumab	3	Recurrent Glioblastoma	January 2018	NCT02017717
[14] Toca 511 [14] Toca FC [2] Lomustine [2] Temozolomide [1] Bevacizumab	2,3	Glioblastoma Multiform	September 2019	NCT02414165
[14] VB-111 [1] Bevacizumab	3	Glioblastoma	December 2017 (primary outcome)	NCT02511405
Dendritic cell vaccine plus [2] Temozolomide	1,2	Glioblastoma Multiform	December 2019	NCT02649582
alpha-IFN [2] Temozolomide	3	Glioblastoma	December 2017	NCT01765088
CIK (Cytokine-Induced Killer Cells) [2] Temozolomide	4	Advanced Malignant Gliomas	July 2030	NCT02496988
[15] DNX-2401 With Interferon Gamma (IFN-γ)	1	Recurrent Glioblastoma or Gliosarcoma Brain Tumors	August 2018	NCT02197169
[15] DNX-2401 [16] Pembrolizumab	2	Brain Cancer Glioma Glioblastoma	June 2020	NCT02798406

[1] VGEF-inhibitor; [2] alchilating agent; [3] EGFR-inhibitor; [4] Thymidylate synthase inhibitor; [5] mTOR (mammalian target of rapamycin)-inhibitor; [6] DNA-binding inhibitor; [7] liposome encapsulating the wtp53 DNA sequence; [8] VEGFR inhibitor; [9] PARP inhibitor; [10] tyrosine kinase inhibitor; [11] Dual Inhibitor of CDK4 (cycline dependent kinase) and CDK6; [12] anti PD-1R (programmed death receptor) antibody; [13] anti CTLA4 (cytotoxic T-lymphocyte antigen 4)-antibody; [14] oncolytic virotherapy; [15] oncolytic adenovirus; [16] anti PD-1.

1.2 Autophagy

Autophagy is an evolutionary conserved self-degradation process that describes the lysosomal mediated turnover of intracellular components or pathogens. The term “autophagy” is derived from the Greek meaning “eating of self” and was invented by Christian de Duve in 1963 (Klionsky, 2008). It serves as basal quality control mechanism and is stimulated in response to stress and nutrient deprivation to maintain cellular homeostasis. Thereby, autophagy removes long-lived and damaged proteins, lipids and organelles as well as invasive microbes and provides the basic building blocks for cellular metabolism.

1.2.1 Molecular machinery

Autophagy is a very complex process that is genetically regulated by over 30 autophagy-related genes (ATGs). The delivery of cytoplasmic materials to the lysosome can be mediated through various types of autophagy: microautophagy, chaperone-mediated autophagy and macroautophagy. In chaperone-mediated autophagy, which only occurs in mammalian cells, proteins with a specific consensus sequence (KFERQ) are recognized by chaperone proteins (e.g. Hsc-70) and translocate across the lysosomal membrane via binding to the lysosomal associated membrane protein LAMP2A (lysosomal associated membrane protein 2A) (Zhang, 2013; Feng et al., 2014). The term microautophagy describes the direct engulfment of cytoplasmic material by the lysosome (Zhang, 2013). It is achieved by the invagination of lysosomal membranes to encircle cellular constituents such as proteins and lipids. Macroautophagy (hereafter referred to as autophagy) is the best characterized type of autophagy. The process requires the formation of double-membrane autophagosomes that sequester proteins, lipids, organelles or invasive microbes and fuse with lysosomes for breakdown by acidic hydrolases (Zhang, 2013).

In mammalian cells, the initiation of the autophagosome after stress stimuli like amino acid starvation mainly occurs at the endoplasmatic reticulum (ER) membrane by formation of the omegasome (Axe et al., 2008). Thereby, the activated ULK1 kinase complex (unc-51 like autophagy activating kinase 1) translocates to an ATG9 marked location of the ER and recruits class III phosphatidylinositol 3-kinase (PI3K). ATG9 vesicles, which can also act at the stage of membrane delivery to the expanding phagophore, appear to originate from the Golgi-endosomal system, and cycling of ATG9 is controlled by diverse mechanisms (Yu et al., 2018). Growth of the phagophore requires the input from several intracellular compartments as membrane sources, which is facilitated by vesicular transport or transient membrane contact (Yu et al., 2018). Subsequently, WIPI2 (WD repeat domain, phosphoinositide interacting 2) attaches to the growing phagophore and recruits the

ubiquitin-like E3-like complex ATG12-ATG5-ATG16L1 (Dooley et al., 2014). Together with the second ubiquitin-like conjugation system LC3 (microtubule associated protein 1 light chain 3), ATG12-ATG5-ATG16L1 catalyzes the conjugation of phosphatidylethanolamine (PE) to LC3 and facilitates the conversion of cytosolic LC3-I into a membrane-associated LC3-II localized on the autophagosomal membrane. Both ubiquitin-like conjugation systems play an essential role in membrane elongation of the autophagosome (He and Klionsky, 2009). Autophagosome closure as well as fusion with the lysosome is mediated by SNARE proteins. The mature autophagosomes are transported close to the lysosomes via trafficking along the microtubules (Fass et al., 2006; Kimura et al., 2007). Subsequently the formation of the autolysosome starts with the fusion of the outer autophogosomal membrane with the lysosomal membrane. Lysosomal hydrolases break up the inner autophagosomal membrane, and the autophagosomal content is degraded. During this process the degraded building blocks are transported out of the lysosome and the lysosome shrinks. Finally, the autolysosomes disintegrate, and the lysosomal membrane proteins are recycled (Yu et al., 2010; Yu et al., 2018) (Figure 1.1).

While nonselective autophagy is used for the degradation of bulk cytoplasm under starvation conditions, selective autophagy specifically targets damaged organelles such as mitochondria (mitophagy), peroxisomes (pexophagy), ribosomes (ribophagy) or ER (reticulophagy), as well as aggregated proteins (aggrephagy) and intracellular microbes (xenophagy) (Dunn et al., 2005; Levine, 2005; Klionsky et al., 2007; Wyant et al., 2018).

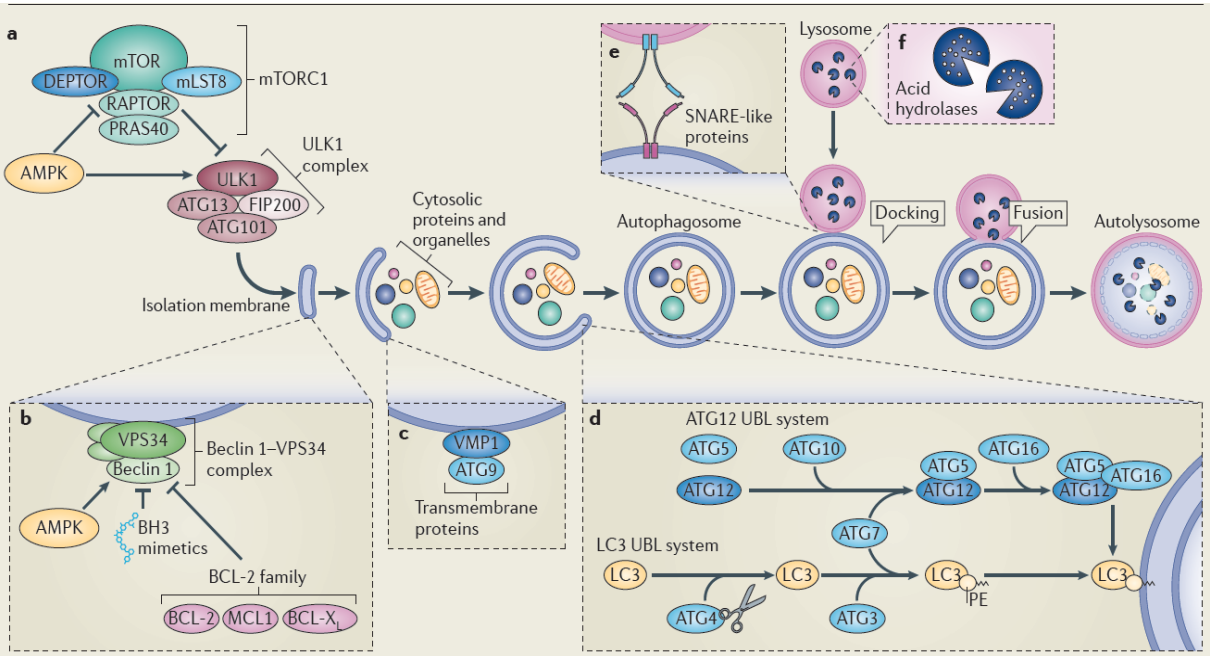

Figure 1.1: Regulation of the autophagic pathway.
In mammals, the initiation of the core autophagic pathway often starts at the endoplasmatic reticulum by formation of the omegasome (Yu et al., 2018). The growing phagophore encloses cytosolic cargo, and the mature autophagosome subsequently fuses with the acidic lysosome, resulting in the

degradation of the autophagosomal content. Thereby, the plasma membrane and several organelles may provide membrane sources for the generation of the autophagosome. Many protein complexes are involved in the regulation of autophagy. a | The mTORC1 complex inhibits ULK1, which is an important initiator of autophagy. b | The VPS34-Beclin-1 complex is usually inactivated by antiapoptotic BCL2 family members, and upon activation, it mediates the nucleation of the isolation membrane. c |The transmembrane proteins VMP1 (vacuole membrane protein 1) and ATG9 are important for the recruitment of lipids to the isolation membrane. d | The elongation and formation of the autophagosome is driven by the ubiquitin-like conjugation systems LC3 and ATG12. e | The closure of the autophagosome and fusion with the lysosome is performed by the interaction of SNARE-like proteins. f | Finally, acidic hydrolases degrade the enclosed cellular cargo in the autolysosome (Mariño et al., 2014).

1.2.2 Signaling pathways that regulate autophagy

Autophagy is upregulated under various types of stress, including starvation, ER stress, oxidative stress, hypoxia and mitochondrial damage (Kroemer et al., 2010). The best-characterized signaling hub for autophagy regulation is the mTORC1 complex (mammalian target of rapamycin complex 1). The autophagy inhibitor mTORC1 is regulated by a wide range of signals, including nutrient-, energy- and growth factor sensing (Goberdhan et al., 2016). Under conditions of starvation, autophagy is upregulated in order to provide the building blocks for cellular metabolism. Upon sensing of amino acids, the mTORC1 complex is activated either directly or indirectly via Rag proteins or class III PI3K (Long et al., 2005; Nobukuni et al., 2005; He and Klionsky, 2009). Thereby, activated mTORC1 inhibits autophagy by regulating the ULK1 complex. In addition, amino acids have been described to inhibit RAF1 (RAF proto-oncogene serine/threonine-protein kinase), which downregulates the mitogen-activated protein kinases MAP2K1/MAP2K2 and ERK1/2 (extracellular signal-regulated protein kinases 1 and 2) and the autophagic activity (Pattingre et al., 2003).

Furthermore, the PI3K-AKT1 (AKT serine/threonine kinase) pathway is an important upstream regulator of mTORC1 (Manning and Cantley, 2007). Sensing of growth factors such as IGF1 (insulin-like growth factor) promotes the phosphorylation of AKT1 at serine 473 (Alessi et al., 1996). When phosphorylated, AKT1 inhibits autophagy by suppressing the inhibitory action of TSC (tuberous sclerosis complex) on mTORC1 activity (Li et al., 2002; Heras-Sandoval et al., 2014). In contrast, activation of the energy sensor AMPKalpha promotes autophagy by suppressing mTORC1 activity on the one hand and by direct activation of the ULK1/2 complex on the other hand (Gwinn et al., 2008; Behrends et al., 2010). AMPKalpha-phosphorylation of the threonine residue 172 in the catalytic α-subunit and subsequent activation of the AMPKalpha pathway is positively regulated by the ratio of AMP/ATP (Alers et al., 2012).

Besides nutrient sensing, stress responses like ER stress, hypoxia or oxidative stress also play fundamental roles in the regulation of autophagy. ER stress results in the unfolded

protein response (UPR) and release of Ca^{2+} into the cytosol and has been described to trigger autophagy. Autophagy induced by hypoxia can be regulated either by mTORC1, by HIF-1 (hypoxia inducible factor 1) signaling or by hypoxia-driven ER-stress (He and Klionsky, 2009). Recently, G protein-coupled receptors (GPCRs) and ion channels have emerged as important mediators of autophagy (Wauson et al., 2014; Kondratskyi et al., 2018). GPCRs regulate autophagy by various downstream molecules, including mTOR, cAMP (cyclic adenosine monophosphate), PLC (phospholipase c), MAPK (mitogen-activated protein kinase) and AMPKalpha. Ion channels can exert stimulatory or inhibitory actions and most reports have focused on calcium channels in this context. However, the effect of on autophagy is complex and highly dependent on the localization of the channel, expression level and cell type.

1.2.3 Selective autophagy of organelles

As mentioned in chapter 1.2.1, several selective forms of autophagy have been elucidated in the recent years. The selective autophagy of organelles is a critical mechanism to maintain organelle integrity on the one hand and an adequate number of organelles on the other hand (Anding and Baehrecke, 2017). Among organelle-specific autophagy, the clearance of mitochondria (mitophagy), peroxisomes (pexophagy), lysosomes (lysophagy), ER (reticulophagy), ribosomes (ribophagy), chloroplasts (chlorophagy) and of the nucleus (nucleophagy) has been identified (Anding and Baehrecke, 2017; Wyant et al., 2018). The following chapters address the selective degradation of mitochondria and lysosomes.

1.2.3.1 Mitophagy

Mitochondria are able to counteract stress conditions either by remodeling of the mitochondrial network or by activation of the mitochondrial UPR, which increases the transcription of mitochondrial chaperons, proteases and antioxidative proteins (Roberts et al., 2016). If these responses are not sufficient to maintain mitochondrial function, the organelle needs to be removed via autophagy. The term mitophagy describes the selective removal mitochondria by autophagy and was introduced by John J. Lemasters (Lemasters, 2005). Mitophagy regulates the number of mitochondria within the cell to match the metabolic demand and acts as a quality control mechanism to remove damaged mitochondria. Impaired mitophagy can lead to the accumulation of damaged organelles and is implicated in a variety of diseases, including cancer, cardiovascular disorders and neurodegenerative diseases (Chourasia et al., 2015).

In yeast, mitophagy has been observed to occur in response to enforced respiration and requires the autophagy protein ATG32 that can interact with ATG8 (homologue of

mammalian LC3 family, which consists of at least six proteins: LC3A, B and C, GABARAP, GABARAPL1 and GABARAPL2) either directly or indirectly through ATG11 (Kanki et al., 2009; Youle and Narendra, 2011).

The elimination of mitochondria takes place via several distinct mechanisms and can be classified in ubiquitin dependent pathways, which include ubiquitination of mitochondrial surface proteins and subsequent recognition by the autophagic machinery, and in ubiquitin independent pathways (Khaminets et al., 2016).

To date, the most studied canonical mitophagy pathway relies on the outer mitochondrial membrane (OMM) kinase PINK1 (PTEN induced putative kinase 1) and the cytosolic E3 ubiquitin ligase Parkin (parkin RBR E3 ubiquitin protein ligase), which is frequently mutated in Parkinson's disease (Kitada et al., 1998; Valente et al., 2004). In healthy mitochondria, PINK1 gets imported into mitochondria and is rapidly degraded by the rhomboid protease PARL (presenilin associated rhomboid like) (Green and Levine, 2014). Upon mitochondrial depolarization (e.g. by protonophores or mitochondrial permeability transition) the mitochondrial import and degradation of PINK1 is impeded, thus allowing its accumulation at the OMM (Lazarou et al., 2012). Subsequently, PINK1 recruits Parkin to the mitochondria (Narendra et al., 2008; Narendra et al., 2010). Parkin mediates ubiquitination of the damaged mitochondria, which is followed by accumulation of the autophagy receptors on the mitochondrial membrane and subsequent recruitment into autophagosomes (Youle and Narendra, 2011). Autophagy receptors such as SQSTM1 (sequestosome 1), NBR1 (neighbor of BRCA1 gene 1), NDP52 (calcium binding and coiled-coil domain 2) and OPTN (optineurin) contain an ubiquitin binding domain and a LC3 interaction region (LIR), which facilitates the recognition of ubiquitinylated mitochondria by the autophagic machinery (Roberts et al., 2016). Ubiquitination of the Parkin substrates MFN1 and MFN2 (mitofusins 1, 2) and subsequent degradation is thought to promote the segregation of damaged mitochondria (Tanaka et al., 2010). Recently, it has been demonstrated that PINK1 is able to recruit autophagy receptors to the mitochondria independent of Parkin (Lazarou et al., 2015).

Reticulocyte maturation is a key developmental process that requires mitophagy, as mature red blood cells completely lack mitochondria. During this type of selective mitophagy, BNIP3L (BCL2 interacting protein 3 like, also called NIX), which is localized on the OMM, binds to LC3 and GABARAP (GABA receptor-associated protein) through the WXXL-like motif (Schweers et al., 2007; Schwarten et al., 2009; Novak et al., 2010). Moreover, BNIP3L and its related protein BNIP3 (BCL2 interacting protein 3) get upregulated under hypoxic conditions via HIF-1 or FOXO3 (forkhead box O3) signaling and promote mitophagy (Zhang et al., 2008; Ding and Yin, 2012). The induction of mitophagy by hypoxia prevents the accumulation of reactive oxygen species (ROS) due to damaged mitochondria and can

circumvent cell death (Zhang et al., 2008). Upon their upregulation, BNIP3 and BNIP3L form homodimers and insert into the OMM. Both proteins act independently of mitochondrial ubiquitination by either direct recruitment of the autophagic machinery to mitochondria via interaction with LC3, or by promoting the release of BECN1 from BCL2 (Schwarten et al., 2009; Zhang and Ney, 2009; Hanna et al., 2012). In addition, another mitochondrial outer membrane protein, FUNDC1 (FUN14 domain containing 1), may promote mitophagy under hypoxic conditions via interaction with LC3 (Liu et al., 2012).

Besides receptor-mediated mitophagy, damaged mitochondria are able to recruit the autophagy machinery itself for *de novo* autophagosome formation independently of LC3 (Itakura et al., 2012). Another mechanism of mitophagy in vertebrates involves cardiolipin exposure on damaged mitochondria and subsequent binding to LC3 (Chu et al., 2013). However, although our understanding of selective autophagy made a great progress in the last decade, the spectrum of autophagy receptors and possible signaling pathways involved in mitophagy regulation is still not completely known.

Besides the removal of whole mitochondria, the degradation of mitochondria-derived vesicles was observed as another defense mechanism of mitochondrial oxidative stress which is thought to take place in higher eukaryotes (Neuspiel et al., 2008). Thereby, vesicles budding from mitochondria are shuttled to the peroxisome or lysosome for degradation (see Figure 1.2) (Soubannier et al., 2012; McLelland et al., 2014; Le Guerroué et al., 2017).

The most commonly used pharmacological agents that induce cellular mitophagy affect the respiratory chain. These agents induce mitochondrial depolarization and mainly stimulate PINK1- and Parkin-dependent mitophagy. Proton ionophores like carbonyl cyanide m-chlorophenyl hydrazine (CCCP) and carbonyl cyanide-4-(trifluoromethoxy)phenylhydrazone (FCCP) are capable of uncoupling the oxidative phosphorylation from the electron transport chain (ETC) by transporting H^+ across the inner mitochondrial membrane (IMM) (Liberman et al., 1969). The K^+ ionophore valinomycin facilitates breakdown of the mitochondrial membrane potential by uncontrolled K^+ influx (Ashrafi and Schwarz, 2013). In addition, mitochondrial toxins such as the respiratory complex III inhibitor antimycin A and the F_1F_O-ATP synthase inhibitor oligomycin induce mitophagy through increased superoxide generation and mitochondrial depolarization. In general, a variety of Parkinsonian toxins have been described to induce ROS accumulation and mitochondrial damage, which finally triggers mitophagy (Georgakopoulos et al., 2017). Furthermore, the loss of iron was identified as a potent inducer of mitophagy. Allen and coworkers demonstrated that the iron chelator deferiprone (DFP) induces mitophagy independently of mitochondrial depolarization and the PINK1-Parkin pathway (Allen et al., 2013). However, a variety of studies reported that the mitophagic response to other iron chelators depends on the collapse of the mitochondrial

membrane potential (Park et al., 2012; Kirienko et al., 2015). In addition, activation of the NAD^+-dependent deacetylase SIRT1 has been described to trigger mitophagy via a not fully understood pathway (Roberts et al., 2016).

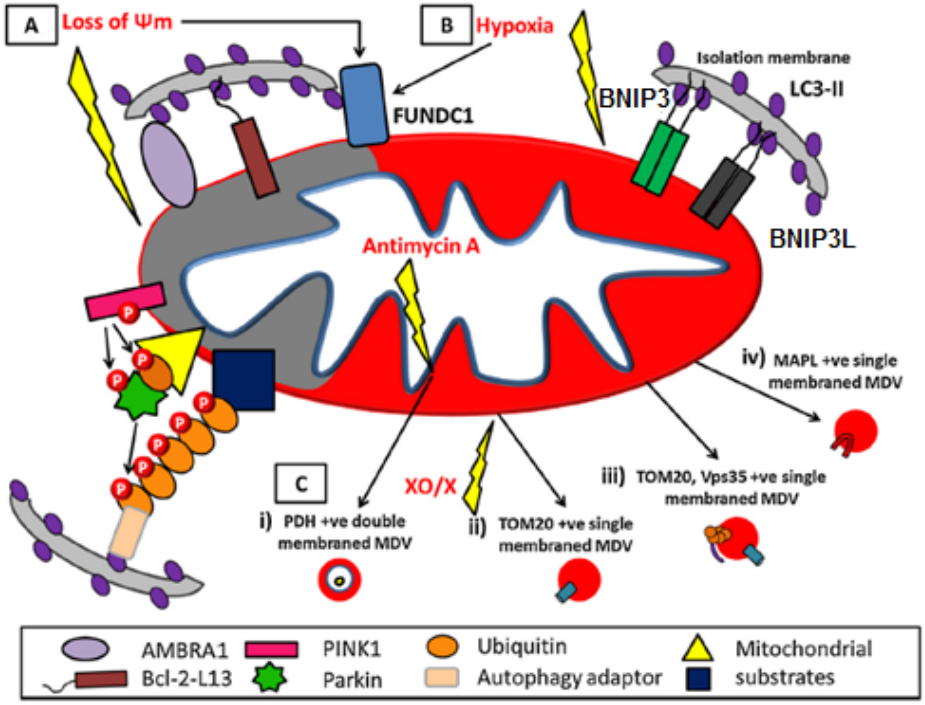

Figure 1.2. Mitochondrial quality control mechanisms.
A I Mitochondrial depolarization (depicted in grey) promotes the accumulation of PINK1 and subsequent recruitment of Parkin, which mediates ubiquitination of the mitochondrion. B I Hypoxia drives the upregulation of BNIP3 and BNIP3L, which can form dimers and recruit autophagosomes to the mitochondrion through their LC3 interaction motifs. In addition, FUNDC1 acts as a mitophagy receptor upon mitochondrial depolarization and hypoxia. C I The generation of different mitochondria-derived vesicles is induced upon treatment with antimycin A (inhibits complex III of the electron transport chain), or treatment with xanthine oxidase/xanthine (XO/X). Figure was adapted from Roberts et al., 2016.

1.2.3.2 Lysophagy

The term lysophagy describes the selective elimination of damaged lysosomes by the autophagic machinery to protect cells from the hazardous release of lysosomal content into the cytosol. Maejima et al. showed that the autophagic machinery is selectively recruited to damaged lysosomes, e.g. following treatment with the lysosmotropic agent Leu-Leu-O-methyl (LLOMe). These lysosomes get engulfed by autophagosomes and are subsequently degraded by a subpopulation of intact lysosomes (Maejima et al., 2013).

Compared to the widely explored field of selective mitophagy, less is known about the recognition targets of selective lysophagy. Recently, galectins have been described to be

implicated in selective lysophagy due to their ability to bind β-galactoside glycoconjugates. These β-galactosides are normally located in the lumen of endomembranes such as lysosomes, but get exposed to the cytosol upon endomembrane damage (Maejima et al., 2013). Moreover, Chauhan et al. reported that the E3 ligase TRIM16 (tripartite motif containing 16) recognizes damaged lysosomes through interaction with galectin-3 and thereby associates with the key autophagy regulators ULK1 and BECN1 (Chauhan et al., 2016). In addition, it has been recently shown that the ubiquitin-directed AAA-ATPase VCP (valosin containing protein) is directed to damaged lysosomes and together with cofactors promotes autophagosome formation (Papadopoulos and Meyer, 2017). Thereby, VCP plays an essential role for the degradation of ruptured lysosomes and cell survival after lysosomal damage.

1.3 Mitochondria in health and disease

Mitochondria, the “power plants” of the cells, arose around two billion years ago from an alpha-proteobacterium engulfed by a eukaryotic progenitor (Lane and Martin, 2010). Although mitochondria maintained the circular genome and double membrane character of their ancestors, their functions have dramatically changed during evolution (Gabaldón and Huynen, 2004). Besides their main function, which is providing energy in terms of ATP, mitochondria host many other biosynthetic pathways and contribute to cellular stress responses like autophagy and apoptosis (Nunnari and Suomalainen, 2012).

1.3.1 The respiratory chain

The inner mitochondrial membrane (IMM) comprises the five protein complexes of the respiratory chain and encloses the mitochondrial matrix. It is separated from the outer mitochondrial membrane (OMM) by the inter membrane space (IMS). Chemical energy in terms of ATP is mainly synthesized through oxidative phosphorylation at the IMM. Thereto, the electron transport chain (ETC) is fed with electron carriers (NADH, $FADH_2$) from the catabolic processes glycolysis, fatty acid oxidation and tricarbolic acid (TCA) cycle. Electrons are transported from complex I to complex IV by intra-protein electron transfer or the mobile carries ubiquinone and soluble cytochrome c. Thereby, the redox potentials along the ETC gradually increase, with molecular oxygen being the final electron acceptor at complex IV. The resulting free energy enables proton translocation from the mitochondrial matrix into the IMS through the proton pumping enzymes complex I (NADH-ubiquinone oxidoreductase), III (cytochrome bc_1) and IV (cytochrome c oxidase). In total, the concerted action of these three complexes leads to the translocation of ten protons from the matrix into the IMS upon

oxidation of one NADH molecule. The electrochemical gradient of protons finally drives the F_1F_O-ATP synthase (complex V) to phosphorylate ADP (Figure 1.3) (Sazanov, 2015).

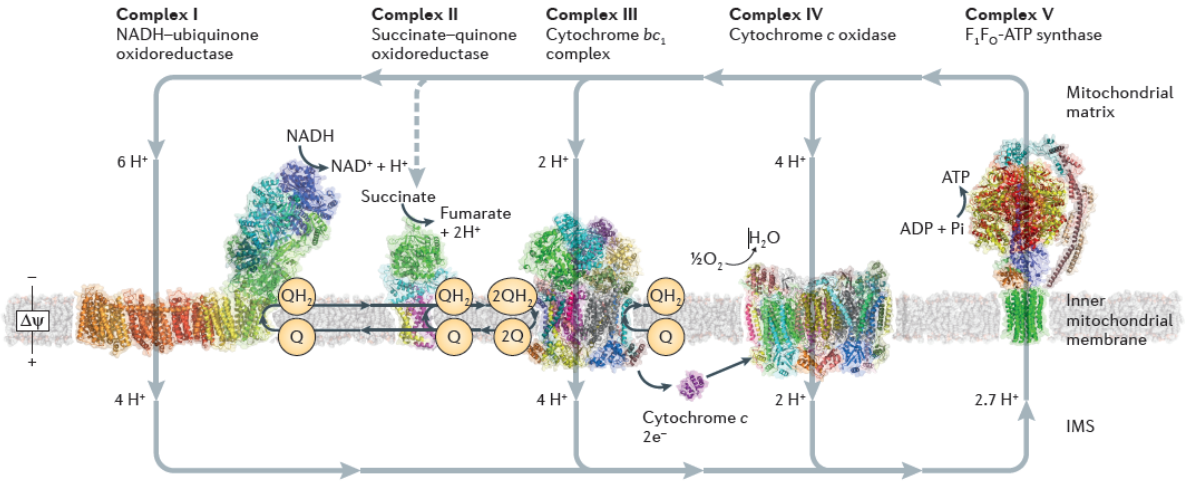

Figure 1.3. The mitochondrial respiratory chain.
The mammalian electron transport chain comprises four main complexes: NADH-ubiquinone oxidoreductase (I), succinate-quinone oxidoreductase (II), cytochrome bc1 (III) and cytochrome c oxidase (IV). Electrons are transported between complex I to complex IV by redox-reactions to finally reduce molecular oxygen. As the redox potentials along the ETC gradually increase, the resulting free energy enables the transport of ten protons per oxidized NADH from the mitochondrial matrix to the IMS. The resulting electrochemical gradient of protons finally drives the F_1F-ATP synthase (complex V) to phosphorylate ADP. (ETC image was prepared by G. Minhas, Medical Research Council, Mitochondrial Biology Unit, Cambridge, UK; (Sazanov, 2015)).

1.3.2 The mitochondrial network

The mitochondrial network is a very dynamic system and undergoes remodeling by fusion and fission events through highly conserved dynamin-related proteins (DRPs). Division is performed by DAPK2 (also called DRP-1) assembly into helical structures at constriction sites of mitochondria and conformational changes upon GTP hydrolysis. Mitochondrial fusion requires the action of MFN1 and MFN2 for the OMM and the mitochondrial dynamin-like GTPase OPA1 for the IMM (Friedman and Nunnari, 2014). Both fusion and fission are essential for maintaining mitochondrial function.

1.3.3 Mitochondria and cell death

Besides the essential metabolic functions of mitochondria, mitochondrial superoxide production is a major source of ROS within the cell. Superoxide is generated at several sites of the mitochondria as toxic byproducts of oxidative phosphorylation (Brand, 2010). ROS production contributes to damage of cellular lipids, nucleic acids and proteins as well as to

retrograde redox signaling from the organelle to the cytosol and nucleus (Murphy, 2009). Mitochondrial oxidative damage can lead to severe mitochondrial dysfunction and subsequent cell death and contributes to a wide range of pathologies (Murphy, 2009).

In general, mitochondria are implicated in different cell death pathways. During apoptosis, increased recruitment of DAPK2 to mitochondria triggers their fragmentation, whereas mitochondrial fusion events, e.g. stimulated by BCL2 proteins, protect the cell from apoptosis (Rolland et al., 2009; Cleland et al., 2011). In addition, DAPK2 positively regulates BAX/BAK1-mediated mitochondrial outer-membrane permeabilization (MOMP) in intrinsic apoptosis (Frank et al., 2001; Wasiak et al., 2007; Nunnari and Suomalainen, 2012). A detailed description of the mitochondrial apoptosis pathway can be found in 1.4.1.

Moreover, the IMM harbors a high conductance channel named mitochondrial permeability transition pore (mPTP). Opening of the pore renders the IMM permeable to solutes up to the size of 1500 Da. Short-term openings might play a physiological role in the regulation of calcium and ROS homeostasis (Zorov et al., 2014), while long lasting openings can lead to severe mitochondrial depolarization and cell death in terms of apoptosis or necrosis (Petronilli et al., 2001; Galluzzi et al., 2018) (see also Table 1.2 in chapter 1.4). Calcium overload of the mitochondrial matrix is the best-known initiator for mPTP opening, but also pronounced accumulation of ROS is thought to induce permeability transition (Zorov et al., 2014; Bernardi and Di Lisa, 2015). The molecular nature of the mPTP has been discussed for several years. However, recent findings suggest that the mPTP possibly forms from the F_1F_O-ATP synthase and is regulated by cyclophilin D (CYPD) (Bernardi, 2013; Bernardi and Di Lisa, 2015; Bernardi, 2018).

1.4 Programmed cell death

Regulated cell death (RCD) is a tightly controlled mechanism that balances the equilibrium between survival and death. Over the past decades, several genetically encoded mechanisms that target the elimination of damaged, superfluous or potentially harmful cells were unraveled. In contrast to accidental cell death that occurs upon intense physical, chemical or mechanical stress and often comes along with inflammation processes, all RCD forms rely on tightly regulated mechanisms. In multicellular life forms, RCD strongly contributes to organismal homeostasis under physiological and pathophysiological conditions (Galluzzi et al., 2018). Indeed, programmed cell death forms also take place in unicellular eukaryotes that live in colonies as well as in some prokaryotes like *Escherichia coli (E. coli*) (Cornillon et al., 1994; Madeo et al., 1997; Green and Fitzgerald, 2016). RCD can occur as physiological program for development or tissue turnover, but also upon intracellular or

extracellular stress when cellular homeostasis cannot be restored by adaptive stress responses. Importantly, RCD operates at the level of the organism or colony to enable overall survival by sacrificing unwanted cells (Galluzzi et al., 2016).

For many years, cell death was classified into three distinct forms by morphological features: apoptosis (type I), autophagy-dependent cell death (type II) and necrosis (type III). However, in 2005, the “Nomenclature Committee on Cell Death” started to define different cell death mechanisms on genetic, biological, pharmacological and functional level to overcome the limitations of only morphological classifications. This work led to the definition of several additional cell death forms (Galluzzi et al., 2018). The regulated cell death models for mammalian cells are listed in Table 1.2. In the following chapters, the RCD forms extrinsic and intrinsic apoptosis, necroptosis, ferroptosis, autophagy-dependent cell death and lysosome-dependent cell death are explained in detail.

Table 1.2. Regulated cell death models of mammalian cells (Galluzzi et al., 2018).

Name	Description
Autophagy-dependent cell death/ Autophagic cell death (ACD)	Mechanistically depends on components of the autophagic machinery
Entotic cell death	Originates from actomyosin-dependent cell-in-cell-internalization and is executed by lysosomes
Extrinsic apoptosis	Driven by perturbations of the extracellular microenvironment, which are detected by plasma membrane receptors and propagated/executed by caspases
Ferroptosis	Induced by oxidative perturbations of the intracellular microenvironment, can be inhibited by iron chelators and lipophilic antioxidants
Immunogenic cell death	Type of cell death that activates an adaptive immune response in immunocompetent hosts
Intrinsic apoptosis	Is initiated by perturbation of the extra- or intracellular microenvironment, includes mitochondrial outer membrane permeabilization (MOMP) and is executed by caspases
Lysosome-dependent cell death/ Lysosomal cell death (LCD)	Is triggered by lysosomal membrane permeabilization (LMP) and executed mainly by cathepsins, with optional involvement of MOMP and caspases
Mitochondrial-permeability transition (MPT)-driven necrosis	Is triggered by perturbations of the intracellular microenvironment and relies on CYPD
Necroptosis	Is initiated by perturbations of extra- or intracellular homeostasis and critically depends on MLKL, RIPK3, and sometimes on RIPK1
NETotic cell death	ROS-dependent type of cell death that is restricted to cells of the hematopoietic derivation and is associated with NET extrusion
Parthanatos	Is induced by PARP1 hyperactivation and precipitated by bioenergetic catastrophe and AIF-dependent and MIF-dependent DNA degradation
Pyroptosis	Is often a consequence of inflammatory caspase activation and depends on the formation of plasma membrane pores by members of the gasdermin family

1.4.1 Intrinsic and extrinsic apoptosis

Apoptosis is the best-studied form of programmed cell death, which operates during embryonic development to build up complex, multicellular tissues as well as in adult organisms to maintain cellular homeostasis and to remove potentially harmful cells. The importance of this pathway was stressed by gain- and loss-of-function mutations of genes essential for the apoptotic machinery. Insufficient apoptosis may lead to cancer and autoimmunity, whereas accelerated apoptosis can contribute to chronic degenerative diseases, immunodeficiency and infertility (Danial and Korsmeyer, 2004).

Apoptosis can be characterized by typical morphological changes including membrane blebbing, cell shrinkage, chromatin condensation and fragmentation (Kerr et al., 1972) and by biochemical changes like MOMP (see below), activation of caspases and activation of catabolic hydrolases (Galluzzi et al., 2009).

The execution of apoptosis requires the cleavage function of caspases, a family of aspartate proteases, which reside in the cytosol as inactive zymogens (Thornberry and Lazebnik, 1998). Activator caspases can autocatalytically activate themselves and subsequently activate other downstream caspases. The caspases participate in a proteolytic cascade that is triggered by two major pathways, the extrinsic and the intrinsic apoptotic pathway (see also Table 1.2.)

Intrinsic apoptosis is activated by several microenvironmental changes and cellular stress conditions, including ER-stress, DNA damage, growth factor withdrawal, replication stress or ROS overload. The critical, irreversible trigger for the execution of intrinsic apoptosis is mitochondrial outer membrane permeabilization (MOMP), which is regulated by BCL2 proteins. This protein family can be categorized into three subgroups according to their four conserved BCL2 homology domains: the proapoptotic multidomain proteins (BAX, BAK1, BOK), the antiapoptotic multi-domain proteins (BCL2, BCL2L1, BCL2L2, MCL1), and the BH3-only proteins (BIM, BID, PUMA, BAD, NOXA etc.) (Czabotar et al., 2014). In response to apoptotic stimuli, BAX and BAK1 get activated by BH3 only proteins and form pores across the outer mitochondrial membrane (OMM) by oligomerization, thereby mediating MOMP. Anti-apoptotic BCL2 proteins antagonize MOMP by direct sequestration and inhibition of BAX and BAK1 or BH3-only proteins (Kim et al., 2006; Galluzzi et al., 2018). It should be stressed that MOMP is distinct from mitochondrial permeability transition pore (mPTP)-opening as described in chapter 1.3.3: MOMP exclusively occurs during apoptosis and relies on BAX and BAK1 as pore-forming proteins. In contrast, an opening of the mPTP can trigger apoptosis as well as necrosis, however, the exact composition of the permeability transition pore complex is still under intense investigation (Figure 1.4) (Petronilli et al., 2001;

Galluzzi et al., 2018). MOMP subsequently results in the release of pro-apoptotic factors such as cytochrome c, apoptosis-inducing factor (AIF) and endonuclease G into the cytosol. Cytochrome c binds to caspase 9 and APAF1 (apoptotic peptidase activating factor 1) and triggers the assembly of the caspase-activating complex called apoptosome. Subsequently, the effector caspases 3 and 6 get activated and mediate apoptosis (Mariño et al., 2014; Galluzzi et al., 2018).

Extrinsic apoptosis is initiated by extracellular signals and depends on the activation of death receptors or dependence receptors including FAS (Fas cell surface death receptor) and members of the TNF (tumor necrosis factor) receptor superfamily. In response to ligation of the death receptors, the death inducing signaling complex (DISC) assembles at the intracellular tail of the receptor. The DISC complex functions as a platform for activation of caspase 8 and 10 by autoproteolytic cleavage, which subsequently activates the executioner caspases 3 and 7 (Galluzzi et al., 2018). In some cell types and in most cancer cells, activation of caspase 3 and 7 is inhibited by XIAP. In that case, extrinsic apoptosis relies on the cleavage on BID (BH3 interacting domain death agonist) by caspase 8. The truncated form of BID (tBID) subsequently triggers apoptosis via MOMP and caspase 9 activation (Figure 1.4) (Luo et al., 1998; Jost et al., 2009).

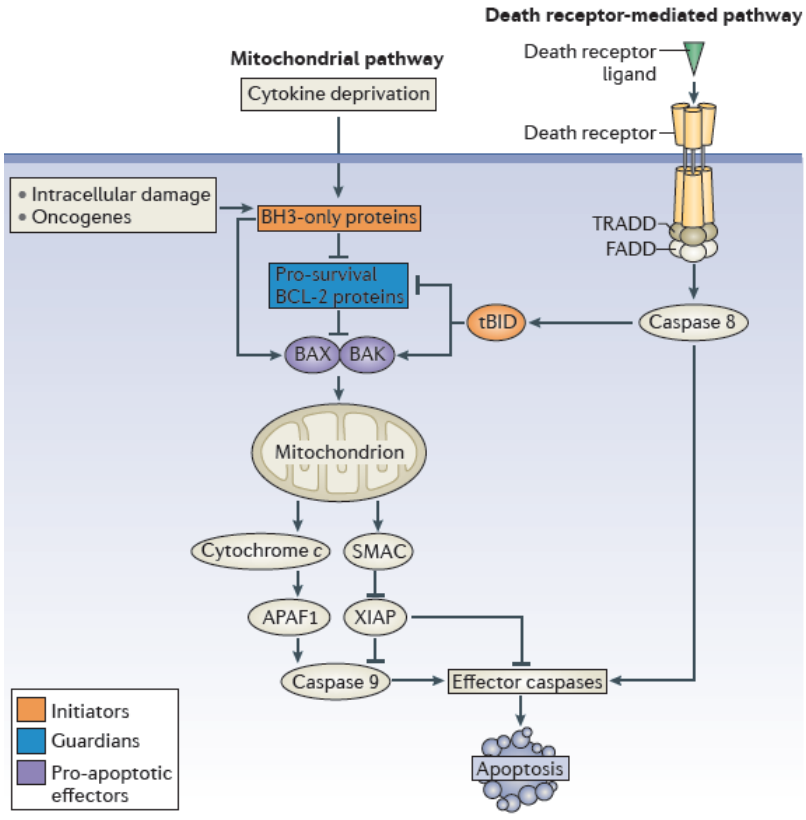

Figure 1.4. Apoptotic pathways.
The mitochondrial apoptotic pathway is regulated by BCL2 family members. Upon cytotoxic stimuli, the BH3 only family members inhibit pro-survival BCL2 proteins, thereby activating the pro-apoptotic BCL2 family members BAX and BAK1, which form pores through the outer mitochondrial membrane. Subsequently, cytochrome c is released and promotes caspase 9 activation on the scaffold protein APAF1. In addition, SMAC (second mitochondria-derived activator of caspases) is also released and blocks XIAP, further promoting caspase 9 activation. The extrinsic pathway of apoptosis is induced by death receptor ligands of the TNF family, leading to caspase 8 activation. Both pathways finally converge at the step of effector caspase activation. Moreover, caspase 8 induces the proteolysis of BID into tBID (truncated BID), which can amplify the apoptotic response (Czabotar et al., 2014).

1.4.2 Regulated (necrotic) cell death forms

For a long time, necrosis has been considered as a form of unregulated cell death that occurs accidentally due to physical or chemical threats. However, in the recent years it has been identified that necrosis can be tightly regulated and therefore therapeutically targeted. These types of regulated (necrotic) cell death include necroptosis, ferroptosis and CYPD-mediated opening of the mitochondrial permeability transition pore (mPTP) (see chapter 1.3.3 and Table 1.2) (Moreno-Gonzalez et al., 2016).

1.4.2.1 Necroptosis

The best-known form of regulated necrosis is necroptosis, which depends on the activation of RIPK3 (receptor interacting protein kinases 3), MLKL (mixed lineage kinase domain like pseudokinase) and, in case of TNFR-1 (tumor necrosis factor receptor 1)-driven necrosis, on RIPK1 (Galluzzi et al., 2018). RIPK1 is also a druggable target of necroptosis that can be inhibited by necrostatin-1 (Zhou and Yuan, 2014). Necroptosis can be activated by ligands of different cell death receptors such as TNF or TRAIL (TNF-related apoptosis inducing ligand) or by pathogen-recognition receptors (Moreno-Gonzalez et al., 2016). However, it is worth mentioning that necroptosis is not the default pathway activated be these mechanisms, which mainly induce inflammation and apoptosis. Still, under particular conditions, activation of these specific death receptors reveals a necroptotic response (Moreno-Gonzalez et al., 2016).

1.4.2.2 Ferroptosis

Ferroptosis is another form of regulated cell death that manifests in a necrotic phenotype following severe lipid peroxidation. Specific ferroptosis-inducing agents include RSL3, erastin and FIN56, while the enzyme GPX4 (gluthatione peroxidase 4) has emerged as the main inhibitor of ferroptosis due to its ability to rescue prevent lipid peroxidation (Yang et al., 2014; Galluzzi et al., 2018). Ferroptosis is dependent on oxidative stress and iron availability and can be inhibited by ROS scavengers as well as iron chelators (Galluzzi et al., 2018).

1.4.3 Autophagy-dependent cell death

Autophagy is generally considered to play a pro-survival role. It provides the cell with essential cellular building blocks under starvation conditions and reduces cellular stress through degradation of damaged organelles and macromolecules. Thereby, autophagy also promotes genomic stability by decreasing the cellular ROS levels.

However, in some developmental settings, autophagy can contribute to cellular demise. For example, stalk cells of *Dictyostelium discoideum* undergo developmental autophagy-dependent cell death (also called “autophagic cell death” [ACD]) (Kosta et al., 2004; Lam et al., 2007), and steroid-induced degradation of larval midgut cells of *Drosophila melanogaster* is reliant on autophagy (Denton et al., 2009). In addition, stress- and drug-induced ACD has been described to take place in several cancer cell models (Voss et al., 2010; Shchors et al., 2015; Dasari et al., 2017; Segala et al., 2017).

Collectively, strong autophagy induction can lead to ACD by excessive self-digestion in some cell types, implicating that the role of autophagy is highly dependent on its extent and the cellular context. Autophagic cell death is defined as a type of regulated cell death that relies on the autophagic machinery (Galluzzi et al., 2018). According to the recommendations of the “Nomenclature Committee on Cell Death 2018”, the term should be exclusively used when robust experimental evidence links cell death to components of the autophagy apparatus and when the execution of cell death does not engage other cell death forms such as apoptosis, necroptosis, or ferroptosis (Galluzzi et al., 2018) (see also Table 1.2.)

1.4.3.1 Autophagy-dependent cell death and cancer

The role of autophagy in cancer development and treatment response is very complex. In the early stages of tumorigenesis, autophagy has tumor-suppressive functions, as it is correlated with decreased oxidative stress and genomic stability (Gozuacik and Kimchi, 2004). Furthermore, it was reported that some autophagy-related genes act as tumor-suppressors (e.g. AMBRA1 [autophagy and beclin1 regulator 1], BECN1) (Sinha and Levine, 2008; Cianfanelli et al., 2015). In contrast, during later stages of tumor progression, autophagy has been reported to act in a tumor-promoting manner. When the tumor cells face environmental stress like hypoxia or nutrient deprivation, elevated autophagy can mitigate the stress conditions, thereby promoting tumor cell survival. Accordingly, pharmacological inhibition of autophagy may be effective for cancer treatment, as the inability to adapt to these stresses may drive the cells towards apoptosis (Maycotte and Thorburn, 2011). In contrast, in apoptosis-deficient cells, inhibition of autophagy might result in pro-inflammatory, necrotic cell death, which further promotes tumorigenesis (Degenhardt et al., 2006; Mantovani et al.,

2010). Moreover, various studies reported the successful pharmacological induction of ACD in different types of cancer as outlined below.

To date, several signaling pathways have been shown to be implicated in autophagic cell death in cancer cells. It was reported that inhibition of the nicotinamide phosphoribosyl-transferase by APO866 triggered ACD in leukemia and lymphoma cells. As cancer cells require a higher NAD^+ turnover rate compared to non-transformed cells, targeting this pathway could be an effective therapy for cancer treatment (Cea et al., 2012; Ginet et al., 2014). Furthermore, histone deacetylase inhibitors (e.g. suberoylanilide hydroxamic acid [SAHA]) have been described to induce an autophagy-associated form of cell death, which might be facilitated via downregulation of the AKT1 and mTOR axis and ER-stress (Liu et al., 2010). The kinases DAPK1 (death associated protein kinase 1) and DAPK2 have been described to regulate autophagy. Overexpression of either DAPK1 or DAPK2 showed hallmarks of ACD in some cancer cell lines, and their depletion attenuated autophagy induction following interferon-gamma treatment or starvation combined with tamoxifen administration (Inbal et al., 2002). Recently, a signalome-wide shRNA-based viability screen in A549 lung cancer cells identified GBA1 (glucosylceramidase beta) as a positive regulator of ACD induced by resveratrol (Dasari et al., 2017). An elevated level of GBA1 increased ceramide generation and was associated with typical autophagic features as well as cell death. Depletion of either *GBA1* or relevant autophagy genes attenuated cellular demise. Lima and coworkers found that SK1-I, an analog of sphingosine and SPHK1 (sphingosine kinase 1) inhibitor, induced autophagy as well as cell death, which could be partially rescued by depletion of the autophagy genes *BECN1* and *ATG5*. Interestingly, TP53 played an important role in SK1-I-induced cell death (Lima et al., 2018). In addition, the cholesterol metabolite dendrogenin A (DDA) was able to induce lethal autophagy in myeloma and acute myeloid leukemia *in vitro* and *in vivo* (Segala et al., 2017). Thereby, DDA increased NUR77 (nuclear receptor subfamily 4 group A member 1), NOR1 (organic solute carrier partner 1) and LC3 expression via LXR (liver X receptor) signaling. Collectively, various new concepts of autophagy dependent cell death in cancer cells emphasize the importance of this pathway for cancer therapy and the need to understand the underlying signaling pathways.

1.4.3.2 Autophagy-dependent cell death and glioblastoma

The dual function of either beneficial or detrimental autophagy in cancer cells is also observed in glioblastoma (GBM). The role of autophagy in temozolomide (TMZ)-induced cell death, which is routinely used for treatment of malignant gliomas, is still controversial and needs to be clarified. On the one hand, it was reported that late stage inhibition of autophagy enhanced TMZ-induced cell death and that TMZ-induced autophagy can even be

cytoprotective (Kanzawa et al., 2004; Katayama et al., 2007). Indeed, the late stage autophagy inhibitor chloroquine is currently in clinical trials for adjuvant therapy in GBM (Jawhari et al., 2016). Nevertheless, on the other hand, it was shown that autophagy potentiates TMZ-induced cytotoxicity, as knockdown of essential autophagy genes reduced cell death (Voss et al., 2010).

In addition, a variety of other cancer drugs are capable of inducing ACD in glioma cells. Cannabinoid receptor signaling was reported to trigger ACD in GBM cells and hepatocellular cancer via EIF2A (eukaryotic translation initiation factor 2A) phosphorylation, ER-stress and induction of TRIB3 (tribbles pseudokinase 3), which led to inhibition of AKT1 and mTOR (Salazar et al., 2009; Vara et al., 2011). In these studies, the cytotoxicity of tetrahydrocannabinol (THC), the main active component of cannabinoids, as well as the cannabinoid receptor-2 selective agonist JWH-015 were attenuated upon genetic or pharmacological inhibition of autophagy.

Gossypol, a natural compound derived from cotton seeds, was initially identified as an antifertility agent during the 1950s. The enantiomer (-)-gossypol (AT 101) is currently investigated in several clinical studies as an anticancer agent alone or in combination with other chemotherapeutics (Fulda and Kögel, 2015). It also has been described to act as a BH3 mimetic, thereby inactivating BCL2, BCL2L2 (BCL2 like 2; also called BCLW), BCL2L1 (BCL2 like 1, also called BCL-xL) and MCL1 (myeloid cell leukemia 1), and thus promoting apoptosis and autophagy by release of BECN1. However, it was recently reported that AT 101 rather indirectly inhibits antiapoptotic BCL2 family members by upregulation of NOXA via PKA (protein kinase A) activation and calcium increase (Soderquist and Eastman, 2016). Furthermore, AT 101 was also implicated in a variety of other signaling pathways, including inhibition of DNA synthesis and cell cycle progression, oxidative stress, iron chelation and BNIP3 activation (Wang and Rao, 1984; Wang et al., 2013; Kaza et al., 2014). Besides the induction of apoptosis, AT 101 has been shown to induce an autophagy-dependent type of cell death in prostate-deficient cancer, peripheral nerve sheath tumor cells and malignant glioma cells (Voss et al., 2010; Lian et al., 2011; Kaza et al., 2014). Still, the distinct mechanism how AT 101 triggers ACD remained to be elucidated.

Recently, it was reported that combination of imipramine, a tricyclic antidepressant, and the anticoagulant ticlopidine effectively triggers ACD in GBM cells *in vitro* and *in vivo* via induction of adenylate cyclase and cAMP elevation (Shchors et al., 2015). The increased cAMP level subsequently induced EPAC1/2 (exchange protein directly activated by cAMP 1) which is known to upregulate ERK1/2 signaling, thereby increasing the autophagic flux (Ugland et al., 2011).

1.4.4 Lysosome-dependent cell death

Lysosomes are considered as the cellular waste disposal system and contain several hydrolases for degradation of cellular macromolecules. Christian de Duve invented the term “suicide bags” for lysosomes in 1983 owing to the potent hydrolytic capacity of lysosomal enzymes (de Duve, 1983). Upon rupture of the lysosomal membrane, the lysosomal content can leak into the cytosol, leading to lysosome-dependent cell death (also called “lysosomal cell death” [LCD; see also Table 1.2]) (Aits and Jäättelä, 2013). The main executioners of LCD are the cathepsin proteases. However, the pathological outcome of LCD is dependent of the extent of lysosomal membrane permeabilization (LMP). While massive rupture of the lysosomal membrane triggers a hydrolysis cascade of cytoplasmic content and results in acidification of the cytosol, leading to uncontrolled necrosis, limited LMP rather induces regulated intrinsic apoptosis or caspase-independent cell death with apoptotic features (Kågedal et al., 2001; Kirkegaard and Jäättelä, 2009; Serrano-Puebla and Boya, 2016).

LMP can be induced under several circumstances. Cationic amphiphilic drugs get protonated after entering the lysosomes, which leads to the accumulation of these compounds in the lysosome. Consequently, these drugs induce the detachment of lysosomal acid sphingomyelinase (ASM), resulting in an altered lipid profile and subsequent destabilization of the lysosome (Kornhuber et al., 2010). Furthermore, bacterial toxins and viral proteins have been described to rupture the lysosomal membrane (Aits and Jäättelä, 2013). Moreover, ROS are also potent inducers of LMP. During oxidative stress, accumulating H_2O_2 reacts with redox-active iron and promotes the production of hydroxyl radicals, finally causing lipid peroxidation and damage of the lysosomal membrane (Kurz et al., 2008b, 2008a). Cathepsins themselves are also capable of inducing LMP, possibly due to increased degradation of highly glycosylated lysosome-associated membrane proteins that form a protective glycocalyx shield of the lysosomal membrane (Figure 1.5) (Fehrenbacher et al., 2008).

LMP has been described to play an important role in a variety of lysosomal storage disorders. This group of diseases (e.g. Gaucher disease and Niemann-Pick disease) is characterized by the accumulation of metabolic products because of lysosomal dysfunction, leading to a late stage autophagy block and lysosomal destabilization (Lieberman et al., 2012; Serrano-Puebla and Boya, 2016). Interestingly, LCD is not restricted to pathologic conditions. During mammary gland involution, gland cells are eliminated by controlled LMP and subsequent release of cathepsins into the cytosol, leading to caspase-independent cell death (Arnandis et al., 2012; Serrano-Puebla and Boya, 2018).

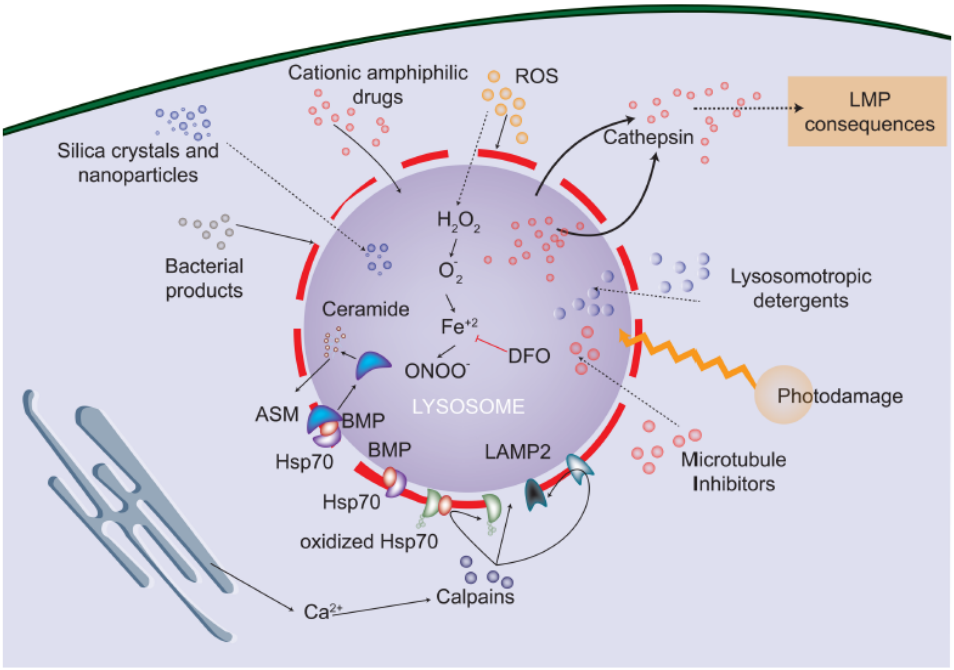

Figure 1.5. Lysosomal membrane permeabilization.
Several agents can induce lysosomal membrane permeabilization, which results in the translocation of lysosomal proteases (such as cathepsins) into the cytoplasm: Cationic amphiphilic drugs, lysosmotropic detergents, photodamage, microtubule inhibitors, bacterial products and nanoparticles. ROS can pass the lysosomal membrane and catalyzes the Fenton reaction in the presence of iron, thereby producing toxic hydroxyl radicals that damage the lysosomal membrane by lipid peroxidation processes. Calpains get activated by increased cytosolic calcium levels and targets lysosomal membrane proteins like LAMP2 and HSP70 (Serrano-Puebla and Boya, 2018).

2 Objective

In general, autophagy is considered as a pro-survival mechanism and protective response to cellular stress in terms of nutrient deprivation or damage of cellular constituents. However, it has been shown that under certain circumstances, e.g. during developmental processes in lower eukaryotes or during chemotherapeutic treatment of cancer cells, autophagy can also exert detrimental effects on cell survival, leading to autophagic cell death (ACD) (Denton et al., 2009; Voss et al., 2010; Shchors et al., 2015; Dasari et al., 2017; Segala et al., 2017). This type of cell death relies on the autophagic machinery and has been added to the expanding list of regulated cell death forms by the “Nomenclature Committee on Cell Death” (Galluzzi et al., 2018). In the recent years, several new cell death pathways have been discovered, however, albeit discrimination is sometimes difficult, and the putative interplay of different cell death forms needs to be further elucidated.

It has been proposed that during ACD, autophagy is upregulated beyond a certain threshold, and cells literally eat themselves to death (Das et al., 2012; Fulda and Kögel, 2015; Bialik et al., 2018). However, the exact pathways involved in ACD often remain unclear, since simple upregulation of autophagy in the absence of cell damage, e.g. by inhibition of the main autophagy negative regulator mTOR with rapamycin, most often exerts pro-survival effects and fails to induce cell death even at high concentrations (Galluzzi et al., 2012; Zielke et al., 2018). Therefore, the aim of this thesis was to elucidate the key mechanisms that shift the general pro-survival effect of autophagy to the execution of cell death.

Moreover, this study aimed to investigate the benefits of ACD inducers for the potential usage in glioblastoma (GBM) therapy. GBM is the most aggressive brain tumor in adults with a median survival of ~ 15 months despite current standard therapy including the best possible resection and radiochemotherapy with temozolomide (TMZ) (Thakkar et al., 2014; Davis, 2016). One key reason for limited therapy benefits is the apoptosis-refractory behavior of these tumors (Wagenknecht et al., 1999; Jiang et al., 2003). Therefore, ACD might be an alternative or additive approach to overcome therapy resistance. Indeed, it has been shown that several anticancer drugs induce ACD in glioblastoma cells, including AT 101, cannabinoids and the combination of imipramine and ticlopidine (Salazar et al., 2009; Voss et al., 2010; Fulda and Kögel, 2015; Shchors et al., 2015).

In a recent study of our lab, Voss et al. demonstrated that AT 101, a natural compound from cotton seeds, was able to induce ACD in different glioblastoma cell lines, which was accompanied by an early fragmentation of mitochondria, but no signs of apoptosis (Voss et al., 2010). However, except for the dependency on parts of the autophagic machinery,

including *ATG5*, *ATG7* and *BECN1*, the mechanisms how cell death was initiated and executed mainly remained elusive. Since mitochondrial fragmentation often precedes mitophagy, the possible contribution of mitochondrial events in ACD induced by AT 101 was further studied here. To this end, mitochondrial depolarization and the possible role of mPTP opening on mitochondrial dysfunction were measured. Moreover, mitophagy induction following AT 101 treatment was assessed by several methods, including electron microscopy, western blot analysis, measurement of mitochondrial versus nuclear DNA levels and two flow cytometry-based assays using the fluorescent probes mito-mKeima and MitoTracker Green FM (MTG). For validation of an increased mitophagic flux after administration of AT 101, autophagy was blocked by either genetic autophagy inhibition using CRISPR/Cas9 *ATG5* KO cells or pharmacologic inhibition using wortmannin, bafilomycin A_1 or chloroquine. In addition, the possible involvement of selective mitophagy receptors were determined. To analyze underlying changes upon AT 101 treatment more globally, a proteomic analysis was performed, and possible candidates involved in mitophagy, autophagy and cell death were selected for further functional analysis.

The second part of this thesis addressed the identification of new ACD inducers and their mode of action in glioblastoma cells. A mid-throughput cell death screen of the Enzo Screen-Well™ autophagy library using MZ-54 WT versus autophagy-deficient CRISPR/Cas9 *ATG5* and *ATG7* KO cells performed by Svenja Zielke revealed three new ACD inducers: loperamide, pimozide and STF-62247 (Zielke et al., 2018). In this thesis, these drugs were intensively investigated according to their ability to increase the autophagic flux and ACD in MZ-54 glioma cells. Therefor autophagy and cell death induction following drug treatment of MZ-54 WT cells was compared to *ATG5* and *ATG7* KO cells, and the autophagic flux was monitored using fluorescent LC3B tandem plasmids.

In contrast to AT 101, these newly investigated ACD inducers failed to induce mitochondrial dysfunction and mitophagy, suggesting a mechanistically different type of ACD. Interestingly, imipramine, loperamide and pimozide have been reported to act as functional inhibitors of the lysosomal enzyme acid sphingomyelinase (ASM) (Kornhuber et al., 2008; Kornhuber et al., 2011), and loss of ASM function is a typical hallmark of lysosomal lipid storage diseases (Niemann-Pick disease type A and B) (Schulze and Sandhoff, 2011; Santos-Lozano et al., 2015). Previous studies could show that impaired lipid trafficking is associated with increased autophagy induction owing to limited cytosolic cholesterol availability on the one hand, and to lysosomal membrane permeabilization (LMP) on the other hand (Xu et al., 2010; Lieberman et al., 2012; Gabandé-Rodríguez et al., 2014). Moreover, it is well established that LMP has detrimental effects on cell survival, leading to lysosomal cell death (LCD) (Serrano-Puebla and Boya, 2016).

Based on these considerations, the possible effects of impaired lipid trafficking and lysosomal lipid overload on autophagy and cell death were addressed in this study. To this end, a global proteome analysis, ASM activity measurements, cholesterol stainings with filipin III and a targeted analysis of sphingolipids were performed. Furthermore, the possible role of hyperactivated autophagy on LMP induction and subsequent LCD was assessed by quantification of cathepsin release, microscopic analysis of pmCherry-GAL3 puncta formation and cell death measurements using cathepsin inhibitors in WT glioma cells compared to autophagy-deficient *ATG5* and *ATG7* KO cells.

3 Material

3.1 Cell culture

Table 3.1: Cell lines.

Cell line	Description and origin	Cell culture medium
MEF *Bax Bak1* DKO	*Bax Bak1* DKO (double knockout) mouse embryonal fibroblasts were generated by Stanley Korsmeyer (Wei et al., 2001)	DMEM
MEF WT	Mouse embryonal fibroblasts (Milosch et al., 2014)	DMEM
MZ-54	Human glioma cell line (grade IV), from an explant of a secondary glioblastoma (Hetschko et al., 2008)	DMEM Glutamax, high glucose
U343 (GOS-3)	Human glioma cell line grade III/IV, p53 wild type (Asai et al., 1994); (DSMZ, ACC 408 [Braunschweig, Germany])	DMEM Glutamax, high glucose
U87MG	Human glioma cell line grade III/IV (ATCC, HTB-1, likely glioblastoma [Manassas, Virginia, USA])	DMEM Glutamax, high glucose

Table 3.2: Stable CRISPR/Cas9 knockout cell lines.
Cell lines were generated by using a combination of two sgRNAs and the vectors PX458 or PX459 expressing Cas9 from *Streptococcus pyogenes*.

Cell line	sgRNA numbers (see Table 3.23)	Vector	Cell culture medium
MZ-54 *ATG5* KO #1	3+4	pSpCas9(BB)-2A-GFP (PX458)	DMEM Glutamax, high glucose
MZ-54 *ATG5* KO #2	1+4	pSpCas9(BB)-2A-GFP (PX458)	DMEM Glutamax, high glucose
MZ-54 *ATG5* KO #3	3+4	pSpCas9(BB)-2A-GFP (PX458)	DMEM Glutamax, high glucose
MZ-54 *ATG7* KO #1	2+4	pSpCas9(BB)-2A-Puro (PX459)	DMEM Glutamax, high glucose
MZ-54 *ATG7* KO #2	2+3	pSpCas9(BB)-2A-Puro (PX459)	DMEM Glutamax, high glucose
MZ-54 *ATG7* KO #3	1+4	pSpCas9(BB)-2A-Puro (PX459)	DMEM Glutamax, high glucose
U343 (GOS-3) *ATG5* KO	3+4	pSpCas9(BB)-2A-GFP (PX458)	DMEM Glutamax, high glucose

Table 3.3: Medium contents.

Medium	Contents	Catalog number
DMEM Glutamax, high glucose	500 mL DMEM high glucose (+4.5 g/L glucose, +L-glutamine, -pyruvate) 50 mL fetal bovine serum (FBS) 5 mL Penicillin-Streptomycin solution 10,000 U/mL (final conc. 100 U/mL) 5 mL glutamine 200 mM (final conc. 2 mM)	61965026
DMEM	500 mL DMEM (+1 g/L glucose, +L-glutamine +pyruvate) 50 mL FBS 5 mL Penicillin-Streptomycin solution 10,000 U/mL	31885023

	(final conc. 100 U/mL) 5 mL glutamine 200 mM (final conc. 2 mM)	
DPBS	Balanced salt solution: - $CaCl_2$, -$MgCl_2$, no phenol red	14190094
Opti-MEM	Reduced serum medium: + L-glutamine, + HEPES, - phenol red	11058021

Table 3.4: Bacteria.

Bacteria strain	Genotype	Company	Catalog number
E. coli - DH5α	F- φ80*lac*ZΔM15 Δ(*lac*ZYA-*arg*F)U169 *deo*R *rec*A1 *end*A1 *hsd*R17 (rk-, mk+) *pho*A*sup*E44 *thi*-1 *gyr*A96 *rel*A1 λ-	Life Technologies, Carlsbad, California, USA	18265017

Table 3.5: Medium and agar for bacteria.

Name	Usage	Company	Catalog number
LB agar	40 g/L solid in purified water, pH 7.5	Carl Roth, Karlsruhe, Germany	X969.1
LB medium	25 g/L solid in purified water, pH 7.5	Carl Roth, Karlsruhe, Germany	X968.1

3.2 Plasmids

Table 3.6: Plasmids.

Plasmid	Catalog number	Company	First publication	Purpose
EGFP-LC3	11546	Addgene	(Jackson et al., 2005)	Mammalian expression of LC3B fused to EGFP to analyze autophagy
pmCherry-GAL3	85662	Addgene	(Papadopoulos et al., 2017)	Mammalian expression of Gal3, fluorescent reporter of lysosomal damage
pMRX-IP-GFP -LC3-RFP-LC3ΔG	84572	Addgene	(Kaizuka et al., 2016)	Mammalian expression of GFP-LC3B-RFP-LC3BΔG to measure autophagic flux
pSpCas9(BB)-2A-Puro (PX459)	48139	Addgene	(Ran et al., 2013)	Mammalian expression of Cas9 from *S. pyogenes* and a cloning backbone for sgRNA to generate CRISPR/Cas9 knockouts
pSpCas9(BB)-2A-GFP (PX458)	48138	Addgene	(Ran et al., 2013)	Mammalian expression of Cas9 from *S. pyogenes* and a cloning backbone for sgRNA to generate CRISPR/Cas9 knockouts
ptfLC3	21074	Addgene	(Kimura et al., 2007)	Mammalian expression of rat LC3B fused to mRFP and EGFP to measure autophagic flux

3.3 Chemicals

Table 3.7: Chemicals for the treatment of cells.
Stocks were prepared with fresh DMSO and stored at -20°C.

Substance	Abbreviation	Company	Catalog Number
DMSO (dimethyl sulfoxide)	DMSO	Carl Roth, Karlsruhe, Germany	A994.1
A23187	A23187	Enzo Life Science, Lausen, Switzerland	ALX-450-001-M001
AS 19	AS 19	Tocris Bioscience, Bristol, UK	1968
AT 101 [(-)-gossypol]	AT 101	Tocris Bioscience, Bristol, UK	1964
Bafilomycin A_1	BAF	LC Laboratories, Woburn, USA	B-1080
Chloroquine diphosphate salt	CQ	Sigma-Aldrich, St. Louis, Missouri, USA	C6628
Cholesterol-methyl-β-cyclodextrin	CHOL	Sigma-Aldrich, St. Louis, Missouri, USA	C4951
DR 4485 hydrochloride	DR4485	Tocris Bioscience, Bristol, UK	5005
E64D	E64D	Biomol, Hamburg, Germany	LKT-E0003.5
Endomorphin-1	Endomorphin-1	Tocris Bioscience, Bristol, UK	1055
FCCP (Carbonyl cyanide-*4*-(trifluoromethoxy) phenylhydrazone)	FCCP	Abcam Biochemicals, Cambridge, UK	ab120081
Hydrogen peroxide (H_2O_2) 30%	H_2O_2	Merck, Darmstadt, Germany	1072090250
Imipramine hydrochloride	IM	Sigma-Aldrich, St. Louis, Missouri, USA	10899
Loperamide hydrochloride	LOP	Enzo Life Science, Lausen, Switzerland	ALX-550-253
Necrostatin-1s	NEC	Biomol, Hamburg, Germany	4311-88-0
Pepstatin A	PEPA	Applichem, Darmstadt, Germany	A2205,0010
Pimozide	PIMO	Sigma-Aldrich, St. Louis, Missouri, USA	2062-78-4
Staurosporine	STS	Enzo Life Science, Lausen, Switzerland	380-014-M001
STF-62247	STF	Santa Cruz, Dallas, Texas, USA	sc-203831
Ticlopidine hydrochloride	TIC	Sigma-Aldrich, St. Louis, Missouri, USA	T6654
TRO 19622 (Olesoxime)	TRO	Sigma-Aldrich, St. Louis, Missouri, USA	T3077
U18666A	U18666A	Abcam Biochemicals, Cambridge, UK	ab133116
Verapamil hydrochloride	Verapamil	Enzo Life Science, Lausen, Switzerland	BML-2837-0100
Wortmannin	WM	Enzo Life Science, Lausen, Switzerland	BML-ST415

Table 3.8. Fluorophores used for flow cytometry experiments.

Fluorescent dye	Company	Catalog number
Annexin-V-FLUOS	Roche Diagnostics, Risch, Switzerland	11828681001
APC-annexin V	BD Biosciences, Franklin Lakes, New Jersey, USA	550475
BODIPY^{TM} 581/591 C11	Thermo Fisher Scientific, Waltham, Massachusetts, USA	D3861
CM-H2DCFDA	Thermo Fisher Scientific, Waltham, Massachusetts, USA	C6827
MTG	Life Technologies, Carlsbad, California, USA	M7514
PI	Sigma-Aldrich, St. Louis, Missouri, USA	P4864
TMRM	Life Technologies, Carlsbad, California, USA	T-668

Table 3.9: List of all other chemicals, cell culture supplements and enzymes that were used for the experiments.

Substance	Company	Catalog number
2-Chloroacetamide	Sigma-Aldrich, St. Louis, Missouri, USA	C0267
2-Mercaptoethanol	Carl Roth, Karlsruhe, Germany	4227.3
Ac-DEVD-AMC [Caspase 3 Substrate (AMC)]	Enzo Life Science, Lausen, Switzerland	ALX-260-031-M005
Acetonitrile (ACN)	VWR, Radnor, Pennsylvania, USA	83640-290
Acrylamide-Bis solution (37,5:1) 40% (PAA)	Serva Electrophoresis, Heidelberg, Germany	10681
Agarose	Serva Electrophoresis, Heidelberg, Germany	11406.02
Albumin Standard	Thermo Fisher Scientific, Waltham, Massachusetts, USA	23209
Ammonium persulfate (APS)	AppliChem, Darmstadt, Germany	A2941
Ampicillin	Sigma-Aldrich, St. Louis, Missouri, USA	10044
Aprotinin	AppliChem, Darmstadt, Germany	A2132,0010
BbsI	New England Biolabs, Ipswich, Massachusetts, USA	R0539S
Bovine Serum Albumin (BSA), Albumin Fraction V	Carl Roth, Karlsruhe, Germany	8076.3
Brij 35	Sigma-Aldrich, St. Louis, Missouri, USA	858366
Bromphenolblue	Sigma-Aldrich, St. Louis, Missouri, USA	115399
Calcium chloride ($CaCl_2$)	Sigma-Aldrich, St. Louis, Missouri, USA	449709
Cathepsin B substrate	Sigma-Aldrich, St. Louis, Missouri, USA	C5429
CHAPS	AppliChem, Darmstadt, Germany	A1099,0010
Chloroform 99.8%	ACROS Organics (Thermo Fisher Scientific), Waltham, Massachusetts, USA	383770250
DEPC-H_2O	Carl Roth, Karlsruhe, Germany	T143.1
Digitonin	Sigma-Aldrich, St. Louis, Missouri, USA	D141
Dithiothreitol (DTT)	AppliChem, Darmstadt, Germany	A1101,0010

dNTP Mix 10 mM	Life Technologies, Carlsbad, California, USA	18427088
EPPS	Sigma-Aldrich, St. Louis, Missouri, USA	E9502
Ethanol (99.8%)	Sigma-Aldrich, St. Louis, Missouri, USA	32205
Ethylenediaminetetraacetic acid (EDTA)	AppliChem, Darmstadt, Germany	A2937
Ethylene glycol-bis(β-aminoethyl ether)-N,N,N′,N′-tetraacetic acid (EGTA)	AppliChem, Darmstadt, Germany	A0878
FastStart Universal Probe Master-mix	Roche Diagnostics, Risch, Switzerland	4913957001
Fetal bovine serum (FBS)	Life Technologies, Carlsbad, California, USA	10270106
Formic acid	Sigma-Aldrich, St. Louis, Missouri, USA	F0507
Geneticin disulfate (G418)	Carl Roth, Karlsruhe, Germany	CP11.3
Glucose	AppliChem, Darmstadt, Germany	A3666,1000
Glutamine (Glutamax supplement)	Life Technologies, Carlsbad, California, USA	35050038
Glycerol	AppliChem, Darmstadt, Germany	A2926,0100
Glycine	AppliChem, Darmstadt, Germany	A1067,5000
HEPES	AppliChem, Darmstadt, Germany	A1069,1000
Hydrochloric acid 37%	VWR, Radnor, Pennsylvania, USA	130278
Hydrogen peroxide (H_2O_2) 30 %	Merck, Darmstadt, Germany	1072090250
Hydroxylamine 50%	Sigma-Aldrich, St. Louis, Missouri, USA	438227
Imipramine hydrochloride	Sigma-Aldrich, St. Louis, Missouri, USA	10899
Imperial Protein Stain	Thermo Fisher Scientific, Waltham, Massachusetts, USA	24615
Isopropanol	Thermo Fisher Scientific, Waltham, Massachusetts, USA	67-63-0
L-cysteine hydrochloride	Sigma-Aldrich, St. Louis, Missouri, USA	C7880
Leupeptin	AppliChem, Darmstadt, Germany	A2183,0010
L-glutamine (200 mM)	Life Technologies, Carlsbad, California, USA	25030024
Lipofectamine 2000	Thermo Fisher Scientific, Waltham, Massachusetts, USA	11668027
Lipofectamine 3000	Thermo Fisher Scientific, Waltham, Massachusetts, USA	L3000015
Lysyl endopeptidase (Lys-C)	Wako Chemicals, Neuss, Germany	125-02543
Magnesium chloride ($MgCl_2$)	Sigma-Aldrich, St. Louis, Missouri, USA	M8266
Methanol	Sigma-Aldrich, St. Louis, Missouri, USA	322415
Milk powder	Carl Roth GmbH, Karlsruhe, Germany	T145.2
Mounting medium with DAPI	Dianova, Hamburg, Germany	SCR-38448
Mounting medium without DAPI (Fluoroshield)	Sigma-Aldrich, St. Louis, Missouri, USA	F6182
NP-40	Abcam Biochemicals, Cambridge, UK	ab142227

Oligo(dT)$_{20}$	Life Technologies, Carlsbad, California, USA	18418020
Paraformaldehyde Solution 4% in PBS	Santa Cruz Biotechnologies, Dallas, Texas, USA	sc-281692
Pefabloc SC	Sigma-Aldrich, St. Louis, Missouri, USA	76307
Penicillin-Streptomycin solution	Life Technologies, Carlsbad, California, USA	15140122
Phenylmethansulfonylfluorid (PMSF)	Carl Roth, Karlsruhe, Germany	6367.1
Phosphate buffered saline (PBS)	AppliChem, Darmstadt, Germany	A0964,9100
PhosphoSTOP Phosphatase inhibitor	Roche Diagnostics, Risch, Switzerland	4906845001
Phusion High-fidelity DNA Polymerase	Thermo Fisher Scientific, Waltham, Massachusetts, USA	F-530S
Potassium chloride (KCL) solution	AppliChem, Darmstadt, Germany	A1164.0250
Potassium phosphate monobasic (KH_2PO_4)	Carl Roth, Karlsruhe, Germany	3904.1
Precision Plus Protein ALL BLUE Standard	Bio-Rad Laboratories, Hercules, California, USA	1610373
Protease inhibitor cocktail	Sigma-Aldrich, St. Louis, Missouri, USA	P8340
Protease Inhibitor cOmplete	Roche Diagnostics, Risch, Switzerland	4693159001
Puromycin Dihydrochloride	Santa Cruz Biotechnologies, Dallas, Texas, USA	sc-108071B
Random primer	Life Technologies, Carlsbad, California, USA	48190011
Roti-Quant	Carl Roth, Karlsruhe, Germany	K015.1
Sodium chloride (NaCl)	Sigma-Aldrich, St. Louis, Missouri, USA	433209
Sodium dodecyl sulfate (SDS)	Carl Roth, Karlsruhe, Germany	CN30.3
Sodium hydroxide (NaOH)	AppliChem, Darmstadt, Germany	A6829,0500
Sodium phosphate dibasic (Na_2HPO_4)	Carl Roth, Karlsruhe, Germany	P030.1
Sucrose	AppliChem, Darmstadt, Germany	A2211,0500
Superscript III reverse transcriptase	Thermo Fisher Scientific, Waltham, Massachusetts, USA	18080085
T4 Ligase	New England Biolabs, Ipswich, Massachusetts, USA	M0202S
TCEP solution pH 7	Sigma-Aldrich, St. Louis, Missouri, USA	646541
TEMED (N,N,N´,N´-Tetramethylethylendiamine)	Sigma-Aldrich, St. Louis, Missouri, USA	T9281
Triethylamine (TEA)	Thermo Fisher Scientific, Waltham, Massachusetts, USA	1862986
Trifluoroacetic acid (TFA)	Sigma-Aldrich, St. Louis, Missouri, USA	302031
Tris(hydroxymethyl)aminomethane (Tris)	Sigma-Aldrich, St. Louis, Missouri, USA	252859
Triton X-100	Sigma-Aldrich, St. Louis, Missouri, USA	T8787
Trypsin, Sequencing Grade Modified	Promega, Madison, Wisconsin, USA	V5113
Trypsin-EDTA (0.25%)	Life Technologies, Carlsbad, California, USA	25200056

Tween 20	AppliChem, Darmstadt, Germany	A1389,0500
Urea	Sigma-Aldrich, St. Louis, Missouri, USA	51456

3.4 Antibodies

Table 3.10: Primary antibodies used for western blot.
All antibodies except for BNIP3, ATG7 and LAMP1 were diluted in TBST with 5% BSA. BNIP3, ATG7 and LAMP1 were diluted in TBST and 5% milk.

Antibody	Company	Cat. Number	Secondary Antibody	MW [kDa]*[1]	Dilution western blot
AKT1 (AKT)	Cell Signaling, Danvers, Massachusetts, USA	9272	anti-rabbit	60	1:1000
AMPKalpha	Cell Signaling, Danvers, Massachusetts, USA	2532	anti-rabbit	62	1:1000
ATG5	Cell Signaling, Danvers, Massachusetts, USA	2630S	anti-rabbit	55	1:1000
ATG7	Cell Signaling, Danvers, Massachusetts, USA	8558	anti-rabbit	78	1:500
BAK1	Cell Signaling, Danvers, Massachusetts, USA	3814	anti-rabbit	25	1:1000
BAX	Merck Millipore, Darmstadt, Germany	ABC11	anti-rabbit	21	1:5000
BNIP3	Abcam Biochemicals, Cambridge, UK	ab10433	anti-mouse	22-28	1:500
BNIP3L	Cell Signaling, Danvers, Massachusetts, USA	12396	anti-rabbit	38,76	1:1000
COX4L1 (COXIV)	Cell Signaling, Danvers, Massachusetts, USA	4850S	anti-rabbit	17	1:1000
CTSB	Cell Signaling, Danvers, Massachusetts, USA	31718	anti-rabbit	24, 27, 44, 5	1:1000
CTSD	Cell Signaling, Danvers, Massachusetts, USA	2284	anti-rabbit	46, 43, 28, 15	1:1000
GAPDH	Merck Millipore, Darmstadt, Germany	CB1001	anti-mouse	36	1: 10,000
HSPD1 (HSP60)	Cell Signaling, Danvers, Massachusetts, USA	12165	anti-rabbit	60	1:1000
LAMP1	Abcam Biochemicals, Cambridge, UK	ab24170	anti-rabbit	120	1:1000
LC3B (MAP1LC3B)	Waltham, Massachusetts, USA	PA1-16930	anti-rabbit	18, 16	1:1000
phospho-AKT1	Cell Signaling, Danvers, Massachusetts, USA	4060	anti-rabbit	60	1:2000
phospho-AMPKalpha	Cell Signaling, Danvers, Massachusetts, USA	2535	anti-rabbit	62	1:1000
SQSTM1 (p62)	BD Biosciences, Franklin Lakes, New Jersey, USA	610833	anti-mouse	62	1:1000
TOMM20	Santa Cruz, Dallas, Texas, USA	sc-11415	anti-rabbit	20	1:500
TUBA4A (alpha - Tubulin)	Sigma-Aldrich, St. Louis, Missouri, USA	T6199	anti-mouse	50	1:5000
VCP (p97)	Abcam Biochemicals, Cambridge, UK	ab11433	anti-mouse	97	1:400
VDAC1 (PORIN)	Abcam Biochemicals, Cambridge, UK	ab15895	anti-rabbit	31	1:1000

*[1] MW refers to human samples.

Table 3.11: Secondary antibodies used for western blot.

Secondary Antibody	Conjugate	Company	Catalog number	Dilution
Goat anti-mouse	IRDye 800CW	Li-cor Biosciences GmbH, Bad Homburg, Germany	926-32210	1:10000
Goat anti-mouse	IRDye 680RD	Li-cor Biosciences GmbH, Bad Homburg, Germany	926-68070	1:10000
Goat anti-rabbit	IRDye 800CW	Li-cor Biosciences GmbH, Bad Homburg, Germany	926-32211	1:10000
Goat anti-rabbit	IRDye 680RD	Li-cor Biosciences GmbH, Bad Homburg, Germany	926-68071	1:10000

Table 3.12: Primary antibodies for immunofluorescent staining.

Antibody	Company	Cat. Number	Secondary Antibody	Dilution Western blot
LAMP1 (H4A3)	DSHB, Iowa City, Iowa, USA	H4A3-s (50 µg/mL)	anti-mouse	1:25
LC3B (MAP1LC3B)	Waltham, Massachusetts, USA	PA1-16930	anti-rabbit	1:200

Table 3.13: Secondary antibodies for immunofluorescent staining.

Secondary Antibody	Conjugate	Company	Catalog number	Dilution
Goat anti-mouse	Alexa Fluor 594 F(ab')2 fragment	Invitrogen/Thermo Fisher Scientific, Waltham, Massachusetts, USA	A-11020	1:750
Goat anti-mouse	Alexa Fluor 488	Invitrogen/Thermo Fisher Scientific, Waltham, Massachusetts, USA	A-11029	1:750
Goat anti-rabbit	Alexa Fluor 488 F(ab')2 fragment	Invitrogen/Thermo Fisher Scientific, Waltham, Massachusetts, USA	A-11017	1:750

3.5 Buffers and solutions

Table 3.14: Buffers and solutions for caspase 3-like activity measurement.

Buffer name	Composition
CA Lysis Buffer	10 mM HEPES pH 7.4 42 mM KCl 5 mM $MgCl_2$ 0.1 mM EDTA 0.5% CHAPS freshly added: 1 mM DTT, 5 µg/mL aprotinin, 1µg/mL leupeptin, 1 µg/mL pepstatin A, 1 mM PMSF
CA Reaction Buffer	25 mM HEPES pH 7.4 1 mM EDTA 0.1% CHAPS 10% sucrose freshly added: 3 µL/mL DTT, 10 µM Ac-DEVD-AMC
Roti-Quant Solution	2 parts Roti-Quant UN 1760, 5.5 parts deionized H_2O

Table 3.15: Buffers for flow cytometry analysis.

Buffer name	Composition
FACS Buffer (for APC-annexin V and PI staining)	10 mM HEPES/NaOH pH 7.4, 140 mM NaCl, 5 mM $CaCl_2$
DPBS Buffer (for all other stainings)	Dulbecco's Phosphate Buffered Saline (DPBS; -$CaCl_2$, -$MgCl_2$)

Table 3.16. Buffers for protein analysis (western blot).

Buffer name	Composition
5 x Loading Buffer	250 mM Tris/HCl pH 6.8 10% SDS 30% glycerol 0.02% Bromphenolblue freshly added: 5% ß-mercaptoethanol
2 x SDS-PAGE Lysis Buffer	137 mM Tris/HCl pH 6.8 4% SDS 20% glycerol 1 mM Protease/Phosphatase inhibitor cocktail
Gel Electrophoresis Running Buffer	25 mM Tris 192 mM glycine 0.1% SDS
Phosphate Buffered Saline (PBS)	9,55 g/L PBS solid in purified water
SDS-PAGE Separation Gel	10/12/15% polyacrylamide (PAA) 375 mM Tris pH 8.8 0.1% SDS freshly added: 0.1% ammonium persulfate (APS), 0.05% tetramethylethylenediamine (TEMED)
SDS-PAGE Stacking Gel	5% PAA 120 mM Tris/HCl pH 6.8 0.1% SDS freshly added: 0.1% APS, 0.05% TEMED
Tris Buffered Saline (TBS)	50 mM Tris 150 mM NaCl, pH 7.4
TBS-Tween (TBS-T)	TBS 0.05% Tween 20
Transfer Buffer	25 mM Tris 192 mM glycin freshly added: 20% methanol

Table 3.17: Buffers for proteome analysis.

Buffer name	Composition
Digestion Buffer	8 M urea 50 mM Tris pH 8.0
EPPS Buffer	10 mM EPPS 1 mM $CaCl_2$
Proteomics Lysis Buffer	2% SDS 150 mM NaCl 50 mM Tris pH 8.5 40 mM chloroacetamide 5 mM TCEP Freshly added: 1 tablet Phosphostop /10 mL lysis buffer 1 tablet cOmplete Protease inhibitor cocktail/10 mL lysis buffer

Table 3.18: Buffers for separation of cytosol and organelle fraction containing intact lysosomes.

Buffer name	Composition
Lysis Buffer 1 (cytosol)	250 mM sucrose 70mM KCL 137 mM NaCl 4.3 mM Na_2 HPO_4 1.4 mM KH_2 PO_4 pH 7.2 Add just before use: 100 µM PMSF, 10 µg/ml leupeptin, 2 µg/mL aprotinin, 50 µg/mL digitonin
Lysis Buffer 2 (intact lysosomes)	50 mM Tris/HCl pH 7.4 150 mM NaCl 2 mM EDTA 2 mM EGTA 0.2% Triton X-100 0.3% NP-40 Add just before use: 10 µg/mL leupeptin, 2 µg/mL aprotinin

Table 3.19: Buffers for cathepsin B assay.

Buffer name	Composition
Digitonin Extraction Buffer	250 mM sucrose 20 mM HEPES 10 mM KCL 1.5 mM $MgCl_2$ 1 mM EDTA 1 mM EGTA Add just before use: Pefabloc SC 0.5 mM, digitonin 22.5 µg/mL
L-Cysteine Buffer	352 mM KH_2PO_4 48 mM Na_2HPO_4 4 mM EDTA pH 6 add just before use: 8 mM L-cysteine
Cathepsin B Reaction Buffer	0.1% Brji 35 solution Add freshly: 0.02 mM Z-Arg-Arg-7-amido-4-methylcoumarin hydrochloride

3.6 Commercial kits

Table 3.20: Commercial kits.

Kit	Cat No	Company
Acidic Sphingomyelinase Assay Kit (Fluorometric)	Ab190554	Abcam Biochemicals, Cambridge, UK
Cholesterol assay kit	ab133116	Abcam Biochemicals, Cambridge, UK
EndoFree Plasmid Maxi Kit	12362	Qiagen, Hilden, Germany
EXTRACTME Total RNA Kit	EM09-100	7Bioscience, Hartheim, Germany
Micro BCA Protein assay KIT	23235	Thermo Fisher Scientific, Waltham, Massachusetts, USA
Pierce BCA Protein Assay Kit	23225	Thermo Fisher Scientific, Waltham, Massachusetts, USA

Pierce High pH Reversed-Phase peptide Fractionation Kit	84868	Thermo Fisher Scientific, Waltham, Massachusetts, USA
QIAamp DNA Mini Kit	51304	Qiagen, Hilden, Germany
QiAquick Gel Extraction Kit	28704	Qiagen, Hilden, Germany
QIAprep Spin Miniprep Kit	27104	Qiagen, Hilden, Germany
QIAshredder	79656	Qiagen, Hilden, Germany
RNeasy Mini Kit	74106	Qiagen, Hilden, Germany
TMT10-131 TM L Reagent 0.8 mg	1862804	Thermo Fisher Scientific, Waltham, Massachusetts, USA

3.7 siRNA oligonucleotides

Table 3.21: siRNA oligonucleotides for transfection.

Name	Target gene	Number	Company
si*BNIP3* #1	BNIP3	SASI Hs01 00131554	Sigma-Aldrich, St. Louis, Missouri, USA
si*BNIP3* #2	BNIP3	SASI Hs01 00131555	Sigma-Aldrich, St. Louis, Missouri, USA
siB*NIP3L* #1	BNIP3L	SASI Hs01 00030000	Sigma-Aldrich, St. Louis, Missouri, USA
si*BNIP3*L #2	BNIP3L	SASI Hs01 00030001	Sigma-Aldrich, St. Louis, Missouri, USA
si*HMOX1* #1	HMOX1	SASI Hs01 00035065	Sigma-Aldrich, St. Louis, Missouri, USA
si*HMOX1* #2	HMOX1	SASI Hs01 00035067	Sigma-Aldrich, St. Louis, Missouri, USA
si*VCP* #1	VCP (p97)	SASI HS01 00118726	Sigma-Aldrich, St. Louis, Missouri, USA
si*VCP* #2	VCP (p97)	SASI HS01 00118728	Sigma-Aldrich, St. Louis, Missouri, USA
siCon	Universal Negative Control	SIC001	Sigma-Aldrich, St. Louis, Missouri, USA

3.8 Oligonucleotides for generation and detection of CRISPR/Cas9 KOs

Table 3.22: PCR primer for detection of CRISPR/Cas9 knockouts.

Primer name	Target gene	Sequence	Company
ATG5 FWD1	ATG5	GGACTGTCAGGATTCACAGGG	Eurofines Scientific, Luxembourg, Luxemburg
ATG5 REV1	ATG5	AGTCCAGAACGCATCATGACA	Eurofines Scientific, Luxembourg, Luxemburg
ATG7 FWD1	ATG7	AGAAGCATAAACATTAAGGCCGC	Eurofines Scientific, Luxembourg, Luxemburg
ATG7 REV2	ATG7	TTTGTTGAGCCCAAGGCGCC	Eurofines Scientific, Luxembourg, Luxemburg

Table 3.23: Oligonucleotides for CRISPR/Cas9 sgRNA generation.

Target gene	sgRNA Number	Sense (S)/ antisense (AS)	Sequence	Company
ATG7	1	AS	aaacGTGTTGTCAAGCTGATTC TC	Eurofines Scientific, Luxembourg, Luxemburg
ATG7	1	S	CACCGAGAATCAGCTTGACA ACAC	Eurofines Scientific, Luxembourg, Luxemburg
ATG7	2	AS	aaacCCGTAGCTGCCGCCATT ATTC	Eurofines Scientific, Luxembourg, Luxemburg
ATG7	2	S	CACCGAATAATGGCGGCAGC TACGG	Eurofines Scientific, Luxembourg, Luxemburg
ATG7	3	AS	aaacATACTCGTTCAGCTTCTT CTC	Eurofines Scientific, Luxembourg, Luxemburg
ATG7	3	S	CACCGAGAAGAAGCTGAACG AGTAT	Eurofines Scientific, Luxembourg, Luxemburg
ATG7	4	AS	aaacCCAGTATAGTGTCAGCTT TC	Eurofines Scientific, Luxembourg, Luxemburg
ATG7	4	S	CACCGAAAGCTGACACTATA CTGG	Eurofines Scientific, Luxembourg, Luxemburg
ATG5	1	AS	aaacCACATCTCGAAGCACAT CTTC	Eurofines Scientific, Luxembourg, Luxemburg
ATG5	1	S	CACCGAAGATGTGCTTCGAG ATGTG	Eurofines Scientific, Luxembourg, Luxemburg
ATG5	2	AS	aaacACTTGTTTCACGCTATAT CAC	Eurofines Scientific, Luxembourg, Luxemburg
ATG5	2	S	CACCGTGATATAGCGTGAAA CAAGT	Eurofines Scientific, Luxembourg, Luxemburg
ATG5	3	AS	aaacTTTCAGTTATCTCATCCT GAC	Eurofines Scientific, Luxembourg, Luxemburg
ATG5	3	S	CACCGTCAGGATGAGATAAC TGAAA	Eurofines Scientific, Luxembourg, Luxemburg
ATG5	4	AS	aaacCTGAGTGGTAGCATTAG AGGC	Eurofines Scientific, Luxembourg, Luxemburg
ATG5	4	S	CACCGCCTCTAATGCTACCA CTCAG	Eurofines Scientific, Luxembourg, Luxemburg

3.9 Primers for qRT-PCR

Table 3.24: FAM-MGP primer for qRT-PCR.

Primer name	Target gene	Company
Hs04195319_s1	CERS1	Thermo Fisher Scientific, Waltham, Massachusetts, USA
Hs00371958_g1	CERS2	Thermo Fisher Scientific, Waltham, Massachusetts, USA
Hs00908756_m1	CERS5	Thermo Fisher Scientific, Waltham, Massachusetts, USA
Hs01372226_m1	CERS6	Thermo Fisher Scientific, Waltham, Massachusetts, USA
Hs00969291_m1	BNIP3	Thermo Fisher Scientific, Waltham, Massachusetts, USA
Hs00188949_m1	BNIP3L	Thermo Fisher Scientific, Waltham, Massachusetts, USA
Hs00608023_m1	BCL2	Thermo Fisher Scientific, Waltham, Massachusetts, USA
Hs00236329_m1	BCL2L1 (BCL-xL)	Thermo Fisher Scientific, Waltham, Massachusetts, USA

Hs00186447_m1	DEGS1	Thermo Fisher Scientific, Waltham, Massachusetts, USA
Hs01050896_m1	MCL1	Thermo Fisher Scientific, Waltham, Massachusetts, USA
Hs00232352_m1	NFE2L2 (NRF2)	Thermo Fisher Scientific, Waltham, Massachusetts, USA
Hs00202227_m1	KEAP1	Thermo Fisher Scientific, Waltham, Massachusetts, USA
Hs01116902_m1	SPTLC1	Thermo Fisher Scientific, Waltham, Massachusetts, USA
Hs00177654_m1	SQSTM1 (p62)	Thermo Fisher Scientific, Waltham, Massachusetts, USA
Hs00427620_m1	TBP	Thermo Fisher Scientific, Waltham, Massachusetts, USA

3.10 Laboratory equipment

Table 3.25: Laboratory equipment.

Item and description	Company
96-well measuring plate, black	Greiner Bio-one, Kremsmünster, Austria
96-well measuring plate, white, clear bottom	Greiner Bio-one, Kremsmünster, Austria
Agarose gel chamber	Bio-Rad Laboratories, Hercules, California, USA
Autoclave: DX23	Systec, Linden, Germany
Autoclave: Varioklav	Biomedis, Gießen, Germany
Automated cell counter: Scepter	Merck Millipore, Darmstadt, Germany
Camera for agarose gel images: Herolab easy B-1228-3U5N	Herolab, Wiesloch, Germany
Cell counting chip (for automated counting)	Tecan, Männedorf, Switzerland
Cell culture flasks: Cellstar	Greiner Bio-one, Kremsmünster, Austria
Cell culture plates (6-well, 24-well and 96-well): Cellstar	Greiner Bio-one, Kremsmünster, Austria
Centrifuge: Biofuge fresco (Microliter rotor, 24 X 2 ml PP, radius 8.5 cm, order no: 7500 3328)	Kendro (Heraeus), Hanau, Germany
Centrifuge: Biofuge stratos (Swing-out rotor 4x180 mL, order no: 75003047)	Heraeus, Hanau, Germany
Centrifuge: Mini Spin table centrifuge (Rotor F-45-12-11, radius 6 cm, cat no: 5452727007)	Eppendorf AG, Hamburg, Germany
Chamberslides	Corning Brand, Corning, New York, USA
Clean bench: Herasave	Heraeus, Hanau, Germany
Clean bench: 2F120-II Tecnoflow	Integra Biosciences, Zizers, Switzerland
Concentrator	Eppendorf, Hamburg, Germany
Cover glasses	NeoLab Migge, Heidelberg, Germany
Electrophoresis system: Mini PROTEAN system	Bio-Rad Laboratories, Hercules, California, USA
Electron microscope: FEI Tecnai G2 Spirit Biotwin TEM	Hillsboro, Oregon, USA

Filter paper: Whatman 3 MM	Whatman, Little Chalfont, Buckinghamshire, United Kingdom
Flow cytometer: BD FACS Canto II	BD Biosciences, Franklin Lakes, New Jersey, USA
Flow cytometer: BD FACS Aria II	BD Biosciences, Franklin Lakes, New Jersey, USA
Flow cytometer: BD Accuri C6	BD Biosciences, Franklin Lakes, New Jersey, USA
Freezer -20°C	Liebherr, Bulle, Switzerland
Freezer -80°C: Thermo Electron Hera freeze	Heraeus, Hanau, Germany
Freezing container: Mr. Frosty	Nalgene, Rochester, USA
Freezing tubes (cryo tubes)	Nalgene, Rochester, USA
Glass bottles	Fisherbrand (Thermo Fisher Scientific GmbH), Waltham, Massachusetts, USA
Gloves: peha soft nitrile	Paul Hartmann AG, Heidenheim, Germany
Ice machine: Scotsman AS80	Hubbars, Ice Systems, Ipswich, UK
Incubator for bacteria	Heraeus, Hanau, Germany
Incubator for cell culture: Hera Cell 150	Heraeus, Hanau, Germany
Infrared imaging system: Li-cor reader Odyssey	LI-COR (Odyssey), Lincoln, Nebrasca, USA
Inoculation loop	Sarstedt, Nürnbrecht, Gemany
Liquid nitrogen tank: CBS Cryosystems 6000 series	CBS Cryosystems, Osaka, Japan
Magnetic mixer: RCT basic	IKA Labortechnik, Staufen, Germany
Measuring glasses, round bottom flasks	Schott AG, Mainz, Germany
MicroAMP Optical Adhesive Film	Applied Biosystems (Thermo Fisher Scientific), Waltham, Massachusetts, USA,
Microplate reader (absorbance and luminescence): Tecan Reader Genios	Tecan, Männedorf, Switzerland
Microscope: Confocal microscope Nikon C1i	Nikon, Tokio, Japan
Microscope: Fluorescent microscope Nikon ecliple TE2000-S	Nikon, Tokio, Japan
Microscope: Nikon eclipse TS100	Nikon, Tokio, Japan
Multistep pipet: Handystep	Gilson, Middleton, Wisconsin, USA
Neubauer Chamber	Paul Marienfeld, Lauda-Königshofen, Germany
Object slides	Engelbrecht Medizin- und Labortechnik, Edermünde, Germany
Parafilm	Pechiney Plastic Packaging, Chicago, Illinois, USA
Pasteur capillary pipets	WU, Mainz, Germany
PCR tube strips 0.2 mL	Eppendorf, Hamburg, Germany
PCR 96 Fast Plate halfskirt	Sarstedt, Nürnbrecht, Gemany
Petri dish	Greiner Bio-one, Kremsmünster, Austria
pH meter: Lab850	Schott AG, Mainz, Germany

Photometer: Eppendorf Bio Photometer	Eppendorf, Hamburg, Germany
Pipet tips	Starlab, Hamburg, Germany
Pipetting device (battery-powered): Pipetus	Hirschmann Laborgeräte, Eberstadt, Germany
Pipettes: 1 ml, 200 µl, 100 µl, 10 µl	Gilson, Middleton, Wisconsin, USA and Eppendorf AG, Hamburg, Germany
Polystyrene round bottom tubes for FACS	Corning Brand, Corning, New York, USA
Power supply: Bio Rad Power Pac HC	Bio-Rad Laboratories, Hercules, California, USA
Real time PCR System Step ONE Plus	Applied Biosciences, Foster City, California, USA
Refrigerator 4°C	Liebherr, Bulle, Switzerland
Rocking and rotating device/ overhead tumbler: Roto shake Genie	Scientific Industries, Bohemia, New York, USA
Scale: BL1500S	Sartorios, Göttingen, Germany
Scale: TE313S-DS	Sartorios, Göttingen, Germany
Semi-dry blotter: Bio Rad Transblot SD Semi-dry-Transfer-Cell	Bio-Rad Laboratories, Hercules, California, USA
Shaker: KM-2	Edmund Bühler, Bodelshausen, Germany
Shaking incubator for bacteria	New Brunswick Scientific, Edison, New Jersey, USA
Sonificator	Bandelin electronic, Berlin, Germany
Spark multimode microplate reader	Tecan, Männedorf, Switzerland
Sterile filters: Steriflip (50 ml) and Steritop-GP (500 ml) 0.22 µm Express TM Membrane	Merck Millipore, Darmstadt, Germany
Thermocycler: Mastercycler	Eppendorf, Hamburg, Germany
Thermomixer: Comfort	Eppendorf, Hamburg, Germany
Tube roller: Roller mixer SRT9	Stuart (Bibby Scientific Limited), Stone, Staffortshire, UK
Tubes: 0.2, 0.5, 1.5 and 2 mL	Eppendorf, Hamburg, Germany
Tubes 1.5, 2.0 mL (Protein LoBind)	Eppendorf, Hamburg, Germany
Tubes: 15 ml and 50 mL	Greiner Bio-one, Kremsmünster, Austria
Ultramicrotome Leica Ultracut UCT	Leica, Deerfield, Illinois, USA
UV gel cutting board	Bachhofer Laboratoriumsgeräte, Reutlingen, Germany
Vacuum Concentrator plus	Eppendorf, Hamburg, Germany
Vacuum Extraction Manifold, 20pos, 16x100mm tubes	Waters, Milford, Massachusetts, USA
Vacuum pump: Sonorex RK 100 H	Bandelin electronic, Berlin, Germany
Vortexer: Vortex-2 Genie	Scientific Industries, Bohemia, New York, USA
Water purification system: Milli-Q	Merck Millipore, Darmstadt, Germany
Waterbath	Köttermann, Uetze, Germany

3.11 Software

Table 3.26: Software

Software	Company
BD FACS DIVA software	BD Biosciences, Franklin Lakes, New Jersey, USA
BD Accuri C6 software	BD Biosciences, Franklin Lakes, New Jersey, USA
Benchling	San Francisco, California, USA
DAVID	Laboratory of Human Retrovirology and Immunoinformatics, National Cancer Institute, Frederick, Maryland, USA
GraphPad Prism 7	GraphPad Software, Inc., La Jolla, California, USA
ImageJ Fiji	NIH, Bethesda, Maryland, USA
jvenn	Designed by GenoToul Bioinfo and Sigenae teams (Bardou et al., 2014)
Microsoft Excel 2007	Microsoft, Redmond, Washington, USA
Microsoft Word 2007	Microsoft, Redmond, Washington, USA
NIS Elements AR 3.2	Nikon, Tokio, Japan
PANTHER	University of Southern California, Los Angeles, California, USA
Perseus	Computational Systems Biochemistry under Prof. Jürgen Cox, Martinsried, Germany
Primer Blast	National Center for Biotechnology Information, Bethesda, USA
Snapgene Viewer	GSL Biotech LLC, Chicago, Illinois, USA

4 Methods

4.1 Cell culture

4.1.1 Cultivation of cells

Mouse embryonal fibroblasts (MEF) with stable *Bax* and *Bak1* double-knockout (DKO) and wild type cells were cultured in Dulbecco's Modified Eagle's Medium (DMEM). The glioma cell lines U87MG, U343 and MZ-54 as well as glioma cells with stable *ATG5* or *ATG7* knockout (KO), stable ptfLC3, pMRX-IP-GFP-LC3-RFP, EGFP-LC3 or pmCherry-GAL3 expression were cultivated in DMEM, high glucose, glutamax. Cell culture media were supplemented with 10% heat inactivated fetal bovine serum (FBS) and 1% penicillin-streptomycin solution (100 U/mL final concentration). DMEM medium was additionally supplemented with 1% glutamine (2 mM final concentration) (Table 3.1). In case of stable plasmid transfections, the selection antibiotics G418 (1 mg/mL; ptfLC3, EGFP-LC3 or pmCherry-GAL3) or puromycin (1 µg/mL; pMRX-IP-GFP-LC3-RFP) were added to the cell culture medium. All cell lines were maintained in a humidified incubator at 37°C and 5% CO_2 at a confluence of 40% - 90% and medium was changed every 24 to 72 hours. For passaging, the medium was aspirated, and cells were washed with Dulbecco's Phosphate Buffered Saline (DPBS; -Mg^{2+}/-Ca^{2+}) to remove residual medium. Then, trypsin-EDTA was added and the cells were incubated for 5 - 10 minutes at 37°C for dissociation. To inactivate the trypsin-EDTA, cell culture medium was added, and the cells were resuspended by pipetting up and down. Subsequently, a defined amount of cell suspension was discarded according to the cell confluence and growth rate, followed by addition of fresh medium. For experimental procedures, a suitable number of cells was seeded the day before treatment to receive a confluence of 60% - 80% on the next day. Treatments were performed with the chemicals listed in Table 3.7. Cells were tested for mycoplasma contamination monthly. Authentication of U87MG, MZ-54 and U343 cells was done by STR profiling at DSMZ (Sammlung von Mikroorganismen und Zellkulturen, Braunschweig, Germany) or Genolytic (Molekularbiologische Diagnostik, Leipzig, Germany).

4.1.2 Determination of the cell number

Before seeding the cells for experimental procedures, the cell number was determined using a Spark multimode microplate reader. Thereto, cells were dissociated with trypsin-EDTA as described in chapter 4.1.1 and centrifuged at 195 x g for 3 minutes. The supernatant was aspirated, and the cell pellet was resolved in fresh medium. An amount of 50 uL cell

suspension was diluted 1:1 with trypan blue solution to stain dead cells. Cell viability was assessed by loading the cell counting chips with 10 uL cell suspension ($1*10^5$ - $1*10^7$ cells). Subsequent counting was performed by taking eight separate images with the Spark multimode microplate reader.

4.1.3 Freezing cells

For long-term storage, cell cultures were cryopreserved at -196°C in the vapor phase of liquid nitrogen. Thereto, 70% to 90% confluent cells of a T175 cell culture flask (175 cm^2) were pelletized and resuspended in 1.5 - 2.5 mL cold cell culture medium. Next, the same amount of freezing medium containing 80% FBS and 20% dimethyl sulfoxide (DMSO) was added dropwise while shaking carefully. Cryoprotective agents such as DMSO minimize the risk of cell damaging ice crystal formation by reducing the cooling rate and the freezing point. The cell suspension was distributed into 3 - 5 freezing tubes and cells were subsequently frozen at -80°C in an isopropanol freezing container to achieve a rate of cooling very close to -1 °C/minute. The next day, the tubes were transferred into a liquid nitrogen tank.

4.1.4 Thawing cells

The tubes containing frozen cells were taken from the liquid nitrogen tank and immediately thawed in a 37°C water bath. Next, the cell suspension was gently transferred into a centrifuge tube containing 20 mL of the appropriate pre-warmed medium, and the cells were centrifuged for 3 minutes at 195 x g. After discarding the supernatant, cells were gently resuspended in medium and plated at high density into a cell culture flask. After 24 hours, the cell culture medium was changed in order to remove dead cells.

4.2 Protein analysis

4.2.1 Whole cell lysates

For preparation of whole cell lysates, $1.2*10^5$ - $1.8*10^5$ cells were seeded into 6-well plates and treatments were performed on the next day. Thereafter, detached cells were collected by transferring the cell culture medium into a centrifuge tube. The remaining adherent cells were washed with DPBS and dissociated with trypsin-EDTA. Subsequently, the cell suspension was added to the centrifuge tube followed by centrifugation for 3 minutes at 195 x g. For all following steps, cells were kept on ice. Cell lysis was performed by dissolving the cell pellets in 2 x SDS lysis buffer by repeated pipetting up and down (Table 3.16). In order to destroy the cell membranes, cells were exposed to 2 x 10 ultrasonic beats with 5 minutes rest on ice

in between to avoid warming. The sonicated cells were centrifuged again for 5 minutes at 16,200 x g to pelletize and remove possible unresolved cell debris. Finally, protein samples were frozen at -20°C for short storage and at -80°C for long term storage (>1 week).

4.2.2 Protein quantification

The protein amount of whole cell lysates was determined using a Pierce BCA protein assay kit according to the manufacturer's instructions (Table 3.20). A standard series of bovine serum albumin (BSA) ranging from 2 µg to 12 µg as well as 3 µL sample lysates and lysis buffer as blank were transferred into a 96-well plate in duplicates. Next, 150 µL 0.9% NaCl and 150 µL of BCA solution were added to each well. After 45 minutes incubation at 37°C, the absorption was measured at 560 nm using the Spark multimode microplate reader. The protein concentration was calculated by subtraction of lysis buffer absorbance and comparing the sample values with the BSA standard curve.

4.2.3 Sodium dodecyl sulfate polyacrylamide gel electrophoresis (SDS PAGE)

The sodium dodecyl sulfate polyacrylamide gel electrophoresis (SDS PAGE) is a common technique used for separation of proteins according to their molecular weight in an electric field and was established by Ulrich Laemmli (Laemmli, 1970). In natively folded proteins, the net charge is dependent on the amino acid composition, and the molecular radius is determined by the tertiary structure. To separate proteins based on their molecular weight, they first need to get linearized using a detergent such as SDS in combination with a reducing agent (2-mercaptoethanol) and heat to disrupt disulfide bonds. In addition, SDS uniformly coats linearized proteins, leading to a charge that is proportional to their molecular weight. Hence, this preparation enables movement of protein samples to the positive anode of an electric field at different rates according to their molecular weight.

SDS gels consist of a stacking gel (pH 6.8) to concentrate the loaded proteins into a narrow zone and a separation gel (pH 8.8), both composed of acrylamide cross-linked with N,N'-methylene-bisacrylamide. Polymerization of the gels requires the catalytic agent tetramethyl-ethylenediamine (TEMED) in combination with the radical initiator ammonium persulfate (APS).

Separation gels with a polyacrylamide amount of 8% and 15% (Table 3.16) were prepared by pouring the solution between two glass plates and adding a layer of 1 mL isopropanol. After gelation, isopropanol was removed and the stacking gel was poured onto the separation gel, followed by insertion of a ten-tooth comb. An amount of 35 µg to 60 µg protein lysate was mixed with 5 x SDS loading buffer (containing 5% 2-mercaptoethanol; Table 3.16), heated for

4 minutes at 95°C and loaded onto the SDS gels. In addition, a prestained kDa marker was applied for later identification of the protein size. The SDS PAGE was performed at an electric tension of 85 V for the first 30 minutes and subsequent electric tension of 135 V for protein separation.

4.2.4 Western blot

After separation of the proteins by SDS PAGE, they were transferred to a nitrocellulose membrane to generate an immobilized replica of the gel. To this end, the proteins were blotted semi-dry at an electric tension of 15 V for 35 minutes. In the next step, the nitrocellulose membrane was blocked with 5% milk or 5% BSA in TBS-Tween (TBS-T; 0.05%; Table 3.16) for 1 hour at room temperature to reduce background interference. When milk was used for blocking, the membrane was washed three times for 10 minutes with TBS-T afterwards. Subsequently, the membranes were incubated with the appropriate antibody solution over night at 4°C. After three washing steps, secondary antibodies were applied at a concentration of 1:10,000 for 1 hour at room temperature. Finally, antibodies were detected with a Li-cor Odyssey reader. For long-term storage, membranes were dried and stored in the dark.

4.3 siRNA transfection

Small-interfering-RNA (siRNA) consists of a small, double-stranded RNA molecule that binds to the complementary region of the target mRNA and causes its degradation. Hence, siRNA is widely used for gene knockdown experiments.

For generation of transient knockdowns, the cells were transfected with siRNA at 60% confluency. Thereto, siRNA (10 nM, 25 nM or 50 nM) was complexed with Lipofectamine 2000 or 3000 at a concentration of 5 µL in 250 µL OptiMEM per 6-well, 1.5 µL in 100 µL OptiMEM per 24-well and 1 µL in 60 µL OptiMEM per chamberslide-well. Transfections were performed according to the manufacturer's instructions. Medium was changed on the next day, and treatments were performed 30 - 48 hours after transfection.

4.4 Fluorescence microscopy

The localization of cellular constituents can be visualized by fluorescent ling and subsequent microscopy. Immunostaining is one of the widespread techniques to detect the levels and localization of target proteins in cells. To this end, specific primary antibodies against the protein of interest are administered to the cells, and the bound antibodies are detected by

fluorophore-conjugated secondary antibodies against the invariant chain of the primary antibody. An alternative method to determine a protein of interest (also by live cell imaging) constitutes the plasmid-based transfection of the specific protein fused to a fluorescent reporter. In addition, several compounds with fluorescent properties can be used to stain other cellular constituents.

For fluorescence microscopy, 12,000 cells were seeded into chamberslides and treatments were performed as indicated. Cells were fixed with 4% paraformaldehyde for 10 minutes and ice-cold methanol for 5 minutes, followed by three washing steps with PBS-Tween (PBS-T). In case of immunostainings, cells were next permeabilized with 0.5% Triton X-100 in PBS for 5 minutes. After three washing steps, the cells were blocked with 4% BSA in PBS. Subsequently, the primary antibody was added, and samples were incubated at 4°C over night. After another three washing steps, the secondary antibody was applied for 1 hour at room temperature, followed by three washing steps. Finally, cover glasses were fixed using mounting medium with or without DAPI and the slides were subsequently sealed with nail polish. Microscope images were taken with the Nikon Eclipse TE2000-S microscope and NIS Elements AR 3.2 software at 60x magnification. The overlay of the different fluorescent dyes and optical zoom was performed with ImageJ.

4.4.1 Determination of autophagic flux by microscopy with the ptfLC3 plasmid

For determination of the autophagic flux, MZ-54 cells were transfected with the ptfLC3 plasmid encoding LC3B fused to EGFP and mRFP. To this end, plasmid DNA was complexed with the lipid reagent Lipofectamine 3000 to mediate efficient delivery into the nucleus. The fluorescent probe allows monitoring of autophagy, as the number of LC3B puncta refers to the number of autophagosomes and EGFP-fluorescence gets quenched upon autophagosome-lysosome fusion, but mRFP does not (Kimura et al., 2007). Cells were transfected at 70% - 80% confluency by using Lipofectamine 3000 according to manufacturer's instructions. Cells were seeded into 6-well plates at 120,000 cells/well. On the next day, cells were transfected with 2.5 μg plasmid DNA and 3.75 μL Lipofectamine 3000 (DNA: Lipofectamine ratio 1:1.5) in fresh medium. Medium was changed after 24 hours. Two days after transfection cells with stable integration of ptfLC3 were selected with 1 mg/mL G418. Cells were permanently cultivated in medium containing selection antibiotic to avoid loss of ptfLC3 expression. For fluorescence microscopy, cells were seeded in the absence of G418.

4.4.2 Determination of lysosomal membrane permeabilization using the pmCherry-GAL3 Plasmid

To visualize lysosomal damage by microscopy, MZ-54 cells were transfected with the pmCherry-GAL3 plasmid. Galectin-3 (GAL3) is widely used as a reporter for lysosomal membrane permeabilization, as it translocates from the cytosol to lysosomes upon damage, which can be seen by puncta formation and colocalization with a lysosomal marker (e.g. LAMP1 [lysosomal associated membrane protein 1]) (Papadopoulos et al., 2017). Transfection of MZ-54 cells with the pmCherry-GAL3 plasmid and subsequent selection with G418 was performed as described in chapter 4.4.1. For fluorescence microscopy, cells were seeded in medium without selection antibiotic.

4.4.3 Staining of cellular cholesterol with filipin III

Cholesterol staining was performed using a cholesterol assay kit containing filipin III (Table 3.20) according to the manufacturer's instructions. Filipin III is a naturally fluorescent polyene antibiotic that binds to unesterified, "free" cholesterol (Maxfield and Wüstner, 2012). The interaction with cholesterol alters the absorption and fluorescence spectrum of filipin III and enables its visualization using a fluorescence microscope.

For co-staining with an antibody against LAMP1, cells were first stained with filipin III (1:100 dilution in PBS as described in the manual of the cholesterol assay kit [Table 3.20]) for 1 hour and subsequently permeabilized, blocked, and incubated with the primary and secondary antibody as described above (chapter 4.4). Incubation with the primary and secondary antibody was performed in the presence of filipin III to enable proper staining.

4.5 Flow cytometry

Flow cytometry is a cell analysis technique that enables measurement of cell characteristics including size, cell number, granularity, cell cycle and fluorescence. Every flow cytometer is composed of a fluidics system that transports the sample into the flow cell, an optical system with lasers for excitation, lenses, emission filters, and an electronic part that processes the detected photocurrent into a digitized signal.

During measurement, a liquid stream that is surrounded by sheath fluid carries single cells through one or more lasers. When the cell gets illuminated by the light beam of the laser, some light scatters due to the cells physical structure. Thereby, the forward scatter (FSC) measures scattered light in the laser direction and is correlated to cell size, whereas the side scatter (SSC) measures light in a 90° angle to the laser path and is correlated to cell

granularity. In addition, the light of the laser excites fluorophores associated to the cell. Subsequently, the fluorescence emission is detected and processed.

Different fluorescent probes were used to assess cell death, autophagic flux, mitochondrial mass, mitochondrial depolarization and ROS levels. For TMRM, MTG, annexin V/PI, pMRX-IP-GFP-LC3-RFP-LC3ΔG, BODIPY^{TM} 581/591 C11 and CM-H2DCFDA measurements (Table 3.8), 20,000 - 35,000 cells were seeded into 24-well plates in triplicates or quadruplicates and treatments were performed on the next day. Afterwards, cells were harvested by transferring the cell culture medium into a FACS tube, followed a washing step with DPBS and subsequent dissociation with trypsin-EDTA for 3 - 10 minutes at 37°C. After adding the cell suspension to the FACS tube, samples were centrifuged for 3 minutes at 195 x g, and pellets were resuspended in either 50 µL DPBS or FACS Buffer (Table 3.15). Subsequently, 5,000 to 10,000 cells were measured in each sample by using a BD Accuri C6 or FACS Canto II.

4.5.1 Assessment of mitochondrial depolarization by TMRM measurements

Tetramethylrhodamine methyl ester (TMRM; ex/em maxima ~ 553/576) is a cationic fluorescent dye that can be used for quantification of mitochondrial membrane potentials. The dye is only sequestered in mitochondria with an intact membrane potential, and depolarization of mitochondria can be detected as decrease in TMRM signal. MEF cells were stained with 100 nM and glioblastoma cells were stained with 50 nM TMRM for 20 minutes at 37°C before harvest. The cell pellets were resuspended in 50 µL DPBS. For assessment of mitochondrial depolarization by BD Accuri C6, the gate in the FL2-H channel was set to 95% - 100% TMRM-positive cells in vehicle-treated controls (Figure 4.1).

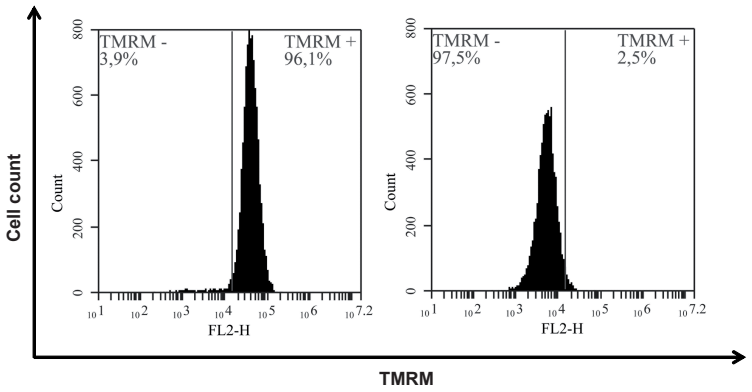

Figure 4.1. TMRM measurement by flow cytometry (BD Accuri C6).
TMRM fluorescence was assessed in the FL2-H channel and the gate was set to 95% - 100% TMRM-positive cells in vehicle-treated controls (left plot).

4.5.2 Determination of mitochondrial mass by MTG measurements

The carbocyanine-based fluorophore MitoTracker Green FM (MTG; ex/em maxima ~ 490/516) was used to detect mitochondrial mass for monitoring of mitochondrial degradation. MTG does not fluoresce until it passively diffuses through the plasma membrane. In the cytoplasm the dye gets oxidized and accumulates in active mitochondria. Cells were stained with 25 nM MTG 30 minutes before harvest. Afterwards, cells were resuspended in 50 µL DPBS and subjected to flow cytometric analysis with a BD Accuri C6. For MTG measurement, the gate in the FL1-H channel was set to 0% - 5% MTG-negative cells in DMSO treated controls, with MTG negative cells being defined as cells with a decrease in mitochondrial mass. The cells were subsequently gated MTG-positive and MTG-negative according to the control.

4.5.3 Monitoring cell death by APC-annexin V-binding and PI uptake

Double stainings with propidium iodide (PI; ex/em maxima ~ 535/617 nm) and APC-annexin V (ex/em maxima 650/660 nm) or annexin-V-FLUOS (ex/em maxima ~ 494/521 nm) enable detection of cell death in general and of phosphatidylserine (PS)-exposing cells. PI intercalates into the DNA and is only absorbed by dying cells with a damaged plasma membrane, such as late apoptotic and necrotic cells. Annexin V detects PS in the external cellular environment. In viable cells, PS is localized on the cytoplasmic surface of the plasma membrane. However, PS is externalized as an early “eat-me” signal in some types of programmed cell death (particularly in early apoptosis).

For assessment of cell death by BD Accuri C6 or FACS Canto II, cell pellets were resuspended in 50 µL FACS Buffer (Table 3.15) with 0.8 µL APC-annexin V and 0.8 µg/mL PI. In case the BD FACS Accuri C6 was used, the APC-annexin V signal was measured in the FL4-A channel and the PI signal was assessed in the FL3-A channel. For cell death analysis with FACS Canto II, annexin-V-FLUOS was measured in the FITC-A channel and PI was measured in the PI-A channel. Vehicle-treated control cells were gated as 95% - 100% PI-negative/annexin V-negative, and following cell fractions were subsequently measured: PI-negative/annexin V-negative, PI-positive/annexin V-negative, PI-negative/annexin V-positive and PI-positive/annexin V-positive (Figure 4.2). For the assessment of overall cell death, only-annexin V-positive, only-PI-positive and double-positive cells were summarized.

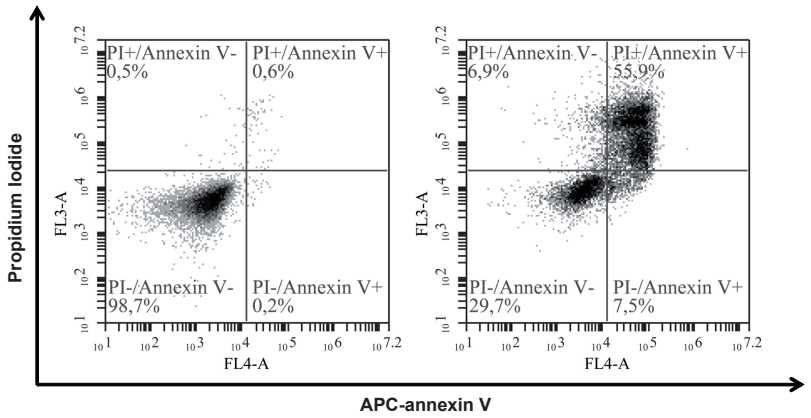

Figure 4.2. Measurement of APC-annexin V and PI by flow cytometry (BD Accuri C6).
The plots display following gates: PI-negative/APC-annexin V-negative, PI-positive/APC-annexin V-negative, PI-negative/APC-annexin V-positive and PI-positive/APC-annexin V-positive. Vehicle-treated control cells were gated as 95% - 100% PI-negative/APC-annexin V-negative (left plot).

4.5.4 Determination of autophagic flux with the pMRX-IP-GFP-LC3-RFP-LC3ΔG plasmid

The pMRX-IP-GFP-LC3-RFP-LC3ΔG plasmid is suitable for measurement of autophagic flux (Kaizuka et al., 2016). During autophagy, the fluorescent probe is cleaved by endogenous ATG4 proteases into equimolar amounts of EGFP-LC3 and RFP-LC3ΔG. While EGFP-LC3 is degraded in the lysosomes, cleaved mRFP1-LC3ΔG remains in the cytosol and serves as an internal control (Figure 4.3). Cells stably expressing the pMRX-IP-GFP-LC3-RFP-LC3ΔG plasmid were generated by Svenja Zielke (Experimental Cancer Research in Pediatrics, working group of Prof. Dr. Simone Fulda, Goethe University Hospital Frankfurt/Main). For determination of autophagic flux, cells were harvested by centrifugation, resuspended in 50 μL PBS and subjected to flow cytometry (BD Accuri C6). Autophagic flux was estimated by calculating the EGFP mean intensity/mRFP1 mean intensity signal ratio (FL1-A/FL3-A).

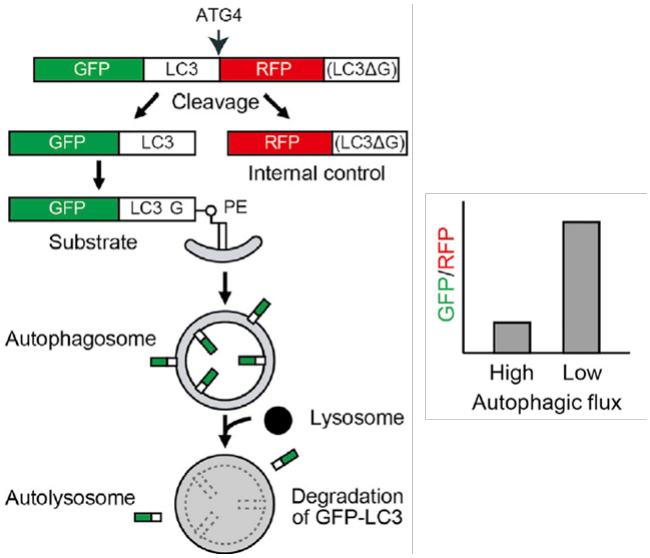

Figure 4.3. Assessment of autophagic flux with the pMRX-IP-GFP-LC3-RFP-LC3ΔG plasmid. Image showing the cleavage of pMRX-IP-GFP-LC3-RFP-LC3ΔG and subsequent degradation of EGFP-LC3. EGFP/mRFP1 ratios are related to the autophagic flux and can be measured by flow cytometry (Kaizuka et al., 2016).

4.5.5 Determination of reactive oxygen species with CM-H2DCFDA

The fluorescent dye CM-H2DCFDA is a general oxidative stress indicator that detects free radicals such as hydroxyl and peroxyl radicals. Oxidation of CM-H2DCFDA results in a fluorescent adduct that is trapped inside the cell and enables quantification of cellular ROS levels. For assessment of cellular ROS, cells were stained with 0.5 µM CM-H2DCFDA in cell culture medium for 30 minutes. Subsequently, cells were washed three times with DPBS, harvested and resuspended in 50 µL DPBS. Cellular ROS levels were determined with a BD Accuri C6 by measuring the mean fluorescent intensity in the FL1-A channel.

4.5.6 Assessment of lipid peroxidation with BODIPY 581/591 C11

The fluorescence emission peak of the lipophilic dye BODIPY^{TM} 581/591 C11 shifts from ~ 590 nm to ~ 510 nm upon oxidation, thus allowing measurement of cellular lipid peroxidation. The fluorophore was added into the cell culture medium at 5 µM for 30 minutes. Afterwards, cells were harvested and resuspended in 50 µL DPBS. Mean fluorescent intensity changes of BODIPY^{TM} 581/591 C11 were assessed with a BD Accuri C6 in the FL1-A channel.

Table 4.1. Laser and emission filters for flow cytometry experiments.

Fluorescent dye	Laser	Emission filters
Annexin-V-FLUOS	488	515/10
APC-annexin V	640 nm	675/25 nm

BODIPY 581/591 C11	488 nm	533/30 nm
CM-H2DCFDA	488 nm	533/30 nm
EGFP	488 nm	533/30 nm
mRFP1	488 nm	670 LP nm
MTG	488 nm	530/33 nm
PI	488 nm	585/40 nm
TMRM	488 nm	585/40 nm

4.6 CRISPR/Cas9 knockout

The RNA-guided CRISPR/Cas9 system (clustered regularly interspaced short palindromic repeats) is derived from a microbial adaptive immune system that cleaves foreign genetic elements and can be used for efficient genome engineering in eukaryotic cells. Thereby, the Cas9 nuclease is guided by a small RNA composed of a scaffold sequence for Cas9 interaction and a defined ~ 20 nucleotides long target sequence that binds the DNA by Watson-Crick base pairing (Garneau et al., 2010; Ran et al., 2013). Cas9 stimulates a double-strand break (DSB) at the target site of the genome that can be repaired by either error-prone non-homologous end joining (NHEJ) or high-fidelity homology directed repair (HDR). In the absence of a repair template, the DSB is fixed by NHEJ, which is prone to insertion or deletion mutations. This system is used for the generation of gene knockouts, as insertion or deletion mutations within the exon of the gene can lead to frameshift mutations or premature stop codons (Ran et al., 2013). In addition, the CRISPR/Cas9 system requires a specific protospacer adjacent motif (PAM) within the DNA target region that varies between the different Cas9 species. Of note, for genomic engineering it is of great importance that the target sequence is unique compared to the rest of the genome.

4.6.1 Vector design for CRISPR/Cas9 knockout

The Cas9 nuclease used for generation of *ATG5* and *ATG7* knockout (KO) is derived from *Streptococcus pyogenes* (*S. pyogenes*) and requires the PAM motif 5' NGG 3' ("N" stands for any base) directly adjacent to the target DNA. Single-guide RNAs (sgRNA) composed of the PAM motif and the target sequence complementary to the selected genomic locus were designed using the online tool Benchling. To this end, the sequences for *ATG5* and *ATG7* were imported and four different sgRNAs that bind within an exon of the protein coding DNA downstream (3') of the transcription start were selected. Only sgRNAs with good "on-" and "off-target values" were picked for highly specific and active sgRNAs with low risk for off-

target modification (Hsu et al., 2013; Doench et al., 2014). If possible, an exon close to the translation start was chosen. Finally, the cloning sites for BbsI were added. For ligation into a vector, the oligonucleotides encoding one sgRNA were annealed by using 1 µL of the sense and antisense guides in 8 µL H_2O. The oligonucleotides were heated for 5 minutes at 95°C, followed by 10 minutes cooling at 25°C and storage at -20°C. (The complete procedure of CRISPR/Cas9 knockout generation is visualized in Figure 4.4.)

The vector pSpCas9(BB)-2A-Puro (PX459) was used for the *ATG7* KOs and the vector pSpCas9(BB)-2A-GFP (PX458) was used for *ATG5* KOs. Both plasmids contain Cas9 from *S. pyogenes* and a cloning backbone for sgRNA. The vectors were digested by mixing 20 µg vector, 6 µL 10x NEBuffer 2.1 and 2 µL BbsI (20 U). H_2O was added up to 60 µL and the vector was digested at 37°C over night. On the next day, the vector was separated by agarose gel electrophoresis for 17 hours at 40 V using a 1% agarose gel. The vector fragments were cut out and the linearized vector DNA was extracted by using a QIAquick Gel Extraction Kit (Table 3.20) according to the manufacturer's instructions. Finally, the DNA was dissolved in elution buffer and concentration was measured. For ligation of the vector with the sgRNAs, 100 ng vector, 50 nM sgRNA, 1 µL 10x ligase buffer and 0.5 µL ligase was mixed and H_2O was added up to 10 µL. Ligation was performed over night at 4°C.

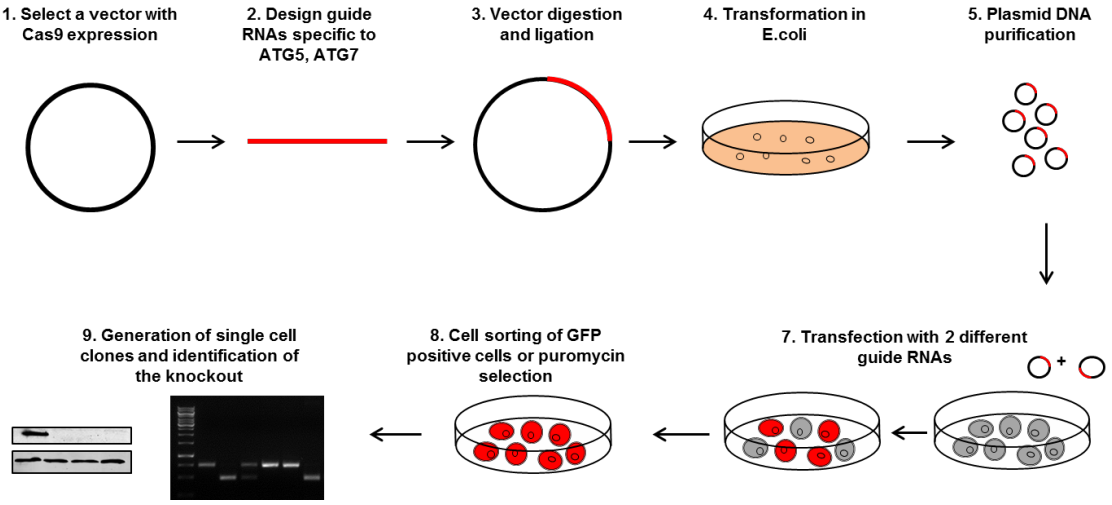

Figure 4.4. Procedure of CRISPR/Cas9 knockout generation.
For further information see chapter 4.6.

4.6.2 Transformation

The high-yield replication of plasmids can be performed by introduction of plasmid DNA into a competent bacterial strain. Therefore, it is necessary that the plasmid DNA contains a bacterial origin of replication and at least one gene for antibiotic resistance. In this study, the plasmids PX458 and PX459 were introduced into *Escherichia coli* (*E. coli)* DH5α.

To this end, DH5α bacteria were thawed on ice and 7.5 ng of the ligated vector containing one of the sgRNAs was added. In addition, 7.5 ng linearized vector was used as negative control. After incubating the bacteria on ice for 30 minutes, a heat shock was applied for 90 seconds at 42°C. Then the bacteria were put on ice for 2 minutes before adding 1 mL LB medium (Table 3.5) without antibiotics. Bacteria were incubated at 37°C and slow shaking for 60 minutes. Afterwards, transformed bacteria were pelletized by centrifugation for 1 minute at 16,060 x g, most of the supernatant was discarded, pellets were resuspended in 150 µL remaining supernatant and plated on the LB-agar plates (with ampicillin 1%). LB-agar plates were incubated overnight at 37°C and the growth of colonies was determined on the next day.

4.6.3 Colony-Screen PCR for determination of colonies that contain the appropriate vector.

For analysis of successful bacterial transformation, a colony-screen PCR was performed. To this end, three single colonies were picked and resuspended in 50 µL H_2O. For every PCR sample, 10x Taq buffer, 200 µM dNTPs, 0.2 µM U6-fwd primer, 0.2 µM of the appropriate antisense guide oligo, 0.5 U Taq polymerase and either 0.5 µL bacteria suspension or H_2O as control were added into a PCR tube and filled up to 20 µL with DNAse free H_2O.

A standard PCR protocol consists of an initial denaturation step for separation of the DNA strands, followed by 25 - 35 cycles of denaturation, annealing (primers form hydrogen bonds with the end of the target sequence) and extension (DNA synthesis by DNA polymerase from 3’ to 5’) and a final prolonged extension step. PCR samples were run at following PCR program:

Table 4.2. PCR program for colony-screen PCR.

Temperature	Time	Repeats
95°C	5 min	1x
95°C	30 sec	35x
52°C	30 sec	
68°C	30 sec	
68°C	2 min	1x

Next, the samples were separated in a 2% agarose gel at 110 V for 30 minutes. In case of correct ligation of the sgRNA-encoding oligonucleotides into the vector, a distinct vector band could be detected.

4.6.4 Plasmid purification

For purification of molecular biology grade plasmid DNA, a QIA-Prep Spin Miniprep Kit was used according to the manufacturer's instructions (Table 3.20). Therefor bacteria colonies that contained the correct vector were transferred into 10 mL LB medium with ampicillin and expanded overnight at 37°C. A small amount of the bacteria suspension was plated onto LB agar and incubated over night at 37°C for subsequent EndoFree Plasmid Purification. The remaining bacteria were harvested by centrifugation. Cell lysis was performed under alkaline conditions, followed by adsorption of DNA onto silica in the presence of high salt. The plasmid DNA was eluted from the silica membrane by adding 50 µL EB buffer.

The plasmid section containing the ligated, sgRNA-encoding oligonucleotide was sequenced, and in case of correct incorporation, transfection-grade plasmid DNA was purified with the EndoFree Plasmid Maxi Kit (Table 3.20) according to the manufacturer's instructions. To this end, a colony was picked from the agar plate and grown in 200 mL LB medium at 37°C over night. After alkaline cell lysis, the lysate was cleared by filtration and endotoxins were removed. Plasmid DNA was bound to a QIAGEN resin under appropriate low-salt and pH conditions. After repeated washing, plasmid DNA was eluted in a high-salt buffer, concentrated and desalted by isopropanol precipitation. Subsequently, the plasmid DNA was washed, air-dried and re-dissolved in a suitable volume of endotoxin-free buffer.

4.6.5 Transfection of cas9 and guide RNA for CRISPR/Cas9 knockouts

MZ-54 cells and U343 cells were transfected with plasmids containing Cas9 and one sgRNA with either 2A-EGFP (PX458) or 2A-Puro (PX459) for selection. Transfection was performed by using Lipofectamine 3000 according to the manufacturer's instructions. Thereto, 120,000 - 150,000 cells were seeded into 6-well plates to receive a confluence of 70% on the next day. Before transfection, cell culture medium was changed. Then cells were transfected with a combination of two different guide RNA plasmids for either *ATG5* or *ATG7* KO by using 2 x 1.25 µg DNA and 3.75 µL Lipofectamine 3000 per 6-well (ratio 1:1.5). Medium was changed the next day. After 48 hours, cells with integration of PX459 were selected with 1 µg/mL puromycin and cells transfected with PX458 were analyzed for EGFP expression by microscopy.

4.6.6 Cell sorting

Cells transfected with PX458 vector containing EGFP as selection marker were sorted 72 hours after transfection. To this end, the FACS Aria II cell sorter was set up following the manufacturer's instructions. Cells were pelletized, resuspended in 1 mL DPBS and

immediately put on ice. For gate settings, a small number of cells were stained with DAPI (dilution 1:100) to visualize dead cells, and in addition, the emission of non-transfected cells was measured to determine background signal. Cells with EGFP positive signal were sorted into a 24-well containing pre-warmed medium. Medium was changed after 24 hours.

4.6.7 Single cell dilution

Single cell colonies were generated for stable CRISPR/Cas9 KOs of *ATG5* and *ATG7*. Therefor the selected cells expressing either PX458 or PX459 were pelletized and resuspended in a small amount of fresh medium six days after transfection. Cells were counted with a Neubauer Chamber and the cell suspension was diluted in three steps to receive a final concentration of 1.2 cells per 150 µL. Four 96-well plates were seeded with 1.2 cells per well in conditioned medium composed of 50% filtered medium harvested from cultured cells of the same cell line and 50% fresh medium.

4.6.8 DNA extraction and PCR for detection of CRISPR/Cas9 knockout clones

For the identification of *ATG5* and *ATG7* knockout clones, cells were pelletized, washed with DPBS and resuspended in different amounts of Quick extract DNA solution to achieve an end concentration of 20, 200 and 2,000 cells per µL. The DNA samples were vortexed for 15 seconds, followed by 6 minutes shaking at 65°C, 15 seconds vortexing and 2 minutes shaking at 98°C. Finally, DNA extracts were stored at -20°C. Primers that flank the genomic region containing the two respective sgRNA binding sites were designed with Primer Blast.

Following reagents were mixed for the PCR reaction and nuclease-free water was added up to 20 µL: 10 mM dNTPs, 10 µM forward and reverse primer (Table 3.22), 1 µL template DNA, 4 µL 5x Phusion HF buffer and 0.2 µL Phusion High-fidelity DNA Polymerase. If no clear single band could be detected, a small amount of DMSO (0.5 µL) was added to the reaction mix. PCR samples were run at following PCR program:

Table 4.3. PCR program for detection of CRISPR/Cas9 knockout clones.

Temperature	Time	Repeats
98°C	30 sec	1x
98°C	10 sec	35x
45 - 72°C	20 sec	
72°C	30 sec per kilo base	
72°C	10 min	1x

The annealing temperature was adjusted according to the melting temperature (Tm) and annealing temperature of the primers, which are based on the primer sequence, concentration and the utilized DNA polymerase. Therefor the Tm calculator tool from NeoLab was used and following melting temperatures were determined: 69°C for *ATG5* and 66°C for *ATG7* primers (Table 3.22).

Subsequently, the samples were separated on a 1% agarose gel. Single cell clones with knockout of *ATG5* or *ATG7* showed a lower band compared to control cells. Figure 4.5 and Figure 4.6 display the deletions within the ATG5 or ATG7 genes and the PCR product for knockout detection.

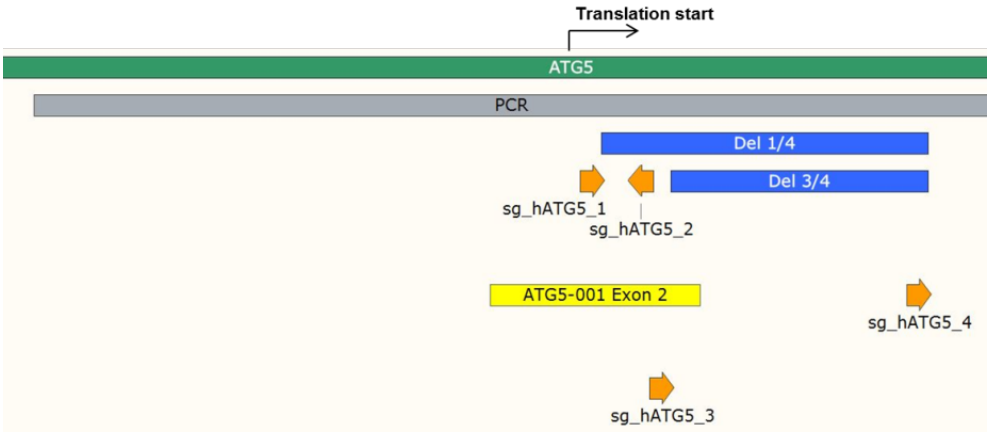

Figure 4.5. CRISPR/Cas9 deletions of the human *ATG5* gene.
The figure displays a part of the human *ATG5* gene (green) including Exon 2 (yellow). The deletions (Del) that could be generated in stable single cell clones are depicted in blue and the numbers refer to the appropriate two sgRNAs (1 and 4; 3 and 4). For detection of *ATG5* KO clones, the depicted PCR product (grey) was amplified. The sgRNAs 1 - 4 that were used to generate *ATG5* KOs are shown in orange. Generated with SnapGene software (from GSL Biotech; available at snapgene.com).

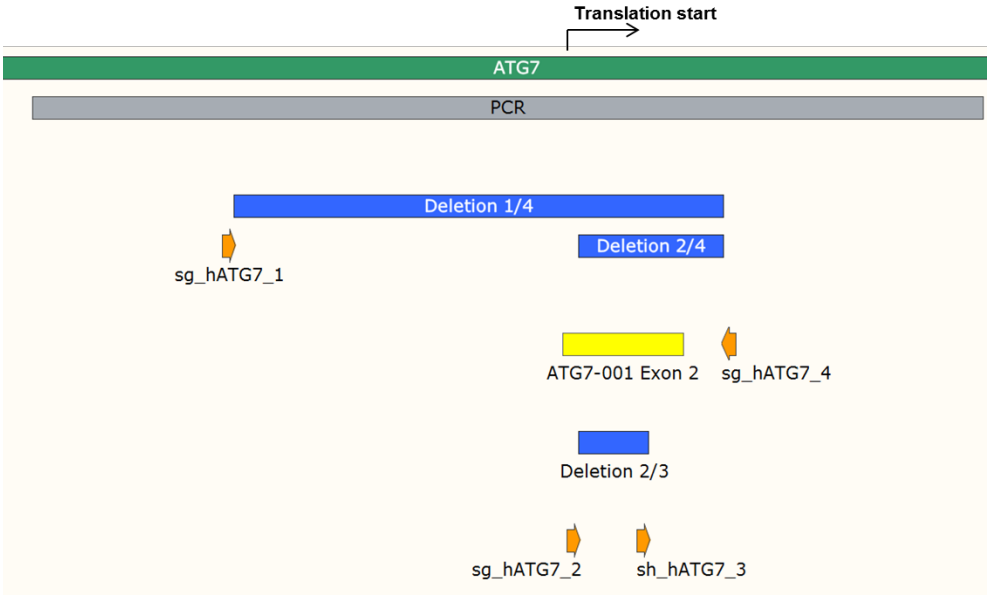

Figure 4.6. CRISPR/Cas9 deletions of the human *ATG7* gene.
Image displaying a part of the human *ATG7* gene (green) including Exon 2 (yellow). The deletions (Del) that could be generated in stable single cell clones are shown in blue; the numbers refer to the appropriate two sgRNAs (1 and 4; 2 and 4; 2 and 3). For detection of *ATG7* KO clones, the depicted PCR product (grey) was amplified. The sgRNAs 1 - 4 that were used to generate *ATG7* KOs are shown in orange. Generated with SnapGene software (from GSL Biotech; available at snapgene.com).

4.7 Assessment of caspase activity

The activation of executioner caspases 3 and 7 takes place during caspase-dependent apoptotic cell death. To analyze caspase 3-like activity, a DEVD cleavage assay was performed, which is based on the cleavage of the tetrapeptide DEVD (Asp-Glu-Val-Asp) by caspases and subsequent release of the DEVD bound fluorophore aminomethylcumarin (AMC). Changes in fluorescence activity of free AMC were measured over a time period of 2 hours and normalized to the protein concentration.

For sample preparation, 30,000 cells were seeded into 24-wells in quadruplicates. Cells were treated on the next day for the appropriate time periods and subsequently lysed with 200 µL CA Lysis Buffer (Table 3.14). Protein quantification was performed with the Roti Quant colorimetric protein assay, which is based on the Bradford dye-binding method (Bradford, 1976). To this end, a BSA-standard curve was pipetted in duplicates into a 96-well plate starting from 1 µg up to 6 µg BSA and diluted 1:5 in 0.9% NaCl. Next, 25 µL sample lysate and CA Lysis Buffer as blank were transferred into the 96-well plate. Each well was filled up to 50 µL with 0.9% NaCl and 200 µL Roti-Quant mix was added. After 5 minutes incubation at 37°C, the absorbance was measured with a Spark multimode microplate reader. For assessment of caspase 3-like activity, 50 µL sample lysate and 150 µL CA Reaction Buffer (Table 3.14) were added into a black 96-well plate and the measurement was immediately

started by using a SPARK multimode microplate reader. The fluorescence of released AMC was measured with an excitation wavelength of 360 nm and emission wavelength of 465 nm at 37°C over a time course of 2 hours. Caspase activation was measured as increase of fluorescence intensity in arbitrary fluorescence units per µg protein and hour.

4.8 Determination of gene expression by quantitative real-time polymerase chain reaction (qRT-PCR)

Quantitative real-time PCR is a method that allows monitoring of target DNA amplification during PCR in real-time, whereas conventional PCR only shows the final product.

Cells were seeded at 120,000 - 150,000 cells per 6-well and treatments were applied the next day. Afterwards, samples were pelletized and washed with DPBS. For isolation of total RNA, the QIAshredder and RNeasy Mini Kit (Table 3.20) or the EXTRACTME total RNA Kit (Table 3.20) were used according to the manufacturer's instructions. Complementary DNA (cDNA) was synthesized by mixing 2 µg of RNA with 1 µL random primers (stock 3 µg/µL), 1 µL of 50 mM Oligo$(dT)_{20}$ and 1 µL of 10 mM dNTP Mix. DEPC-H_2O was added to a total volume of 14 µL. Next, samples were incubated at 65°C for 5 minutes, followed by 1 minute cooling on ice. Then 4 µL First Strand Buffer, 1 µL 0.1 M DTT and 0.5 µL Superscript III reverse transcriptase and 0.5 µL DEPC-H_2O were added and cDNA was synthesized in a thermocycler: 25°C for 5 minutes, 50°C for 60 minutes and 70°C for 15 minutes. Afterwards, the cDNA was diluted with 180 µL DEPC-H_2O.

Subsequently, a TaqMan gene expression assay was performed, which uses a fluorogenic probe for detection of the accumulating DNA product during the qRT-PCR. The TaqMan probe consists of an oligonucleotide that is complementary to the target cDNA and led with a fluorophore as well as a quencher in close proximity. During the elongation step, the *Taq* polymerase cleaves the fluorophore, which results in a fluorescence signal that is proportional to the amount of cDNA template during the exponential phase of the qRT-PCR (Bustin, 2000).

Thereto, 5 µL cDNA, 1 µl FAM-MGP primer (TaqMan Gene Expression Assay primer) (Table 3.24) and 10 µl 1x FastStart Universal Probe Master-mix were mixed and transferred into a 96-well qRT-PCR plate. The qRT-PCR reaction was carried out as follows:

Table 4.4. Thermo cycler program for qRT-PCR.

Temperature	Time	Repeats
50°C	2 min	1x
95°C	10 min	1x

95°C	15 sec	40x
60°C	1 min	

Relative expression levels of the target genes were calculated by using the comparative C_T method (Schmittgen and Livak, 2008). To this end, the relative gene expression of the gene of interest was normalized to the amplification value of the reference gene *TBP* (TATA-box binding protein). In the next step, the difference in the ΔCt values between the treated and control samples was calculated (ΔΔCt).

4.9 Proteomics (TMT-labeled approach)

Mass spectrometry is a technique that enables detection and quantification of molecules by measurement of the mass-to-charge ratio of ions. Proteins can be identified from the mass of its peptide fragments. In this study, a combination of liquid chromatography and mass spectrometry (LC-MS/MS) was performed to determine the whole proteome of MZ-54 cells treated with different autophagy inducers compared to control. Therefor the experiment was performed in duplicates.

4.9.1 Cell lysis, reduction and alkylation

For proteomic analysis, $4*10^6$ MZ-54 cells were seeded for each condition and treatments were performed on the next day. Afterwards, the samples were washed two times with chilled DPBS, and 1 mL Proteomics Lysis Buffer (Table 3.17) was used to scrape the cells off the plate. Cells were transferred into 2 mL low-bind tubes, and viscosity was decreased by pipetting up and down several times. Next, the samples were boiled for 10 minutes at 95°C, sonicated for 2 minutes (1 sec on, 1 sec off, 45% amplitude), and boiled again for 5 minutes at 95°C.

4.9.2 Methanol/chloroform precipitation

For methanol/chloroform precipitation, the samples were transferred into 15 mL tubes. Four parts of ice-cold methanol plus one part of ice-cold chloroform were added, followed by vigorous mixing. Afterwards, three parts of ice-cold, deionized H_2O were added, and the samples were centrifuged at 4,000 x g and 4°C for 25 minutes. The top layer was removed without disturbing the interphase and after adding three parts of ice-cold methanol, the samples were again vortexed and centrifuged for 10 minutes at 4,000 x g and 4°C. The supernatant was aspirated, and the remaining protein pellet was washed with three parts ice-

cold methanol by vortexing and centrifugation for 10 minutes at 4°C and 4,000 x g. Protein pellets were transferred into low-bind tubes. For the last washing step, 1 mL ice-cold methanol was added, and samples were vortexed and centrifuged for 5 minutes at 15,000 - 20,000 x g and 4°C. Afterwards, the supernatants were removed, and pellets were dried for 10 minutes.

4.9.3 Dissolving the protein pellet

The protein pellets were dissolved in 1 mL Digestion Buffer (Table 3.17) by pipetting up and down several times and heating to 37°C for 30 minutes while shaking, followed by sonication (2x 10 beats, 1 second on, 1 second off, 45% amplitude). Next, protein quantification was performed with the Roti Quant colorimetric protein assay according to the manufacturer's instructions. Therefor the protein lysates were diluted 1/20 and 1/40.

4.9.4 Digestion with lysyl endopeptidase and trypsin

For digestion of the protein samples with Lys-C and trypsin, 100 µg protein in 100 µL were used and diluted 1:1 with 50 mM Tris (pH 8.5) to receive a urea concentration of 4 M. Then 1 µg lysyl endopeptidase/100 µg proteins was added and the samples were incubated for 3 hours at 37°C and 550 rpm shaking on a thermomixer. In the next step, the samples were diluted 1:1 in EPPS buffer (Table 3.17) to receive a urea concentration of 2 M. After addition of 1 µg trypsin /100 µg proteins, the samples were incubated over night at 37°C and 550 rpm shaking. Lastly, the digest was stopped with a final concentration of 1% trifluoroacetic acid (TFA).

4.9.5 Desalting and concentration of the peptides

To desalt the samples, reverse-phase Sep-Pak tC18 cartridges with 50 mg sorbent were connected to a vacuum manifold. The cartridges were activated with 1 mL methanol, followed by 1 mL 60% acetonitrile (ACN)/0.1% TFA and 3 mL 1% ACN/0.1% TFA for equilibration. Before sample loading the vacuum was decreased. Cartridges with bound peptides were washed with 3 mL 1% ACN/0.1% TFA. The peptides were eluted in two steps with 500 µL 40% ACN and 500 µL 60% ACN and subsequently concentrated for 2 hours at 30°C in a vacuum concentrator. Next, the peptides were filled up 100 µL with H_2O and a Micro BCA assay was performed according to manufacturer's instructions.

4.9.6 TMT-labeling of protein digests

Isobaric labeling with Tandem Mass Tag (TMT) reagents was performed for deep profiling of the proteome. This method enables identification and quantitation of proteins in pooled and fractionated samples by mass spectrometry. For TMT labeling, an amount of 10 µg peptides was dried in a concentrator at 30°C. The peptides were resuspended in 10 µL 0.2 M EPPS (pH 8.2)/20% ACN and Ten-plex TMT reagent (Table 3.20) in a TMT:protein ratio of 2.5:1 was added. After incubation for 1 hour at room temperature, the labeling reaction was quenched with 5% hydroxylamine to a final concentration of 0.5%, followed by 15 minutes incubation. For acidification, TFA was added to an end concentration of 1%.

To test for proper labeling and correct mixing ratios, 0.5 µg of each peptide sample was pooled. A stage tip was activated with 30 µL methanol and centrifugation at 2,000 x g for 1 minute. Next, 30 µL 60% ACN/0.1% TFA was added, followed by centrifugation for 1 minute at 2,000 x g. For equilibration, 70 µL 1% ACN/0.1% TFA was applied and centrifuged at 2,000 x g. Then the stage tip was loaded with the pooled peptides and centrifuged for 1 min at 2,000 x g. After washing with 70 µL 5% ACN/0.1% TFA, the peptides were eluted with 40 µL 80% ACN/0.1% formic acid (FA) and centrifugation at 2,000 x g for 1 minute. The pooled peptides were dried in a concentrator at 30°C and resuspended in H_2O with 0.1% FA to 2 µg/µL peptides and liquid chromatography-mass spectrometry was performed to verify labeling efficiency (> 99%).

4.9.7 Fractionation of peptides

The peptides were fractionated to reduce the sample complexity and to allow detection of low-abundant proteins. To this end, the samples were pooled and adjusted to the lowest peptide concentrations measured in the test run. After drying the peptides at 30°C in a concentrator, the fractionation was performed using a Pierce High pH Reverse-Phase Peptide Fractionation Kit (Table 3.20). Conditioning of the columns was carried out according to the manufacturer's instructions. To wash unbound TMT labels, 300 µL 4% ACN/ 0.1% triethylamine (TEA) was applied and the column was centrifuged at 3,000 g for 2 minutes. Then the pooled sample was fractionated into 16 fractions by adding 300 µL of the following solutions and subsequent centrifugation at 3,000 g for 2 minutes: 7.5, 10, 12.5, 15, 17.5, 20, 22.5, 25, 27.5, 30, 32.5, 35, 37.5, 42.5, 47.5 and 60% ACN in 0.1% TEA. The fractions 1+9, 2+10, 3+11, 4+12, 5+13, 6+14, 7+15 and 8+16 were pooled and evaporated to dryness and stored at -80°C. The prepared samples were given to Dr. Georg Tascher (Institute of Biochemistry II, working group of Christian Münch, Goethe University Hospital Frankfurt/Main, Germany) for mass spectrometry measurement.

4.9.8 Proteome analysis

Statistics and analysis of proteomic data was performed by using the tool Perseus (Tyanova et al., 2016) and PANTHER (Ashburner et al., 2000; The Gene Ontology Consortium, 2017).

4.10 Fractionation of cytosol and membrane and immunoblot analysis

The fractionation method with digitonin can be used to separate the cytosol and cellular organelles including lysosomes, mitochondria and ER and was described by Adrian and coworkers (Adrain et al., 2001). In this experimental approach, the aim was to separate fully intact lysosomes from the cytosol. For that purpose, the digitonin concentration and incubation time for the cytosol extraction is pivotal and must be precisely determined for every cell line.

Thereto, $2*10^6$ - $3*10^6$ cells were seeded into T175 flasks. After treatment, the cells were harvested with trypsin-EDTA, washed with chilled PBS and put on ice. The cells were carefully resuspended with 500 µL chilled PBS, then 500 µL Lysis Buffer 1 (Table 3.18) was added and the samples were incubated for 15 minutes at room temperature on an overhead tumbler. Afterwards, the lysed cells were centrifuged at 1,035 x g and 4°C for 5 minutes (centrifugation step 1) to separate the cytosol. The supernatants containing the cytosolic fraction were transferred into new 1.5 ml tubes and centrifuged down again for 30 seconds at 1,677 x g (centrifugation step 2) to remove residual cell debris.

Next, the pellet from centrifugation step 1 was resuspended in 300 µl Lysis Buffer 2 (Table 3.18), followed by incubation for 5 minutes and 10 minutes centrifugation at 10,278 x g. Supernatants were transferred into new tubes, centrifuged again for 30 seconds at 6,708 x g, and the organelle-containing fraction was collected. To determine cathepsin release from the lysosomes into the cytosol by immunoblot analysis, protein quantification, SDS-PAGE and western blots were performed as described in the chapters 4.2.2 - 4.2.4. Therefor a protein amount of 20 - 25 µg was used for separation by SDS-PAGE. The cytosolic fractions and organelle fractions were loaded onto the same gel and antibodies against TUBA4A (α-Tubulin) and LAMP1 were used to determine the respective fractions.

4.11 Cathepsin B assay

For quantification of lysosomal membrane permeabilization, the cathepsin activity in the cytosol was measured by using a fluorogenic substrate for cathepsin B. To this end, 30,000 cells were seeded into 24-wells in triplicates and treatments were performed as indicated. For cytosol extraction, the cells were incubated in Digitonin Extraction Buffer (Table 3.19) for

15 minutes on ice while shaking slowly (lifting frequency 50 times per minute). The exact amount of digitonin and the incubation time is critical and must be titrated for every cell line to ensure proper permeabilization of the cell membrane and to avoid damage of the lysosomes. Afterwards, 180 µL cytosol extracts were transferred into a 96-well plate on ice. For measurement of cathepsin B activity, 100 µL cytosol extract was mixed with 75 µL L-Cysteine Buffer (Table 3.19) in a black 96-well plate and incubated at 37 °C for 10 minutes. Then, 75 µL Cathepsin B Reaction Buffer (Table 3.19) was added and the 96-well plate was immediately placed into a SPARK multimode microplate reader. The fluorescence was measured at an excitation wavelength of 348 nm and emission wavelength of 440 nm every 5 min at 40°C over a time period of 2 hours. Cathepsin B activity was measured as increase of fluorescence intensity in arbitrary fluorescence units per µg protein and hour.

4.12 Acid sphingomyelinase activity assay

The acid sphingomyelinase (ASM) assay enables fluorometric analysis of the acid sphingomyelinase activity in cell extracts. Thereby, a fluorogenic probe (AbRed) serves as an indicator for quantification of phosphocholine, which is produced by hydrolysis of sphingomyelin by ASM. The fluorescence intensity of AbRed is proportional to ASM activity and can be measured using a microplate reader.

MZ-54 cells were seeded at 30,000 cells per well in a 24-well plate and treatments were performed on the next day. Afterwards, the medium was removed, followed by addition of 200 µL CA Lysis Buffer (Table 3.14) and incubation for 15 minutes while shaking. For storage, cell extracts were kept at -80°C.

Measurement of ASM activity was performed as described in the manufacturer's instructions (Table 3.20). First, all assay materials were equilibrated to room temperature. An amount of 50 µL test sample was pipetted a black 96-well plate and 50 µL assay buffer was added as blank. After addition of 50 µL sphingomyelin working solution, the plate was incubated for 2 - 3 hours at 37°C. Next, 50 µL sphingomyelinase assay mixture containing AbRed was added in each well. After incubation for 1 - 2 hours at room temperature, the mean fluorescent intensity was measured with the SPARK multimode microplate reader at an extinction wavelength of 540 nm and emission wavelength of 590 nm.

4.13 Sample preparation for targeted analysis of sphingolipids and ceramides

For analysis of active sphingolipids, MZ-54 cells were seeded at $3*10^6$ cells per T175 flask in octuplicates. On the next day, cells were treated with loperamide in medium supplemented

with 2% FBS or with pimozide in medium supplemented with 5% FBS. Cell culture medium of the respective DMSO-treated controls was supplemented with the same amount of FBS. (FBS concentration was reduced to decrease lipid background signal.) Afterwards, cells were harvested using trypsin, washed four times with DPBS, and immediately frozen at -80°C. The samples were given to Prof. Dr. Irmgard Tegeder (Institute of Clinical Pharmacology, Goethe University Hospital Frankfurt/Main, Germany) for further preparation and the targeted analysis of sphingolipids/ceramides.

4.14 Statistics

Statistical analysis of the data was performed with GraphPad Prism 7. A Shapiro Wilk normality test was used to determine if the variables of a data set are well-modeled by a normal distribution. Statistical significances of normally distributed data were calculated with a Student's t-test for comparison of two groups or with an analysis of variance to compare three or more independent groups (ANOVA). The influence of one independent variable was examined with a one-way-ANOVA (e.g. treatment of the cells with different compounds), while the influence of two independent variables were examined with a two-way-ANOVA (e.g. knockdown with siRNA against the gene of interest and control siRNA, followed by treatment with different compounds). When the data set was not normally distributed, non-parametric rank-sum tests were applied. Therefor a Mann-Whitney U test was used for comparison of two groups and a Kruskal-Wallis test was applied for comparison or three or more groups. The minimum level of statistical significance was set at $P \leq 0.05$ and significances are depicted as $P \leq 0.05$: *, $P \leq 0.01$: **, $P \leq 0.001$: *** of n.s. not significant between control and treated cells or as indicated with brackets.

5 Results

5.1 AT 101 induces mitochondrial dysfunction

AT 101, a natural polyphenolic compound derived from cotton seeds, has been shown to induce autophagy in several different cancer cell lines (Voss et al., 2010; Wei et al., 2016; Lu et al., 2017). To confirm these previous findings, induction of the autophagic flux upon treatment with AT 101 in the human glioma cell lines U343 and MZ-54 was investigated by western blot analysis of LC3B conversion (Figure 5.1A, B). LC3B exists in two different isoforms, the cytosolic LC3B-I isoform (~ 18 kDa) and the phosphatidylethanolamine (PE)-conjugated LC3B-II isoform (~ 16 kDa). The increase of LC3B-II is correlated to an increased number of autophagosomes as a result of either autophagy induction or late stage inhibition. To distinguish between induction and inhibition of autophagy, combination treatments with AT 101 and the late-stage autophagy inhibitor bafilomycin A_1 were performed. Bafilomycin A_1 prevents lysosomal acidification by inhibition of vacuolar type H^+-ATPase (V-ATPase) and therefore blocks fusion of autophagosomes with lysosomes and final degradation of the autophagic cargo (Yoshimori et al., 1991; Yamamoto et al., 1998). Hence, further increase of LC3B-II levels upon addition of bafilomycin A_1 would indicate an upregulation of the autophagic flux by AT 101. Treatment with AT 101 strongly increased LC3B-II after 24 - 48 hours in U343 cells (Figure 5.1A) and after 6 - 48 hours in MZ-54 cells (Figure 5.1B). Combined treatment with AT 101 and bafilomycin A_1 further intensified the LC3B switch from LC3B-I to LC3B-II after 24 hours in U343 cells and after 6 hours in MZ-54 cells, indicating induction of the autophagic flux by AT 101. At later time points, AT 101 treatment alone resulted in the maximal LC3B-II signal intensity, and further increase following addition of bafilomycin A_1 could not be detected.

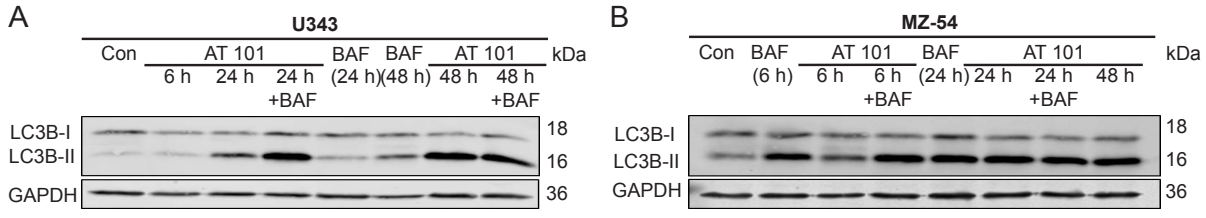

Figure 5.1. AT 101 induces the autophagic flux.
(A, B) Immunoblot analysis of LC3B-I and LC3B-II protein levels. GAPDH was used as housekeeping protein control. U343 cells (A) and MZ-54 cells (B) were treated with 15 µM AT 101 for 6, 24 and 48 h or with DMSO (Con) for 48 h in the presence or absence of 10 nM bafilomycin A_1 (BAF). BAF was added to the cells 4 h prior to harvest. The numbers in brackets refer to the time points when the cells were harvested. Experiments were repeated three times with similar results. Figure adapted from Meyer et al., 2018.

Moreover, in previous studies, AT 101 has been described to induce an autophagic type of cell death in glioblastoma (GBM) cells, which was accompanied by an early fragmentation of mitochondria (Voss et al., 2010). To investigate the potential impact and time-dependent effects of AT 101 treatment on mitochondrial dysfunction, TMRM measurements were performed to analyze mitochondrial membrane potentials using flow cytometry (Figure 5.2). The number of cells with intact mitochondrial membrane potentials correlates to the population of TMRM-positive cells. AT 101 treatment led to an almost complete mitochondrial depolarization in the glioma cell lines MZ-54 (Figure 5.2A), U343 (Figure 5.2B), and U87MG Figure 5.2C) after 24 - 48 hours. To determine the potential connection of AT 101-induced mitochondrial depolarization with the mitochondrial pathway of apoptosis, the mitochondrial membrane potentials of MEF WT and MEF *Bax Bak1* DKO cells were compared following AT 101 treatment. BAX and BAK1 belong to the proapoptotic BCL2 protein family and mediate mitochondrial outer membrane permeabilization (MOMP) by forming pores across the mitochondrial outer membrane, which subsequently leads to apoptosis (Galluzzi et al., 2018). However, MEF WT and apoptosis-deficient MEF *Bax Bak1* DKO cells showed a nearly identical decrease of mitochondrial membrane potentials upon AT 101 treatment for 6 - 48 hours, indicating that apoptosis is irrelevant for AT 101-induced mitochondrial depolarization (Figure 5.2D)

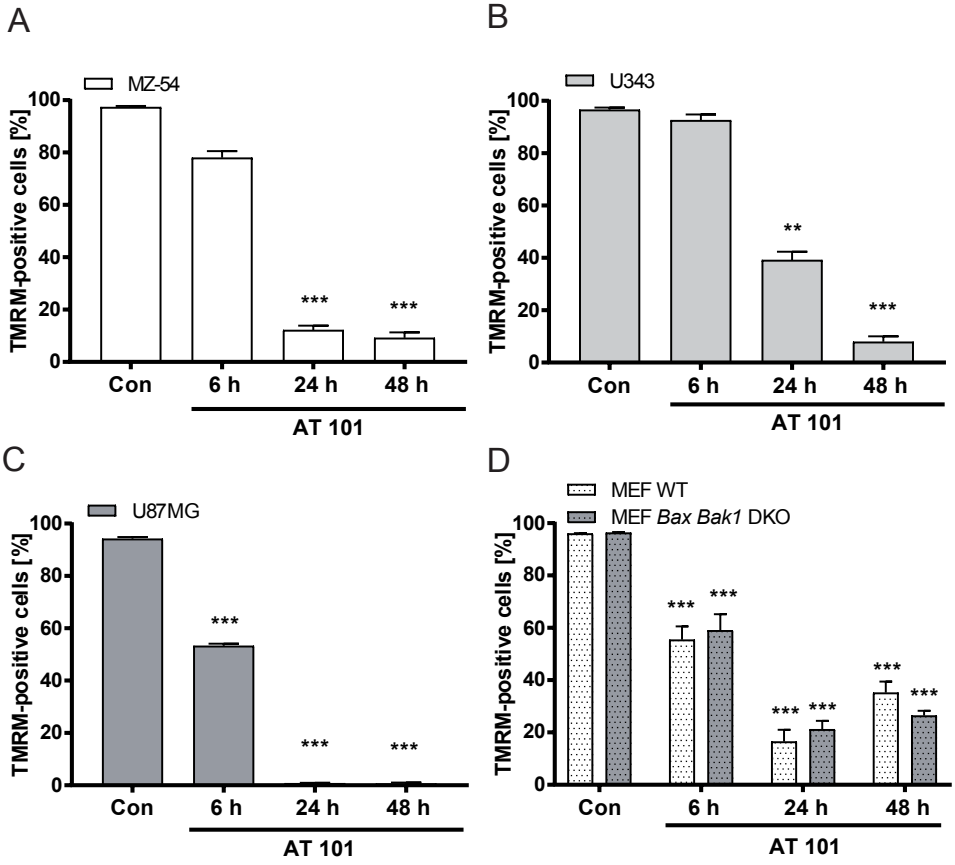

Figure 5.2. AT 101 induces mitochondrial depolarization.
(A-D) Flow cytometric analysis of TMRM positive cells, which is equivalent to the number of cells with intact mitochondrial membrane potential. The human glioma cell lines MZ-54 (A), U343 (B) and U87MG (C) as well as MEF WT and MEF *Bax Bak1* DKO cells (D) were treated with 15 µM AT 101 for 6, 24 and 48 h. DMSO was used as control (Con, 48 h). For flow cytometry measurements, the gate was set to 95% - 100% TMRM positive cells in DMSO treated controls. All experiments were repeated at least three times. Data are means + SEM from *n* = 9 - 12 samples (10,000 cells measured in each sample, 3 - 4 samples per experiment). Statistical significances were calculated with a Kruskal-Wallis test (A-C) or one-way ANOVA (D) ($P \leq 0.05$: *, $P \leq 0.01$: **, $P \leq 0.001$: ***, n.s.: not significant; difference from control). Figure adapted from Meyer et al., 2018.

The well-known uncoupler of the mitochondrial oxidative phosphorylation, FCCP, was used as a positive control for mitochondrial depolarization (Figure 5.3). As expected, FCCP exposure resulted in a significant decrease of the mitochondrial membrane potentials after 6 - 48 hours in the glioma cell lines MZ-54 (Figure 5.3A), U343 (Figure 5.3B) and U87MG (Figure 5.3C), and also in MEF WT and MEF *Bax Bak1* DKO cells (Figure 5.3D).

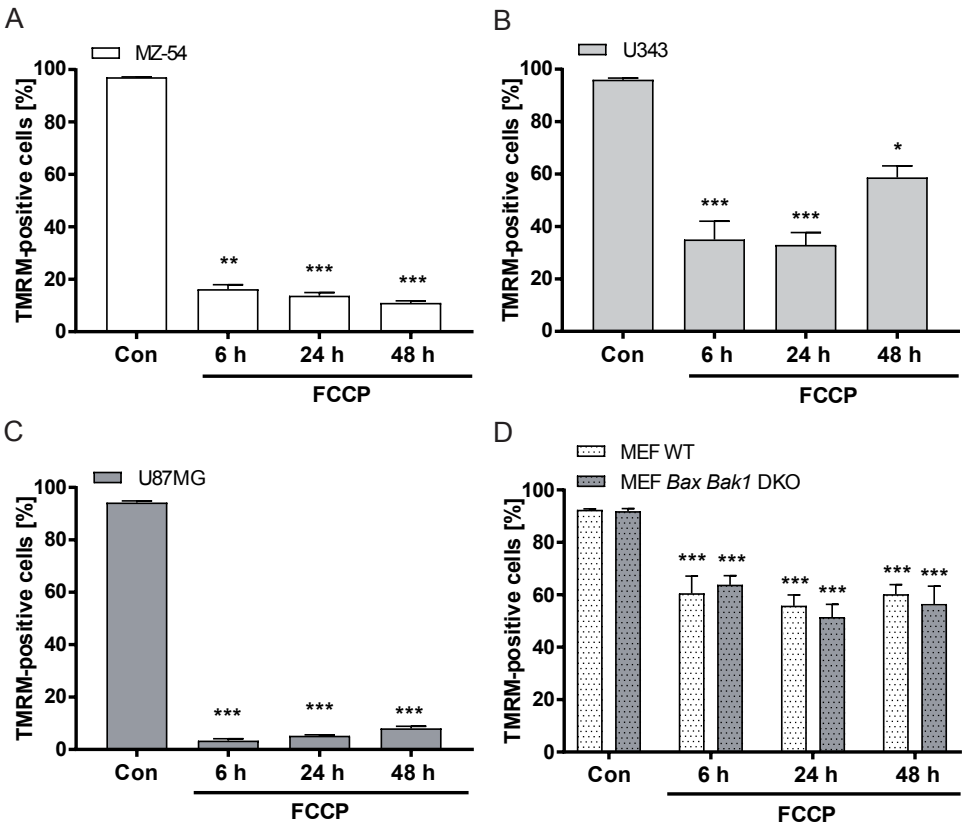

Figure 5.3. FCCP induces mitochondrial depolarization.
(A-D) Flow cytometric analysis of TMRM positive cells, which is equivalent to the number of cells with intact mitochondrial membrane potential. The human glioma cell lines MZ-54 (A), U343 (B) and U87MG (C) as well as MEF WT and MEF *Bax Bak1* DKO cells (D) were treated with 20 µM FCCP for 6, 24 and 48 h or DMSO as control (Con, 48 h). The gate was set to 95% - 100% TMRM positive cells in the DMSO treated controls. All experiments were repeated at least three times. Data are means + SEM from *n* = 9 - 12 samples (10,000 cells measured in each sample, 3 - 4 samples per experiment). Statistical significances were calculated with a Kruskal-Wallis test ($P \leq 0.05$: *, $P \leq 0.01$: **, $P \leq 0.001$: ***, n.s.: not significant; difference from control). Figure adapted from Meyer et al., 2018.

Interestingly, the detected decrease of mitochondrial membrane potentials upon administration of AT 101 is consistent to previous findings that could show strong impairment of mitochondrial respiration by AT 101 in U343 cells and MEF *Bax Bak1* DKO cells as well as the ageing model *P. anserina* (Warnsmann et al., 2018). Of note, mitochondrial depolarization and subsequent breakdown of respiratory chain activity by AT 101 might be the consequence of prolonged opening of the mitochondrial permeability transition pore (mPTP), leading to uncontrolled permeability of the inner mitochondrial membrane (Petronilli et al., 2001). To verify this hypothesis, the impact of mPTP inhibition on AT 101-induced mitochondrial depolarization and cell death was investigated next. To this end, U343 cells were exposed to either AT 101 alone or in combination with olesoxime (TRO), which has been described to inhibit mPTP opening by binding to the outer mitochondrial membrane proteins VDAC (voltage dependent anion channel 1) and TSPO (translocator protein) (Bordet et al., 2007). Consistent with the proposed role of the mPTP, TRO significantly diminished AT 101-induced mitochondrial depolarization (Figure 5.4A) and cell death (Figure 5.4B). However, the calcium ionophore A23187, which was used as positive control for mPTP opening, induced mitochondrial depolarization to a lesser extent than AT 101, and combined treatment with TRO slightly, but not significantly rescued this effect.

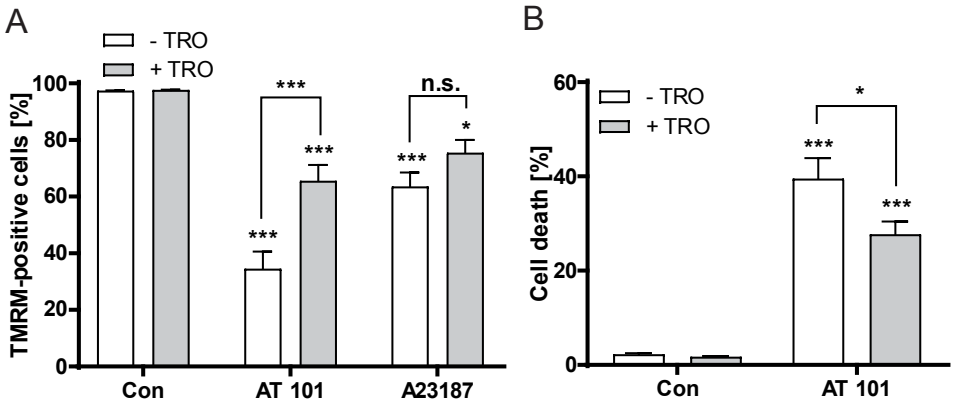

Figure 5.4. Effect of mPTP inhibition on AT 101-induced mitochondrial depolarization and cell death.
(A) Flow cytometric quantification of TMRM positive cells (with an intact mitochondrial membrane potential). U343 cells were exposed to 30 µM AT 101, 20 µM A23187 or DMSO (Con) for 3 h alone or in combination with the mPTP inhibitor olesoxime (TRO). TRO was added at a concentration of 5 µM to the cells 15 min before the other treatments. The gate was set to 95% - 100% TMRM positive cells in the DMSO treated controls. (B) Quantification of cell death by flow cytometric analysis of APC-annexin V binding and PI uptake. U343 cells were treated with 15 µM AT 101 for 48 h in the presence or absence of 2 µM TRO. TRO was applied to the cells 24 h before treatment with AT 101. Experiments were repeated at least three times. Data are means + SEM from n = 9-12 samples (10,000 cells measured in each sample, 3-4 samples per experiment). Statistical significances were calculated with a two-way ANOVA ($P \leq 0.05$: *, $P \leq 0.01$: **, $P \leq 0.001$: ***, n.s.: not significant; difference from control or as indicated). Figure adapted from Warnsmann et al., 2018.

Collectively, these data are in line with previous findings of my master thesis and other studies, showing that AT 101 induced autophagy and strongly impaired mitochondrial

function by opening of the mPTP and subsequent mitochondrial membrane depolarization (Voss et al., 2010; Meyer, 2015; Warnsmann et al., 2018)

5.2 AT 101 treatment decreases mitochondrial protein abundance and shows features of mitophagy induction

Hitherto, AT 101 has been shown to induce an autophagic type of cell death in glioma cells, and mitochondrial events are assumed to play a decisive role in this context, but the exact underlying mechanisms still need to be elucidated (Voss et al., 2010; Warnsmann et al., 2018). For this reason, a global proteome analysis of U343 and U87MG cells following treatment with AT 101 or DMSO as control for 48 hours was performed by Stefanie Rakel (Experimental Neurosurgery, working group of Prof. Dr. Kögel, Goethe University Hospital Frankfurt/Main, Germany) and Prof. Dr. Christian Behrends (Institute of Biochemistry II, Goethe University Hospital Frankfurt/Main, Germany; Medical Faculty, Ludwig-Maximilians-University Munich, Germany). U87MG cells were SILAC (stable isotope labeling with amino acids in cell culture)-labeled with heavy and light isotopes of L-arginine and L-lysine. The proteome analysis was carried out in duplicates with reverse SILAC labels. Since U343 cells did not incorporate enough isotopes for sufficient SILAC-labeling, a label-free proteome analysis was done in triplicates.

A total number of 4,185 proteins were detected in U343 cells, including 354 significantly up-, and 279 proteins significantly downregulated proteins that showed a $\log_2$-difference of at least 0.2 after AT 101 treatment (Figure 5.5A). Of all downregulated proteins 14.7% were mitochondria-related, and of the top 20 downregulated proteins 5 were mitochondria-related (25%). The list of the top 20 up- and downregulated proteins is shown in Table 10.1 (supplements). The bioinformatics tools DAVID and PANTHER were used to elucidate the biological relevance of the up- and downregulated proteins, and the proteins were clustered according to their Gene Ontology (GO) terms for Cellular Component (CC) or Biological Process (BP). Figure 5.5B displays a selection of up- and downregulated GO terms and the respective number of proteins. GO terms with strongly upregulated proteins included tRNA aminoacylation for mRNA translation, gluconeogenesis and smooth endoplasmic reticulum (ER), whereas GO terms with abundantly downregulated proteins included mitochondrion, mitochondrial inner membrane, cell division and mitochondrial translation elongation.

For proteome analysis of U87MG cells, the reverse-labeled duplicates of the SILAC-labeled U87MG cells were combined. In total, 1,452 proteins were detected and of those, 56 were significantly up- and 44 were significantly downregulated and showed a $\log_2$-difference of ≤-1 and ≥1, respectively (Figure 5.5C). The top 20 up- and downregulated proteins are listed in Table S1 (supplements). Bioinformatics analysis with DAVID and PANTHER revealed that 16

(28.6%) of all downregulated proteins were mitochondria-related (Figure 5.5C) and 8 of the top 20 downregulated proteins (40%) clustered for mitochondria-related GO terms. Enriched GO terms for upregulated proteins upon AT 101 exposure of U87MG cells included cell-cell adhesion, positive regulation of NFKB (NF-kappa-B) transcription factor activity and cell-cell adherens junction. GO terms with strongly downregulated proteins comprised mitochondrion, mitochondrial matrix, nucleoplasm and DNA replication (Figure 5.5D). Taken together, the proteome analysis of U343 and U87MG cells following AT 101 exposure demonstrated an abundant downregulation of mitochondrial protein clusters in the two glioma cell lines.

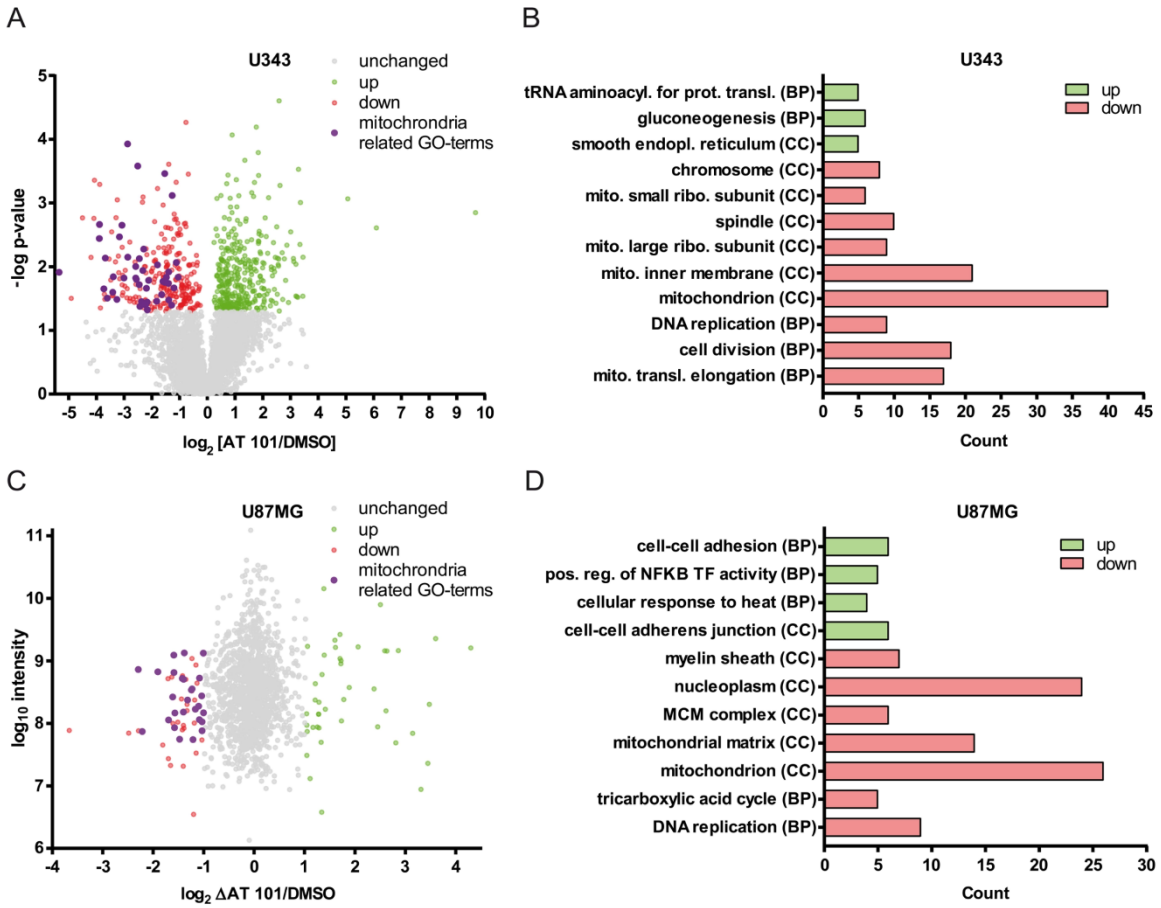

Figure 5.5. Proteome analysis of U87MG and U343 glioma cells treated with AT 101.
(A) Volcano Plot showing the protein ratios (in log_2) as a function of the -log p-value of label-free quantification proteomic-data from U343 cells treated with 15 µM AT 101 or DMSO for 48 h. Of 4,185 detected proteins in total, 279 were significantly ($p<0.05$) downregulated (red dots) and 354 upregulated (green dots) (log_2-difference of at least 0.2). Mitochondria-related GO terms that were significantly downregulated are shown in purple. (B) Quantification of the up- or downregulated proteins that cluster for selected Gene Ontology (GO) terms for Cellular Component (CC) and Biological Process (BP) of U343 cells with a log p-value of $p<10^{-3}$. (C) Volcano plot showing the protein ratios in log_2 as a function of the log_{10} intensity of SILAC proteomic data from U87MG cells treated with 15 µM AT 101 or DMSO for 48 h. Of 1,452 detected proteins in total, 56 (red dots) were significantly downregulated and 44 (green dots) were significantly upregulated and displayed a log_2-difference of +/-1 or greater. Mitochondria-related GO terms that were significantly downregulated are shown in purple. (D) Quantification of up- or downregulated proteins that cluster for selected GO terms for CC and BP of U87MG cells with a p-value of $p<10^{-3}$. Figure adapted from Meyer et al., 2018. Sample preparation was done by Stefanie Rakel (Experimental Neurosurgery, working group of Prof. Dr. Kögel, Goethe University Hospital Frankfurt/Main, Germany) and measurements were performed by Prof. Dr. Christian Behrends (Institute of Biochemistry II, Goethe University Hospital Frankfurt/Main,

Germany; Medical Faculty, Ludwig-Maximilians-University Munich, Germany). Dr. Benedikt Linder (Experimental Neurosurgery, working group of Prof. Dr. Kögel, Goethe University Hospital Frankfurt/Main, Germany) helped with the data analysis.

As confirmed in Figure 5.1, AT 101 strongly induced autophagy in MZ-54 and U343 cells. Hence, the robust downregulation of mitochondria-related GO terms following AT 101 treatment (Figure 5.5) might have resulted from selective degradation of mitochondria by autophagy. To decipher the cause of mitochondrial decrease, an electron microscopy analysis of U343 cells treated with AT 101 for 48 hours was carried out by Prof. Dr. Michel Mittelbronn (Institute of Neurology [Edinger Institute], Goethe University Frankfurt/Main, Germany; Luxembourg Centre of Neuropathology [LCNP], Luxembourg) (Figure 5.6). Indeed, electron microscopy analysis showed a structure with the size and appearance of a mitochondrion that is surrounded by a double-membrane, representing the engulfment of a mitochondrion into a phagophore, which points to the induction of mitophagy upon treatment with AT 101 (Figure 5.6).

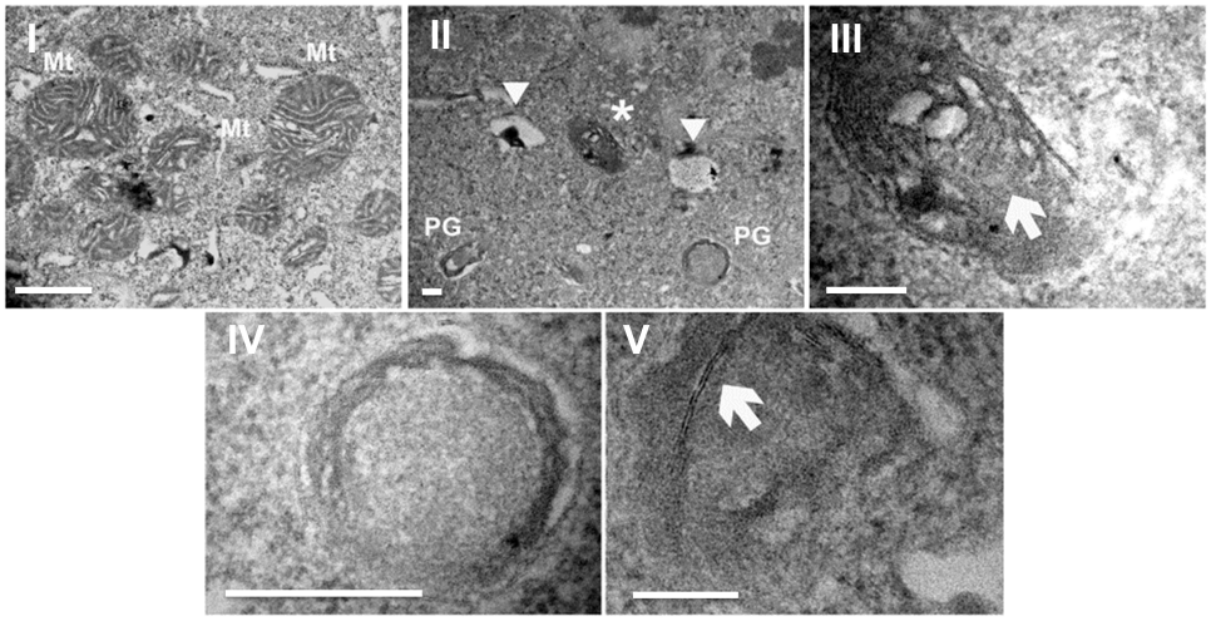

Figure 5.6. AT 101 induces mitophagy in U343 human glioma cells.
Electron microscopy analysis of U343 cells treated with DMSO (I) or 15 µM AT 101 for 48 h (II-V). (I) shows mitochondria (Mt) of DMSO-treated cells with normal morphology and regular cristae structures. Treatment with AT 101 resulted in the induction of autophagy indicated by the formation of phagophores (PG), autolysosomes (arrowheads) and the engulfment of mitochondria (asterisk) with altered cristae structure (II). (III) and (IV) represent higher magnifications of (II). The arrow in (III) points to a mitochondrion that is surrounded by a double membrane as a sign of mitophagy and (IV) displays a phagophore. (V) represents the initiation membranes (arrow) of phagophores. Figure adapted from Meyer et al., 2018. Preparation and electron microscopy were done by Prof. Dr. Michel Mittelbronn (Institute of Neurology [Edinger Institute], Goethe University Frankfurt/Main, Germany; Luxembourg Centre of Neuropathology [LCNP], Luxembourg).

To further verify the induction of mitophagy after AT 101 exposure, the levels of the mitochondrial proteins HSPD1 (heat shock protein family D [Hsp60] member 1), VDAC1

(voltage dependent anion channel 1), TOMM20 (translocase of outer mitochondrial membrane 20) and COX4I1 (cytochrome c oxidase subunit 4I1 pseudogene 1; also called COXIV) was analyzed by western blot (Figure 5.7). Interestingly, MEF WT (Figure 5.7A), MEF *Bax Bak1* DKO cells (Figure 5.7B) as well as the glioma cell lines U343 (Figure 5.7C) and U87MG (Figure 5.7D) revealed a strong decrease of all mitochondrial markers upon AT 101 treatment for 6 - 48 hours (MEF cells and U343 cells) and 6 - 24 hours (U87MG cells). Quantification of the mean protein levels showed a significant decrease of VDAC1 and TOMM20 after 24 hours in U343 cells (Figure 5.7E) and of VDAC1 and COX4I1 after 16 hours in U87MG cells (Figure 5.7F).

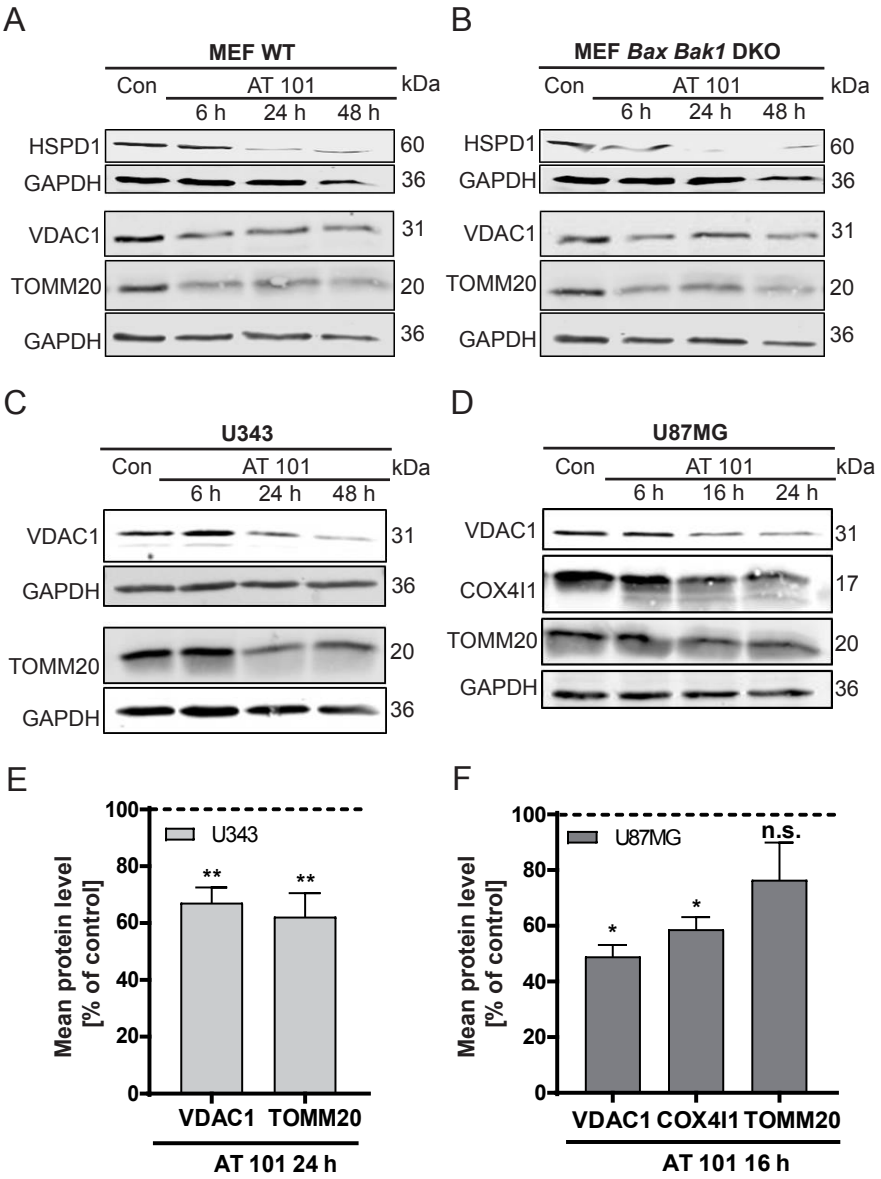

Figure 5.7. Effect of AT 101 on mitochondrial proteins.
(A-D) Assessment of mitochondrial protein levels by immunoblot analysis of VDAC1, TOMM20, COX4I1 and HSPD1. GAPDH was used as housekeeping protein control. MEF WT (A), MEF *Bax Bak1* DKO cells (B) and U343 cells (C) were exposed to 15 µM AT 101 for 6, 24 and 48 h. U87MG cells were treated with 15 µM AT 101 for 6, 16 and 24 h (D). DMSO was used as control (Con, 48 h in A-C, 24 h in D). (E, F) Quantification of the mean protein level of U343 (E) and U87MG cells (F).

Experiments were repeated 3 - 5 times. Data are means + SEM, statistical significances in E and F were calculated with a one-way ANOVA ($P \leq 0.05$: *, $P \leq 0.01$: **, $P \leq 0.001$: ***, n.s.: not significant; difference from control). Figure adapted from Meyer et al., 2018.

Next, the impact of autophagy inhibition on AT 101-induced decrease of mitochondrial proteins was investigated. To this end, MZ-54 and U343 cells with stable CRISPR/Cas9 knockout of the autophagy gene *ATG5* were generated, which is essential for the conjugation of LC3B to PE (LC3B-II isoform) and autophagosome formation. Figure 5.8A displays the PCR amplification of *ATG5* DNA derived from MZ54 or U343 WT cells and the respective *ATG5* knockout clones with different CRISPR/Cas9 base pair deletions. The *ATG5* KO cell lines displayed a deletion of approximately 200 - 250 base pairs compared to the WT cells. In addition, western blot analysis confirmed the absence of ATG5 and of LC3B-II in all knockout clones (Figure 5.8B). Unfortunately, it was not possible to generate more than one *ATG5* KO clone of U343 cells. Therefore, MZ-54 *ATG5* KO cells were used in most experiments.

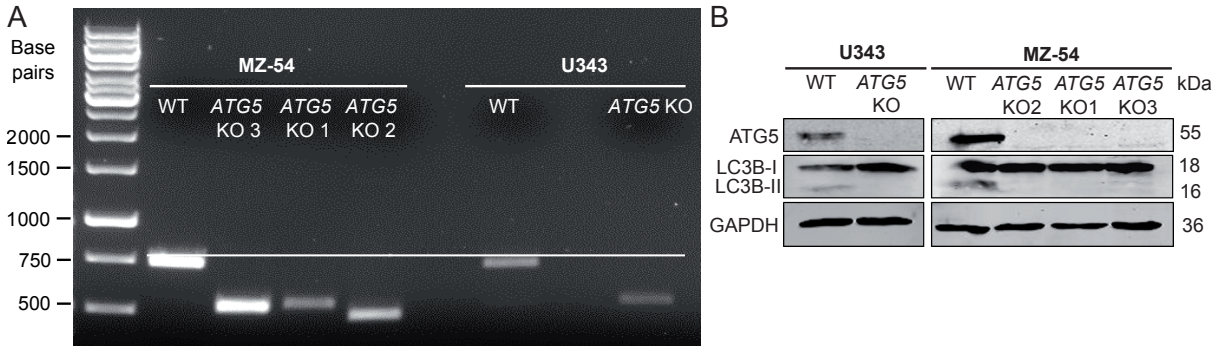

Figure 5.8. Generation of CRISPR/Cas9 *ATG5* KOs.
(A) Separation of PCR amplificates by agarose gel electrophoresis. DNA of the *ATG5* gene containing the CRISPR/Cas9 base pair deletions of MZ-54 and U343 cells was amplified by PCR using the primers shown in Table 3.22. (B) Immunoblot analysis of ATG5 and LC3B levels of U343 and MZ-54 WT cells and the respective *ATG5* KOs. GAPDH was used as housekeeping protein control. Experiments were repeated two times with similar results.

Furthermore, analysis of the LC3B-switch upon administration of AT 101 and bafilomycin A_1 revealed that even under conditions of strong autophagy induction as well as late-stage inhibition, the LC3B-II isoform was completely absent in *ATG5* KO cells, clearly pointing to the functional inhibition of autophagy in these cells (Figure 5.9).

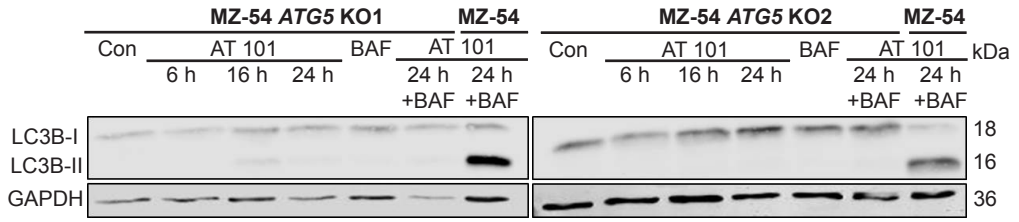

Figure 5.9. *ATG5* KO blocks AT 101-induced autophagy.
Immunoblot analysis of LC3B-I, LC3B-II and GAPDH as housekeeping protein control. MZ-54 control and *ATG5* KO cells were treated with 15 µM AT 101 in the presence or absence of 10 nM bafilomycin A_1 (BAF) for 6, 16 and 24 h or with DMSO (Con) for 24 h. BAF was applied to the cells 4 h before harvest. Experiments were repeated three times with similar outcome. Figure adapted from Meyer et al., 2018.

Next, the levels of the mitochondrial proteins VDAC1, TOMM20 and COX4I1 following AT 101 treatment for 6 - 24 hours was compared in MZ-54 WT cells and two different MZ-54 *ATG5* KO cell lines (Figure 5.10A-C). Strikingly, quantification of the mean protein abundance after 16 hours AT 101 exposure revealed a significant decrease of all mitochondrial proteins in MZ-54 WT cells, but not in the *ATG5* KOs.

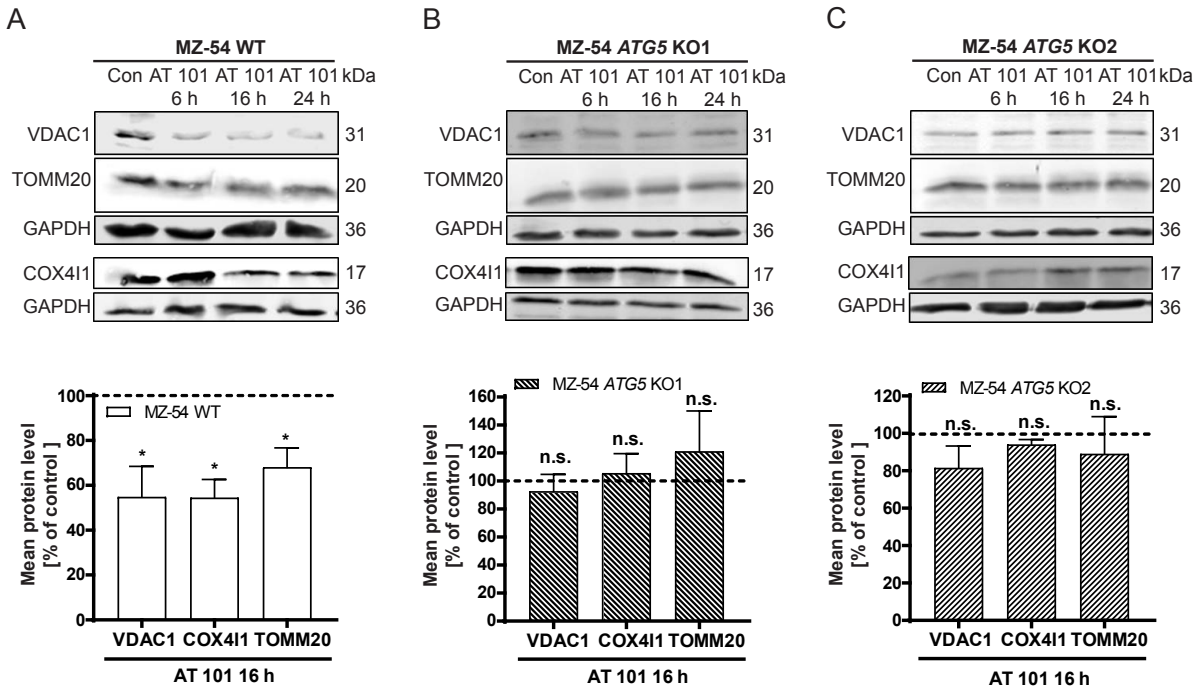

Figure 5.10. *ATG5* KO prevents AT 101-induced decrease of mitochondrial protein abundance.
(A-C) Immunoblot analysis of the mitochondrial proteins VDAC1, TOMM20 and COX4I1 and GAPDH as housekeeping protein control. Quantification of the mean protein level was performed with 3 - 4 biological replicates. MZ-54 WT (A) and *ATG5* KO cells (B, C) were treated with 15 µM AT 101 for 6, 16 and 24 h or with DMSO (Con) for 24 h. Data are means + SEM, statistical significances were calculated with a one-way ANOVA ($P \leq 0.05$: *, $P \leq 0.01$: **, $P \leq 0.001$: ***, n.s.: not significant; difference from control). Figure adapted from Meyer et al., 2018.

Collectively, the data provide evidence that AT 101-treated cells display features of mitophagy and show a pronounced decrease of mitochondrial protein abundance, an effect that is abrogated by *ATG5* deletion.

5.3 AT 101 triggers mitophagy induction that can be reduced by pharmacological and genetic autophagy inhibition

To confirm the previous findings pointing to AT 101-induced mitophagy, three different assays were performed to quantify mitophagy following AT 101 exposure under control conditions compared to genetic/pharmacologic inhibition of autophagy: flow cytometric measurements of 1) cells stained with MitoTracker Green FM (MTG) or 2) with stable expression of mito-mKeima and 3) measurement of mitochondrial versus nuclear DNA levels by qRT-PCR.

Assessment of the MTG intensities enables the detection of changes in the mitochondrial mass of cells. However, it should be considered that the uptake of MitoTracker dyes into mitochondria is dependent on the mitochondrial membrane potential to some extent (Xiao et al., 2016). To exclude major confounding effects of this technical limitation for mitophagy measurements in this study, the early effects of FCCP and AT 101 on mitochondrial depolarization (TMRM measurements) and MTG intensities were compared first (Figure 5.11). For measurement of MTG, the cells were gated either MTG positive or negative according to the control, and MTG-negative cells were defined as cells with a decreased mitochondrial mass. While treatment with FCCP led to an extensive decrease of TMRM-positive cells to 5% already after 2 hours (Figure 5.11A), no significant changes of MTG intensity could be observed (Figure 5.11B). The missing induction of mitophagy upon FCCP treatment might be explained by the low or absent Parkin (parkin RBR E3 ubiquitin protein ligase) protein levels in gliomas (Yeo et al., 2012; Lin et al., 2015). AT 101 treatment led to a slight mitochondrial depolarization after 2 hours, which further decreased to less than 20% TMRM-positive cells within 6 hours (Figure 5.11C). In contrast to TMRM, the MTG-negative cell population only increased up to 30% within 6 hours treatment (Figure 5.11D), clearly showing that MTG intensities are largely independent of the mitochondrial membrane potentials in this experimental approach. Accordingly, assessment of MTG intensities was suggested to be a suitable technique to analyze mitophagy.

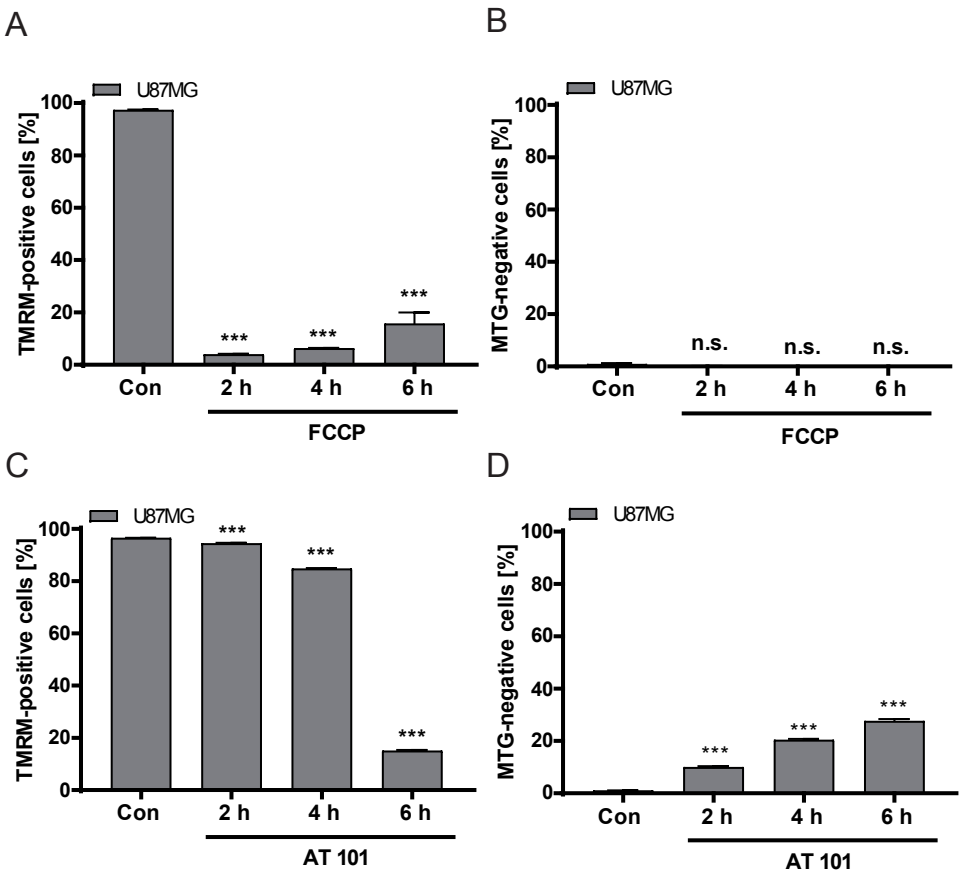

Figure 5.11. Early effects of AT 101 and FCCP on mitochondrial depolarization and mitochondrial mass.
(A, C) Flow cytometric analysis of TMRM positive cells, which is equivalent to the number of cells with intact mitochondrial membrane potential. U87MG cells were exposed to 20 µM FCCP (A) or 15 µM AT 101 (C) for 2, 4 and 6 h or to DMSO (Con) for 48 h and subjected to flow cytometry. The gate was set to 95% - 100% TMRM positive cells in DMSO treated controls. (B, D) Determination of MTG-negative cells by flow cytometry. U87MG cells were treated with 20 µM FCCP (B) or 15 µM AT 101 (D). The gate was set to 0% - 5% MTG negative cells in DMSO treated controls. Data represent means + SEM of one experiment with three replicates and 10,000 cells measured in each sample. Statistical significances were calculated with a one-way ANOVA ($P \leq 0.05$: *, $P \leq 0.01$: **, $P \leq 0.001$: ***, n.s.: not significant; difference from control). Figure adapted from Meyer et al., 2018.

In subsequent experiments, the MTG intensities in U87MG cells treated with AT 101 alone or in combination with the autophagy inhibitors wortmannin, bafilomycin A_1 and chloroquine were quantified. The general phosphatidylinositol 3-kinase (PI3K) inhibitor wortmannin blocks autophagy at an early stage by inhibiting the class II and III PI3K (Blommaart et al., 1997; Devereaux et al., 2013). In contrast, bafilomycin A_1 and chloroquine are both late stage inhibitors of autophagy. While bafilomycin A_1 blocks lysosomal acidification by inhibition of the vacuolar type H^+-ATPase (V-ATPase), but it can also impair fusion between autophagosomes and lysosomes, chloroquine mainly inhibits autophagy by blocking the delivery of sequestered cargo to the lysosomes (Mauthe et al., 2018). AT 101 treatment of U78MG cells for 24 hours resulted in an increase of the MTG-negative cell population up to 50%, which could be significantly diminished by addition of all three autophagy inhibitors

(Figure 5.12A). Figure 5.12B displays a representative flow cytometric analysis of the MTG intensity of U87MG cells and the gate settings. Moreover, the MTG intensities of MZ-54 WT and *ATG5* KO cells upon AT 101 treatment for 24 hours were compared (Figure 5.12C, D). Notably, *ATG5* KO partially rescued the decrease of MTG intensity, and combined treatment with AT 101 and bafilomycin A_1 diminished the MTG-negative cell population to a similar extent as the *ATG5* knockout.

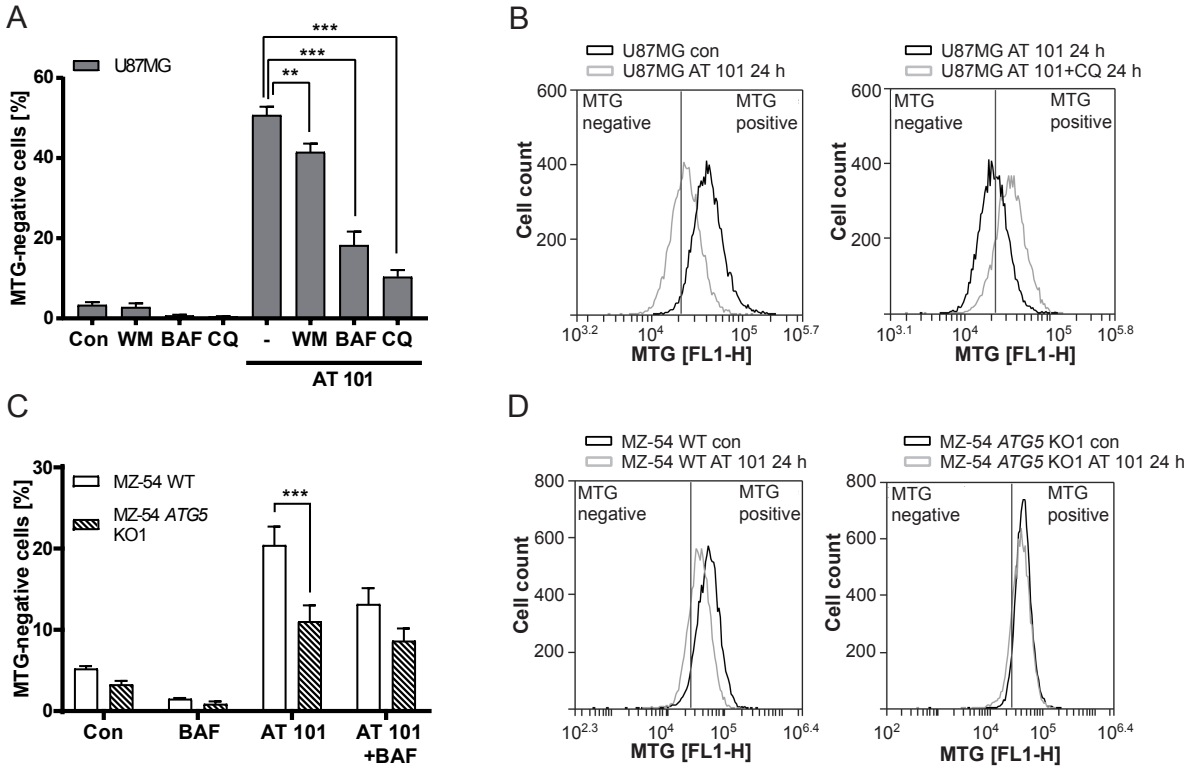

Figure 5.12. AT 101-induced mitophagy is decreased by autophagy inhibition.
(A-D) Assessment of MTG-negative cells by flow cytometry. The gate was set to 0% - 5% MTG-negative cells in the control (Con). (A) U87MG cells were exposed to 15 µM AT 101 or DMSO (Con) alone or in combination with 100 nM wortmannin (WM), 10 nM bafilomycin A_1 (BAF) and 20 µM chloroquine (CQ) for 24 h. WM was added to the cells 24 h prior to AT 101 treatment. (C) MZ-54 WT and *ATG5* KO cells were treated with 15 µM AT 101 in the presence or absence of 10 nM bafilomycin A_1 (BAF) for 24 h. (B, D) Representative experiment of U87MG (B) and MZ-54 cells (D). Experiments were repeated three times. Data are means + SEM from n = 9 - 12 samples (5,000 - 10,000 cells measured in each sample, 3 - 4 samples per experiment). Statistical significances were calculated with a two-way ANOVA ($P \leq 0.05$: *, $P \leq 0.01$: **, $P \leq 0.001$: ***, n.s.: not significant). Figure adapted from Meyer et al., 2018.

In a parallel approach to determine mitophagy, flow cytometry-based measurements of mito-mKeima were performed by Jonas Michaelis (Institute of Biochemistry II, working group of Dr. Christian Münch, Goethe University Hospital Frankfurt/Main, Germany). To this end, MZ-54 and U87MG cells were stably transfected with the mito-mKeima construct, which encodes for mKeima tagged with a mitochondrial targeting peptide sequence. Mito-mKeima changes its excitation wavelength in a pH-dependent manner from 488 nm (pH 7) to 561 nm (pH 4), thus, it allows monitoring of the delivery of mitochondria to lysosomes (Katayama et al.,

2011). Figure 5.13A displays the 561:488 excitation ratio of U87MG cells after treatment with vehicle and AT 101 alone or in combination with bafilomycin A_1. Remarkably, the cell population shifted towards 561 nm excitation upon administration of AT 101 for 6 hours, which corresponds to an increased number of mitochondria enclosed by lysosomes (Figure 5.13A, B). Blockage of lysosomal acidification with bafilomycin A_1 completely inhibited 561:488 ratio changes. Moreover, addition of bafilomycin A_1 in vehicle-treated cells also resulted in a shift towards 488 nm excitation, indicative of ongoing basal mitophagy. In addition, mito-mKeima experiments were carried out in a second glioma cell line to confirm the results. Treatment of MZ-54 cells with AT 101 for 6 hours resulted in more than 50% increase in 561:488 ratio and addition of bafilomycin A_1 significantly diminished this effect (Figure 5.13C). On the contrary, FCCP only led to a slight 561:488 ratio increase, which is in accordance with the low Parkin levels of glioma cells (Yeo et al., 2012; Lin et al., 2015) (Figure 5.13D). Collectively, these measurements clearly point to an early and strong induction of mitophagy by AT 101 in glioma cells.

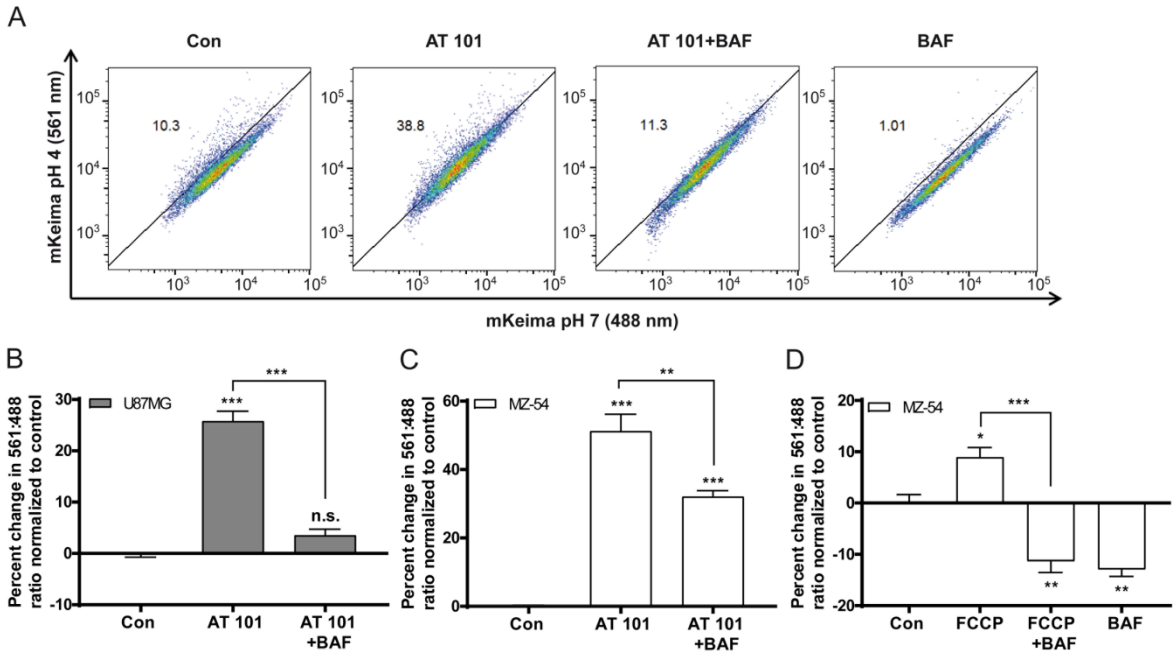

Figure 5.13. AT 101 induces uptake of mitochondria into lysosomes.
(A-D) Determination of mitophagy by flow cytometric analysis of mito-mKeima expressing cells. U87MG and MZ-54 cells stably expressing mito-mKeima were treated with DMSO (Con), 15 µM AT 101 (A-C) or 20 µM FCCP (D) in the presence or absence of 100 nM bafilomycin A_1 (BAF) for 6 h. (A) Representative experiment of U87MG cells. (B-D) Percent changes in the 561:488 mean value ratio of U87MG cells (B) and MZ-54 cells (C, D) were normalized to vehicle-treated cells. The 561:488 ratio corresponds to the pH where mKeima is located. Experiments were repeated three times. Data represent means + SEM of three replicates with 10,000 cells measured in each sample. Statistical significances were calculated with a one-way ANOVA ($P \leq 0.05$: *, $P \leq 0.01$: **, $P \leq 0.001$: ***, n.s.: not significant; difference from control or as indicated). Figure adapted from Meyer et al., 2018. The mito-mKeima measurements were performed by Jonas Michaelis (Institute of Biochemistry II, working group of Dr. Christian Münch, Goethe University Hospital Frankfurt/Main, Germany).

In a third approach to investigate mitophagy, the mitochondrial mass was determined by measuring ratio changes between mitochondrial and nuclear DNA levels. The experiment was performed by Svenja Zielke (Experimental Cancer Research in Pediatrics, working group of Prof. Dr. Simone Fulda, Goethe University Hospital Frankfurt/Main, Germany). Thereto, DNA of the mitochondrial gene *MT-ND1* (mitochondrially encoded NADH:ubiquinone oxidoreductase core subunit 1) and the nuclear gene *LPL* (lipoprotein lipase) was quantified by qRT-PCR. Strikingly, AT 101 treatment led to a significant 20% - 40% decrease of mitochondrial mass in all three investigated glioma cell lines and genetic inhibition of autophagy by *ATG5* KO diminished this effect (Figure 5.14A: MZ-54, Figure 5.14B: U87MG, Figure 5.14C: U343).

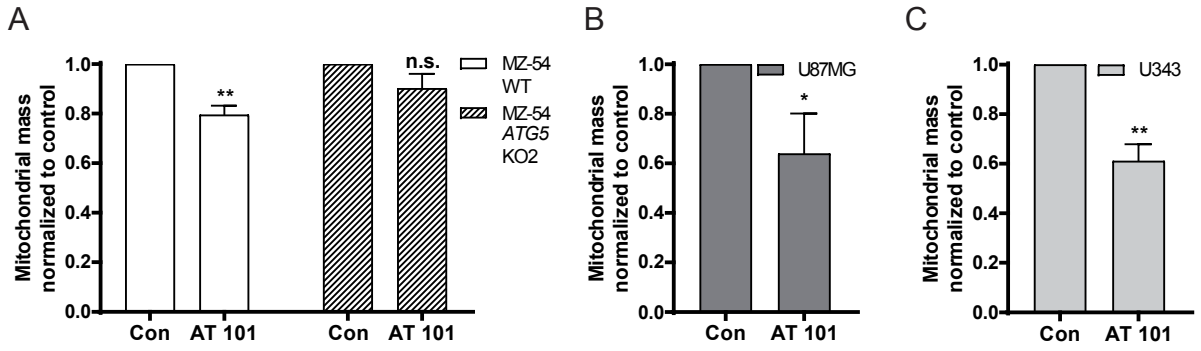

Figure 5.14. AT 101-induced reduction of mitochondrial mass is blocked by *ATG5* KO.
(A-C) Monitoring mitochondrial mass by qRT-PCR. The glioma cell lines MZ-54 WT and MZ-54 *ATG5* KO (A), U87 (B) and U343 (C) were exposed to 15 µM AT 101 for 30 h. The mitochondrial mass was determined as the ratio between the DNA levels of the mitochondrial gene *MT-ND1* and the nuclear gene *LPL* normalized to DMSO-treated cells. Experiments were repeated 3 - 4 times. Data are means + SEM from n = 9 - 12 samples (three technical replicates per experiment). Statistical significances were calculated with a student's t-test ($P \leq 0.05$: *, $P \leq 0.01$: **, $P \leq 0.001$: ***, n.s.: not significant; difference from control. Figure adapted from Meyer et al., 2018. Assessment of mitophagy by qRT-PCR was performed by Svenja Zielke, working group of Prof. Dr. Simone Fulda, Experimental Cancer Research in Pediatrics, Goethe University Hospital Frankfurt/Main, Germany.

In conclusion, the data of two independent experimental approaches, namely flow cytometric measurement of MTG and assessment of ratio changes between mitochondrial and nuclear DNA levels by qRT-PCR, clearly demonstrated the decrease of mitochondrial mass following AT 101 treatment. Furthermore, mito-mKeima experiments revealed the engulfment of mitochondria into lysosomes upon 6 hours AT 101 exposure. Strikingly, the decrease of mitochondrial mass as well as mitochondrial enclosure into lysosomes could be significantly rescued by either genetic or pharmacologic blockage of autophagy in three different glioma cell lines, being a clear sign for ongoing mitophagy.

5.4 AT 101 induces an autophagic cell death in glioma cells

In a previous publication from our lab it was shown that knockdown of *ATG5*, *ATG7* and *BECN1* significantly rescued AT 101-induced cell death in glioma cells, indicative of autophagic cell death (ACD) (Voss et al., 2010). To verify these results in the established CRISPR/Cas9 *ATG5* KO models, cell death upon treatment with AT 101 and the apoptosis inducer staurosporine was measured in U343 and MZ-54 WT cells compared to the respective *ATG5* KOs (Figure 5.15). AT 101 exposure led to cell death in ~ 30% of cells after 48 hours and in ~ 80% of cells after 72 hours in U343 cells (Figure 5.15A). In line with the study of Voss et al., *ATG5* KO significantly diminished cell death induced by AT 101 in U343 cells (Voss et al., 2010). On the contrary, *ATG5* KO failed to reduce staurosporine-induced apoptotic cell death (Figure 5.15B). MZ-54 WT cells reacted with cell death at an extent of ~ 50% following treatment with AT 101 for 48 hours or staurosporine for 6 hours, and knockout of *ATG5* partially rescued AT 101-induced, but not staurosporine-induced cellular demise (Figure 5.15C, D).

Moreover, the cytotoxic effects of AT 101 and staurosporine exposure in MEF WT and apoptosis-resistant MEF *Bax Bak1* DKO cells were determined (Figure 5.15E). Staurosporine led to cell death in nearly 100% of MEF WT cell cultures, which was strongly rescued by *Bax Bak1* DKO, confirming that staurosporine-induced lethality is dependent on the apoptosis machinery. Unexpectedly, AT 101 induced even more cell death in MEF *Bax Bak1* DKO cells compared to MEF WT cells after 24 hours, whereas no differences between both cell lines were observed after 48 hours. Similar observations were reported by Moretti et al., showing that inhibition of apoptosis by *Bax Bak1* DKO resulted in increased radiosensitivity (Moretti et al., 2007).

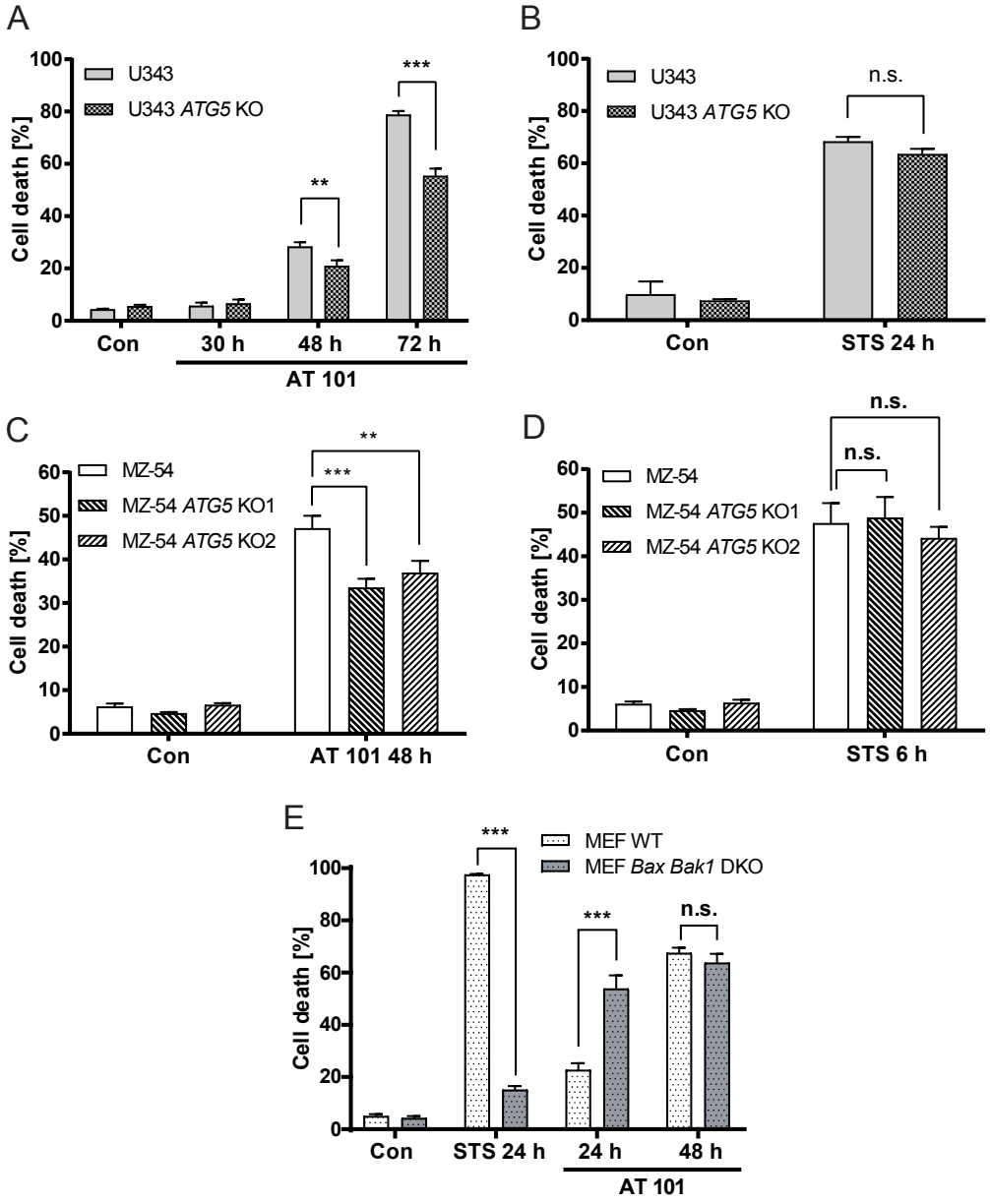

Figure 5.15. Effect of *ATG5* KO on AT 101- and STS-induced cell death.
(A, B) Monitoring of cell death by flow cytometric analysis of APC-annexin V binding and PI uptake. U343 WT and *ATG5* KO cells were exposed to either 15 µM AT 101 for 30, 48 and 72 h (A) or 3 µM staurosporine (STS) for 24 h (B). (C, D) MZ-54 WT and *ATG5* KO cells were exposed to 15 µM AT 101 for 48 h (C) or 3 µM STS for 6 h (D). (E) MEF WT and MEF *Bax Bak1* DKO cells were treated with 3 µM STS for 24 h or 15 µM AT 101 for 24 and 48 h. DMSO was used as control (Con). Experiments were repeated three times. Data are means + SEM from n = 9 - 12 samples (10,000 cells measured in each sample, 3 - 4 samples per experiment). A two-way ANOVA was performed to determine statistical significance ($P \leq 0.05$: *, $P \leq 0.01$: **, $P \leq 0.001$: ***, n.s.: not significant). Figure adapted from Meyer et al., 2018.

To exclude that AT 101 induces a necroptotic type of cell death in glioma cells, the effect of the RIPK1 inhibitor necrostatin-1s on AT 101-induced cytotoxicity was assessed (Figure 5.16A, B). However, necrostatin-1s failed to increase cell survival in MZ-54 and U87MG glioma cells following AT 101 treatment, indicating that AT 101-induced cellular demise is independent of necroptosis.

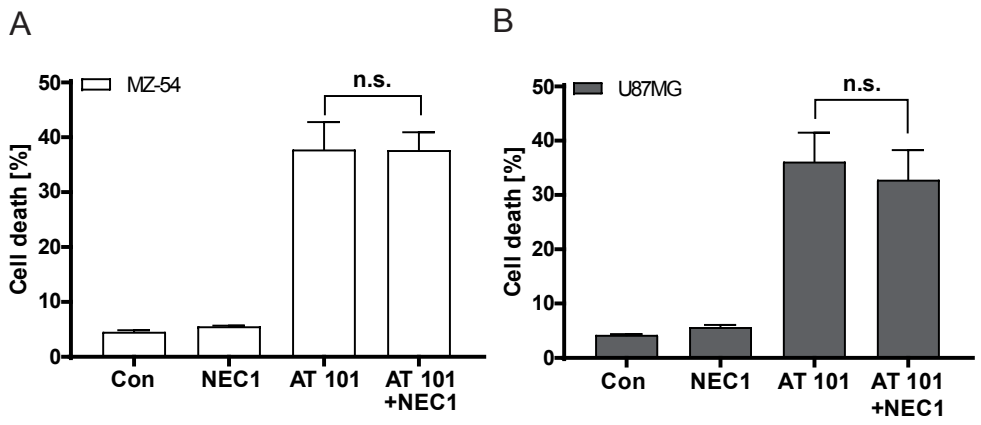

Figure 5.16. AT 101 does not induce necroptotic cell death.
(A, B) Flow cytometric analysis of APC-annexin V binding and PI uptake for quantification of cell death. MZ-54 cells (A) and U87MG cells (B) were treated with 15 µM AT 101 or DMSO (Con) in the absence or presence of 20 µM necrostatin-1 (NEC1). Experiments were repeated three times. Data are means + SEM from n = 9 samples (10,000 cells measured in each sample, 3 samples per experiment). A Kruskal-Wallis test was performed to determine statistical significance ($P \leq 0.05$: *, $P \leq 0.01$: **, $P \leq 0.001$: ***, n.s.: not significant).

5.5 AT 101 induces lethal mitophagy that is dependent on the selective mitophagy receptors BNIP3 and BNIP3L

Hitherto, this study revealed the robust induction of mitophagy as well as autophagic cell death (ACD) by AT 101. In the following section, several experiments were performed to unravel the molecular mechanisms of mitophagy induction and the impact of mitophagy on cellular demise. First, the mitophagy receptors that might be involved in AT 101-driven mitophagy were determined. Thereto, the RNA expression levels of the mitophagy receptors BNIP3 (BCL2 interacting protein 3), BNIP3L (BCL2 interacting protein 3 like) and SQSTM1/p62 (sequestosome 1) were assessed by qRT-PCR (Figure 5.17A-C). Of note, BNIP3 and BNIP3L have been shown to be involved in hypoxia-induced mitophagy (Zhang et al., 2008; Ding and Yin, 2012), whereas SQSTM1 has been described to participate in PINK1-Parkin-dependent mitophagy (Roberts et al., 2016).

Strikingly, AT 101 induced a vast increase of BNIP3 and BNIP3L RNA expression after 16 - 24 hours in MZ-54 (Figure 5.17A), U87MG (Figure 5.17B) and U343 glioma cells (Figure 5.17C). Moreover, SQSTM1 expression was strongly increased in U343 cells and to a lesser extent in MZ-54 cells following 16 - 24 hours AT 101 exposure. In contrast, AT 101 failed to induce significant expression changes of SQSTM1 mRNA in U87MG cells. In addition, BNIP3, BNIP3L and SQSTM1 protein levels upon AT 101 treatment for 6, 16 and 24 hours was analyzed by western blot (Figure 5.17D-F). However, no changes of SQSTM1 levels could be detected at any time point. In contrast, BNIP3L remarkably increased over time in all three cell lines. Moreover, BNIP3 protein levels could not be detected in MZ-54 and U343

cells, but U87MG cells showed a clear increase of BNIP3 upon AT 101 exposure. Due to these findings, the cell line U87MG was chosen for further investigation of mitophagy.

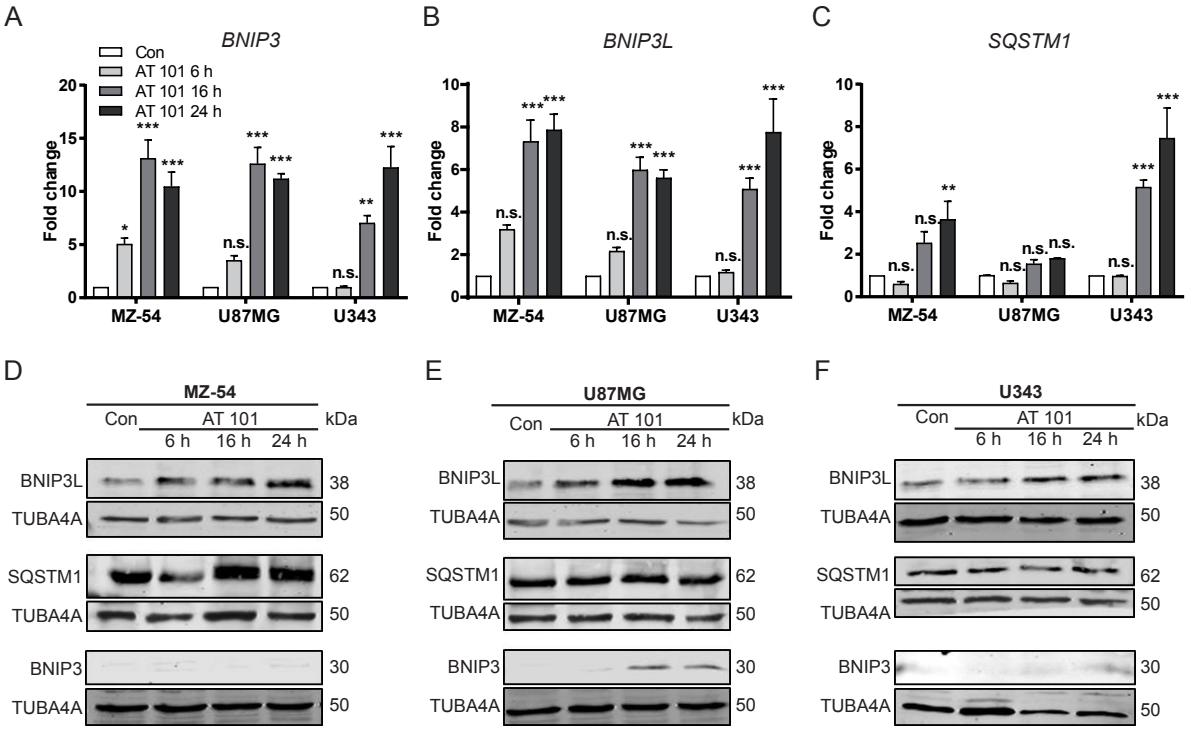

Figure 5.17. Investigation of mitophagy receptors.
(A-C) Assessment of the expression levels of *BNIP3*, *BNIP3L* and *SQSTM1* mRNA normalized to *TBP* by qRT-PCR. MZ-54 (A), U343 (B) and U87MG cells (C) were exposed to 15 µM AT 101 for 6, 16 and 24 h or DMSO for 24 h (Con). Data are means + SEM from three independent experiments with three technical replicates. Statistical significances were calculated with a one-way ANOVA ($P \leq 0.05$: *, $P \leq 0.01$: **, $P \leq 0.001$: ***, n.s.: not significant; difference from control). (D-F) Immunoblot analysis of the protein levels of BNIP3L, SQSTM1 and BNIP3 in MZ-54 (D), U87MG (E) and U343 cells (F) upon treatment with 15 µM AT 101 for 6, 16, and 24 h or DMSO (Con) for 24 h. TUBA4A was used as housekeeping protein control. Experiments were repeated three times with similar results. Figure adapted from Meyer et al., 2018.

Next, the putative role of hyperactivated mitophagy in AT 101-induced lethality was investigated. To this end, the effect of siRNA-mediated knockdown (KD) of *BNIP3* and *BNIP3L* expression on the induction of mitophagy and cell death in AT 101-treated cells was determined. For detection of BNIP3 and BNIP3L knockdown on protein level, cells were exposed to AT 101 for 16 hours to increase the protein levels. Figure 5.18A, B shows that two different siRNAs against *BNIP3* and *BNIP3L* strongly diminished the respective protein levels.

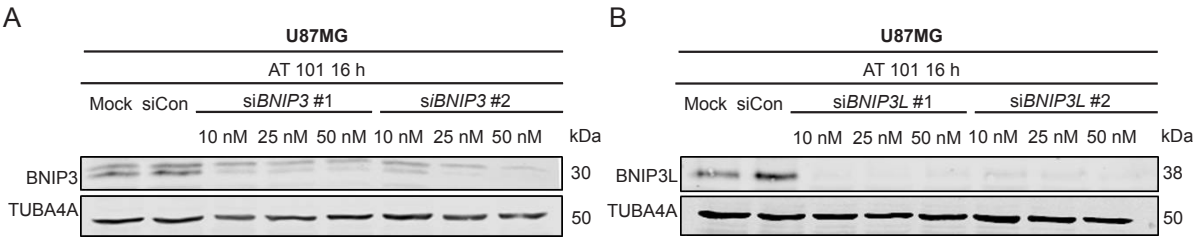

Figure 5.18. SiRNA-mediated knockdown of *BNIP3* and *BNIP3L*.
(A, B) Immunoblot analysis of BNIP3 (A) and BNIP3L (B) levels. TUBA4A (Tubulin) was used as housekeeping protein control. U87MG cells were treated with 15 µM AT 101 for 16 h in the presence of siRNA against *BNIP3* (si*BNIP3* #1 or si*BNIP3* #2; 10 nM, 25 nM, 50 nM) (A) and *BNIP3L* (si*BNIP3L* #1 or si*BNIP3L* #2; 10 nM, 25 nM, 50 nM) (B) or universal negative control (siCon). Experiments were repeated two times. Figure adapted from Meyer et al., 2018.

In the next experiment, AT 101-induced mitophagy of U87MG cells transfected with control siRNA was compared to cells transfected with siRNA against *BNIP3*, *BNIP3L* or a combination of *BNIP3* and *BNIP3L*. Thereto, U87MG cells were treated with AT 101 for 24 hours, stained with MTG, and subjected to flow cytometric analysis. Strikingly, knockdown of *BNIP3* and *BNIP3L* slightly, but significantly diminished the number of MTG-negative cells upon treatment with AT 101, indicative of partial mitophagy inhibition (Figure 5.19A). These effects were further enhanced by combined knockdown of *BNIP3* and *BNIP3L* (Figure 5.19B). Figure 5.19C shows a representative MTG measurement by flow cytometry including the MTG-positive and MTG-negative cell populations.

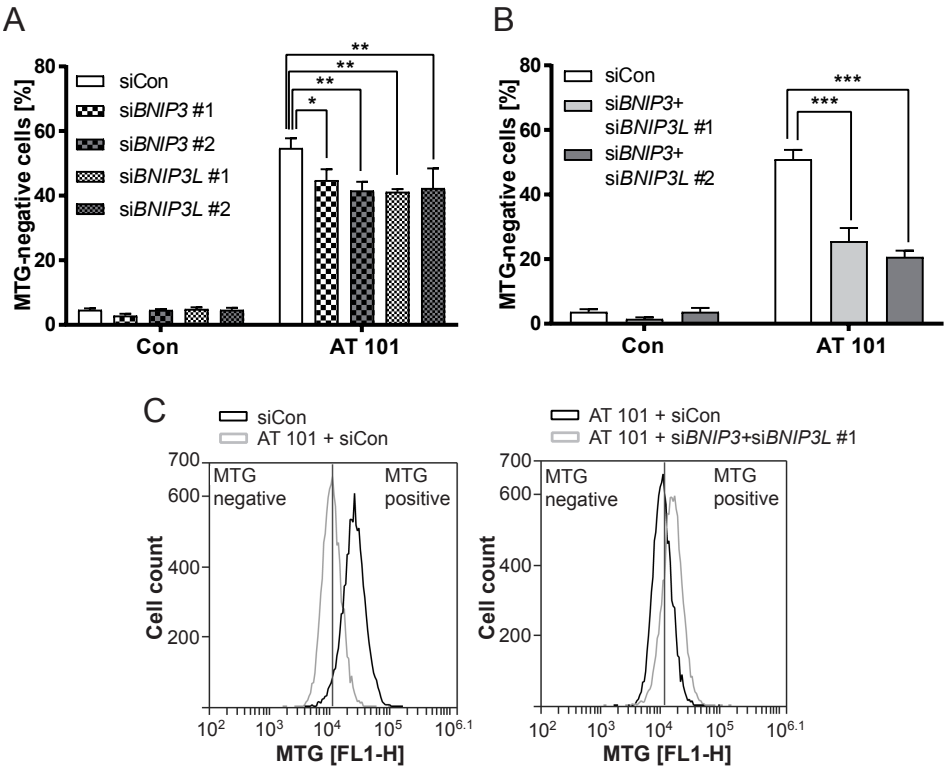

Figure 5.19. Depletion of *BNIP3* and *BNIP3L* reduces AT 101-induced mitophagy.
(A, B, C) Assessment of MTG-negative cells by flow cytometry. U87MG cells were exposed to 15 µM AT 101 or DMSO (Con) for 24 h in the presence of siRNA against *BNIP3* (si*BNIP3* #1 or si*BNIP3* #2; 25 nM) or *BNIP3L* (si*BNIP3L* #1 or si*BNIP3L* #2; 25 nM) (A) or a combination of *BNIP3* and *BNIP3L* siRNAs (si*BNIP3* #1 and si*BNIP3L* #1 or si*BNIP3* #2 and si*BNIP3L* #2; 25 nM each) (B) compared to universal negative control (siCon). (C) Representative MTG measurement. Measurements were repeated at least three times. Data are means + SEM from n = 9 - 12 samples (5,000 - 10,000 cells measured in each sample, 3 - 4 samples per experiment). Statistical significances were calculated with a two-way ANOVA ($P \leq 0.05$: *, $P \leq 0.01$: **, $P \leq 0.001$: ***, n.s.: not significant). Figure adapted from Meyer et al., 2018.

Furthermore, the impact of *BNIP3* and *BNIP3L* KD on AT 101-induced cellular demise was investigated. Intriguingly, administration of AT 101 for 48 hours induced 40% cell death in U87MG WT cells, and knockdown of *BNIP3L* with both siRNAs reduced cell death to 20%. In addition, knockdown of *BNIP3* with one siRNA also slightly diminished cell death, however, the other *BNIP3* siRNA already led to an increase of cell death in vehicle-treated cells, pointing to off-target effects (Figure 5.20A). Combined knockdown of *BNIP3* and *BNIP3L* did not intensify the rescue effects compared to *BNIP3L* KD alone, indicating a more important role of BNIP3L than of BNIP3 for the induction of cell death in this line (Figure 5.20B).

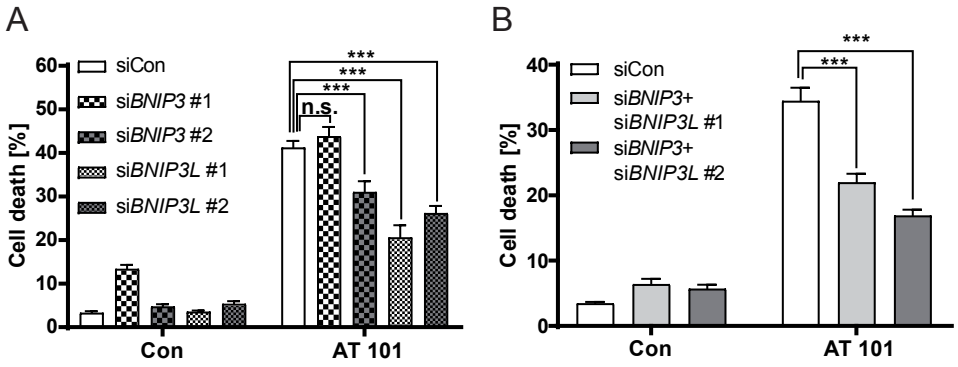

Figure 5.20. Knockdown of *BNIP3* and *BNIP3L* diminishes cell death induced by AT 101.
(A, B) Monitoring cell death by flow cytometric measurement of APC-annexin V binding and PI uptake. U87MG cells were treated with 15 µM AT 101 or DMSO (Con) for 48 h and siRNA against *BNIP3* (si*BNIP3* #1 or si*BNIP3* #2; 25 nM) or *BNIP3L* (si*BNIP3L* #1 or si*BNIP3L* #2; 25 nM) (A) or a combination of *BNIP3* and *BNIP3L* siRNAs (si*BNIP3* #1 and si*BNIP3L* #1 or si*BNIP3* #2 and si*BNIP3L* #2; 25 nM each) (B). At least three independent experiments were performed. Data represent means + SEM from n = 9 - 12 samples (5,000 - 10,000 cells measured in each sample, 3 - 4 samples per experiment). Statistical significances were calculated using a two-way ANOVA ($P \leq 0.05$: *, $P \leq 0.01$: **, $P \leq 0.001$: ***, n.s.: not significant). Figure adapted from Meyer et al., 2018.

Collectively, these data highlight the involvement and functional redundancy of the selective mitophagy receptors BNIP3 and BNIP3L in AT 101-induced mitophagy in U87MG glioma cells. Moreover, it was observed that U87MG glioma cells undergo a lethal form of mitophagy following AT 101 exposure that can be diminished by *BNIP3* and *BNIP3L* KD. However, depletion of *BNIP3* and *BNIP3L* only led to a partial cell death rescue, thus it is supposed that other cell death modalities might be involved in AT 101-induced cell demise.

5.6 HMOX1 is involved in AT 101-induced mitophagy and cell death

Besides the strong and robust downregulation of mitochondrial proteins, the proteome analysis of AT 101-treated glioma cells (Figure 5.5) also revealed a significant upregulation of some proteins, including BAG3 (BCL2 associated athanogene 3), HSPA1A (heat shock protein family A [Hsp70] member 1A; also called HSP70) , APP (amyloid beta precursor protein), CLU (clusterin) and HMOX1 (heme oxygenase 1). Interestingly, the inducible

enzyme HMOX1 was the second strongest upregulated protein in U87MG cells. Its main function is the degradation of pro-oxidant heme into carbon monoxide, biliverdin and iron. Moreover, HMOX1 is induced by several stress stimuli and has been described to modulate anti-oxidant, anti-apoptotic, and anti-inflammatory responses. Intriguingly, HMOX1 has also been described to promote mitochondrial biogenesis and mitophagy (Constantin et al., 2012; Hull et al., 2016; Suliman et al., 2017). Based on these findings, it was hypothesized that elevated levels of HMOX1 following AT 101 treatment might also affect the pool of mitochondria in U87MG glioma cells.

To this end, *HMOX1* was knocked down using two different siRNAs (Figure 5.21A). As expected, addition of AT 101 strongly increased HMOX1 levels in U87MG WT cells after 24 hours and 48 hours, but not in *HMOX1* KD cells (Figure 5.21B, C).

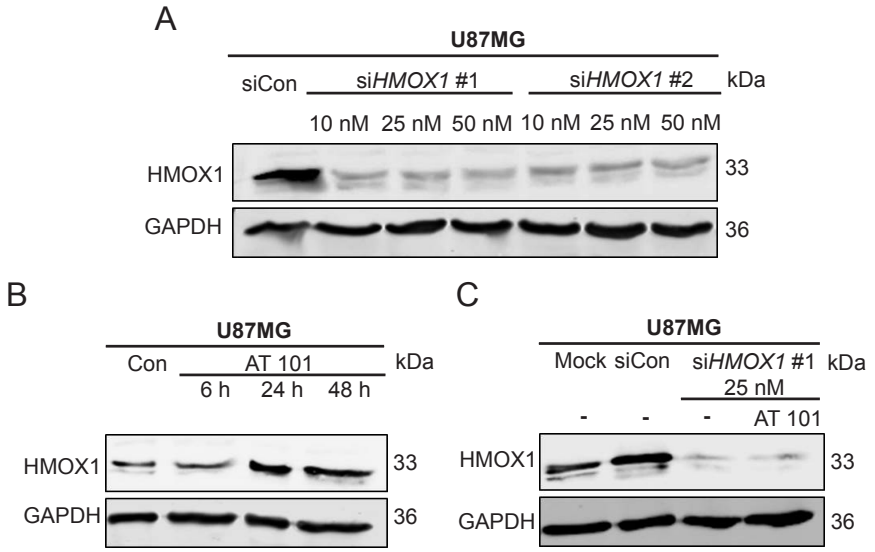

Figure 5.21. Determination of *HMOX1* knockdown and AT 101-induced increase of HMOX1.
(A-C) Immunoblot analysis of HMOX1 and GAPDH as housekeeping protein control. (A) U87MG cells were treated with two different siRNAs against *HMOX1* (si*HMOX1* #1 and si*HMOX1* #2; 10 nM, 25 nM, 50 nM) and siRNA universal negative control (siCon) for 48 h. (B) U87MG cells were treated with 15 µM AT 101 for 6, 24 and 48 h or DMSO (Con) for 48 h. (C) U87MG cells were exposed to 15 µM AT 101 and/or siRNA against *HMOX1* (si*HMOX1* #1; 25 nM), mock transfection or siRNA universal negative control (siCon). Experiments were repeated three times with similar outcome. Figure adapted from Meyer et al., 2018.

Next, MTG measurements were performed to investigate the impact of HMOX1 levels on mitophagy. Notably, AT 101 treatment for 24 hours led to approximately 50% increase of MTG negative cells, and knockdown of *HMOX1* with both siRNAs significantly reduced the number of MTG-negative cells to 25% - 30% (Figure 5.22A). Hence, it was suggested that *HMOX1* expression also affects cell death upon AT 101 treatment. To this end, U87MG cells were exposed to AT 101 for 48 hours and subjected to cell death analysis. Strikingly, *HMOX1* knockdown significantly alleviated cell death induced by AT 101 (Figure 5.22B).

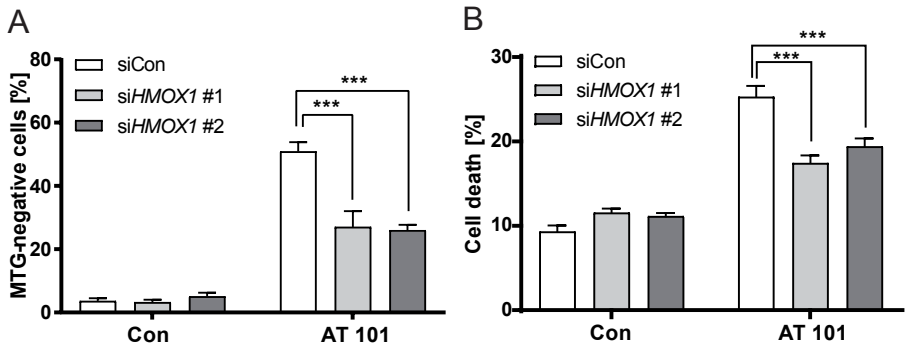

Figure 5.22. HMOX1 depletion rescues AT 101-induced mitophagy and cell death.
(A) Assessment of MTG-negative cells by flow cytometry. U87MG cells were treated with 15 µM AT 101 or DMSO (Con) for 24 h in the presence of two different siRNAs against *HMOX1* (si*HMOX1* #1 and si*HMOX1* #2; 10 nM) or siRNA universal negative control (siCon). (B) Monitoring of cell death by flow cytometric analysis of annexin-V-FLUOS binding and PI uptake. U87MG cells were exposed to 15 µM AT 101 for 24 h in the presence of two different siRNAs against *HMOX1* (si*HMOX1* #1 and si*HMOX1* #2; 10 nM) or siRNA universal negative control (siCon). Measurements were repeated at least three times. Data are mean + SEM from n = 9 - 12 samples (10,000 cells measured in each sample, 3 - 4 samples per experiment). Statistical significances were calculated with a two-way ANOVA ($P \leq 0.05$: *, $P \leq 0.01$: **, $P \leq 0.001$: ***, n.s.: not significant). Figure adapted from Meyer et al., 2018.

Notably, HMOX1 has also been implicated in a ferroptotic type of cell death recently (Kwon et al., 2015). To rule out that ferroptosis accounts for the cell death effects of elevated HMOX1 levels after AT 101 exposure, different glioma cells were treated with AT 101 alone or in combination with the ferroptosis inhibitor ferrostatin-1. In addition, the well-known ferroptosis inducer RSL3 was used as positive control. The experiment was performed by Svenja Zielke (Experimental Cancer Research in Pediatrics, working group of Prof. Dr. Simone Fulda Goethe University Hospital Frankfurt/Main, Germany). Figure 5.23A-C shows that addition of ferrostatin-1 failed to rescue MZ-54, U343 and U87MG cells from AT 101-induced cell death, whereas inhibition of ferroptosis completely abrogated RSL-induced cellular demise.

Taken together, these data indicate that increased HMOX1 expression plays an essential role in AT 101-induced mitophagy and subsequent mitophagy-dependent cell death. In contrast to a previous study, HMOX1 does not trigger ferroptosis in this experimental setup.

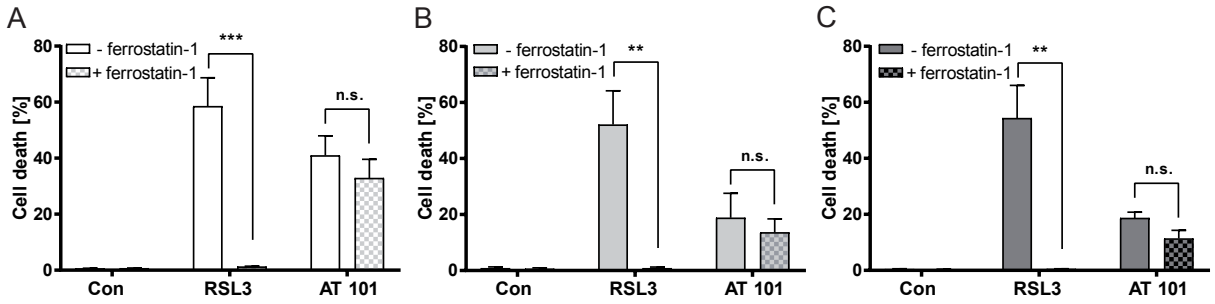

Figure 5.23. Assessment of ferroptosis induced by AT 101.
(A-C) Monitoring of cell death by PI and Hoechst-staining of the nuclei and analysis by fluorescence microscopy. MZ-54 (A), U343 (B) and U87MG cells (C) were exposed to 15 µM AT 101 or 500 nM RSL3 alone or in combination with 5 µM ferrostatin-1 for 48 h (A, B) or 72 h (C). Ferrostatin-1 was applied 1 h prior to the other treatments. Data are means and SEM of 5 - 7 experiments performed in triplicate. Statistical significances were calculated with a two-way ANOVA ($P \leq 0.05$: *, $P \leq 0.01$: **, $P \leq 0.001$: ***, n.s.: not significant). Figure adapted from Meyer et al., 2018. Assessment of ferroptosis by fluorescence microscopy was performed by Svenja Zielke, working group of Prof. Dr. Simone Fulda, Experimental Cancer Research in Pediatrics, Goethe University Hospital Frankfurt/Main, Germany.

5.7 Identification of new autophagic cell death inducers

After detailed investigation of AT 101-mediated autophagic cell death (ACD) in chapters 5.1 - 5.6, the second part of the results is focused on the identification of new ACD inducers and the underlying pathways. The aim was to determine general mechanisms involved in ACD and to decipher under which condition autophagy turns from a generally pro-survival pathway into a death-promoting pathway.

First, *ATG7* CRISPR/Cas9 knockouts were established in MZ-54 cells as a second genetic model for autophagy inhibition. Like *ATG5*, *ATG7* is essential for the conjugation of LC3B to PE and autophagosome formation. PCR amplification of *ATG7* DNA of MZ-54 WT cells and three different knockout cell lines revealed the deletion of approximately 100 to 700 base pairs in the different *ATG7* KOs (Figure 5.24A). Western blot analysis confirmed the knockout of *ATG7* as well as the absence of the LC3B-switch upon bafilomycin A_1 treatment, indicating functional inhibition of autophagy (Figure 5.24B, C). In addition, instead of the usually detected 55 kDa band for ATG5, which represents the ATG5-ATG12 conjugate, *ATG7* KO cells only displayed the 33 kDa band of single ATG5. These observations are in line with previous publications showing that ATG7 is essential for the conjugation of ATG12 to ATG5 (Nakatogawa, 2013; Zielke et al., 2018)

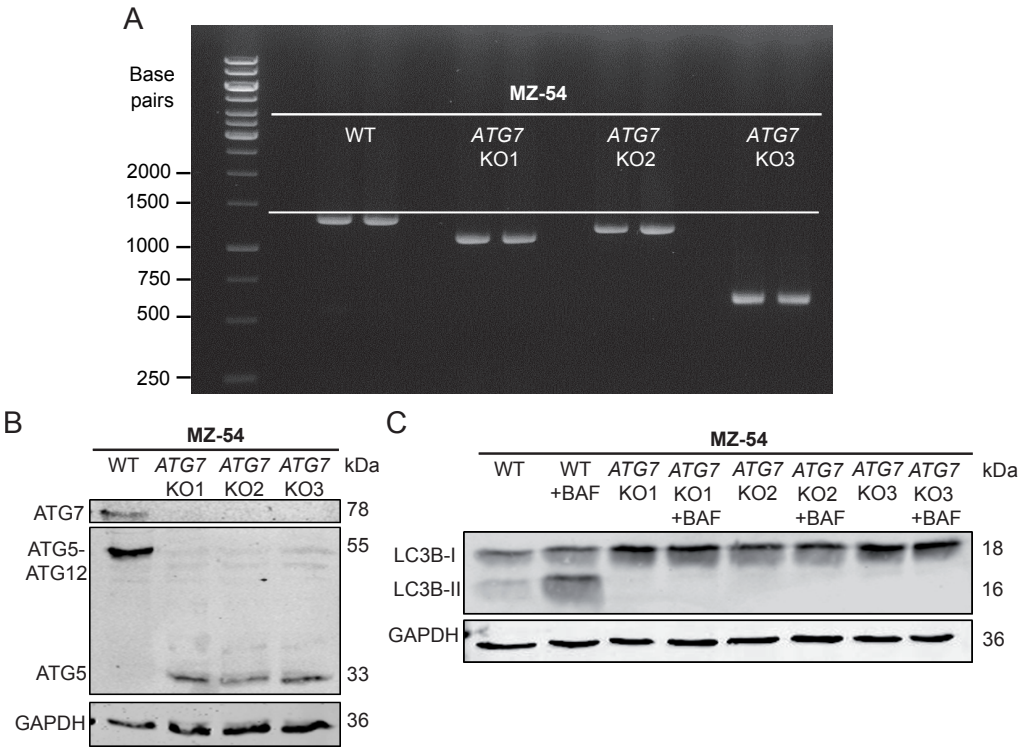

Figure 5.24. Generation of CRISPR/Cas9 *ATG7* KOs.
(A) Separation of PCR amplificates by agarose gel electrophoresis. DNA of the *ATG7* gene containing the CRISPR/Cas9 base pair deletions of MZ-54 cells was amplified by PCR using the primers shown in Table 3.22. (B, C) Immunoblot analysis of ATG5 (ATG5-ATG12 conjugate and single ATG5), ATG7 and LC3B levels in MZ-54 WT cells and the respective *ATG7* KOs. GAPDH was used as housekeeping protein control. Experiments were repeated two times with similar results.

To identify new inducers of ACD, a screen was performed by comparing cell death induction of MZ-54 WT, *ATG5* KO and *ATG7* KO cells upon addition of more than 70 different autophagy inducers of the Enzo Screen-Well™ autophagy library (Zielke et al., 2018). The screen was carried out by Svenja Zielke (Experimental Cancer Research in Pediatrics, working group of Prof. Dr. Simone Fulda, Goethe University Hospital Frankfurt/Main, Germany). To this end, all compounds were titrated to detect a suitable concentration that induces cell death in the range between 40% and 80% after 48 hours. The cells were stained by using Hoechst 33342 to visualize the nuclei of all living and death cells together with the cell-impermeant dye propidium iodide (PI), which only stains the nuclei of dead cells, and cell death was assessed using a high-throughput microscope. Of note, the screen revealed three compounds that significantly induced ACD: STF-62247, loperamide hydrochloride (loperamide) and pimozide. STF-62247 is a small-molecule agonist and has been reported to reduce tumor growth of von Hippel-Lindau (VHL)-deficient renal cell carcinomas in an autophagy-mediated manner (Turcotte et al., 2008). Loperamide is an antidiarrheal drug and opioid receptor agonist that inhibits voltage-gated P/Q-type Ca^{2+} channels (Church et al., 1994; DeHaven-Hudkins et al., 1999). Pimozide is an antipsychotic agent, which antagonizes

D2, D3 and D4 dopamine receptors as well as 5-HT7 serotonin receptor and is used to treat patients with Tourette syndrome (Freedman et al., 1994; Elmaci and Altinoz, 2018).

Several measurements were performed for further validation of ACD and autophagic flux induction by these compounds. Thereto, a combination of the antidepressant imipramine hydrochloride (imipramine) and the anticoagulant ticlopidine hydrochloride (ticlopidine) was used as well-established positive control for ACD in glioma cells (Shchors et al., 2015). Imipramine + ticlopidine have been described to trigger massive autophagy induction and subsequent cell death by elevating cellular cAMP levels and EPAC1/2 signaling.

Immunoblot analysis of MZ-54 cells revealed a strong LC3B-switch from LC3B-I to LC3B-II upon addition of imipramine + ticlopidine, STF-62247, loperamide and pimozide (Figure 5.25A). Notably, combined treatment of all compounds with bafilomycin A_1 further increased the LC3B-switch, indicative of autophagic flux induction, and knockout of either *ATG5* or *ATG7* completely abrogated this LC3B-switch (Figure 5.25A, B).

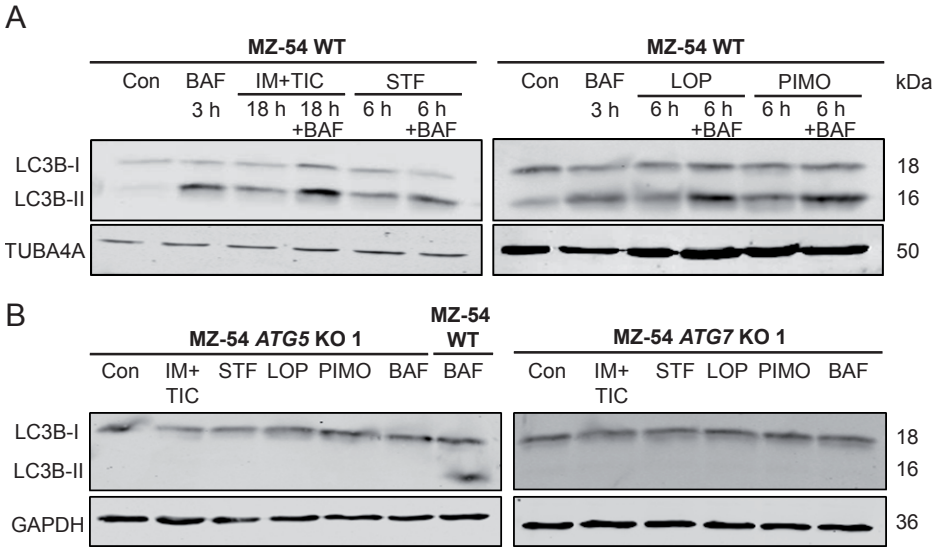

Figure 5.25. Imipramine + ticlopidine, STF-62247, loperamide and pimozide induce autophagic flux.
(A-B) Immunoblot analysis of LC3B-I (18 kDa), LC3B-II (16 kDa) and GAPDH or TUBA4A as housekeeping protein control. (A) MZ-54 WT cells were exposed to 20 µM imipramine (IM) + 100 µM ticlopidine (TIC) for 18 h and to 40 µM STF-62247 (STF), 7.5 µM loperamide (LOP) and 7.5 µM pimozide (PIMO) for 6 h. DMSO (Con) was used as vehicle. Bafilomycin A_1 (BAF) was applied at 10 nM to the cells 3 h before harvest. (B) MZ-54 *ATG5* KO and *ATG7* KO cells were treated for 24 h with the same substances and concentrations as described in A. Experiments were repeated two times with similar outcome.

To confirm the induction of ACD by imipramine + ticlopidine, STF-62247, loperamide and pimozide, MZ-54 WT cells and three different *ATG5* and *ATG7* KO cell lines were treated for 48 hours and subjected to flow cytometric analysis afterwards. Intriguingly, all compounds induced massive cell death of 70% - 90% in MZ-54 WT cells that was significantly decreased by *ATG5* or *ATG7* KO (Figure 5.26A, C, E, G). However, inhibition of autophagy was not able

to fully block cell death, suggesting that other cell death modalities might also be involved. Of imipramine + ticlopidine-treated cells, 10% - 20% were gated APC-annexin V-positive/PI-negative, which might be a sign of marginal ongoing apoptosis (Figure 5.26B). However, the APC-annexin V-positive/PI-negative cell fraction of STF-62247-, loperamide-, and pimozide-treated cells contained only 10% or even less of the whole cell population (Figure 5.26D, F, H). These results are in line with the findings reported by Zielke et al., showing that the broad-range caspase inhibitor zVAD.fmk partially rescues imipramine + ticlopidine-induced cell death, but has no effect on loperamide-, pimozide- or STF-62247-induced cell death (Zielke et al., 2018).

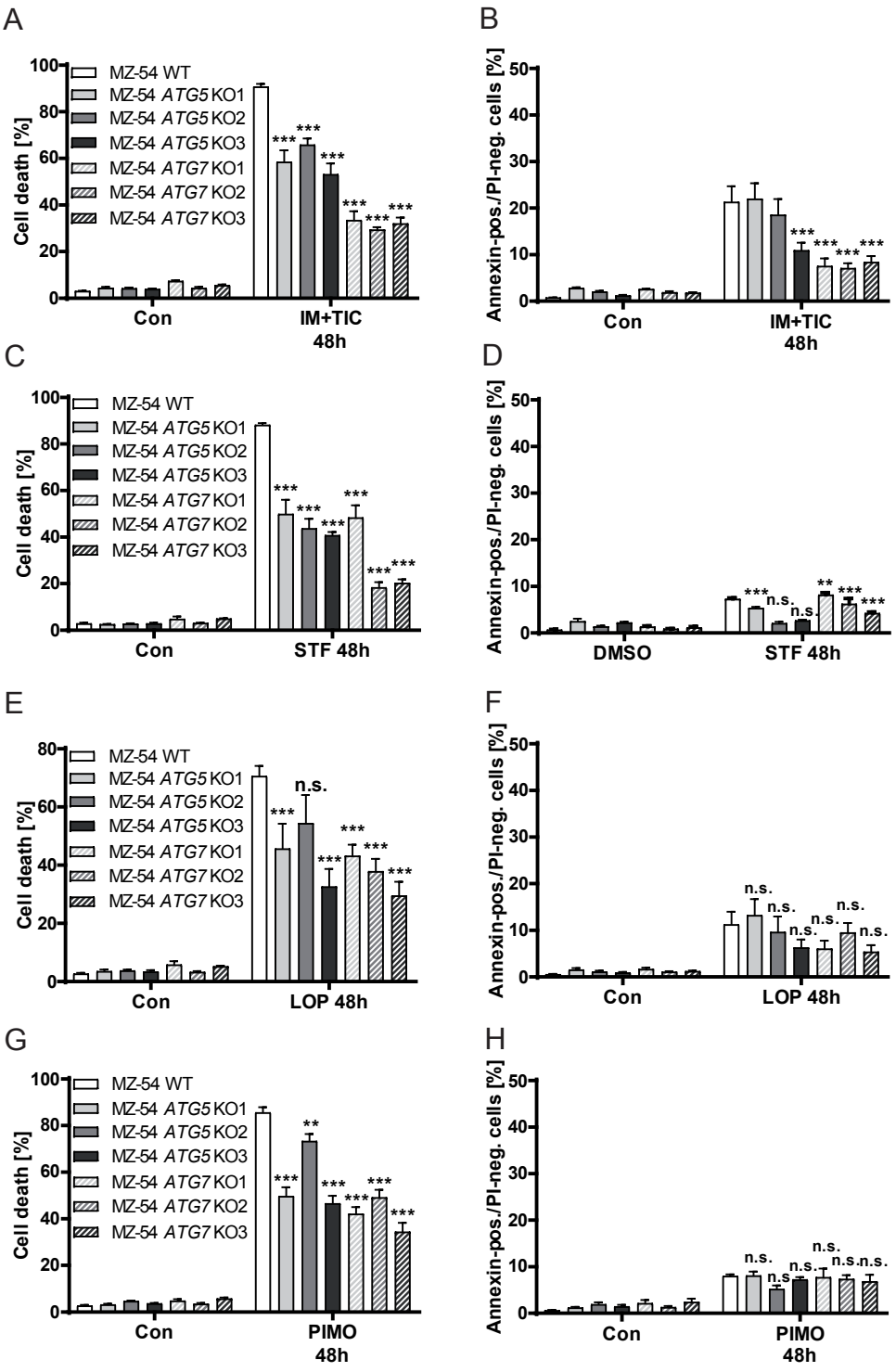

Figure 5.26. Autophagy inhibition rescues imipramine + ticlopidine-, STF-62247-, loperamide- and pimozide-induced cell death.
(A-H) Monitoring cell death by flow cytometric analysis of APC-annexin V binding and PI uptake. A, C, E, and G display overall cell death (only-APC-annexin V-positive, only-PI-positive and double-positive cells) and B, D, F, and H exclusively show APC-annexin V-positive/PI-negative cells. MZ-54 WT cells and three different CRIPR/Cas9 *ATG5* and *ATG7* KOs were exposed to a combination of 20 µM imipramine and 100 µM ticlopidine (IM+TIC) (A, B), 40 µM STF-62247 (STF) (C, D), 12.5 µM loperamide (LOP) (E, F) or 12.5 µM pimozide (PIMO) (G, H) for 48 h. DMSO was used as control (Con, 48 h). Data represent means + SEM of at least three experiments with three replicates and 5,000 - 10,000 cells measured in each sample. Statistical significances were calculated with a two-way ANOVA ($P \leq 0.05$: *, $P \leq 0.01$: **, $P \leq 0.001$: ***, n.s.: not significant; difference from control).

To rule out that autophagy inhibition has an impact on apoptosis, the effect of *ATG5* and *ATG7* KO on staurosporine-mediated cell death was assessed. Staurosporine is a common inducer of apoptosis. Addition of staurosporine for 6 hours induced cell death in ~ 50% of MZ-54 WT cells, and *ATG5* as well as *ATG7* KO cells showed no significant differences compared to WT cells except for one of the *ATG7* KO lines, which was slightly protected against cell death (Figure 5.27A, C). Moreover, staurosporine treatment increased the APC-annexin V-positive/PI-negative-gated cell population to 35% - 40%, being a sign for early apoptosis (Figure 5.27B, D). While knockout of *ATG5* had no effect on APC-annexin V staining, two *ATG7* KO clones showed a small decrease of the APC-annexin V-positive/PI-negative-gated cell population, indicating slight variations between the different clones (Figure 5.27B, D).

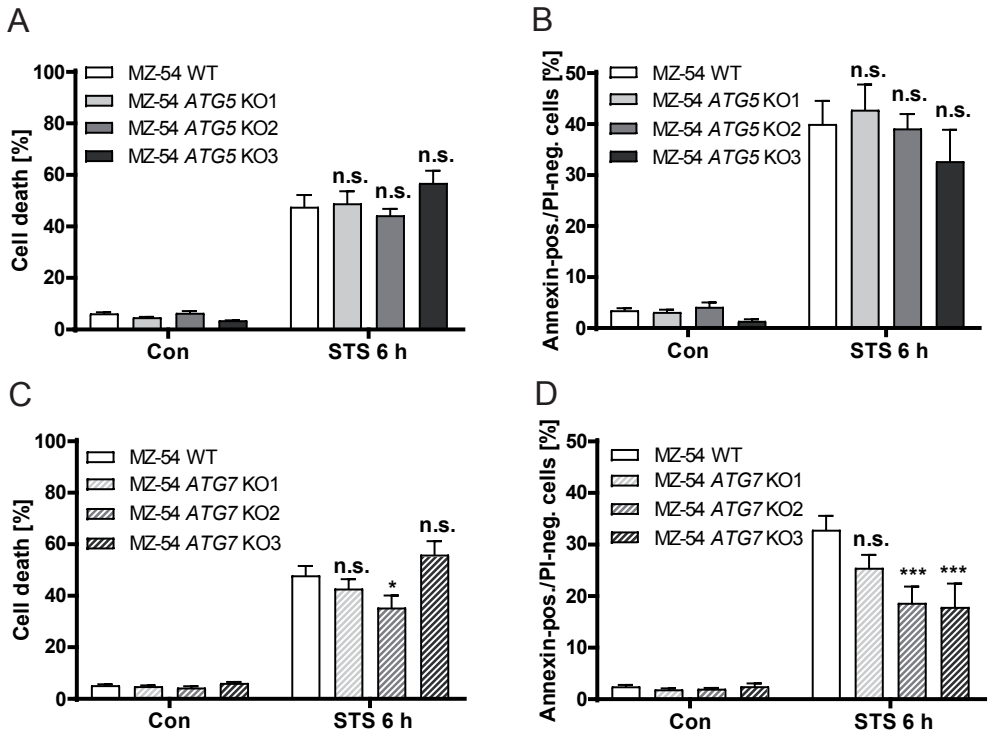

Figure 5.27. Effect of autophagy inhibition on staurosporine-induced cell death.
(A-D) Monitoring cell death by flow cytometric analysis of APC-annexin V binding and PI uptake. A and C show overall cell death (only-APC annexin V-positive, only PI-positive and double-positive cells), B and D display APC annexin V-positive/PI-negative cells. MZ-54 WT cells and three different CRISPR/Cas9 *ATG5* (A, B) and *ATG7* KOs (C, D) were exposed to 3 µM staurosporine (STS) or DMSO (Con) for 6 h. Data represent means + SEM of at least three experiments with three replicates and 5,000 - 10,000 cells measured in each sample. Statistical significances were calculated with a two-way ANOVA ($P \leq 0.05$: *, $P \leq 0.01$: **, $P \leq 0.001$: ***, n.s.: not significant; difference from control).

Taken together, these data highlight that knockout of *ATG5* as well as *ATG7* protects from imipramine + ticlopidine-, STF-62247-, loperamide- and pimozide-induced cell death, but has only marginal effects on staurosporine-induced apoptosis.

To confirm the negligible role of apoptosis following treatment with imipramine + ticlopidine, STF-62247, loperamide and pimozide, effector caspase (DEVDase) activity was assessed in MZ-54 cells as an indicator of apoptosis (Figure 5.28). Caspases usually show the strongest activation a few hours before the cells ultimately undergo cell death. To this end, the above-named compounds were applied for 16 and 24 hours prior to measurement of caspase activity. In addition, the cells were treated with staurosporine for 6 hours. Indeed, staurosporine markedly increased caspase activity, whereas the other compounds completely failed to activate effector caspases. These data strengthen the assumption that apoptosis does not engage in cell death induction/execution by imipramine + ticlopidine, STF-62247, loperamide and pimozide.

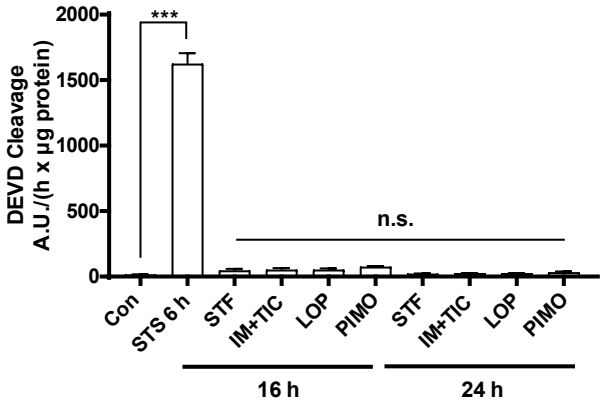

Figure 5.28. Monitoring of effector caspase activity induced by imipramine + ticlopidine, STF-62247, loperamide and pimozide.
MZ-54 cells were exposed to 3 µM staurosporine (STS) for 6 h and 20 µM imipramine + 100 µM ticlopidine (IM+TIC), 40 µM STF-62247 (STF), 15 µM loperamide (LOP) or 15 µM pimozide (PIMO) for 16 h and 24 h. DMSO was used as control (Con, 48 h). Caspase 3-like activity was measured as cleavage of the DEVD substrate (increase of fluorescence intensity in arbitrary fluorescence units per µg protein and hour). Data represent means + SEM of three experiments with four replicates. Statistical significances were calculated with a one-way ANOVA ($P \leq 0.05$: *, $P \leq 0.01$: **, $P \leq 0.001$: ***, n.s.: not significant). Figure adapted from Zielke et al., 2018.

Of note, it has been previously reported that autophagy deficiency is associated with activation of the NFE2L2 (nuclear factor, erythroid 2 like 2; also called NRF2) signaling pathway, which may lead to general cell death resistance (Lau et al., 2010; Lau et al., 2013; Jiang et al., 2015). To rule out that the rescuing effects of *ATG5* and *ATG7* deletions rely on the compensatory activation of general cell death resistance pathways, the expression levels of central stress-responsive survival genes were measured by qRT-PCR (Figure 5.29). Interestingly, autophagy inhibition did not lead to significant changes in the expression of the anti-apoptotic *BCL2* family members *BCL2, BCL2L1* (*BCL-xL)* and *MCL1* (Figure 5.29A) (Dai et al., 2016). In addition, neither *ATG5* KO, nor *ATG7* KO affected the essential members of the *NFE2L2* signaling pathway including *KEAP1* (kelch like ECH associated protein 1), *NFE2L2* and *SQSTM1* (Figure 5.29B) (Lau et al., 2010; Lau et al., 2013; Jiang et al., 2015).

Collectively, these data confirm that cell death resistance of *ATG5* and *ATG7* knockouts following imipramine + ticlopidine, STF-62247, loperamide and pimozide exposure indeed results from autophagy deficiency rather than from deregulation of other signaling pathways.

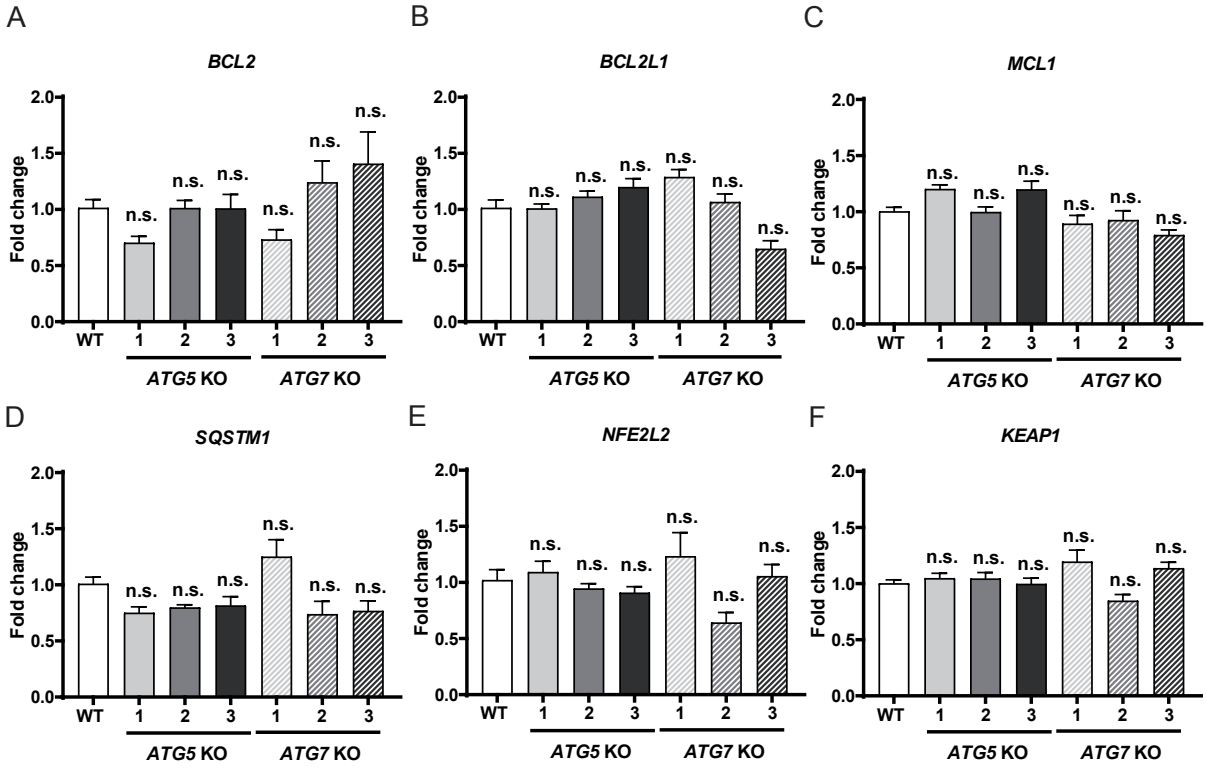

Figure 5.29. Effect of autophagy depletion on stress response genes.
(A-F) Determination of the expression levels of *BCL2* (A)*, BCL2L1 (BCL-xL)* (B)*, MCL1* (C), *SQSTM1* (D), *NFE2L2* (*NRF2*) (E) and *KEAP1* (F) mRNA normalized to *TBP* by qRT-PCR in MZ-54 WT cells (con) and three different *ATG5* and *ATG7* knockouts. Data are means + SEM from six biological replicates. Statistical significances were calculated with a one-way ANOVA ($P \leq 0.05$: *, $P \leq 0.01$: **, $P \leq 0.001$: ***, n.s.: not significant; difference from control).

5.8 Imipramine + ticlopidine, STF-62247, loperamide and pimozide increase the autophagic flux

After detailed investigation of ACD in the preceding chapter, the subsequent experiments focused on induction of the autophagic flux by imipramine + ticlopidine, STF-62247, loperamide and pimozide. First, the autophagic flux was quantified in MZ-54 cells expressing the tandem construct pMRX-IP-GFP-LC3-RFP. In detail, the fluorescent probe is cleaved by endogenous ATG4 proteases into equimolar amounts of EGFP-LC3, which is degraded in the lysosomes, and mRFP1-LC3ΔG, which remains in the cytosol as an internal control (Kaizuka et al., 2016). Measurement of the mean fluorescent intensity ratio of EGFP/mRFP1 by flow cytometry is therefore a well-acquainted method to quantify the autophagic flux (see chapter 4.5.4). MZ-54 WT, *ATG5* and *ATG7* KO cells were exposed to imipramine + ticlopidine, STF-62247, loperamide and pimozide for 16 hours in the presence or absence of

bafilomycin A_1. Strikingly, all four compounds strongly decreased the EGFP/mRFP1 ratio to 40% in MZ-54 WT cells, and addition of bafilomycin A_1 completely abrogated these effects (Figure 5.30A). In line with previous results (Figure 5.25), knockout of *ATG5* and *ATG7* almost entirely prevented this increase of the autophagic flux shown in MZ-54 WT cells following treatment with imipramine + ticlopidine, STF-62247, loperamide and pimozide (Figure 5.30A versus B and C).

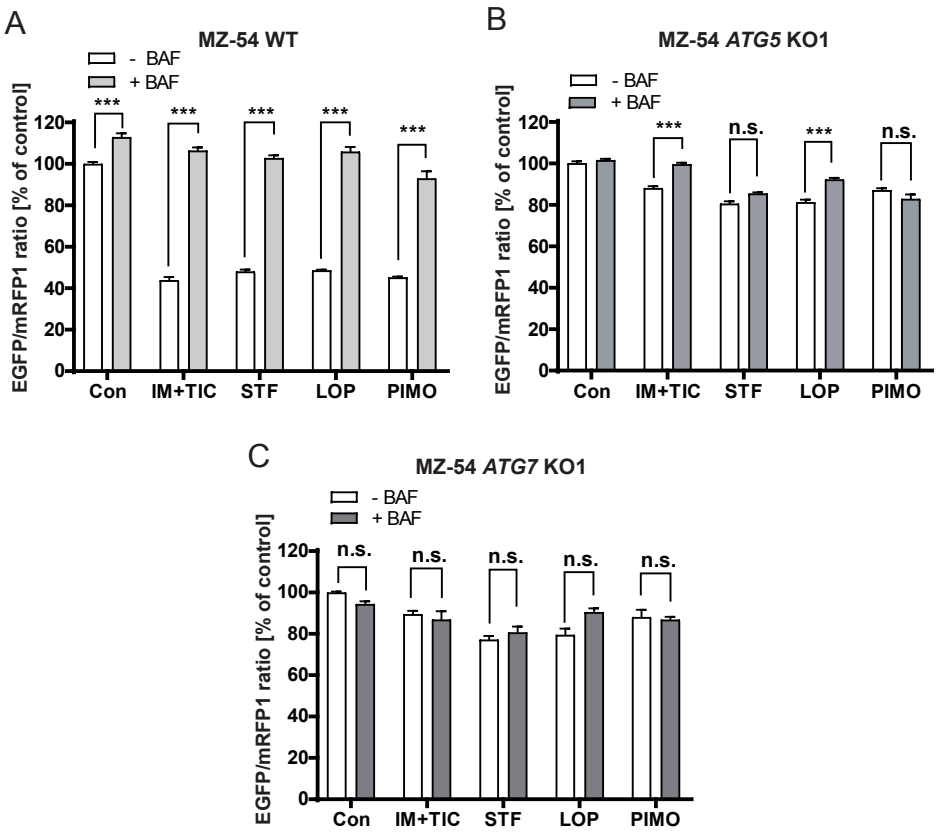

Figure 5.30. Imipramine + ticlopidine, STF-62247, loperamide and pimozide increase the autophagic flux in an *ATG5*- and *ATG7*-dependent manner.
(A-C) Monitoring of the autophagic flux by flow cytometric analysis of pMRX-IP-GFP-LC3-RFP-expressing cells. MZ-54 WT (A), *ATG5* KO (B) and *ATG7 KO* cells (C) were exposed to a combination of 20 µM imipramine and 100 µM ticlopidine (IM+TIC), 40 µM STF-62247 (STF), 15 µM loperamide (LOP), 15 µM pimozide (PIMO) or DMSO (Con) for 16 h in the presence or absence of 10 nM bafilomycin A_1 (BAF) and subjected to flow cytometric analysis. The mean fluorescent intensities of EGFP and mRFP1 were measured, and the EGFP/mRFP1 ratio was calculated as percentage of the DMSO control (Con). The decrease in EGFP/mRFP1 ratio is equivalent to an increase of the autophagic flux. Data represent means + SEM of three independent experiments performed in triplicates and 10,000 cells measured in each sample. Statistical significances were calculated with a two-way ANOVA ($P \leq 0.05$: *, $P \leq 0.01$: **, $P \leq 0.001$: ***, n.s.: not significant). Figure adapted from Zielke et al., 2018.

Furthermore, the LC3B tandem construct ptfLC3 was utilized to validate the increase of the autophagic flux by fluorescence microscopy. Instead of getting cleaved by ongoing autophagy like pMRX-IP-GFP-LC3-RFP, this fluorescent probe enables monitoring of the autophagic flux due to acid quenching of EGFP, but not mRFP in the lysosomal compartment. The majority of ptfLC3 is evenly distributed throughout the whole cell under

basal conditions (LC3B-I isoform) but forms small puncta upon autophagy induction (LC3B-II isoform). During ongoing autophagy, a portion of ptfLC3 gets enclosed by lysosomes, thus leading to disappearance of the EGFP signal, and subsequent degradation of the whole fluorescent probe (Kimura et al., 2007).

Treatment of MZ-54 cells stably expressing ptfLC3 with imipramine + ticlopidine, STF-62247, loperamide and pimozide for 30 hours markedly increased yellow (red + green) as well as red-only puncta, clearly pointing at autophagic flux induction. Moreover, addition of bafilomycin A_1 for the whole treatment period led to a pronounced reduction of red-only puncta (Figure 5.31).

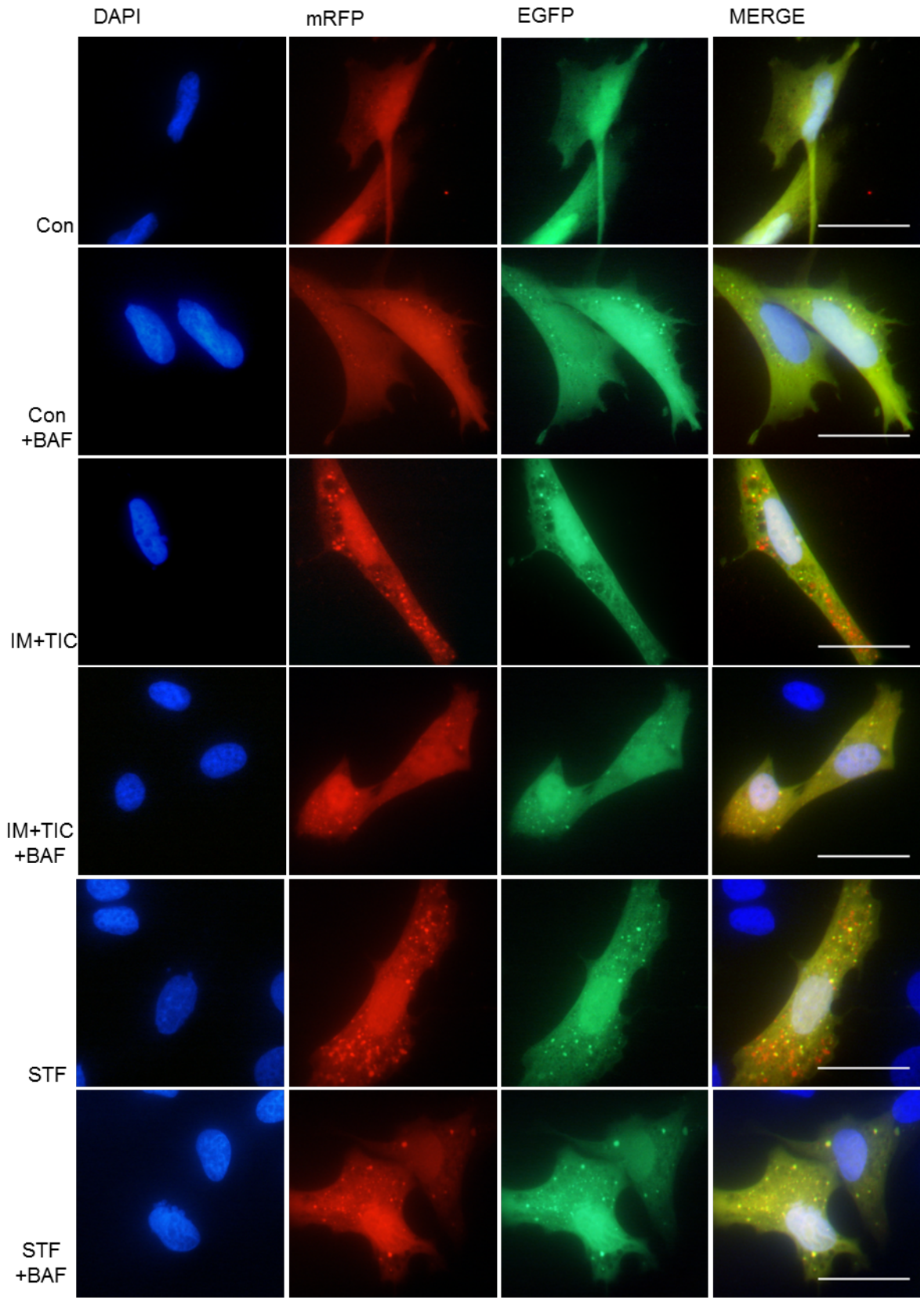
DAPI
mRFP
EGFP
MERGE
Con
Con +BAF
IM+TIC
IM+TIC +BAF
STF
STF +BAF

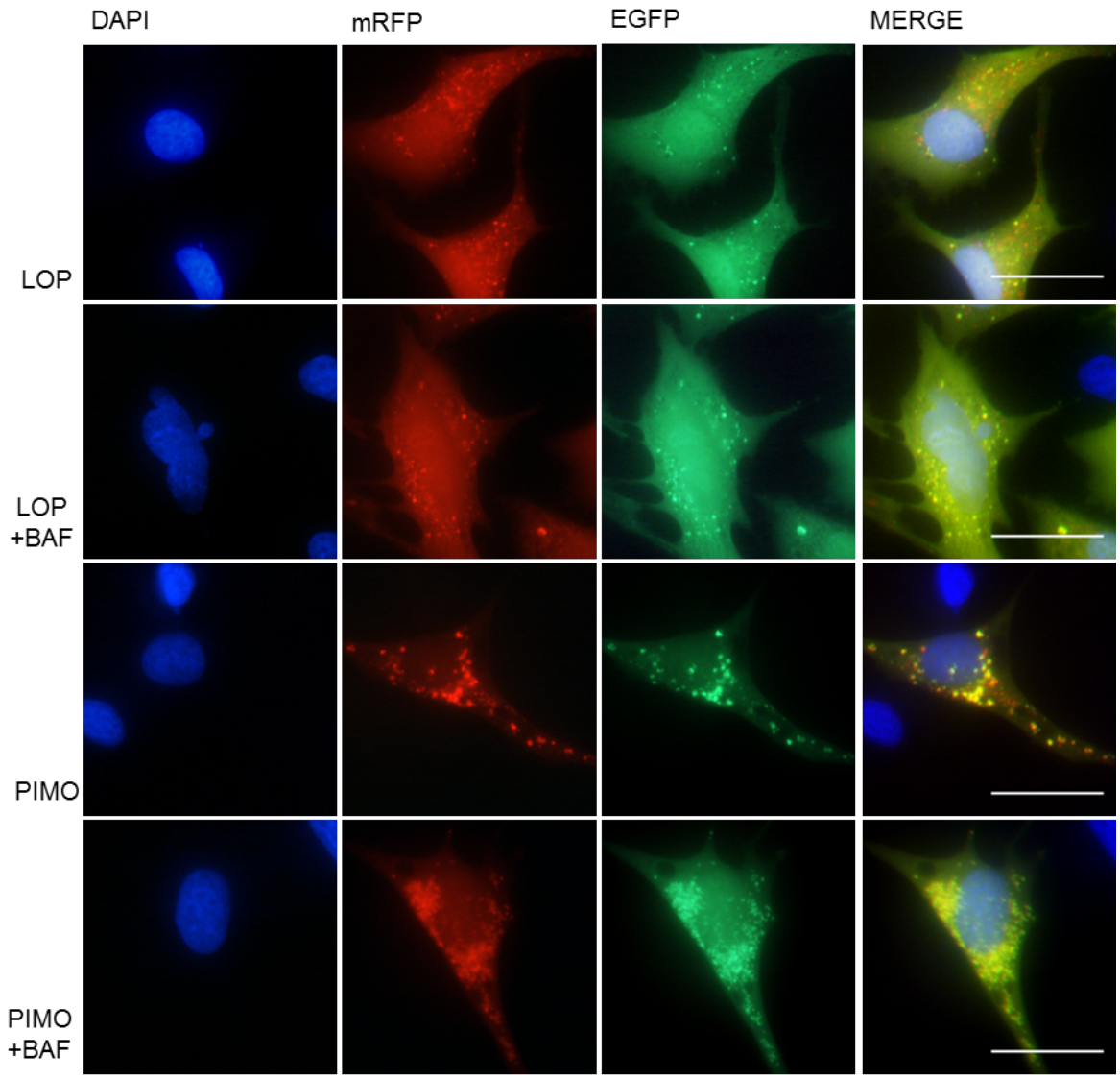

Figure 5.31. Analysis of the autophagic flux by fluorescence microscopy of imipramine + ticlopidine-, STF-62247-, loperamide- and pimozide-treated cells.
Fluorescence microscopy of ptfLC3-expressing MZ-54 cells. Cells were exposed to 20 µM imipramine + 100 µM ticlopidine (IM+TIC), 40 µM STF-62247 (STF), 15 µM loperamide (LOP), 15 µM pimozide (PIMO) or DMSO (Con) for 30 h in the presence or absence of 10 nM bafilomycin A_1 (BAF) 4 h prior to harvest. The nuclei were stained with DAPI and imaged were taken with 60x magnification. Experiments were repeated 3 - 5 times and at least three different pictures were taken per experiment (scale bar = 50 µm). Figure adapted from Zielke et al., 2018.

Quantification of ptfLC3 puncta revealed a significant increase of yellow puncta per cell upon addition of imipramine + ticlopidine, loperamide and pimozide (Figure 5.32A). However, STF-62247 treatment only showed a slight, but no significant increase of yellow puncta per cell. Late stage blockage of autophagy with bafilomycin A_1 further enhanced the number of yellow puncta in all treatments. Furthermore, the number of red puncta per cell was significantly increased by all single agent treatments except for DMSO and bafilomycin A_1 (Figure 5.32B). Combined treatment with bafilomycin A1 remarkably decreased the number of red-only

puncta, an effect which is allegeable by the rise of lysosomal pH and subsequent impairment of EGFP quenching.

Taken together, these results demonstrate the strong and robust enhancement of the autophagic flux by imipramine + ticlopidine, STF-62247, loperamide and pimozide using two different LC3B tandem constructs. Moreover, genetical as well as pharmacological inhibition of autophagy impeded induction of the autophagic flux by all four compounds.

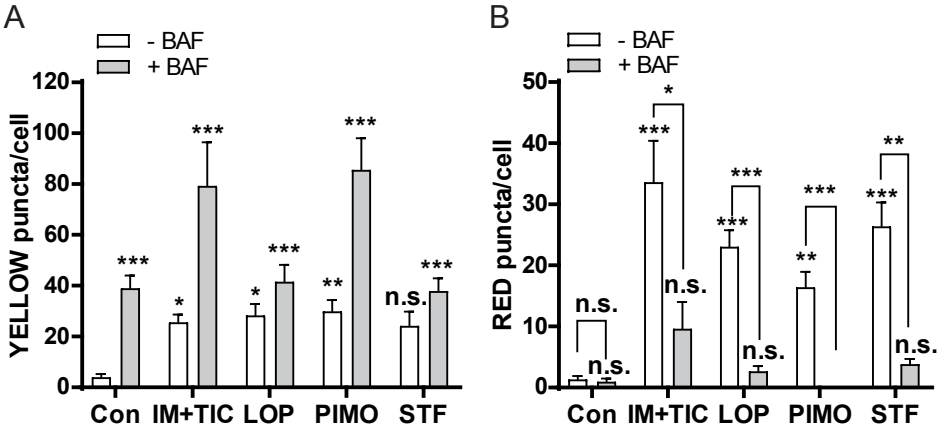

Figure 5.32. Imipramine + ticlopidine, STF-62247, loperamide and pimozide induce autophagic flux.
(A, B) Quantification of ptfLC3 puncta (see also Figure 5.31) per cell. MZ-54 cells were treated with 20 µM imipramine + 100 µM ticlopidine (IM+TIC), 40 µM STF-62247 (STF), 15 µM loperamide (LOP), 15 µM pimozide (PIMO) or DMSO (Con) for 30 h in the presence or absence of 10 nM bafilomycin A_1 (BAF) added 4 h before harvest. In total, yellow (red + green) (A) and red puncta (B) per cell of 9 microscope images from 3 independent experiments were counted. Data represent means + SEM and statistical significances were calculated with a Kruskal-Wallis test ($P \leq 0.05$: *, $P \leq 0.01$: **, $P \leq 0.001$: ***, n.s.: not significant; difference from control or as indicated). Figure adapted from Zielke et al., 2018.

5.9 Signaling pathways involved in imipramine + ticlopidine-, STF-62247-, loperamide- and pimozide-induced autophagy and cell death

Previous experiments clearly revealed the induction of autophagy and cell death in MZ-54 glioma cells following imipramine + ticlopidine, STF-62247, loperamide and pimozide treatment. To shed light on the underlying autophagy signaling pathways induced by these compounds, the downregulation of SQSTM1 as an indicator for ongoing autophagy and the phosphorylation status of the upstream autophagy regulators AMPKalpha (protein kinase AMP-activated catalytic subunit alpha) and AKT1 (AKT serine/threonine kinase 1) were determined by immunoblot analysis (Figure 5.33). Treatment with all compounds elevated phospho-AMPKalpha levels either after 24 hours (imipramine + ticlopidine and STF-62247) or after 6 - 16 hours (loperamide and pimozide) and induced a time-dependent decrease of phospho-AKT1 levels, both events being consistent with the induction of autophagy (Zhao

and Klionsky, 2011; Wang et al., 2012). Unexpectedly, the level of SQSTM1 was increased by all compounds, indicative of either enhanced *SQSTM1* expression and/or autophagy inhibition at some stage (Klionsky et al., 2016).

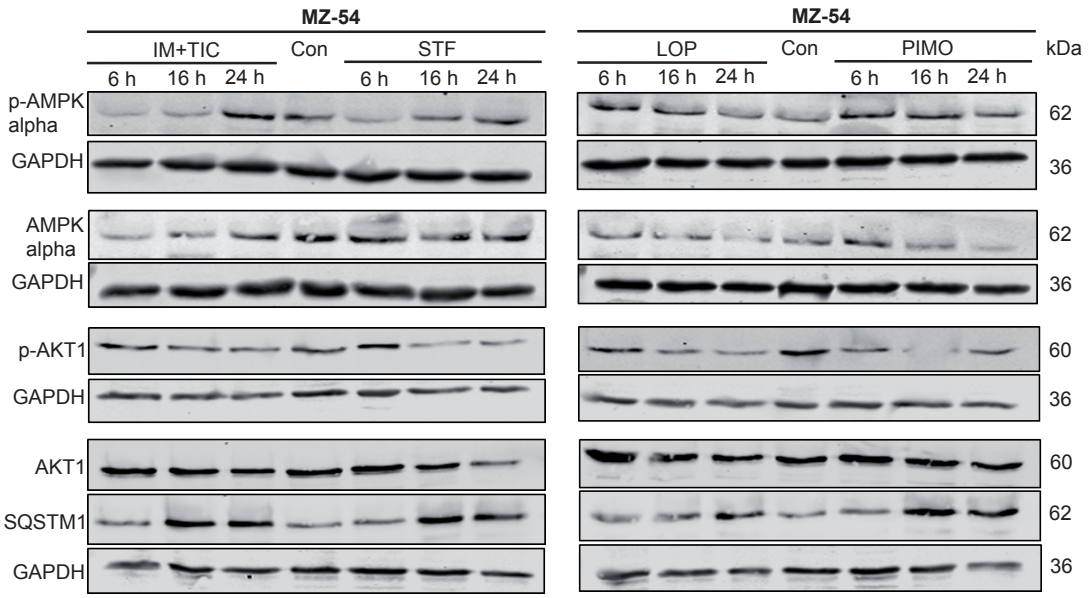

Figure 5.33. Effect of imipramine + ticlopidine, STF-62247, loperamide and pimozide on SQSTM1 protein levels and phosphorylation of AMPKalpha and AKT1.
Immunoblot analysis of phospho-AMPKalpha (p-AMPKalpha, phosphorylation at Thr172), phospho-AKT1 (p-AKT1, phosphorylation at Ser473) and SQSTM1. GAPDH was used as housekeeping protein control. MZ-54 cells were treated with 20 µM imipramine (IM) + 100 µM ticlopidine (TIC), 40 µM STF-62247 (STF), 15 µM loperamide (LOP) and 15 µM pimozide (PIMO) for 6, 16 and 24 h or DMSO (Con) for 24 h. Experiments were repeated three times.

Next, receptor signaling pathways that may lead to autophagy induction and subsequent cell death following treatment with loperamide and pimozide were analyzed. Since STF-62247 has been described to exert its effect via impaired Golgi-trafficking rather than in a cell-surface receptor-dependent way, the compound was not considered in this experiment (Turcotte et al., 2008).

The antipsychotic drug pimozide has been reported to antagonize the dopamine D2, D3 and D4 receptor subfamily and the 5-HT7 serotonin receptor (Freedman et al., 1994; Elmaci and Altinoz, 2018). Interestingly, the 5-HT7 receptor has been shown to be overexpressed in malignant glioma cells (Kast, 2010; Elmaci and Altinoz, 2018). To investigate the potential relevance of 5-HT7 receptor signaling in autophagic cell death of GBM cells, MZ-54 cells were exposed to the highly selective 5-HT7 receptor antagonist DR4485 prior to assessment of cell death and autophagy. Similar to pimozide, DR4485 induced a switch of LC3B-I to LC3B-II after 24 hours that was further increased by addition of bafilomycin A_1, indicative of autophagic flux induction (Figure 5.34A). Furthermore, treatment of MZ-54 cells with DR4485 for 40 hours resulted in pronounced cell death induction, which was significantly reduced in

ATG5 and *ATG7* KO cells (Figure 5.34B). To verify that pimozide induces cell death via inhibition of 5-HT7 receptor signaling, MZ-54 cells were treated with pimozide in the presence or absence of the potent 5-HT7 receptor agonist AS 19. In fact, administration of AS 19 significantly diminished cell death induced by pimozide (Figure 5.34C). Taken together, these results provide evidence that 5-HT7 receptor inhibition is involved in pimozide-induced cell death. However, AS 19 administration only partially rescued pimozide-induced cellular demise, indicating that pimozide also exerts its death-promoting effect in a 5-HT7 receptor independent way.

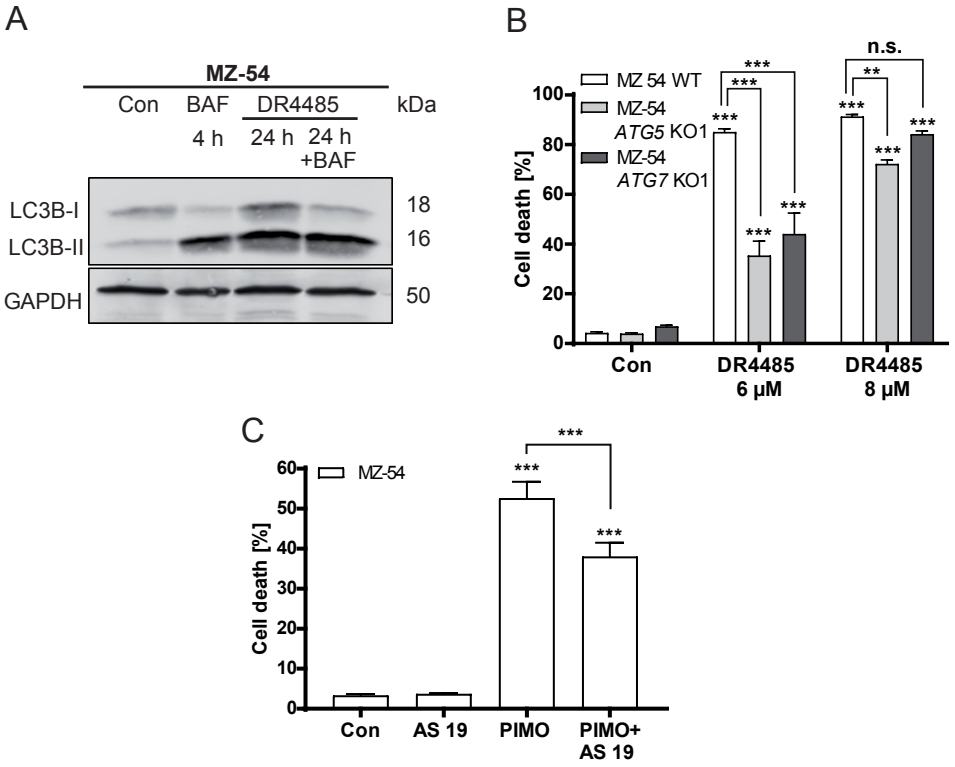

Figure 5.34. Inhibition of 5-HT7 receptor signaling induces autophagic cell death.
(A) Immunoblot analysis of LC3B levels of MZ-54 cells treated with 6 µM DR4485 for 24 h in the presence or absence of 10 nM bafilomycin A_1 4 h before harvest. GAPDH was used as housekeeping protein control. (B, C) Assessment of cell death by analysis of APC-annexin V binding and PI uptake. (B) MZ-54 WT, *ATG5* and *ATG7* KO cells were treated with 6 µM and 8 µM DR4485 for 40 h following flow cytometric analysis. (C) MZ-54 cells were exposed to 12.5 µM pimozide (PIMO) alone or in combination with 10 µM AS 19. AS 19 was administered 2 h prior to pimozide treatment. DMSO was used as vehicle. Data represent means + SEM of three experiments with three replicates and 5,000 - 10,000 cells measured per sample. A two-way ANOVA was performed to calculate statistical significance ($P \leq 0.05$: *, $P \leq 0.01$: **, $P \leq 0.001$: ***, n.s.: not significant; difference from control or as indicated).

Loperamide is a potent agonist of the mu-opioid receptor and voltage-dependent calcium channel inhibitor (Church et al., 1994; DeHaven-Hudkins et al., 1999). To investigate receptor dependency of loperamide-induced ACD, cells were treated with the mu-opioid receptor agonist endomorphin-1 in several doses up to 50 uM (Figure 5.35A). However, in contrast to loperamide, treatment with endomorphin-1 had no effect on cell viability of MZ-54

cells, leading to the hypothesis that loperamide-induced decrease of cellular calcium may trigger ACD instead. Hence, MZ-54 cells were exposed to different concentrations of the voltage-gated calcium channel inhibitor verapamil. However, concentrations up to 30 µM failed to induce cell death, indicating that decrease in intracellular calcium (alone) does not influence cell survival in this experimental setup (Figure 5.35B). Based on these findings it is suggested that loperamide exerts its autophagy-dependent cytotoxicity in glioblastoma cells by a receptor-independent pathway.

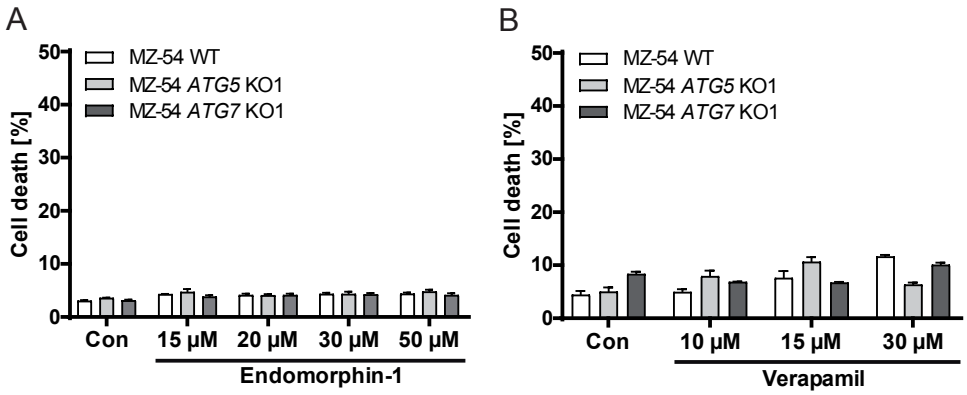

Figure 5.35. Assessment of cell death following treatment with endomorphin-1 and verapamil. (A, B). Determination of cell death (only-APC-annexin V-positive, only-PI-positive and double-positive cells) by flow cytometric analysis of APC-annexin V binding and PI uptake. MZ-54 WT and the respective *ATG5* and *ATG7* KO cells were exposed to 15, 20, 30 and 50 µM endomorphin-1 for 48 h (A) or 10, 15 and 30 µM verapamil for 40 h (B). DMSO (Con) was used as vehicle. Data represent mean + SEM of one experiment performed in triplicate and 5,000 - 10,000 cells measured in each sample.

5.10 The cellular lipid metabolism is altered in imipramine + ticlopidine-, STF-62247-, loperamide- and pimozide-treated cells

Investigation of receptor-dependent pathways was not able to fully explain the molecular mechanisms upstream of ACD induction. Thus, a global proteomic analysis was performed to elucidate protein changes associated with cellular toxicity induced by imipramine + ticlopidine, STF-62247, loperamide and pimozide. Thereto, imipramine + ticlopidine, STF-62247, loperamide and pimozide were applied to MZ-54 cells for 24 hours, and changes in the proteome were subsequently analyzed by a TMT-labeled approach (see chapter 4.9). In total, 6,298 proteins were measured with 176 to 214 proteins being upregulated and 103 to 191 proteins being downregulated following treatment with the different compounds (Figure 5.36A, B). Interestingly, the proteomic profiles revealed a strong similarity between loperamide- and pimozide-treated cells, whereas exposure to imipramine + ticlopidine and STF-62247 resulted in a more diverse protein pattern (Figure 5.36C). However, treatment

with all compounds revealed a closer similarity among each other than compared to the DMSO-treated controls.

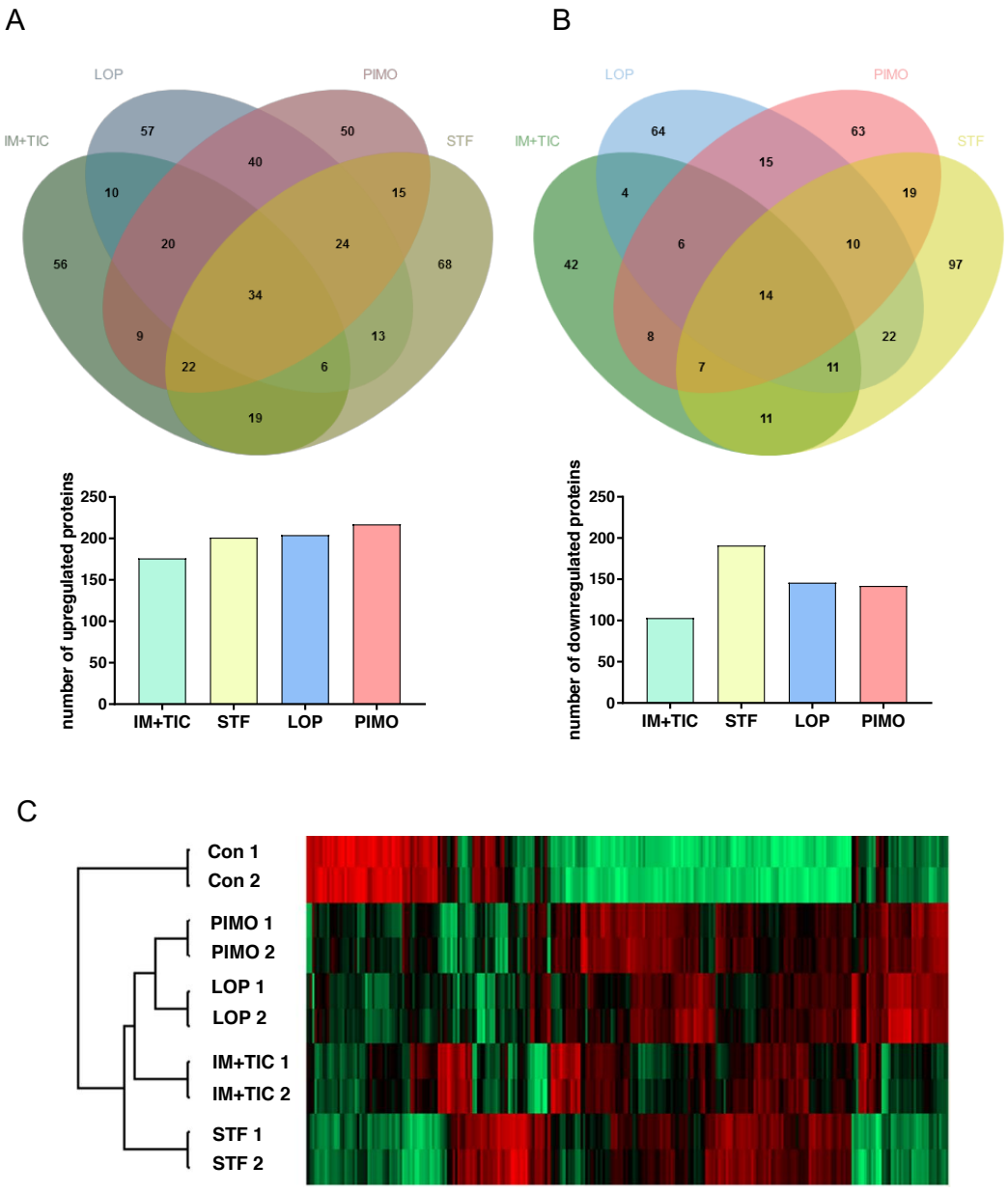

Figure 5.36. Proteomic analysis of MZ-54 glioma cells treated with imipramine + ticlopidine, STF-62247, loperamide and pimozide.
(A, B) Venn diagram (Bardou et al., 2014) and bar chart showing the number of upregulated (A) or downregulated (B) proteins of TMT-labeled proteomic-data from MZ-54 cells exposed to 20 µM imipramine and 75 µM ticlopidine (IM+TIC), 40 µM STF-62247 (STF), 12.5 µM loperamide (LOP) and 12.5 µM pimozide (PIMO) for 24 h and the overlap between different treatments. In total, 6,298 proteins were detected. (C) Proteomic profile of MZ-54 cells treated as described in A and B. The color profile shows differences/similarities of significantly regulated proteins between treatments and the dendrogram displays the hierarchical clustering of the samples. Experiments were performed in duplicates. The threshold for significance was set at $p<0.01$. After sample preparation, LC-MS/MS measurements of MZ54 cells and initial analysis with Perseus were performed by Dr. Georg Tascher, working group of Dr. Christian Münch, Institute of Biochemistry II, Goethe University Hospital Frankfurt/Main, Germany.

Surprisingly, subsequent PANTHER enrichment analysis of Gene Ontology (GO) terms showed a significant and robust upregulation of lipid metabolic processes and especially cholesterol metabolic processes upon treatment with all compounds (Figure 5.37). However, loperamide and pimozide treated cells revealed the strongest increase of proteins associated to these GO terms. Out of the top 50 significantly upregulated proteins after loperamide exposure, 13 (26%) were categorized to the GO term cholesterol metabolism and 18 (36%) were related to lipid metabolic processes. Pimozide treatment had similar effects with 9 proteins (18%) being related to cholesterol metabolism and 14 proteins (28%) out of the top 50 being related to lipid metabolic processes. The top 50 upregulated and downregulated proteins are listed in Table 10.2 (see supplements).

Among the proteins associated to cholesterol metabolic processes, SCARB1, APOB, LDLR, HMGCR, APP, APLP2, FDFT1 and HMGCS1 were significantly increased in loperamide- as well as pimozide-treated cells, and partly in imipramine + ticlopidine and STF-62247-treated cells. SCARB1 (scavenger receptor class B member 1) is a receptor that facilitates the uptake of cholesteryl esters from high- and low-density lipoproteins and free cholesterol efflux to lipoprotein acceptors (Rhainds and Brissette, 2004). APOB (apolipoprotein B) is an important component of lipoprotein particles (German et al., 2006). The LDLR (low density lipoprotein receptor) transports cholesterol from LDL into the cells by endocytosis (Go and Mani, 2012). Transmembrane glycoprotein HMGCR (3-hydroxy-3-methylglutaryl-coenzyme A reductase) is a rate-limiting enzyme in cholesterol biosynthesis (Sharpe and Brown, 2013). HMGCS1 (hydroxymethylglutaryl-CoA synthase, cytoplasmic) condenses acetyl-CoA with acetoacetyl-CoA to form HMG-CoA (Vögeli et al., 2018). APP (amyloid beta precursor protein) as well as APLP2 (amyloid beta precursor like protein 2) belong to the amyloid precursor protein family and have been implicated in Alzheimer's disease and cholesterol metabolism (Marzolo and Bu, 2009). FDFT1 (farnesyl-diphosphate farnesyltransferase 1) is an enzyme involved in cholesterol biosynthesis (Do et al., 2009).

Moreover, autophagy- and lysosome-related GO terms were significantly upregulated by imipramine + ticlopidine, STF-62247, loperamide and pimozide treatment, which is in line with the increased autophagic flux by all four drugs (Figure 5.37B, D, F, H). In addition, the GO term vesicle-mediated transport was significantly upregulated following treatment with all compounds. Vesicle-mediated transport is implicated in several steps of autophagy and lipid metabolism, thus, it might be linked to the strong induction of lipid metabolic processes as well as increased autophagic flux by all four compounds (McMaster, 2001; Amaya et al., 2015; Noda, 2017). Among the significantly downregulated protein clusters by imipramine + ticlopidine, STF-62247, loperamide and pimozide were cell cycle and nucleic acid metabolic processes, indicating a growth arrest upon treatment with all four compounds (Figure 5.37B, D, F, H).

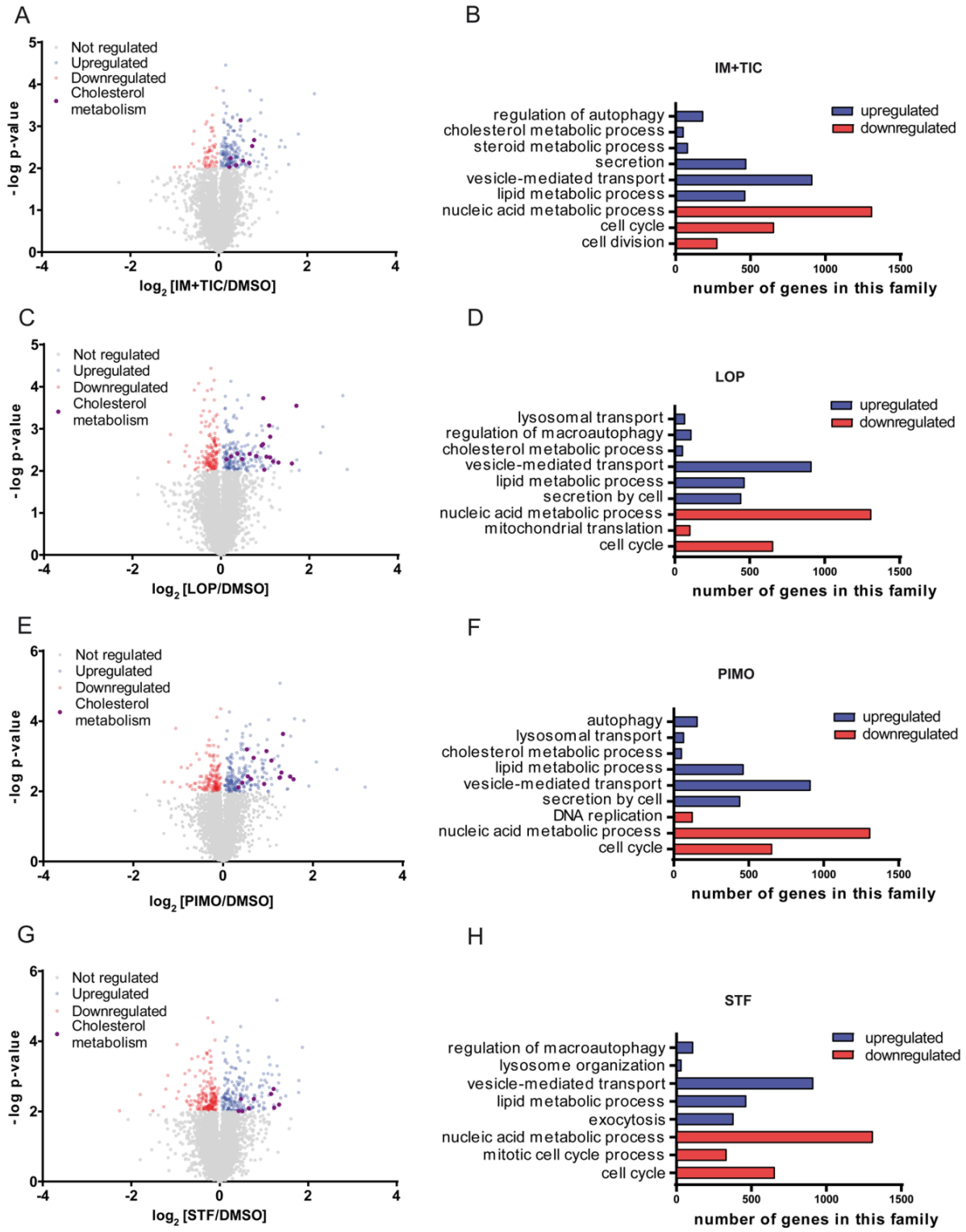

Figure 5.37. Proteomic analysis of MZ-54 glioma cells treated with imipramine + ticlopidine, STF-62247, loperamide and pimozide.
(A, C, E, G) Volcano Plot showing the protein ratios (in log_2) as a function of the -log p-value of TMT-labeled proteomic-data from MZ-54 cells treated with 20 µM imipramine and 75 µM ticlopidine (IM+TIC), 12.5 µM loperamide (LOP), 12.5 µM pimozide (PIMO) and 40 µM STF-62247 (STF) for 24 h. Proteins not significantly altered are depicted in grey, upregulated proteins are shown in blue and downregulated proteins in red. Significantly upregulated proteins that cluster for the GO term cholesterol metabolism (GO:0008203) are highlighted in purple. A total of 6,298 proteins were quantified in each sample. Experiments were performed in duplicates. The threshold for significance was set to $p<0.01$. (B, D, F, H) Quantification of upregulated and downregulated proteins of TMT-

labeled proteomic-data from MZ-54 cells that cluster for selected gene ontology (GO) terms for biological processes. MZ-54 glioma cells were treated as described above. For identification of significantly regulated protein clusters, all up- or downregulated proteins were considered and analyzed with the PANTHER enrichment tool (version 14.0). The bar charts display a selection of the significantly increased or decreased biological processes and the overall number of genes in this family. The p-value was set at $p<0.05$. After sample preparation, LC-MS/MS measurements of MZ54 cells and initial analysis with Perseus were performed by Dr. Georg Tascher, Institute of Biochemistry II, working group of Dr. Christian Münch, Goethe University Hospital Frankfurt/Main, Germany.

The upregulation of proteins involved in cholesterol metabolism might be the consequence of dysfunctional cellular lipid transport. Interestingly, it has been shown that decreased cytosolic cholesterol levels cause the constitutive activation of the transcription factor sterol regulatory element binding proteins (SREBP), leading to upregulated lipogenic gene transcription (Kristiana et al., 2010). Moreover, elevated levels of proteins involved in lipid metabolism has been described for a variety of lipid storage diseases such as Niemann-Pick diseases (type A - D), which are characterized by the accumulation of lipids in the lysosomes. Thereby, efflux of cholesterol from late endosomes and lysosomes is disturbed because of mutations of different genes (NPC1, NPC2, SMPD1), and the lipids are retained in the lysosomes instead of being transported into the cytosol (Schulze and Sandhoff, 2011; Santos-Lozano et al., 2015)

To scrutinize the hypothesis that cholesterol transport is altered upon treatment with imipramine + ticlopidine, STF-62247, loperamide and pimozide, cholesterol was stained using filipin III in combination with immunostaining of the lysosomal protein LAMP1 (Figure 5.38). Vehicle-treated MZ-54 cells displayed a weak, evenly distributed filipin III staining throughout the whole cell. After treatment with the positive control U18666A, which is a steroidal cationic amphiphile that inhibits intracellular cholesterol trafficking (Kristiana et al., 2008), the cells showed several filipin III puncta that colocalized with LAMP1. Strikingly, treatment with imipramine + ticlopidine, STF-62247, loperamide and pimozide also resulted in a clear colocalization of filipin III puncta and LAMP1, pointing to the strong accumulation of cholesterol in the lysosomes (Figure 5.38).

Since the proteomic profiles induced by loperamide and pimozide displayed the highest similarities, and both compounds revealed the strongest effects on lipid metabolic processes compared to the other tested drugs, most of the subsequent experiments focused on loperamide and pimozide in comparison to the established ACD inducer imipramine + ticlopidine.

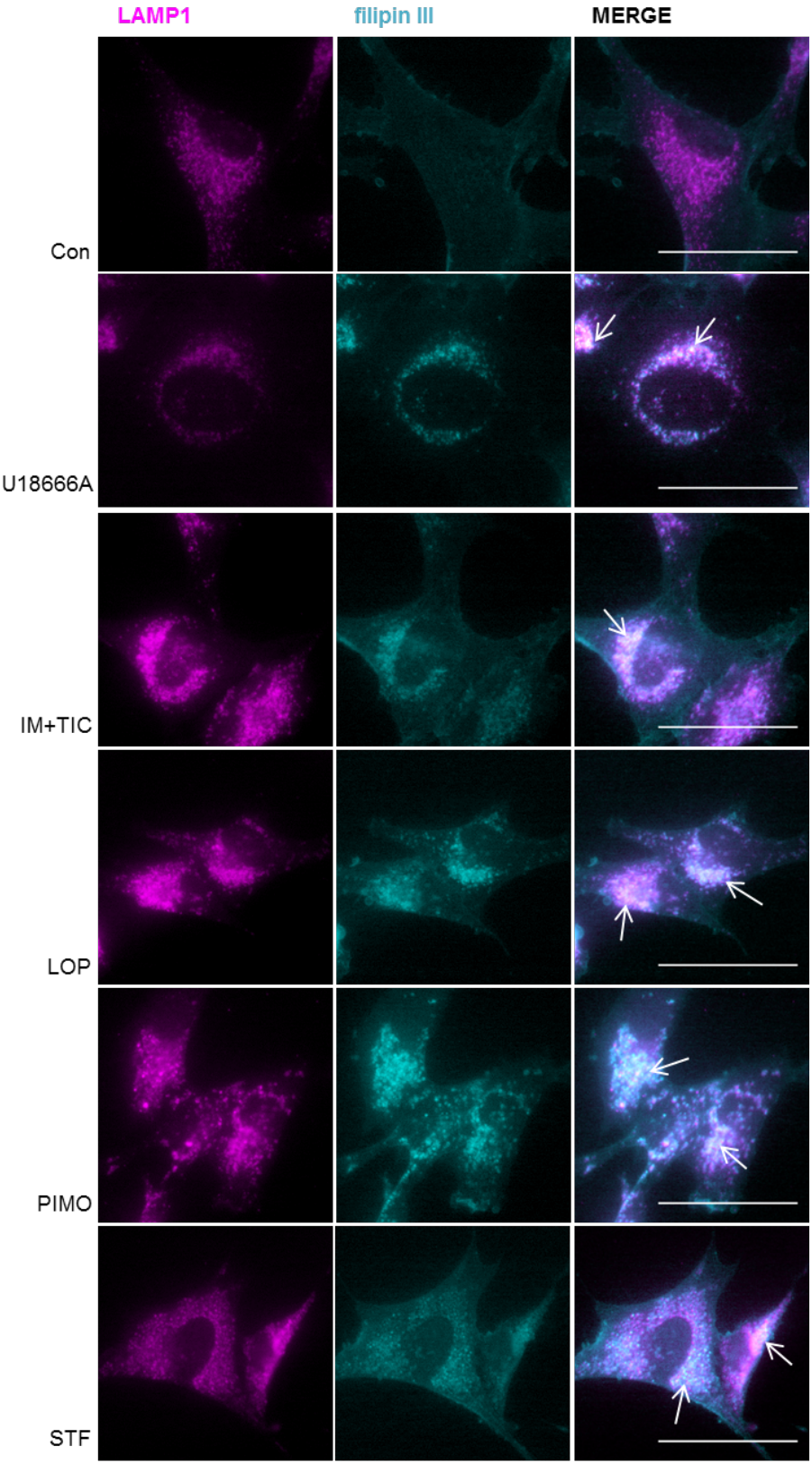

Figure 5.38. Accumulation of cholesterol in the lysosomes.
Monitoring of cholesterol colocalization to the lysosomes by fluorescence microscopy of the lysosomal marker LAMP1 and cholesterol staining with filipin III (depicted with arrows). MZ-54 cells were exposed to 1.25 µM U18666A, 20 µM imipramine and 75 µM ticlopidine (IM+TIC), 40 µM STF-62247 (STF), 12.5 µM loperamide (LOP), 12.5 µM pimozide (PIMO) or DMSO (Con) for 18 h. Images were taken with 60x magnification. Experiments were repeated three times and at least three different pictures were taken per experiment (scale bar=50 µM).

As outlined above, pronounced lysosomal cholesterol accumulation following treatment with imipramine + ticlopidine, STF-62247, loperamide and pimozide is caused by severe blockage of cholesterol transport, thus implying reduced cytosolic cholesterol concentrations. Interestingly, it has been published that cytosolic cholesterol negatively regulates autophagy via induction of mTOR and AKT1 signaling (Xu et al., 2010). As shown in Figure 5.33 and by Zielke et al., imipramine + ticlopidine, STF-62247, loperamide and pimozide reduced mTOR and AKT1 signaling, thereby promoting autophagy (Zielke et al., 2018). To investigate the potential correlation of decreased cytosolic cholesterol levels and autophagy induction, MZ-54 cells were treated with imipramine + ticlopidine, loperamide and pimozide alone or in combination with water soluble cholesterol (complexed with beta-methyl-cyclodextrin). Strikingly, the decrease of phospho-AKT1 levels after treatment with imipramine + ticlopidine, loperamide and pimozide for 16 hours was impeded by addition of cholesterol (Figure 5.39A). Furthermore, cholesterol reduced the LC3B-switch in loperamide- and pimozide-treated MZ-54 cells (Figure 5.39B). However, the LC3B-switch induced by imipramine + ticlopidine was not influenced by addition of cholesterol. These results point out that impaired cholesterol trafficking promotes the induction of autophagy, at least by loperamide and pimozide.

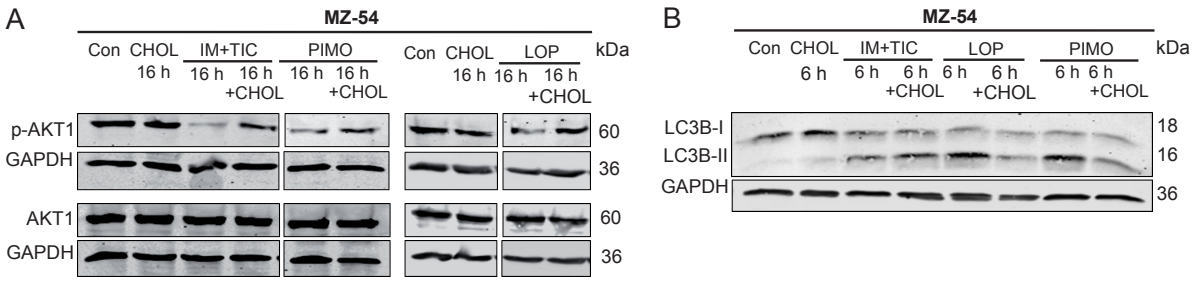

Figure 5.39. Effect of cholesterol on phospho-AKT1 and LC3B-switch.
(A, B) Immunoblot analysis of phospho-AKT1 (p-AKT1, phosphorylation at Ser473), LC3B and GAPDH as housekeeper. MZ-54 cells were treated with 20 µM imipramine (IM) + 100 µM ticlopidine (TIC), 15 µM loperamide (LOP), 15 µM pimozide (PIMO) or DMSO (Con) for 16 h (A) or 6 h (B). Experiments in A were repeated four times and experiments in B were repeated two times.

Of note, imipramine, loperamide and pimozide are cationic amphiphilic drugs that have been shown to act as functional inhibitors of acid sphingomyelinase (FIASMAs) (Kornhuber et al., 2008; Kornhuber et al., 2011). The acid sphingomyelinase (ASM) is a lysosomal enzyme that catalyzes the conversion of sphingomyelin to phosphorylcholine and ceramide. FIASMAs show lipophilic and weakly basic properties and cross the lysosomal membrane in their uncharged form. Inside the lysosome, the compounds subsequently get protonated because of the acidic milieu and thus accumulate in the lysosome, as the lysosomal membrane is less permeable for charged molecules. FIASMAs trapped in the lysosome disturb the binding of

ASM to the membrane, leading to its detachment and subsequent inactivation and degradation (Kölzer et al., 2004; Kornhuber et al., 2008). Notably, disturbed function of the acid sphingomyelinase is a well-known feature of the lysosomal lipid storage disease Niemann-Pick type A and B (Schulze and Sandhoff, 2011). Moreover, elevated sphingomyelin levels resulting from ASM inhibition have been described to induce lysosomal damage and a block of autophagy (Gabandé-Rodríguez et al., 2014).

To validate the inhibitory effect of imipramine + ticlopidine, loperamide and pimozide on ASM, an acid sphingomyelinase activity assay was performed according to the manufacturer's instructions (see chapter 4.12). Loperamide and pimozide decreased ASM activity to 60% after 16 hours, whereas imipramine + ticlopidine treatment resulted in a slighter activity decrease to 70% (Figure 5.40). These results clearly confirm that imipramine + ticlopidine, loperamide and pimozide reduce ASM activity in MZ-54 cells.

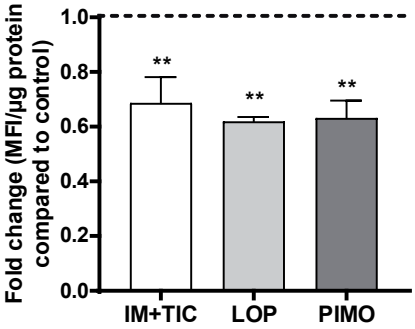

Figure 5.40. Imipramine + ticlopidine, loperamide and pimozide reduce acid sphingomyelinase activity.
Assessment of acid sphingomyelinase (ASM) activity. MZ-54 cells were treated with 20 mM imipramine + 75 µM ticlopidine (IM+TIC), 12.5 µM loperamide (LOP) and 12.5 µM pimozide (PIMO) for 16 h. ASM activity was determined as fold change of mean fluorescence intensity (MFI) per µg protein compared to vehicle-treated cells. Data are mean + SEM from three independent experiments. Statistical significances were calculated using a one-way ANOVA ($P \leq 0.05$: *, $P \leq 0.01$: **, $P \leq 0.001$: ***, n.s.: not significant; difference from control).

In addition to sphingomyelin, several ceramides, which represent a group of bioactive sphingolipids, have been described to affect autophagy as well as cell death (Scarlatti et al., 2004; Ordoñez et al., 2015; Hernández-Tiedra et al., 2016; Wang et al., 2017). To investigate potential changes in bioactive sphingolipid levels, a targeted analysis of sphingolipids/ceramides was performed upon treatment with loperamide and pimozide for 16 hours. Strikingly, nearly all measured sphingolipids (sphingosine, sphinganins, ceramides and glucosylceramides) were strongly increased by loperamide and pimozide (Figure 5.41, Figure 5.42). In contrast, lactosylceramide levels were significantly decreased by pimozide but were not affected by loperamide, indicating some drug-specific effects on galactosidase alpha. Moreover, sphingosine levels were significantly elevated following loperamide treatment on the one hand, but significantly decreased upon pimozide administration on the

other hand. Collectively, these data point to a global effect of loperamide and pimozide on sphingolipid metabolism. In any case, ASM inhibition by loperamide and pimozide does not explain these findings, as a reduction of this enzyme is associated with decreased ceramide generation.

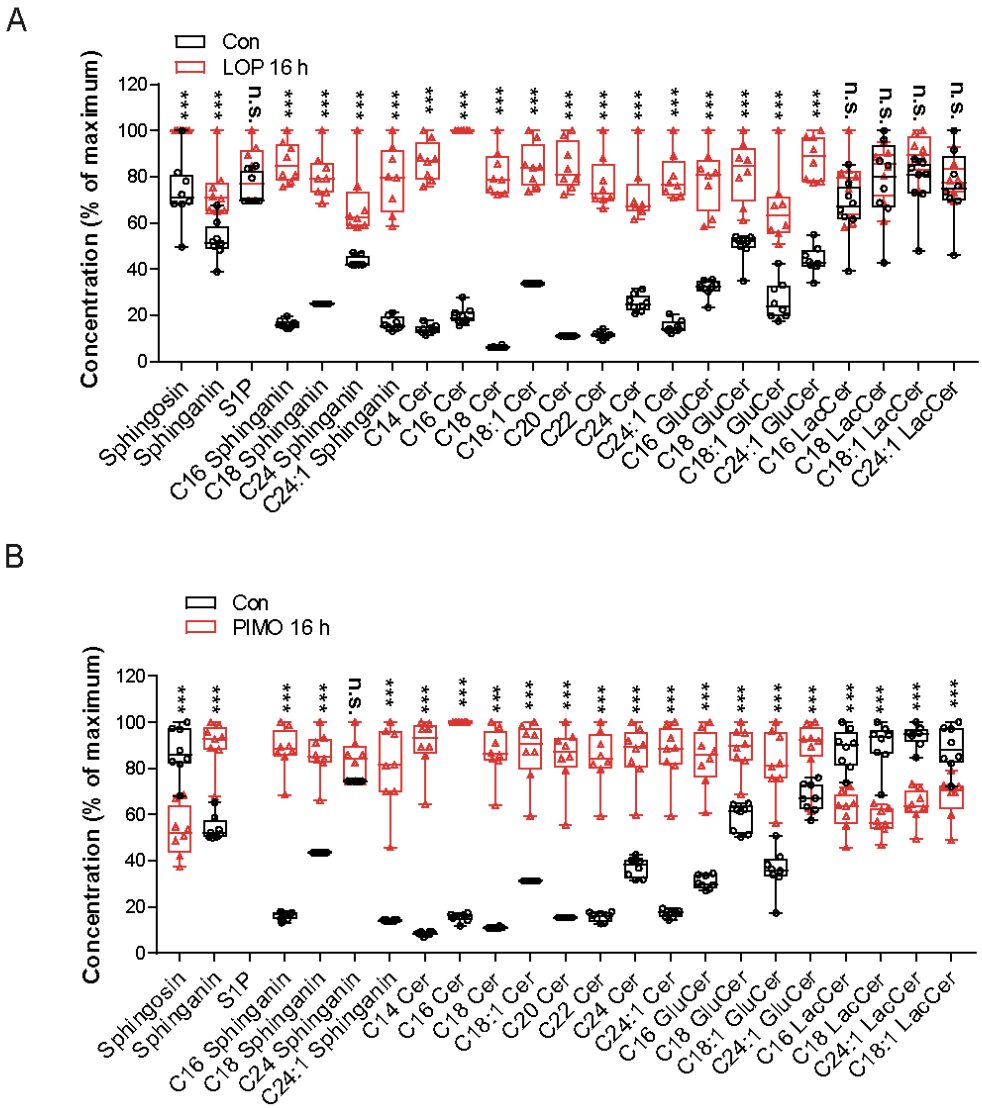

Figure 5.41. Lipidomics screen of MZ-54 cells treated with loperamide and pimozide.
(A, B) Boxplots display the interquartile range of different sphingolipids (sphingosine, sphinganins, ceramides, glucosylceramides and lactosylceramides) as percentage of the maximum. The line is the median and min and max values of the eight replicates are depicted with whiskers. MZ-54 cells were exposed to 12.5 µM loperamide (LOP) (A) and 12.5 µM pimozide (PIMO) (B). The percentage of FBS in cell culture medium was reduced to 2% in loperamide-treated cells and to 5% in pimozide treated cells to reduce background lipids. Statistical significances were calculated with a two-way ANOVA ($P \leq 0.05$: *, $P \leq 0.01$: **, $P \leq 0.001$: ***, n.s.: not significant; difference from control). Abbreviations: S1P, sphingosine-1-phosphate; C14Cer etc. ceramide with 14 C-atoms; C24:1Cer etc., ceramide with 24 C-atoms and one unsaturated bound; GluCer, glucosylceramide; LacCer, lactosylceramide. After collecting the cell pellets, samples were given to Prof. Dr. Irmgard Tegeder (Institute of Clinical Pharmacology, Goethe University Hospital Frankfurt/Main,Germany) for further preparation and the lipidomics screen.

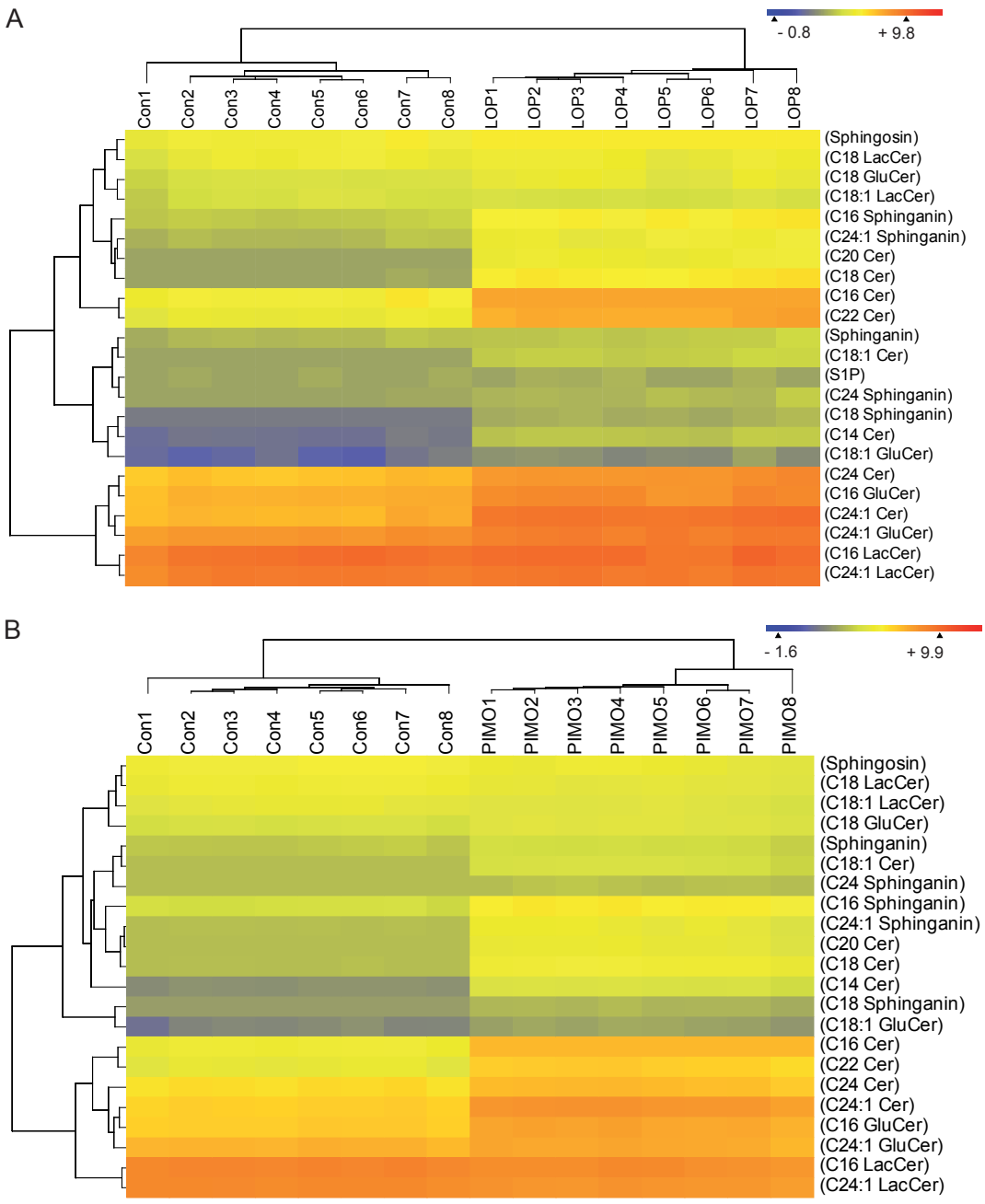

Figure 5.42. Heat maps of the lipidomics screen of MZ-54 cells treated with loperamide and pimozide.
Dendrogramm representing the hierarchical Euclidean clustering of the lipids on the y-axis and of the experimental replicates on the x-axis, and heatmap showing the differences in concentrations between all lipids and between groups. Cells were treated as described in Figure 5.41. Abbreviations: S1P, sphingosine-1-phosphate; C14Cer etc. ceramide with 14 C-atoms; C24:1Cer etc., ceramide with 24 C-atoms and one unsaturated bound; GluCer, glucosylceramide; LacCer, lactosylceramide. After collecting the cell pellets, samples were given to Prof. Dr. Irmgard Tegeder (Institute of Clinical Pharmacology, Goethe University Hospital Frankfurt/Main, Germany) for further preparation and the lipidomics screen.

Accelerated ceramide levels can be a result of either increased *de novo* synthesis at the ER, or blockage of lysosomal degradation. Therefore, the expression of a variety of enzymes (*CERS* [ceramide synthase] *1, CERS2, CERS5, CERS6,* DEGS1 [delta 4-desaturase,

sphingolipid 1]*, SPTLC1* [serine palmitoyltransferase long chain base subunit 1]) involved in ceramide synthesis was determined next. However, solely the expression of *CERS1*, which is responsible for synthesis of 18-carbon (C18) ceramide, was significantly increased upon treatment with pimozide and showed an increasing trend following loperamide addition (Figure 5.43). Since *de novo* synthesis of ceramides was mainly not affected by loperamide and pimozide, it is assumed that rather blockage of lysosomal degradation triggers the accumulation of sphingolipids.

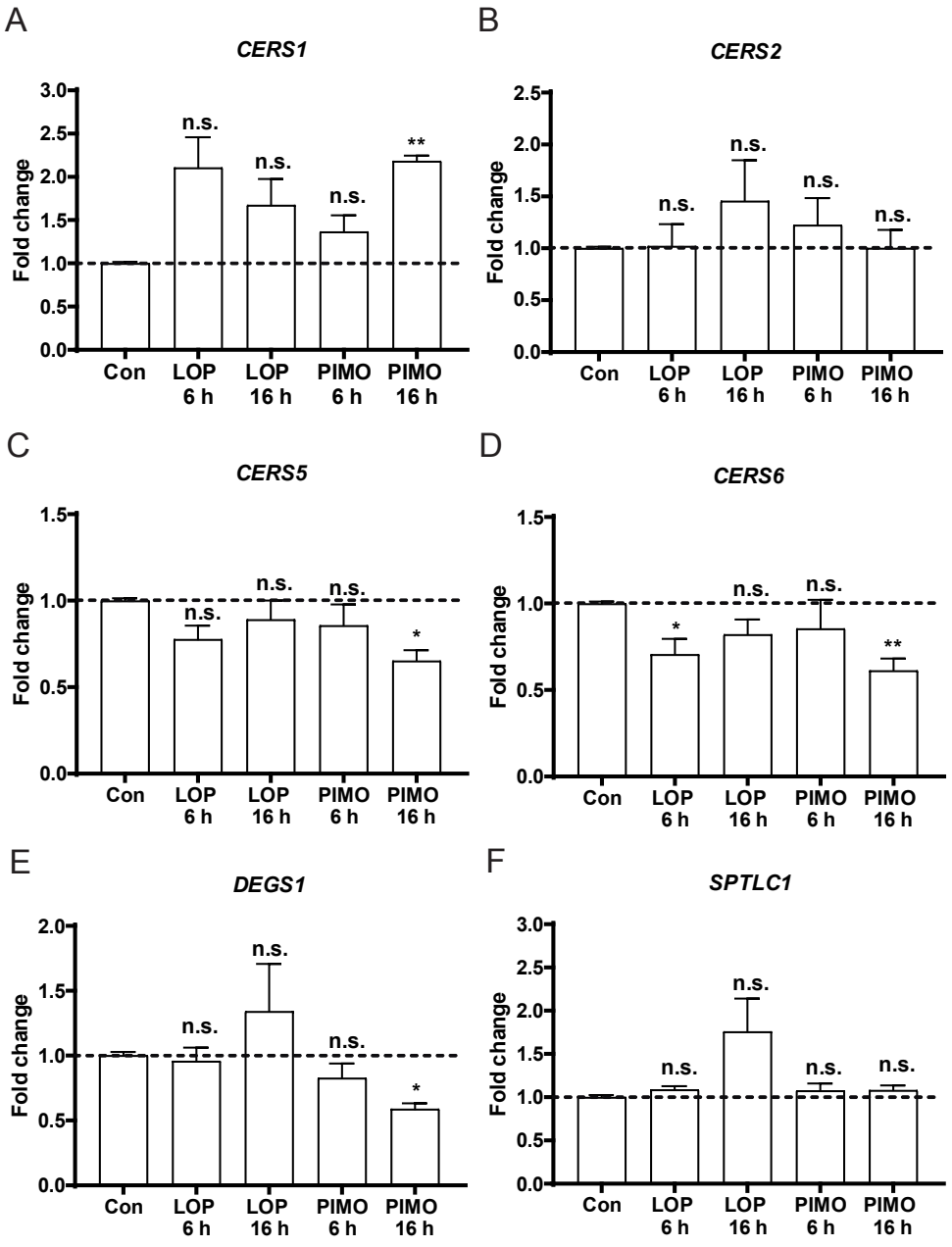

Figure 5.43. Investigation of *de novo* ceramide synthesis.
Assessment of the expression levels of *CERS1, CERS2, CERS5, CERS6, DEGS1* and *SPTLC*1 mRNA normalized to *TBP* by qRT-PCR. MZ-54 cells were exposed to 12.5 µM loperamide (LOP), 12.5 µM pimozide (PIMO) or DMSO (Con) for 6 h and 16 h. Data show mean + SEM of three independent experiments with three technical replicates. Statistical significances were calculated with a Kruskal-Wallis test ($P \leq 0.05$: *, $P \leq 0.01$: **, $P \leq 0.001$: ***, n.s.: not significant; difference from control).

Although several experiments revealed an induction of the autophagic flux by imipramine + ticlopidine, STF-62247, loperamide and pimozide, treatment with at least three of these compounds (imipramine + ticlopidine, loperamide and pimozide) seems to culminate in a late stage autophagy block due to functional inhibition of ASM, lipid accumulation and subsequent impairment of lysosomal function, suggesting the breakdown of the autophagic flux at later time points. In line with these considerations, it has been reported that accumulation of lipids in the lysosomes is associated with disturbed degradative function and a late stage autophagy block (Lieberman et al., 2012; Serrano-Puebla and Boya, 2016). Moreover, it is suggested that blockage of lysosomal sphingolipid degradation leads to massive accumulation of these lipids and outweighs the effects of ASM inhibition on ceramide levels.

5.11 Loperamide and pimozide induce lysosomal membrane permeabilization

Of note, lysosomes massively filled with lipids are prone to get damaged by oxidative stress (Schulze and Sandhoff, 2011). To determine whether treatment with imipramine + ticlopidine, loperamide and pimozide induces oxidative stress, cellular lipid-ROS and general ROS levels were assessed by flow cytometric measurement of the lipid-peroxidation sensor BODIPY™ 581/591 C11 and the general oxidative stress indicator CM-H2DCFDA, which measures hydroxyl, peroxyl and other reactive oxygen species activity within the cell. Treatment with pimozide and loperamide for 16 hours led to a significant increase of lipid-ROS levels, which was abrogated by addition of the lipid-ROS scavenger α-tocopherol (Figure 5.44A). However, imipramine + ticlopidine treatment had no visible effect on the cellular lipid-ROS levels. Furthermore, pimozide treatment led to a pronounced increase of general ROS levels and α-tocopherol significantly diminished this effect, while loperamide only slightly enhanced general oxidative stress (Figure 5.44B). In accordance with the increased lipid-ROS levels by loperamide and pimozide shown in Figure 5.44A, α-tocopherol was also able to significantly reduce pimozide- and loperamide-induced cell death, but not imipramine + ticlopidine-induced cellular demise (Figure 5.44C). Taken together, these data point to a cell death promoting effect of (lipid)-ROS accumulation by loperamide and pimozide.

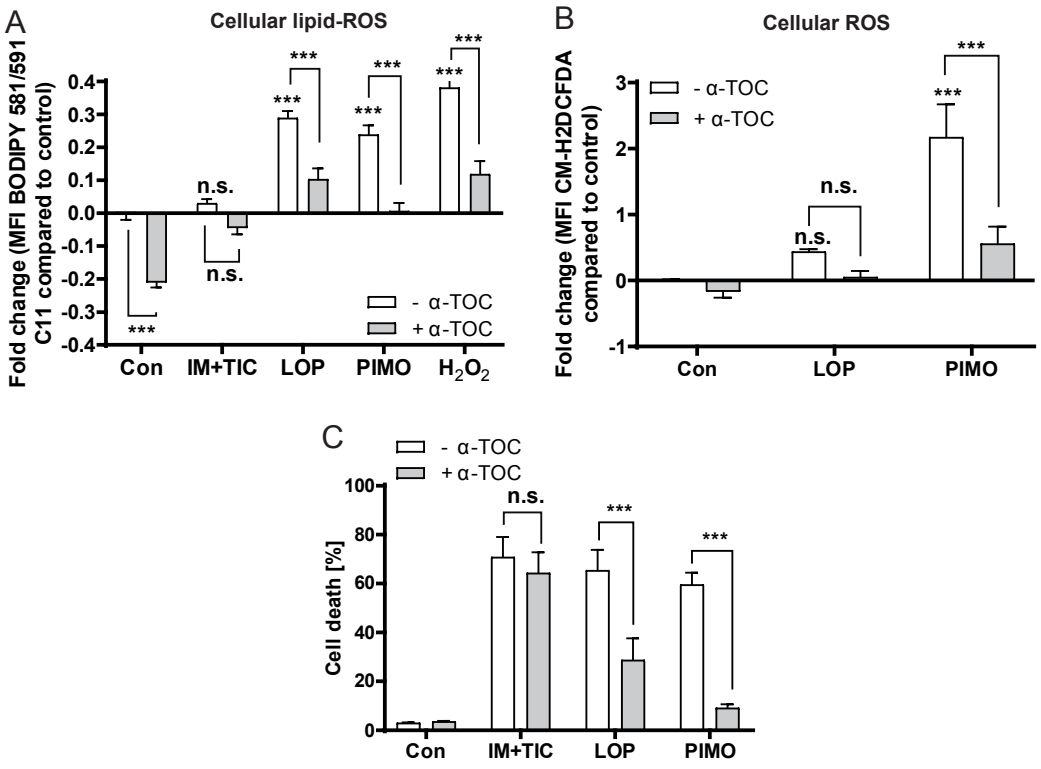

Figure 5.44. Loperamide and pimozide induce ROS accumulation.
(A, B) Assessment of cellular lipid-ROS and overall ROS levels by flow cytometric analysis of the lipid peroxidation sensor BODIPY™ 581/591 C11 (A) and the general oxidative stress indicator CM-H2DCFDA (B). MZ-54 cells were exposed to 20 µM imipramine and 75 µM ticlopidine (IM+TIC), 15 µM loperamide (LOP), 12.5 µM pimozide (PIMO) or DMSO (Con) in the presence or absence of α-tocopherol (α-TOC, added 1 h prior to other treatments) for 18 h. ROS levels were quantified by comparing the fold change of the mean fluorescent intensities of controls and treated cells. (C) Determination of cell death by flow cytometric analysis of APC-annexin V binding and PI uptake. Data represent mean + SEM of at least three experiments with three replicates and 5,000 - 10,000 cells measured in each sample. Statistical significances were calculated with a two-way ANOVA ($P \leq 0.05$: *, $P \leq 0.01$: **, $P \leq 0.001$: ***, n.s.: not significant; difference from control or as indicated).

The accumulation of lipids in lysosomes and subsequent oxidative stress are both well-known inducers of lysosomal membrane permeabilization (LMP), which is associated with lysosomal rupture and subsequent release of the lysosomal content into the cytosol (Serrano-Puebla and Boya, 2016).

For visualization of LMP in MZ-54 cells, the pmCherry-GAL3 reporter was utilized (Papadopoulos et al., 2017). Under basal conditions, pmCherry-GAL3 (mCherry fused to galectin-3) is distributed throughout the cytoplasm, but translocates to lysosomal membranes upon their rupture, which can be seen by puncta formation. To this end, MZ-54 cells were stably transfected with pmCherry-GAL3, followed by treatment with loperamide or pimozide for 16 hours. Notably, MZ-54 cells showed almost no GAL3 puncta in vehicle-treated cells, whereas pimozide and loperamide treatment for 16 hours strongly increased the number of puncta per cell that were colocalized with LAMP1 (Figure 5.45). Unexpectedly, treatment with imipramine + ticlopidine did not result in GAL3 puncta formation (data not shown). In

addition, hardly any GAL3 puncta could be detected upon treatment with loperamide and pimozide followed by washout of the compounds for 24 hours, suggesting a functional recovery of these cells.

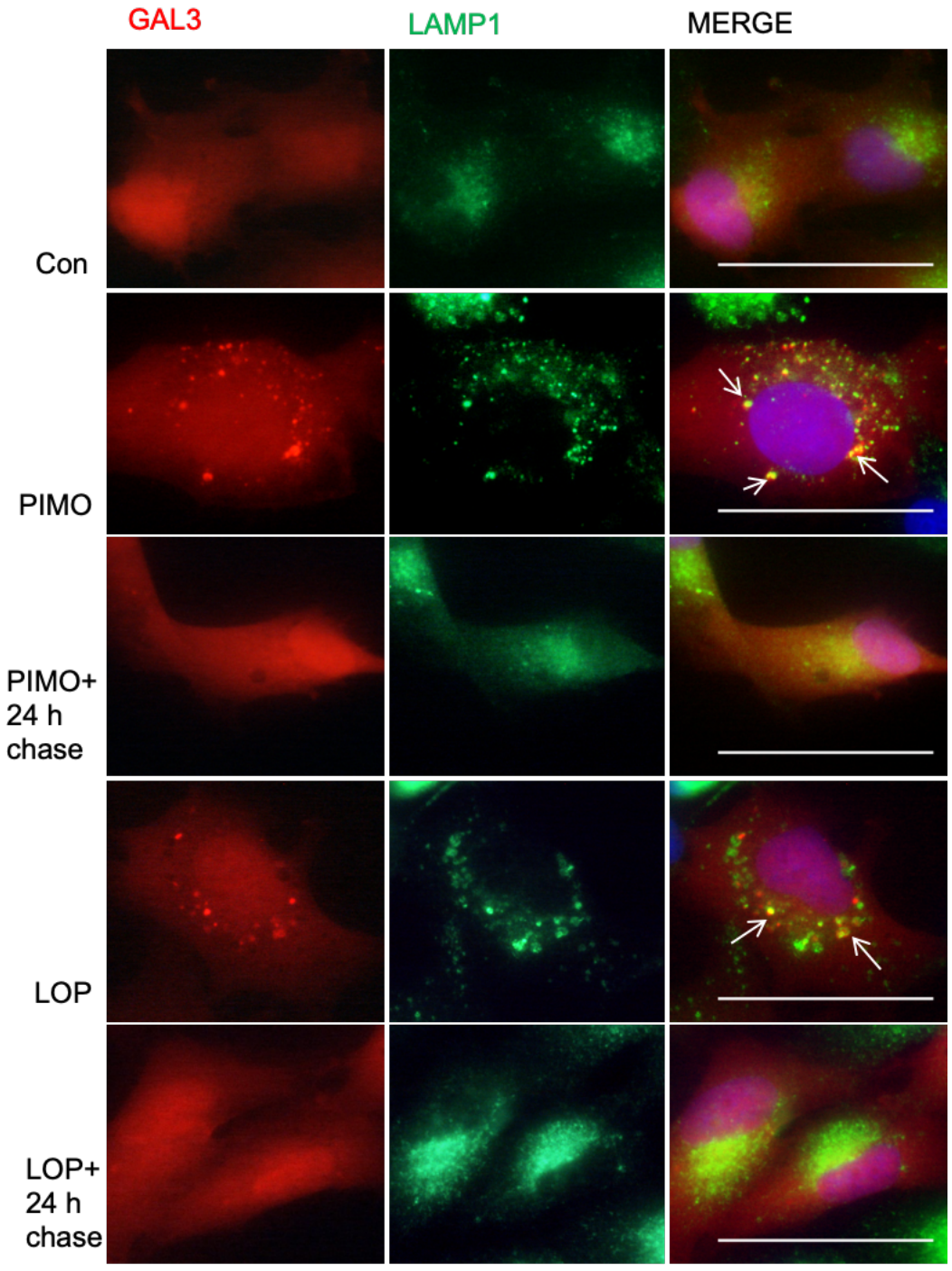

Figure 5.45. Loperamide and pimozide induce lysosomal rupture.
Microscopic determination of pmCherry-GAL3 puncta and colocalization with LAMP1 as an indicator of lysosomal membrane permeabilization (LMP) (depicted with arrows). MZ-54 cells were treated with 15 µM loperamide (LOP), 12.5 µM pimozide (PIMO) or DMSO (Con) for 16 h. For chase experiments, loperamide and pimozide was removed after 16 h and cells were incubated in fresh medium for additional 24 h. Images were taken at 60x magnification. Experiments were repeated three times and at least three different pictures were taken per experiment (scale bar=50 µM).

Next, the impact of autophagy deficiency on loperamide- and pimozide-induced GAL3 puncta formation was investigated by using MZ-54 *ATG5* and *ATG7* KO cells. Remarkably, *ATG5* and *ATG7* KO cells clearly showed less puncta formation after loperamide and pimozide treatment compared to WT cells (Figure 5.45, Figure 5.46).

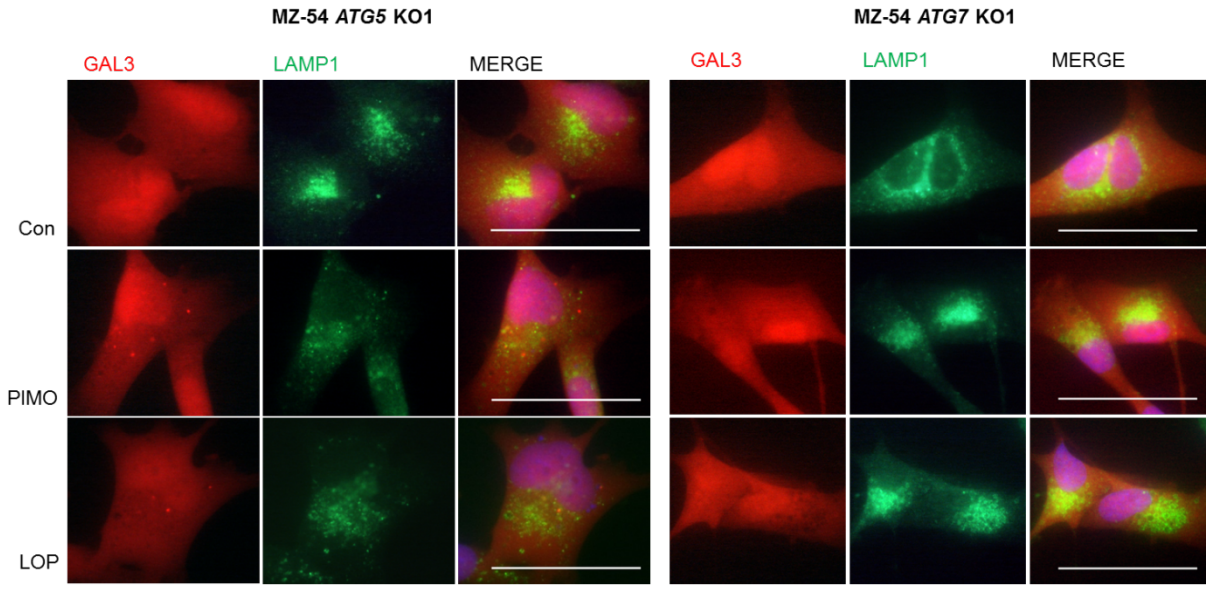

Figure 5.46. *ATG5* and *ATG7* knockout reduces pmCherry-GAL3 puncta formation upon pimozide and loperamide treatment.
Microscopic analysis of pmCherry-GAL3 puncta and colocalization with LAMP1 as an indicator for lysosomal membrane permeabilization. MZ-54 cells were exposed to 15 µM loperamide (LOP), 12.5 µM pimozide (PIMO) or DMSO (Con) for 16 h. Images were taken with 60x magnification. Experiments were repeated three times and at least three different pictures were taken per experiment (scale bar=50 µM).

Quantification of GAL3 puncta formation in MZ-54 WT cells compared to the respective *ATG5* and *ATG7* knockouts revealed that autophagy inhibition significantly decreased GAL3 puncta formation after loperamide and pimozide treatment for 16 hours (Figure 5.47A). Moreover, after washout of loperamide and pimozide and additional incubation for 24 hours in fresh medium without the drugs, the number of puncta was fully recovered to control conditions (Figure 5.47B). These findings lead to the assumption that hyperactivated autophagy promotes lysosomal damage and can be rescued by autophagy inhibition. Furthermore, the recovery from lysosomal damage over time might be attributed to selective degradation of ruptured lysosomes by lysophagy (Papadopoulos et al., 2017).

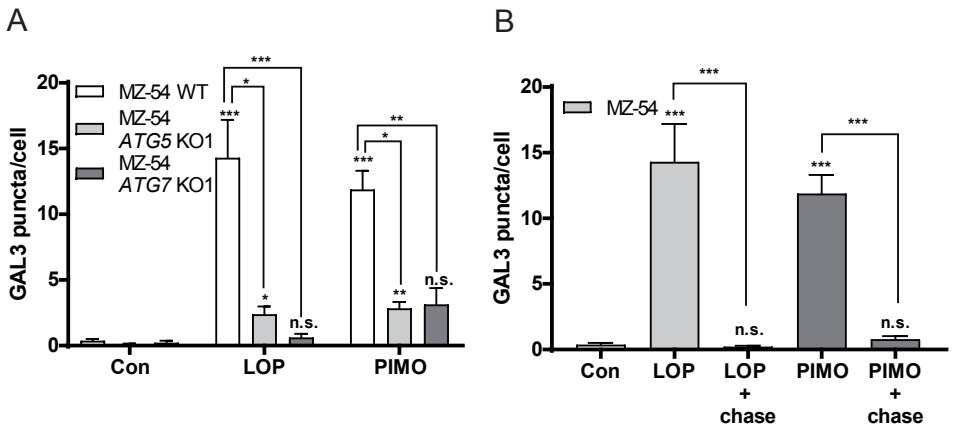

Figure 5.47. Quantification of pmCherry-GAL3 puncta per cell.
(A, B) The number of GAL3 puncta was determined by counting the puncta per cell of at least nine images from three independent experiments (at least three images per experiment) (see also Figure 5.45, Figure 5.46). MZ-54 WT, *ATG5* and *ATG7* KO cells were exposed to 15 µM loperamide (LOP) or 12.5 µM pimozide (PIMO) or DMSO (Con) for 16 h. For the chase experiments, loperamide and pimozide was removed after 16 h and cells were incubated in fresh medium for 24 h. Data represent mean + SEM. Statistical significances were calculated with a Kruskal-Wallis test ($P \leq 0.05$: *, $P \leq 0.01$: **, $P \leq 0.001$: ***, n.s.: not significant; difference from control or as indicated).

To verify the induction of LMP, lysosomal cathepsin release into the cytosol was assessed in cytosolic fractions of MZ-54 cells. Thereto, MZ-54 cells were exposed to imipramine + ticlopidine, loperamide and pimozide for 16 hours, and the cytosol was carefully fractionated by using a precisely titrated amount of digitonin. Subsequently, cathepsin B activity in the cytosolic fractions was quantified in a fluorescence-based activity assay as described in chapter 4.11. Strikingly, cathepsin B activity in the cytosol was strongly increased after exposure to all three compounds and knockout of *ATG5* was able to significantly reduce cathepsin B activity in all treatment settings (Figure 5.48A). Moreover, *ATG7* KO significantly reduced imipramine + ticlopidine-induced cathepsin B release, but only slightly diminished cathepsin B release by loperamide and pimozide. Because of the rescuing effects of loperamide and pimozide-induced lipid-ROS and cell death by α-tocopherol, it was suggested that the lipid-ROS scavenger might also promote lysosomal membrane stability, thereby reducing LMP. In line with the previous results, addition of α-tocopherol was able to significantly reduce loperamide and pimozide-driven cathepsin B release, but not imipramine + ticlopidine-triggered LMP (Figure 5.48B).

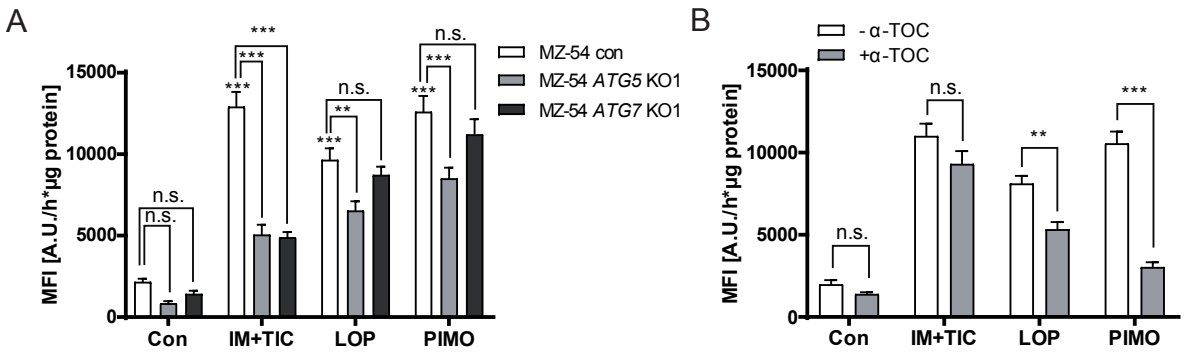

Figure 5.48. Assessment of lysosomal cathepsin B release into the cytosol upon treatment with imipramine + ticlopidine, loperamide and pimozide.
(A, B) Determination of cathepsin B in the cytosolic fraction by fluorescence-based quantification of cathepsin B activity. MZ-54 cells and the respective *ATG5* and *ATG7* KOs were treated with 20 µM imipramine + 75 µM ticlopidine (IM+TIC), 12.5 µM loperamide (LOP), 12.5 µM pimozide (PIMO) or DMSO (Con) for 16 h. (B) 100 µM α-tocopherol (α-TOC) was added to the MZ-54 cells 1 h prior to other treatments. The cytosol was extracted with digitonin. Data represent mean + SEM of four independent experiments with six replicates. Statistical significances were calculated with a two-way ANOVA ($P \leq 0.05$: *, $P \leq 0.01$: **, $P \leq 0.001$: ***, n.s.: not significant; difference from control or as indicated).

To validate the increase of cathepsins in the cytosol upon treatment with imipramine + ticlopidine, loperamide and pimozide, the cytosolic and organelle fractions (containing intact lysosomes) of MZ-54 WT and *ATG5* KO cells were analyzed by western blot (see chapter 4.10). LAMP1 staining could only be detected in the organelle fractions and not in the cytosol, indicating proper separation of the cytosolic fractions (Figure 5.49A). However, TUBA4A signal, which should be only detectable in the cytosolic fractions, was visible in all fractions, pointing to some residual cytosolic material in the organelle fractions.

Addition of imipramine + ticlopidine, loperamide and pimozide resulted in an increase of mature cathepsin B and D in MZ-54 WT cells, whereas MZ-54 *ATG5* KO cells did not show any changes of cathepsin B and D levels (Figure 5.49A). Semiquantitative analysis of the cathepsin B and D bands of MZ-54 WT cells revealed a pronounced, significant increase of cathepsin B and an average increase of cathepsin D that however was not significant due to high variation between the measurements (Figure 5.49B, D). In contrast, MZ-54 *ATG5* KO cells did not show any changes of the cathepsin B and D protein levels (Figure 5.49C, E). Taken together these results confirm the induction of autophagy-dependent LMP by imipramine + ticlopidine, loperamide and pimozide.

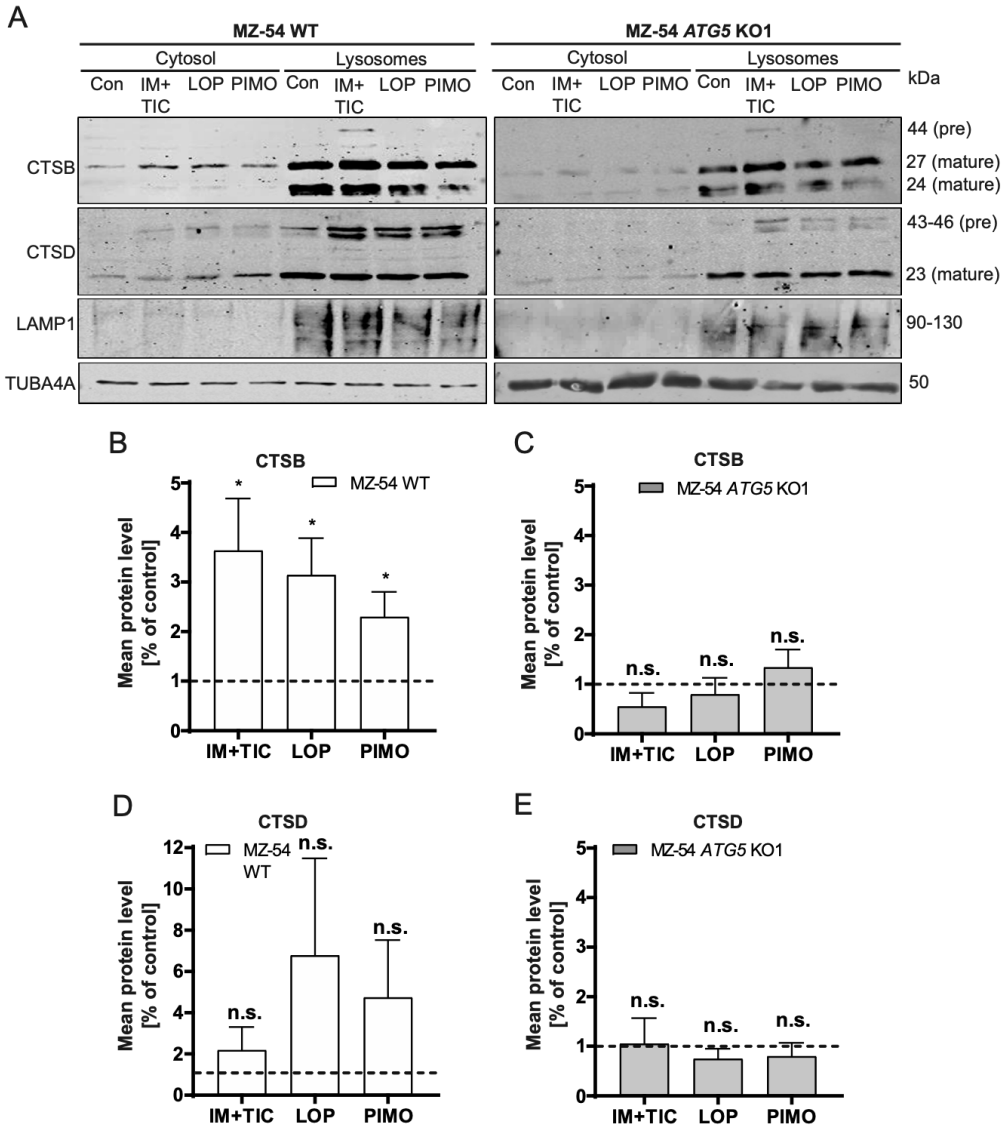

Figure 5.49. Determination of lysosomal cathepsin release into the cytosol by immunoblot analysis.
(A) Immunoblot analysis of CTSB (cathepsin B) and CTSD (cathepsin D) in the cytosolic fraction (extracted with digitonin) and the organelle fraction containing lysosomes. LAMP1 was used as control for the lysosomal part and TUBA4A was used as housekeeping protein for the cytosolic fraction. MZ-54 cells were treated with 20 µM imipramine + 75 µM ticlopidine (IM+TIC), 12.5 µM loperamide (LOP), 12.5 µM pimozide (PIMO) or DMSO (Con) for 16 h. (B-E) Quantification of the mean protein levels of CTSB (B, C) and CTSD (D, E) in the cytosol of MZ-54 WT cells and MZ-54 *ATG5* KO cells detected by immunoblot analysis. Data represent mean + SEM of three to five independent experiments. Statistical significances were calculated with a Student's t-test ($P \leq 0.05$: *, $P \leq 0.01$: **, $P \leq 0.001$: ***, n.s.: not significant; difference from control).

Rupture of the lysosomal membranes has detrimental effects on cellular survival, as it goes along with the release of lysosomal content into the cytosol, leading to cytosolic acidification and hydrolysis of the cytoplasmic material by cathepsin proteases (Serrano-Puebla and Boya, 2016). Accordingly, lysosomal membrane permeabilization is associated with lysosomal cell death (LCD). To investigate the induction of LCD by pimozide, loperamide, imipramine + ticlopidine and STF-62247 treatment for 40 hours, MZ-54 cells were exposed to

these compounds in the presence or absence of the cathepsin inhibitors E64D (inhibitor of cathepsin B, H and L) and pepstatin A (inhibitor of cathepsin D). Addition of E64D and pepstatin A diminished loperamide- and pimozide-induced cell death at all three concentrations and slightly impaired imipramine + ticlopidine-induced cell death at higher concentrations (Figure 5.50). In line with the previous results, cell death triggered by STF-62247 was not influenced by addition of cathepsin inhibitors, indicating that STF-62247-induced cellular demise does not rely on LMP and LCD (Figure 5.50). However, it should be noted that besides cathepsin B, H, L and D release, the release of other lysosomal hydrolases as well as cytosolic acidification may also account for cell death induction following LMP, thus limiting the rescue effects of E64D and pepstatin A (Kågedal et al., 2001; Kirkegaard and Jäättelä, 2009; Serrano-Puebla and Boya, 2016).

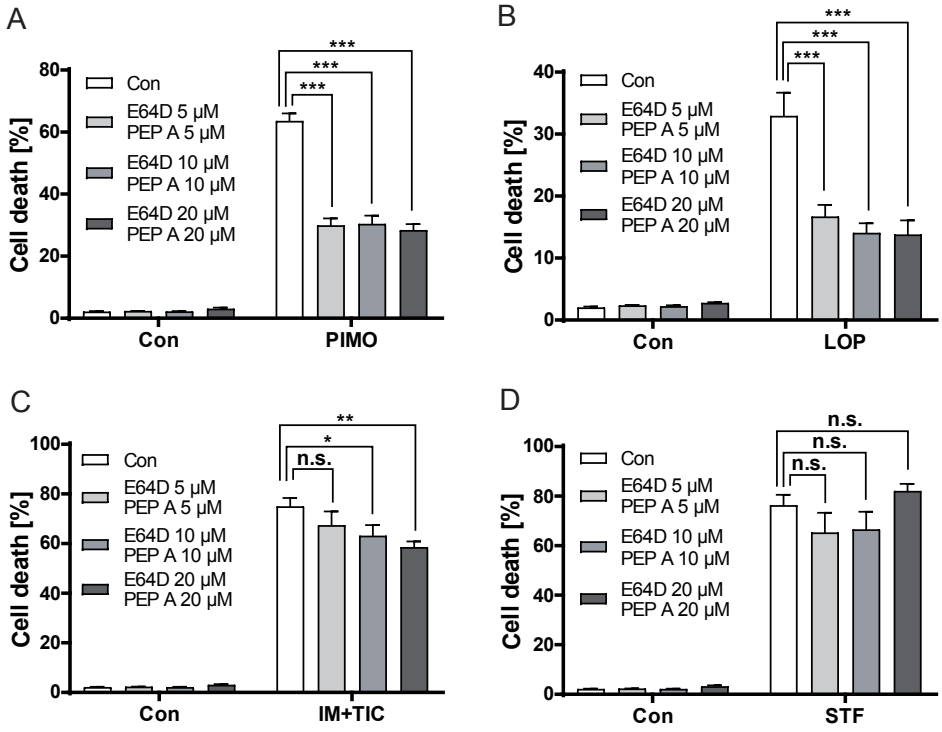

Figure 5.50. Investigation of lysosomal cell death induced by loperamide, pimozide, imipramine + ticlopidine and STF-62247.
(A-D) Assessment of cell death by flow cytometric analysis of APC-annexin V binding and PI uptake. MZ-54 cells were exposed to 12.5 µM pimozide (PIMO), 12.5 µM loperamide (LOP), 20 µM imipramine + 75 µM ticlopidine (IM+TIC) and 40 µM STF (STF) for 40 h alone or in combination with the cathepsin inhibitors E64D and pepstatin A (PEP A; 5 µM, 10 µM or 20 µM, respectively). E64D and pepstatin A were applied to the cells 2 h before the other treatments. DMSO was used as control (Con, 40 h). Data represent mean + SEM of at least three experiments with three replicates and 5,000 - 10,000 cells measured in each sample. Statistical significances were calculated with a two-way ANOVA (A-C) or Kruskal-Wallis test (D) ($P \leq 0.05$: *, $P \leq 0.01$: **, $P \leq 0.001$: ***, n.s.: not significant).

Moreover, the impact of autophagy inhibition on LCD was determined by using MZ-54 *ATG5* and *ATG7* KO cells (Figure 5.51). Similar to MZ-54 WT cells, cathepsin inhibition failed to rescue STF-62247-induced cell death, but significantly diminished imipramine + ticlopidine as well as loperamide-induced cell death. Strikingly, in contrast to MZ-54 WT cells, the rescue

effect of cathepsin inhibition on pimozide-induced cellular demise was completely abrogated in *ATG5* and *ATG7* KO cells, supporting the notion that autophagy inhibition impairs cathepsin release and subsequent LCD. However, the role of autophagy in loperamide and imipramine + ticlopidine-induced LCD needs to be further elucidated.

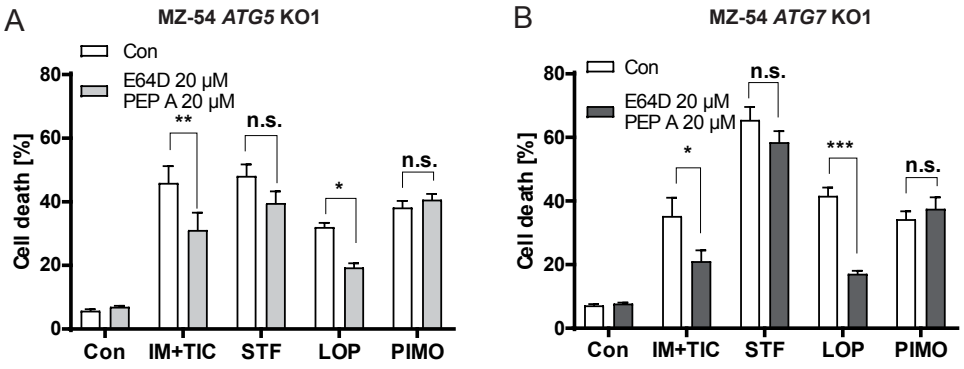

Figure 5.51. Assessment of lysosomal cell death induced by loperamide, pimozide, imipramine + ticlopidine and STF-62247 in *ATG5* and *ATG7* KO cells.
(A, B) Flow cytometric analysis of APC-annexin V-binding and PI uptake. MZ-54 *ATG5* (A) and *ATG7* KO cells (B) were exposed to 20 µM imipramine + 75 µM ticlopidine (IM+TIC), 40 µM STF (STF), 12.5 µM loperamide (LOP), 12.5 µM pimozide (PIMO) or DMSO (Con) for 48 h alone or in combination with 20 µM of the cathepsin inhibitors E64D and pepstatin A (PEP A). E64D and PEP A were added to the cells 2 h prior to the other treatments. Data represent mean + SEM of three experiments with three replicates and 5,000 - 10,000 cells measured in each sample. Statistical significances were calculated with a two-way ANOVA ($P \leq 0.05$: *, $P \leq 0.01$: **, $P \leq 0.001$: ***, n.s.: not significant).

5.12 Loperamide- and pimozide-induced lysophagy promotes cell survival and is dependent on VCP

In the experiments depicted in Figure 5.45 it was shown that the number of GAL3 puncta fully recovered to control conditions after treatment with the LMP inducers loperamide and pimozide and subsequent washout of the compounds for 24 hours. This recovery might be explained by selective degradation of damaged lysosomes via lysophagy (Papadopoulos and Meyer, 2017). To prove this hypothesis, MZ-54 cells stably transfected with pmCherry-GAL3 were exposed to loperamide and pimozide for 24 hours and subsequently stained with an antibody against LC3B for fluorescence microscopy. Interestingly, several pmCherry-GAL3 puncta colocalized with LC3B following loperamide and pimozide treatment, indicative of the degradation of ruptured lysosomes by autophagy (Figure 5.52).

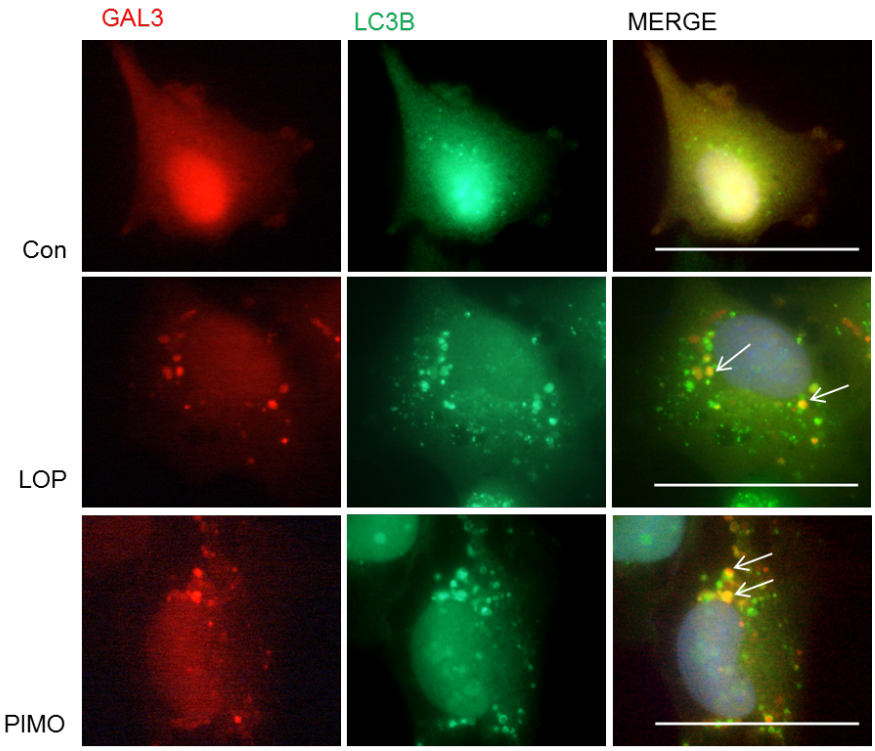

Figure 5.52. Loperamide and pimozide induce colocalization of LC3B and GAL3.
Microscopic analysis of pmCherry-GAL3 puncta and colocalization with LC3B (depicted with arrows). An amount of 15 µM loperamide (LOP), 15 µM pimozide (PIMO) or DMSO (Con) was applied to the MZ-54 cells for 24 h. Images were taken with 60x magnification. Three independent experiments were performed and at least three different pictures were taken per experiment (scale bar=50 µM).

However, investigation of lysophagy is complicated owing to the limited current knowledge about selective lysophagy receptors. Still, it has been recently reported that the AAA+-type ATPase VCP serves as a lysophagy receptor that is essential for cell survival after lysosomal damage (Papadopoulos et al., 2017). Therefore, *VCP* was depleted by siRNA-mediated knockdown to elucidate the putative role of lysophagy in the clearance of ruptured lysosomes upon loperamide and pimozide treatment. Both siRNAs against *VCP* effectively decreased VCP protein levels in MZ-54 cells (Figure 5.53).

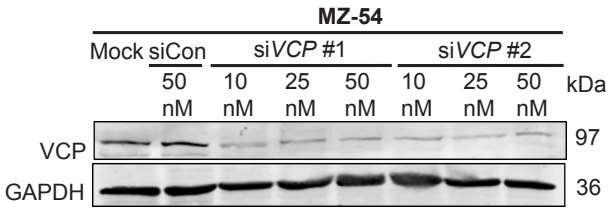

Figure 5.53. Determination of siRNA-mediated knockdown of *VCP*.
Immunoblot analysis of VCP and GAPDH (housekeeper) in MZ-54 cells following transfection of two different siRNAs against *VCP*. Cells were transfected with either si*VCP* #1 (10, 25 or 50 nM) or si*VCP* #2 (10, 25 or 50 nM). Universal negative control (siCon) was used at a concentration of 50 nM and Mock-transfected cells were only treated with transfection reagent. Cells were harvested 72 h after transfection. Experiments were repeated two times.

Moreover, the reduction of pmCherry-GAL3 puncta after pimozide washout was assessed in MZ-54 cells transfected with control siRNA and siRNA against *VCP*. In line with the putative role in lysophagy, cells with siRNA-mediated knockdown of *VCP* showed a higher number of GAL3 puncta per cell after 24 hours washout than cells treated with control siRNA (Figure 5.54).

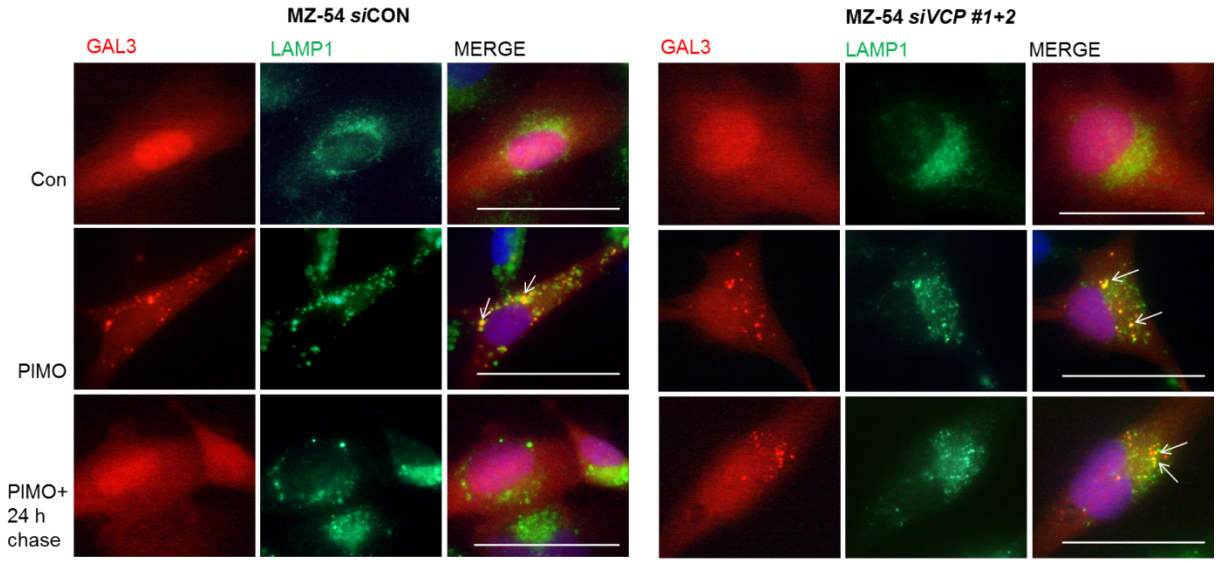

Figure 5.54. Knockdown of *VCP* impairs degradation of ruptured lysosomes after pimozide washout.
Microscopic analysis of pmCherry-GAL3 puncta and colocalization with LAMP1 as a marker for lysosomal membrane permeabilization (depicted with arrows). MZ-54 cells were treated with 15 µM pimozide (PIMO) or DMSO (Con) for 24 h. For chase measurements, pimozide was removed after 24 h treatment and cells were incubated in fresh medium for additional 24 h. Images were taken with 60x magnification. Experiments were repeated three times and at least three different pictures were taken per experiment (scale bar=50 µM).

Quantification of pmCherry-GAL3 puncta revealed a significant decrease of GAL3 puncta following pimozide washout in MZ-54 cells transfected with universal negative control siRNA (Figure 5.55). In contrast, siRNA-mediated knockdown of *VCP* prevented this decrease of pmCherry-GAL3 puncta. These results point to an essential role of VCP in the degradation of ruptured lysosomes.

To determine if *VCP* depletion also affects cell viability, MZ-54 cells were transfected with either control siRNA or siRNA against *VCP*, followed by treatment with loperamide or pimozide. In line with previously published data, *VCP* depletion further enhanced cell death by loperamide and pimozide, pointing to a pro-survival role of lysophagy after lysosomal rupture (Figure 5.55) (Papadopoulos et al., 2017).

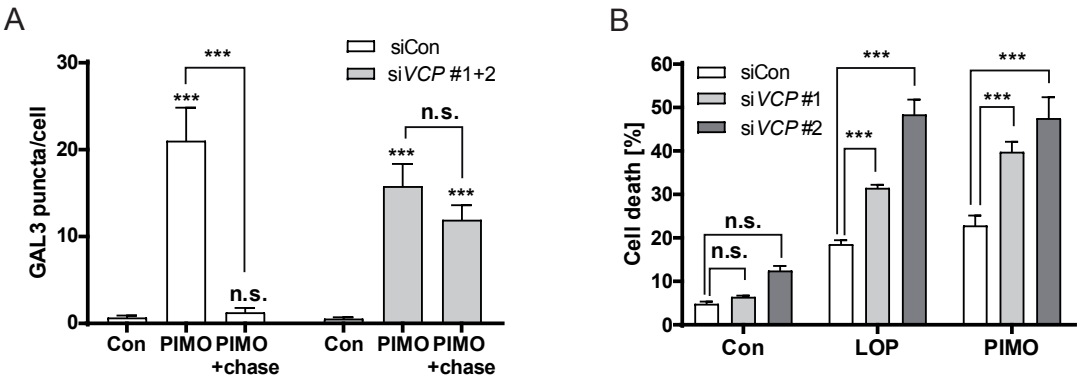

Figure 5.55. VCP depletion impairs degradation of ruptured lysosomes and promotes cell death.
(A) Quantification of pmCherry-GAL3 puncta/cell of MZ-54 cells transfected with two siRNAs against *VCP* (si*VCP* #1+2) or universal negative control (Con) (see Figure 5.54). The number of GAL3 puncta was calculated by counting the puncta/cell of at least three images per experiment. In total, three independent experiments were performed and the puncta of 11 - 23 cells were counted for each condition. Data represent mean + SEM. Statistical significances were calculated with a Kruskal-Wallis test ($P \leq 0.05$: *, $P \leq 0.01$: **, $P \leq 0.001$: ***, n.s.: not significant; difference from control or as indicated). (B) Monitoring cell death (only APC-annexin V-positive, only PI-positive and double-positive cells) by flow cytometry. MZ-54 cells were transfected with siRNA against *VCP* (25 nM si*VCP* #1 or si*VCP* # 2) or universal negative control (siCon, 25 nM) 48 h prior to treatment with 12.5 µM loperamide or 12.5 µM pimozide for 30 h. The bar chart represents mean + SEM from three independent experiments performed in triplicate (5,000 - 10,000 cells measured in each sample). Statistical significances were calculated using a two-way ANOVA ($P \leq 0.05$: *, $P \leq 0.01$: **, $P \leq 0.001$: ***, n.s.: not significant; difference from control or as indicated).

In conclusion, it was observed that selective lysophagy is induced following lysosomal damage by loperamide and pimozide. Moreover, depletion of the lysophagy receptor VCP enhanced cell death induced by loperamide and pimozide, suggesting that lysophagy is required for cell survival after LMP.

6 Discussion

The term “autophagic cell death” (ACD) describes a type of regulated cell death that relies on components of the autophagic machinery. Notably, autophagy is often activated during other types of cell death, but in most cases, it rather mediates cytoprotective effects in response to stress by degrading harmful material and providing basic cellular building blocks to overcome nutrient deprivation. However, a number of independent studies reported that in certain developmental, pathophysiological and drug-induced settings, autophagy directly promotes cell death, which can be prevented by genetic or pharmacological inhibition of autophagy (Kosta et al., 2004; Denton et al., 2009; Fulda and Kögel, 2015; Dasari et al., 2017; Segala et al., 2017).

Interestingly, most anticancer agents as well as radiation therapy have been described to induce autophagy. Yet, the impact of autophagy on cancer cell survival is complex, as it can exert either cytotoxic or cytoprotective effects. Therefore, it is of high interest for current cancer therapies to decipher the role of autophagy in every special context. Of note, especially apoptosis-refractory glioblastoma cells have been described to undergo ACD following treatment with different anticancer agents (Salazar et al., 2009; Voss et al., 2010; Shchors et al., 2015). In a recent study of our lab, AT 101, a natural compound from cotton seeds that is clinically developed for cancer treatment, has been shown to trigger ACD in glioma cells, which was accompanied by an early mitochondrial fragmentation, but no signs of apoptosis (Voss et al., 2010).

The first part of this thesis followed up the previous findings on AT 101-induced glioma cell death in order to investigate the putative role of mitochondrial damage in AT 101-triggered ACD. In the second part, the newly identified ACD inducers loperamide, pimozide and STF-62247 were analyzed concerning the induction of autophagy, cell death, and the involved mechanisms and signaling pathways.

6.1 AT 101-induced mitochondrial damage and mPTP opening in glioma cells

Similar to the mitochondrial uncoupler FCCP, AT 101 induced severe mitochondrial depolarization in three different glioma cell lines, MEF WT as well as MEF apoptosis-resistant *Bax Bak1* DKO cells, demonstrating that the decrease of mitochondrial membrane potentials occurs independent of the apoptosis machinery (Meyer et al., 2018). Furthermore, AT 101 triggered the opening of the mitochondrial permeability transition pore (mPTP), and inhibition of the mPTP using the VDAC and TSPO inhibitor olesoxime was able to diminish AT 101-induced cell death (Warnsmann et al., 2018). Consistent with these findings, further

studies during my master thesis on the ageing model *P. anserina*, MEF *Bax Bak1* DKO and U343 cells could demonstrate that AT 101 severely impairs mitochondrial respiration (Meyer, 2015; Warnsmann et al., 2018). However, while early studies on the mPTP suggested that TSPO, VDAC and ANT (adenine nucleotide translocator) are involved in mPTP formation, recent findings propose that the pore forms from the F_1F_O-ATP synthase (Bernardi and Di Lisa, 2015). Of note, it should be stressed that except for the crucial involvement of CYPD, the composition of the mPTP is still under intense investigation. Knockdown of any proteins that were supposed to constitute the mPTP failed to prevent mitochondrial permeability transition triggered by MPT-inducing stimuli such as Ca^{2+} ionophores and hydrogen peroxide in mouse knockdown models, which challenges the effects seen by olesoxime treatment in this study (Izzo et al., 2016). Nevertheless, it must be taken into account that the significance of these knockdown experiments is limited owing to the fact that many putative constituents of the mPTP exist in several isoforms (such as VDAC and ANT) and may functionally replace each other (Izzo et al., 2016). Moreover, it was shown by Warnsmann et al. that CYPD-mediated opening of the mPTP is responsible for AT 101-induced mitochondrial dysfunction in *P. anserina,* supporting the proposed effect of AT 101 on mPTP opening (Warnsmann et al., 2018).

6.2 The role of ATG5-dependent mitophagy induced by AT 101

Dysfunctional mitochondria are prone to get degraded by mitophagy. Thus, the possible induction of mitophagy upon AT 101 exposure was determined by several methods. Indeed, proteome analysis of AT 101-treated glioma cells revealed a strong and robust decrease of mitochondrial protein clusters. Consistent with these findings, electron microscopy of AT 101-treated U343 cells demonstrated the engulfment of mitochondria into autophagosomes, and immunoblot analysis of mitochondrial markers including VDAC1, COX4I1, TOMM20, and HSPD1 confirmed the significant reduction of mitochondrial proteins (Meyer et al., 2018).

To further validate the role of mitophagy in AT 101-induced cell death, CRISPR/Cas9 knockouts of the core autophagy gene *ATG5* were generated in two different glioma cell lines. Consistent with the induction of mitophagy, knockout of *ATG5* blocked the decrease of mitochondrial protein markers upon AT 101 treatment. Additionally, the induction of mitophagy upon AT 101 treatment was confirmed by flow cytometric analysis of MTG and mito-mKeima as well as qRT-PCR of mitochondrial versus nuclear DNA. Strikingly, a pronounced uptake of mitochondria into lysosomes could be already detected after 6 hours treatment, suggesting mitophagy is directly affected by AT 101 and precedes cell death. In all three experimental approaches, mitophagy could be attenuated by pharmacologic autophagy blockage using wortmannin, bafilomycin A_1, and chloroquine, or by genetic autophagy

inhibition using *ATG5* KO cells, confirming that mitochondrial degradation relies on the autophagic machinery (Meyer et al., 2018).

Despite these observations, the role of ATG5 in mitophagy is controversially discussed. On the one hand, it has been described that mitophagy can still be efficiently induced in *ATG5* KO mouse embryonic fibroblasts, thus indicating an ATG5-independent type of mitophagy (Hirota et al., 2015). On the other hand, Rao et al. reported that mitophagy is impaired in KRas; *ATG5*fl/fl mice (Rao et al., 2014). Additionally, *Leishmania major* lacking *ATG5* showed an increase of mitochondrial mass along with reduced mitochondrial membrane potentials and elevated levels of ROS, indicative of blocked mitophagy (Williams et al., 2012).

The results of this thesis point to an ATG5-dependent type of mitophagy induced by AT 101. However, since *ATG5* KO was not able to completely block mitophagy, it is supposed that other ATG5-independent forms of mitophagy may take place in parallel. Interestingly, an alternative mitophagy pathway that requires RAB9 for autophagosomal degradation of mitochondria and is independent of ATG5, ATG7, ATG12 and LC3 has been recently described (Hirota et al., 2015; Huang et al., 2018). Moreover, it was found that budding of mitochondria-derived vesicles and subsequent direct transport to lysosomes/peroxisomes allows the ATG5-independent degradation of smaller mitochondrial parts. This process was described as defense mechanism for cells with huge energy requirements like neurons and cardiomyocytes, which cannot tolerate the removal of a large portion of damaged mitochondria (Neuspiel et al., 2008; Roberts et al., 2016). Accordingly, these described mitophagy mechanisms might accompany ATG5-dependent mitophagy following AT 101-treatment and may explain the confined rescue effects of the *ATG5* knockout.

6.3 Hyperactivated autophagy following AT 101 treatment promotes cell death and may be beneficial for cancer treatment

In this study, the induction of autophagic cell death (ACD) upon AT 101 treatment was confirmed in the glioma cell lines MZ-54 and U343 by using *ATG5* KO cells compared to wild type cells, which is in accordance with previous findings showing that knockdown of *ATG5*, *ATG7* or *BECN* rescues AT 101-induced cell demise (Voss et al., 2010; Meyer et al., 2018). Of note, Voss et al. demonstrated that human glioma cells are more sensitive to AT 101 treatment than astrocytes. As many glioma cells are highly resistant against caspase-dependent apoptosis and the majority of chemotherapeutics target the apoptotic pathway in order to kill tumor cells, there is an urgent need to explore new cell death mechanisms to overcome cell death resistance (Kögel et al., 2010). To date, several studies revealed that glioma cells undergo an autophagy-dependent type of cell death upon treatment with a

variety of substances, including cannabinoids, imipramine + ticlopidine and ceramide (Salazar et al., 2009; Vara et al., 2011; Shchors et al., 2015; Wang et al., 2017). It is assumed that ACD relies on the induction of continuous, hyperactivated bulk autophagy beyond a point of no return (Das et al., 2012; Fulda and Kögel, 2015; Bialik et al., 2018). Similar threshold effects have been reported for other stress responses, e.g. for the unfolded protein response that primarily functions as a pro-survival stress adaptation to alleviate ER stress by reducing the amount of misfolded proteins in the ER lumen. However, prolonged ER stress switches to pro-apoptotic signaling (Urra et al., 2013). Moreover, TP53 has been observed to play a dual role in pro-survival and pro-death mechanisms. On the one hand, TP53 contributes to cellular survival under mild metabolic stress by regulating metabolism and reducing ROS production. But on the other hand, under persistent stress conditions, TP53 transcriptionally activates the expression of several pro-apoptotic BCL2 family proteins, thereby promoting cell death (Kruiswijk et al., 2015). According to these threshold effects, the extent and duration of autophagy is supposed to be critical for its pro-survival versus pro-death function.

6.4 The pro-death function of selective mitophagy induced by AT 101

In the present study, different mitophagy receptors were investigated to elucidate the putative role of mitophagy in ACD. Notably, the mitophagy receptors BNIP3 and BNIP3L were strongly upregulated upon AT 101 exposure, and depletion of both receptors was able to diminish mitophagy as well as cell death. Based on these observations, it is supposed that AT 101 triggers selective, BNIP3-BNIP3L-dependent mitophagy, which has a cell death promoting effect in glioma cells (Meyer et al., 2018) (Figure 6.1).

Like autophagy, selective mitophagy is generally considered as a pro-survival mechanism that allows the removal of damaged or superfluous mitochondria. In line with the threshold effects discussed above, there is a growing body of evidence showing that the selective removal of mitochondria can also be lethal when it exceeds a certain level (Kim et al., 2007; Sentelle et al., 2012; Wang et al., 2014). While moderate degradation of old and damaged mitochondria is of great importance for cellular homeostasis, excessive mitophagy has been described to trigger cell death in various cancer cell types: In melanoma cells it was shown that the orphan nuclear receptor NUR77 translocates to mitochondria by interaction with BNIP3L, thereby inducing mPTP-opening and mitochondrial depolarization, which was associated with massive mitochondria clearance and cell death (Wang et al., 2014). These observations are in accordance with the AT 101-induced mitochondrial depolarization and mPTP-opening observed in our study and by Warnsmann et al. (Warnsmann et al., 2018). Moreover, Sentelle and coworkers demonstrated that C18-ceramide induces lethal

mitophagy in head and neck squamous cell carcinoma cell lines by anchoring autophagolysosomal LC3B-II to the mitochondrial membrane (Sentelle et al., 2012). Furthermore, sodium selenite was reported to induce mitophagic cell death in glioma cells, which was accompanied by superoxide anion generation and mitochondrial damage (Kim et al., 2007). Collectively, these findings support the potential lethal effect of hyperactivated mitophagy as observed in this study.

Of note, in contrast to the initial idea of Otto Warburg, describing that cancer cells harbor defective mitochondria and thus predominantly rely on glycolysis to produce ATP, recent studies demonstrated that cancer cell mitochondria are mainly not defective. Instead, mitochondrial metabolism is reprogrammed to synthesize macromolecules essential for cancer cell proliferation (Ward and Thompson, 2012). According to these considerations, overactivation of selective mitophagy might be a promising approach for treatment of GBM.

6.5 The role of BNIP3 and BNIP3L in selective mitophagy and cell death

Hitherto, the Parkin-PINK1 pathway is considered as the key regulator and best-known type of selective mitophagy. Though, in the recent years, several studies demonstrated the existence of functional mitophagy in the absence of Parkin and identified additional mitophagy receptors including BNIP3L, BNIP3, FUNDC1 and AMBRA1 (Villa et al., 2018). In accordance to these studies, the induction of selective BNIP3L- and BNIP3-dependent mitophagy upon AT 101 treatment was observed in glioma cells with low or absent Parkin protein levels in this thesis (Yeo et al., 2012; Lin et al., 2015; Meyer et al., 2018).

The transmembrane proteins BNIP3 and BNIP3L are closely related and possess approximately 50% identical amino acids (Zhang and Ney, 2009). Notably, depletion of BNIP3 and BNIP3L in various cancer types has been linked to increased metastasis and tumor progression (Drake et al., 2017). Both proteins are key mediators of hypoxia-induced mitophagy. They are located in the outer mitochondrial membrane and directly interact with LC3-related molecules associated to the phagophores, thereby targeting mitochondria to the autophagosomes for degradation (Zhang and Ney, 2009). Additionally, both proteins are categorized as BH3-only proteins and have been implicated in cell death (Hardwick and Youle, 2009; Zhang and Ney, 2009). However, a recent study demonstrated that the BH3 domain of BNIP3 and BNIP3L is rather weakly conserved (Chourasia et al., 2015). Moreover, both proteins failed to induce prominent cytochrome c efflux, and elevated expression of BNIP3 and BNIP3L did not directly result in cellular demise, suggesting that their classification as proapoptotic BH3-only proteins is not generally linked to cell death induction (Kim et al., 2006; Chourasia et al., 2015). In line with the observed mPTP opening upon AT 101-treatment in this thesis, BNIP3 and BNIP3L are atypical BH3-only proteins that have

been described to facilitate mPTP-driven cell death, which is associated with loss of the mitochondrial membrane potential (Zhang and Ney, 2009).

Interestingly, BNIP3 has been linked to mitochondrial fission due to positive interaction with the fission-regulator DAPK2 and negative regulation of the fusion-regulator OPA1 (mitochondrial dynamin like GTPase) (Chourasia et al., 2015). Accordingly, the overexpression of BNIP3 upon AT 101 treatment observed in this study might explain the early mitochondrial fragmentation induced by AT 101, possibly mediated by DAPK2. Furthermore, BNIP3 has been implicated in ACD in glioma cells upon exposure to C2-ceramide and arsenic trioxide (Daido et al., 2004; Kanzawa et al., 2005). However, the impact of BNIP3 depletion on AT 101-induced mitophagy and cell death was smaller than the effects of BNIP3L depletion, and knockdown of both did not further enhance cellular survival compared to BNIP3L knockdown alone (Meyer et al., 2018). Therefore, it is assumed that BNIP3L plays the predominant role in inducing lethal mitophagy upon AT 101 treatment in glioma cells.

Indeed, two putative signaling pathways have been described for the induction of BNIP3L-dependent mitophagy: 1) BNIP3L may trigger mitochondrial depolarization, which in turn induces mitophagy. 2) A second model assumes that BNIP3L functions as an adaptor protein and thus is able to directly recruit autophagosomes to the mitochondria independent of mitochondrial depolarization (Zhang and Ney, 2009). In this study, mitochondrial depolarization preceded mitophagy, indicating that elevated BNIP3L levels may promote dissipation of the mitochondrial membrane potential, which in turn triggers excessive mitophagy (Meyer et al., 2018). Similar to the reported induction of ACD by BNIP3, BNIP3L may promote ACD by permanent hyperactivation of mitophagy. However, the exact mechanisms how BNIP3L and BNIP3 are contributing to glioma cell death need to be further elucidated.

6.6 The role of HMOX1 in death induced by AT 101

Global proteome analysis of the AT 101-treated glioma cell lines U87MG and U343 in this thesis revealed an upregulation of HMOX1 in both cell lines (Meyer et al., 2018). HMOX1 is an inducible, catalytic enzyme, which exerts the breakdown of prooxidant heme into carbon monoxide, iron and biliverdin (Constantin et al., 2012). Additionally, HMOX1 was found to be induced upon chemical and physical stress in a variety of cell culture studies. In that context, HMOX1 has been shown to confer protective effects, including modulation of the inflammatory response and apoptosis (Ryter et al., 2006; Constantin et al., 2012). In addition, the HMOX1 end-products carbon monoxide and biliverdin have also been described to exert protective effects upon inflammatory stress or tissue injury (Otterbein et al., 2000; Nakao et

al., 2005). Therefore, HMOX1 is generally considered as a cytoprotective molecule due to the detoxification of prooxidant heme as well as its ability to cope with cellular stress.

Despite the general cytoprotective role of HMOX1, cellular demise of AT 101-treated glioma cells was accompanied by upregulation of HMOX1 levels in this study. Moreover, siRNA-mediated depletion of HMOX1 diminished AT 101-induced mitophagy and cell death, suggesting that HMOX1 overactivation might actually promote the induction of lethal mitophagy (Meyer et al., 2018).

Recently, a putative role of HMOX1 in the regulation of autophagy and mitophagy has emerged, supporting the observations of HMOX1-induced mitophagy upon AT 101 exposure in this study. Several studies reported that upregulation of autophagy by HMOX1 was associated with either cytoprotective or cytotoxic effects, depending on the cellular and pathological context. A cytoprotective role of HMOX1-induced autophagy was found in hepatocytes in response to sepsis and lipopolysaccharides. In that context, pharmacological inhibition of autophagy using 3-methyladenine increased apoptosis (Carchman et al., 2011). Furthermore, mitophagy induction of HMOX1 has been described to protect cardiomyocytes from cell death due to maintenance of an effective mitochondrial quality control (Suliman et al., 2017). In contrast, it was shown that HMOX1 translocates to mitochondria under hypoxic conditions, leading to elevated ROS production, decreased cytochrome c oxidase activity, and mitophagy induction in macrophages (Bansal et al., 2014). In another study, upregulated HMOX1 has been reported to trigger mitophagy and sequestration of redox-active iron in Alzheimer and Parkinson disease, which was associated with oxidative stress and opening of the mitochondrial permeability transition pore (mPTP) (Zukor et al., 2009). In line with this notion, the increase of HMOX1 levels might be linked to the mPTP opening upon AT 101 treatment observed in this thesis.

6.7 Involvement of additional cell death mechanisms in AT 101-induced cell demise

In this study, depletion of ATG5, BNIP3, BNIP3L and HMOX1 only partially rescued glioma cells from AT 101-mediated lethal mitophagy, indicating that additional cell death routes may be activated in parallel (Meyer et al., 2018). However, AT 101-induced cell death occurred without major caspase activation and cytochrome c release, which argues against ongoing apoptosis (Voss et al., 2010). Additionally, the ferroptosis inhibitor ferrostain-1 failed to reduce glioma cell death following AT 101 treatment. Another putative cell death type of emerging interest is necroptosis, which describes a type of regulated cell death that relies on the activation of RIPK3 and MLKL, and in some settings on RIPK1 (Galluzzi et al., 2018). Recently, it was shown that RIPK1 gets activated during extracellular matrix detachment and

triggers mitophagy induction, leading to reduced NADPH production, subsequent elevation of ROS levels and non-apoptotic cell death (Hawk et al., 2018). Nevertheless, we found that inhibition of RIPK1 by necrostatin-1 was not able to reduce AT 101-mediated cell death. Moreover, it is worth mentioning that RIPK3 expression was not detectable in all three investigated glioma cell lines (data not shown), indicating that glioma cells are unable to undergo necroptosis.

Of note, AT 101 is categorized into the class of BH3-mimetics, which are small molecules capable of mimicking BH3-only proteins, thereby promoting apoptosis through antagonization of antiapoptotic BCL2 proteins (Lian et al., 2011). However, only the highly selective BH3 mimetics (ABT-199, ABT-737) seem to act as bona fide BCL2 inhibitors, while several putative BH3 mimetics have been described to induce cell death primarily via alternative mechanisms (Soderquist and Eastman, 2016). In agreement with these considerations, AT 101 failed to induce apoptosis in glioma cells (Voss et al., 2010). Furthermore, AT 101 has been shown to trigger cell death in *P. anserina*, which lacks the expression of BCL2, indicating that the effect of AT 101 on mitochondrial damage and subsequent cell death are independent of its role as a BH3 mimetic (Warnsmann et al., 2018).

Still, AT 101 induced severe mitochondrial damage and opening of the mPTP, which was accompanied by mitochondrial depolarization and impaired respiration (Warnsmann et al., 2018). These findings suggest that mitochondrial damage and mPTP opening could be the key drivers of AT 101-induced cell death. Several cell death effectors have been described to participate in mPTP-driven cellular demise, including pro-apoptotic factors such as cytochrome C, AIF (apoptosis-inducing factor), SMAC (second mitochondria derived activator of caspases)/DIABLO (direct IAP-binding protein with low PI) and endonuclease G (Bonora and Pinton, 2014), but also non-caspase proteases such as calpains (Smith et al., 2012) and cathepsins (Mrschtik and Ryan, 2015). Additionally, mPTP-driven necrosis has been added to the expanding list of regulated forms of cell death, encompassing rapid mitochondrial depolarization, osmotic breakdown of both mitochondrial membranes and subsequent cell death (Galluzzi et al., 2018). Based on these considerations, it is supposed that AT 101-induced lethal mitophagy/autophagy is accompanied by mPTP-driven cell damage, culminating in cellular demise with necrotic features (Figure 6.1).

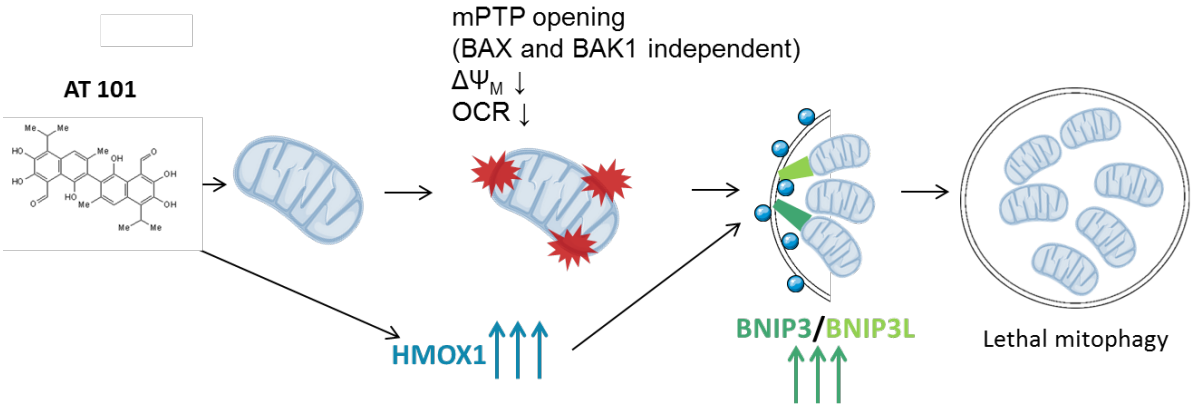

Figure 6.1. Hypothetical model of AT 101-induced lethal mitophagy.
AT 101 directly acts on mitochondria by opening of the mPTP, which is linked to mitochondrial depolarization (ΔΨM ↓) and impaired respiration (OCR; oxygen consumption rate). Subsequently, mitochondria are degraded by mitophagy to prevent damage-induced cytotoxicity and ROS generation. In parallel, AT 101 strongly enhances the protein levels of HMOX1 and the selective mitophagy receptors BNIP3 and BNIP3L, thereby further promoting mitophagy. Therefore, it is proposed that HMOX1 induction and mitochondrial damage synergize to promote hyperactivated, selective mitophagy and subsequent cell death in glioma cells, which is accompanied by parallel mPTP-driven cellular demise. (modified from Servier Medical Art, licensed under a Creative Common Attribution 3.0 Generic License. http://smart.servier.com/.)

6.8 Determination of ACD induction following loperamide, pimozide and STF-62247 treatment by using *ATG5* and *ATG7* knockout models

In addition to AT 101, an increasing number of compounds were found to trigger an autophagy-dependent type of cell death in different cancer cell models in the recent years (Salazar et al., 2009; Shchors et al., 2015; Dasari et al., 2017; Segala et al., 2017). However, the functional involvement of autophagy in the effect of these compounds is highly dependent on the cell type, as several of these compounds failed to induce ACD in the glioma cell lines used in this study (data not shown). Nevertheless, ACD induction following treatment with the antidepressant imipramine and the anticoagulant ticlopidine, which has recently been described to efficiently induce ACD in glioma cells, could be confirmed in this thesis (Shchors et al., 2015). Accordingly, this combination treatment served as a reliable positive control for ACD in the experiments performed in this study.

To investigate new inducers of ACD, a cell death screen of the Enzo Screen-Well™ autophagy library was performed using MZ-54 WT compared to *ATG5* and *ATG7* KO cells (Zielke et al., 2018). The screen revealed three hit compounds, loperamide, pimozide and STF-62247, and significant induction of ACD by these drugs was validated in this thesis by using three different *ATG5* and *ATG7 KO* cell lines. In addition, an increase of the autophagic flux by these compounds was confirmed in several experiments, including immunoblot analysis of LC3B, fluorescence microscopy, and flow cytometric measurements with the fluorescent probe pMRX-IP-GFP-LC3-RFP-LC3ΔG. In line with these findings, the

study of Zielke et al. demonstrated that imipramine + ticlopidine, loperamide, pimozide and STF-62247 all failed to induce other well-known types of regulated cell death, including apoptosis, necroptosis and ferroptosis, supporting the important role of ACD in cell demise by these drugs (Zielke et al., 2018). Moreover, in contrast to AT 101, these drugs failed to induce mitochondrial damage (data not shown). Still, autophagy inhibition was not able to fully rescue cell death induced by these compounds, suggesting the participation of other cell death modalities.

In addition, it is worth mentioning that autophagy inhibition has been associated with deregulation of other cellular stress responses besides ACD. Of note, it has been previously reported that autophagy deficiency may induce the activation of stress response genes such as NFE2L2 in a SQSTM1-dependent manner, which may lead to an increase in general cell death resistance (Lau et al., 2010; Lau et al., 2013; Jiang et al., 2015). The autophagy adaptor SQSTM1 is selectively incorporated into autophagosomes upon binding to LC3B and subsequently degraded during the autophagic process (Komatsu et al., 2012; Klionsky et al., 2016). Therefore, autophagy inhibition should go along with increased SQSTM1 levels, which is linked to prolonged NFE2L2 activation (Jiang et al., 2015). The NFE2L2-KEAP1 axis controls the expression of various cytoprotective proteins, thereby regulating the cellular defense mechanism against oxidative stress.

Based on these considerations, upregulation of stress response genes in *ATG5* and *ATG7* KO MZ-54 cells might impair cell death in general, thereby possibly affecting the interpretation of the results of this study. However, autophagy inhibition by *ATG5* and *ATG7* KO failed to increase the expression of *NFE2L2*, *KEAP1*, *SQSTM1*, as well as antiapoptotic *BCL2* family members compared to WT cells, indicating that cell death resistance pathways are not influenced by autophagy inhibition in MZ-54 cells.

In contrast, other studies demonstrated that autophagy inhibition by *ATG5* KO was associated with upregulated apoptotic cell death, e.g. by increased caspase expression and accumulation of cytotoxic products (Garcia-Garcia et al., 2013; Lin et al., 2014; Shroff and Reddy, 2018). However, cell death induced by the common apoptosis inducer staurosporine was not affected by genetic autophagy inhibition in this thesis. Collectively, these findings suggest that the impact of autophagy inhibition on apoptosis is dependent on the cellular context and the cytotoxic stimulus. In case of the present study, autophagy depletion by *ATG5* and *ATG7* KO in MZ-54 cells was neither linked to a higher vulnerability to cell death, nor to general cell death resistance.

6.9 Implication of upstream autophagy regulators in loperamide-, pimozide- and STF-62247-induced autophagy and ACD

The PI3K-AKT1 and the AMPKalpha pathways play an important role in controlling autophagy, mainly via regulation of the major autophagy inhibitor mTORC1 (Manning and Cantley, 2007; Gwinn et al., 2008; Behrends et al., 2010). While sensing of growth factors induces AKT1 activation/phosphorylation, thereby inhibiting autophagy, AMPKalpha gets phosphorylated upon a rise in the AMP/ATP ratio, which subsequently promotes autophagy induction (Endo et al., 2006; Alers et al., 2012).

In this study, imipramine + ticlopidine, loperamide, pimozide and STF-62247 induced the downregulation of phospho-AKT1 and upregulation of phospho-AMPKalpha, both consistent with the induction of autophagy. In agreement with these findings, all four compounds have been shown to dephosphorylate mTOR, implying that autophagy induction by these drugs is at least partially dependent on impaired mTOR signaling, a well-known negative regulator of autophagy (Goberdhan et al., 2016). However, inhibition of mTOR with rapamycin was insufficient to induce cell death in MZ-54 glioma cells, indicating that other key mechanisms must be involved in the induction of ACD by imipramine + ticlopidine, loperamide, pimozide and STF-62247 (Zielke et al., 2018).

Moreover, the cAMP signaling pathway plays an important role in the regulation of autophagy. On the one hand, treatment with the ACD positive control imipramine + ticlopidine leads to highly elevated cAMP levels, resulting in activation of the EPAC1/2 signaling pathway and massive autophagy (Shchors et al., 2015). On the other hand, downregulation of cAMP has also been linked to autophagy induction (Williams et al., 2008). In that context, Ca^{2+}-activated calpains have been shown to inhibit autophagy by increasing cAMP levels, thus, Ca^{2+} channel inhibitors like loperamide potentially counteract this autophagy blockage (Rubinsztein et al., 2012). However, the voltage-gated P/Q-type Ca^{2+} channel inhibitor verapamil completely failed to induce glioma cell death, suggesting that the autophagy-inducing effect of calcium channel inhibition alone is not able to trigger ACD.

6.10 Pimozide-, but not loperamide-induced ACD is dependent on receptor-mediated signaling

Loperamide and pimozide are approved clinical drugs that have been described to exert their therapeutic effects via receptor-mediated signaling pathways. Of note, besides inhibiting voltage-gated P/Q-type Ca^{2+} channels, loperamide also acts as an agonist of the mu-opioid receptor (DeHaven-Hudkins et al., 1999). Still, in the present study, the mu-opioid receptor

agonist endomorphin-1 failed to induce any cytotoxic effects in MZ-54 cells, implying that loperamide-induced cell death relies on other, receptor-independent mechanisms.

The antipsychotic drug pimozide has been reported to antagonize the dopamine D2/D3/D4 receptor subfamily and the 5-HT7 serotonin receptor (Freedman et al., 1994; Elmaci and Altinoz, 2018). Interestingly, the DRD2 signaling pathway has been described to promote tumor growth in patient-derived-GMB lines and pancreatic cancer (Li et al., 2014; Jandaghi et al., 2016). Moreover, the 5-HT7 receptor is commonly overexpressed in glioblastoma cells, and antagonization of this pathway may contribute to GBM treatment due to inhibition of the ERK1/2 pathway and IL-6 (interleukin-6) synthesis (Kast, 2010; Elmaci and Altinoz, 2018). In the present study, it was observed that inhibition of 5-HT7 receptor signaling by pimozide participates in autophagy activation and subsequent ACD. Nevertheless, administration of the 5-HT7 receptor agonist AS 19 was not able to fully rescue pimozide-induced cellular demise, indicating that pimozide partially exerts its effects in a 5-HT7 receptor-independent fashion. Still, this newly identified effect of 5-HT7 receptor antagonists in the induction of autophagy and ACD might be of potential clinical interest for the usage of pimozide and other antipsychotics as repurposed drugs for glioma therapy.

6.11 Loperamide and pimozide impair cholesterol trafficking and induce lipotoxicity in glioma cells

The global proteomic analysis of imipramine + ticlopidine-, loperamide-, pimozide- and STF-62247-treated MZ-54 cells revealed a significant upregulation of several proteins involved in lipid- and cholesterol metabolic processes. Furthermore, this study observed the strong accumulation of cholesterol in the lysosomal compartment of MZ-54 cells exposed to all four compounds, suggesting a severe blockage of cholesterol trafficking. In agreement with these data, antipsychotic drugs such as imipramine and pimozide have been reported to increase the expression of lipogenic genes, which results from impaired transport of lipoprotein-derived cholesterol from the lysosomes to the ER (Kristiana et al., 2010; Wiklund et al., 2010). Under normal conditions, cholesterol is esterified in the ER and suppresses sterol regulatory element binding proteins (SREBP), the master transcriptional regulators of lipid metabolism. Consequently, defective cholesterol transport leads to transcriptional upregulation of genes involved in the lipid metabolism.

Interestingly, cholesterol has been described to negatively regulate autophagy via mTOR and AKT1 (Xu et al., 2010). In line with these observations, this study demonstrated that blockage of cholesterol transport by imipramine + ticlopidine, loperamide and pimozide was associated with impaired AKT1 signaling as well as autophagy induction in case of loperamide and pimozide, which could be reverted by addition of water-soluble cholesterol

(complexed with methyl-β-cyclodextrin). These findings emphasize the importance of intact cholesterol trafficking for the regulation of autophagy.

Imipramine, loperamide and pimozide are cationic, amphiphilic drugs, which act as functional inhibitors of acid sphingomyelinase (FIASMAs) (Kornhuber et al., 2008; Kornhuber et al., 2011). Inhibition of the lysosomal enzyme acid sphingomyelinase (ASM) is linked to the accumulation of sphingomyelin and the decrease of its metabolite ceramide in the lysosomes. Indeed, inhibition of ASM activity could be confirmed upon administration of imipramine + ticlopidine, loperamide and pimozide in MZ-54 glioma cells. Of note, mutations of *SMPD1* (sphingomyelin phosphodiesterase 1) encoding for ASM is a common hallmark of the lysosomal storage disorder Niemann-Pick disease type A and B, which is associated with impaired ASM activity and defective lipid trafficking (Schulze and Sandhoff, 2011). However, a moderate, therapeutic reduction of ASM activity might be of potential value for tumor therapy. Interestingly, Klutzny et al. reported that ASM inhibition by the antipsychotic drug fluphenazine causes cellular sphingomyelin accumulation, which induces cancer cell death specifically in hypoxic tumor spheroids (Klutzny et al., 2017). In addition, it was shown that sphingomyelin controls autophagosome biogenesis, as excess sphingomyelin disturbs ATG9A trafficking and autophagosome closure in NPA-fibroblasts as well as MCF7 cancer cells depleted for *SMPD1* (Corcelle-Termeau et al., 2016). Accordingly, defective autophagosome biogenesis by sphingomyelin overload may additionally contribute to imipramine + ticlopidine-, loperamide- and pimozide-induced autophagic stress.

Unexpectedly, the targeted screening of bioactive sphingolipids revealed a significant, global increase of ceramides, sphinganins and glucosylceramides by loperamide and pimozide. This outcome cannot be explained by ASM inhibition, which should rather lead to a reduction of ceramide levels instead of their accumulation. Moreover, *de novo* synthesis of ceramides was largely unaffected by loperamide and pimozide treatment, indicating that impaired degradation might account for the severe increase of sphingolipid levels instead.

Interestingly, Petersen et al. reported that besides acting as FIASMAs, cationic, amphiphilic drugs also impede the lysosomal enzyme acid ceramidase, which is responsible for hydrolysis of ceramide to sphingosine (Petersen et al., 2013). Hence, the elevated ceramide levels in the present study might be partially explained by acid ceramidase inhibition. However, the global accumulation of several sphingolipids/ceramides rather suggests a general disruption of lysosomal sphingolipid degradation, which eventually outweighs the drug-evoked block of sphingomyelin to ceramide conversion via ASM.

Furthermore, Gulbins and coworkers found that ASM inhibition by antidepressants leads to the accumulation of sphingomyelin in the lysosomal and Golgi compartments, which is linked to an increase of ceramides in the ER. Ceramides in the ER then in turn upregulate

autophagy via PP2A (protein phosphatase 2 phosphatase activator) activation and dephosphorylation of ULK (Gulbins et al., 2018). These considerations indicate that the ceramide and sphingolipid accumulation observed in this study might not be restricted to the lysosomal compartment. However, further experiments need to be performed to clarify the subcellular localization of increased ceramide after loperamide and pimozide treatment.

Of note, it has been reported that ASM inhibition and severe accumulation of lipids in the lysosome is linked to an impaired degradative function of the lysosomes, implying a blockage of autophagolysosomal degradation induced by loperamide and pimozide (Schulze and Sandhoff, 2011; Lieberman et al., 2012). Additionally, the cargo adaptor SQSTM1 was found to be strongly increased upon treatment with these compounds, supporting the assumption that autophagy is blocked to a certain extent. However, it should be considered that SQSTM1 participates in several other pathways and is expressionally regulated by several molecules such as the oncogene Ras, p38 MAPK (mitogen-activated protein kinases), and NFE2L2, as well as by cellular stress. Therefore, conclusions on the autophagic status based on the protein levels of SQSTM1 should be taken with caution (Martinet et al., 2017).

In contrast to these signs of autophagy blockage, several experiments performed in this study and by Zielke et al. confirmed an increase of the autophagic flux by imipramine + ticlopidine, loperamide and pimozide (Zielke et al., 2018). Accordingly, it is proposed that autophagy is indeed strongly induced by these compounds, but ASM inhibition and lysosomal lipid accumulation over time culminate in severe lysosomal impairment, thereby likely blocking the final degradation of autophagic cargo at later time points. Moreover, it should be mentioned that measurements of the autophagic flux by LC3B-tandem plasmids performed in this study refer to autophagosome-lysosome fusion, as the EGFP-signal is quenched by the acidic lysosomal pH, and not to the final degradation of autolysosomal cargo, which constitutes a later step in the autophagy cascade.

6.12 Deregulated lipid homeostasis leads to autophagy-dependent LMP and subsequent lysosomal cell death that is partially rescued by selective lysophagy

Lysosomal membrane permeabilization (LMP) is implicated in cell demise under different physiological conditions such as mammary gland involution or clearance of intracellular bacterial infections and also contributes to the pathogenic features of several diseases like neurodegeneration or lysosomal storage disorders (Serrano-Puebla and Boya, 2016). Furthermore, the induction of LMP is currently discussed as a putative mechanism to kill cancer cells (Serrano-Puebla and Boya, 2018). In case of lysosomal storage disorders, deregulation of lysosomal lipid homeostasis such as accumulation of cholesterol oxidation

products or increased sphingomyelin levels has been directly linked to lysosomal stress and LMP (Boya and Kroemer, 2008; Petersen et al., 2013; Gabandé-Rodríguez et al., 2014). In accordance with these publications, massive accumulation of lipids such as cholesterol, ceramides and sphingomyelin in the lysosome upon imipramine + ticlopidine, loperamide and pimozide treatment was accompanied by lysosomal cathepsin B release into the cytosol. In addition, loperamide- and pimozide-induced LMP could be confirmed by pmCherry-GAL3 puncta formation, which is a widely-used marker for lysosomal rupture.

Of note, ceramides have been recently described to trigger LMP in various cancer cell lines (Zhang et al., 2016; Yamane et al., 2017). In brief, Zhang et al. reported that CD20-TNFR1 colocalization stimulated *de novo* ceramide synthesis and subsequently triggered LMP. Furthermore, lysosomal C16:0 ceramide accumulation has been linked to lysosomal damage owing to formation of ceramide channels in the lysosomal membrane, which was accompanied by necrotic cell death (Yamane et al., 2017). Based on these findings, it is supposed that the highly elevated levels of ceramides and especially of C16:0 ceramide following treatment with loperamide and pimozide might contribute to LMP induction.

Besides lysosomal lipid overload increased cellular ROS levels have been reported to contribute to LMP by causing lipid peroxidation and damaging lysosomal membrane proteins. Moreover, various antioxidants and redox regulators have been described to protect cells against oxidative-stress-induced LMP (Kurz et al., 2008a; Aits and Jäättelä, 2013). In the present study, loperamide and pimozide significantly increased lipid-ROS levels measured by the lipid peroxidation sensor BODIPY™ 581/591 C11, which could be reverted by addition of the lipid-ROS scavenger α-tocopherol. Strikingly, α-tocopherol also attenuated loperamide- and pimozide-induced lysosomal cathepsin B release as well as cell death, indicating that lipid-peroxidation plays a prominent role in the induction of LMP and subsequent cell demise. In addition, pimozide treatment resulted in a pronounced increase of general ROS levels.

Oxidative stress might be the consequence of various cellular stress reactions, such as upregulated NADPH oxidases, mitochondrial- or ER stress (Kurz et al., 2008a; Burton and Jauniaux, 2011). In contrast to AT 101, loperamide and pimozide treatment for 24 hours failed to induce mitochondrial depolarization, indicating that mitochondrial integrity is not affected by these compounds (data not shown). However, the global proteome analysis of MZ-54 cells treated with loperamide and pimozide showed no changes of NADPH oxidases but revealed a significant increase of protein clusters involved in ER-stress. Accordingly, it is supposed that ER-stress and massive lysosomal accumulation of lipids and other undegraded material contributes to ROS generation and lipid peroxidation following treatment with loperamide and pimozide, though, putative key players that account for the observed elevated ROS levels should be closer investigated in future experiments.

LMP results in leakage of the lysosomal content into the cytosol, which has detrimental effects on cellular homeostasis and viability. Thereby, the concerted action of lysosomal hydrolases, Ca^{2+} and ROS as well as cytosolic acidification has been described to trigger lysosomal cell death (LCD) (Aits and Jäättelä, 2013; Papadopoulos and Meyer, 2017). Indeed, imipramine + ticlopidine-, loperamide- and pimozide-induced LMP was followed by LCD, which could be diminished by addition of the cathepsin inhibitors E64D and pepstain A. However, it is supposed that the abundant release of lysosomal lipids as well as ROS contributes to cell death induction by these compounds, thereby limiting the rescuing effect of cathepsin inhibitors.

Strikingly, imipramine + ticlopidine, loperamide and pimozide-induced LMP was strongly attenuated in MZ-54 *ATG5* and *ATG7* KO cells compared to WT cells, indicating that hyperactivated autophagy extensively promotes lysosomal rupture. Furthermore, cathepsin inhibition completely failed to rescue cell death induced by pimozide in *ATG5* and *ATG7* KO cells, pointing out that autophagy inhibition prevents LMP and subsequent LCD following pimozide exposure. In contrast, cathepsin inhibition attenuated cell death in *ATG5* and *ATG7* KO cells after imipramine + ticlopidine and loperamide treatment to a similar extent than in WT cells. Therefore, future experiments need to be done to clarify the role of bulk autophagy on lysosomal cell death, e.g. by using cathepsin knockout models.

LMP has recently been described to promote the induction of selective lysophagy in order to degrade damaged lysosomes and reduce cellular stress levels (Chauhan et al., 2016; Papadopoulos et al., 2017; Papadopoulos and Meyer, 2017; Yoshida et al., 2017). Moreover, it was found that the AAA+-type ATPase VCP participates in the induction of lysophagy and is essential for cell survival after lysosomal damage. In line with this observation, knockdown of *VCP* reduced the recovery of pmCherry-GAL3 puncta after loperamide and pimozide washout, indicative of impaired lysophagy. In line with the findings of Papadopoulos et al., knockdown of *VCP* had a cell death promoting effect after exposure to loperamide and pimozide, pointing to an essential role of lysophagy for cellular survival after LMP in this experimental setup (Papadopoulos et al., 2017).

In conclusion, this part of the thesis demonstrates that impaired lipid trafficking induced by imipramine + ticlopidine, loperamide and pimozide is associated with autophagy induction as well as severe accumulation of lipids in the lysosome, which is accompanied by oxidative stress, a late-stage autophagy block, LMP and subsequent LCD. Of note, knockout of *ATG5* and *ATG7* significantly diminished LMP induced by imipramine + ticlopidine, loperamide and pimozide, suggesting that hyperactivated autophagy contributes to lysosomal damage and cell death. Based on these observations, it must be considered that autophagy inhibition does not only impair ACD, but also prevents LMP and its detrimental consequences, at least in case of ACD inducers that additionally affect lysosomal homeostasis. Moreover, this study

highlights the dual role of autophagy. While excessive bulk autophagy was associated with a pro-death effect in this experimental setup, selective lysophagy was shown to promote cellular survival following lysosomal damage (Figure 6.2).

6.13 Implications of impaired lipid trafficking and lysosomal damage for cancer therapy

Certain cancers have a high demand of cholesterol, what renders them more vulnerable for inhibitors of cholesterol transport. Of note, Kuzu and coworkers observed that ASM inhibitors reduced tumor growth and induced caspase-independent cancer cell death by impairing cholesterol trafficking in melanoma cells (Kuzu et al., 2017). Moreover, it has been reported that glioblastoma cells rely on the uptake of exogenous cholesterol, while normal human astrocytes fulfill their cholesterol demand by *de novo* synthesis and supply cholesterol to neighboring cells (Villa et al., 2016). Based on these findings, it is suggested that impairment of lipid-trafficking by imipramine-ticlopidine, loperamide and pimozide might be of potential therapeutic interest, as exogenous cholesterol mainly enters the cells via receptor-mediated endocytosis of plasma LDL and delivery into endosomes/lysosomes (Chu et al., 2015).

In addition, it has been shown that cancer cells upregulate lysosomal activity to fulfill their increased metabolic demand (Perera et al., 2015). Moreover, cathepsins are upregulated in various cancer types, which is often associated with invasive and metastatic phenotypes (Gondi and Rao, 2013; Sun et al., 2016; Yang et al., 2016). Besides, several studies reported that cancer cell lysosomes are less stable, e.g. due to degradation of LAMP1 and LAMP2, than non-transformed cells (Fehrenbacher et al., 2008; Domagala et al., 2018). Accordingly, it is assumed that the high reliance of cancer cells on the lysosomal pathway combined with altered stability of the lysosomal membrane renders cancer cells more sensitive to LMP-inducing agents. Therefore, targeting of lysosomal stability and cholesterol transport might be of potential interest for current cancer therapy.

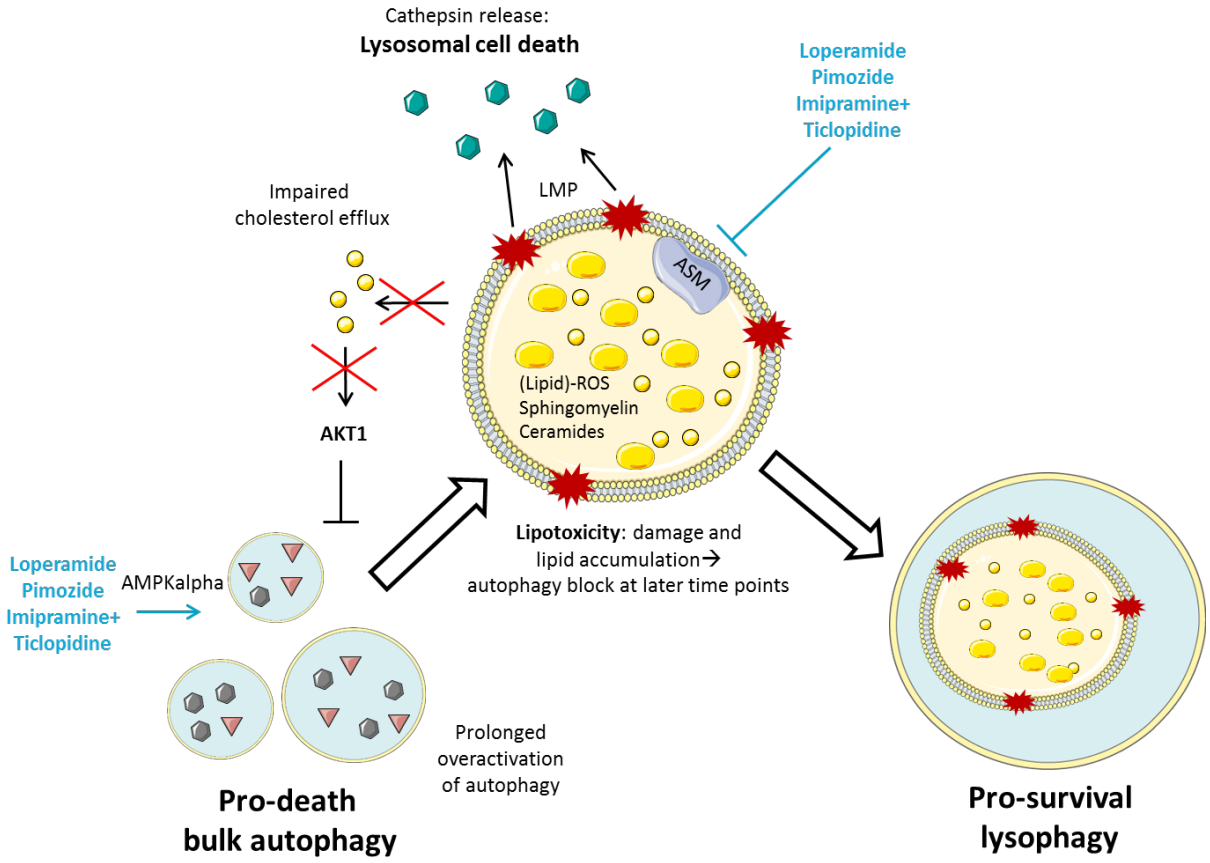

Figure 6.2. Hypothetic pathway of imipramine + ticlopidine-, loperamide- and pimozide-induced lipotoxicity, and the dual role of autophagy in cell survival and death.
Imipramine + ticlopidine, loperamide and pimozide induce autophagy by activation of AMPKalpha. In parallel, the compounds functionally inhibit ASM (and presumably other enzymes involved in sphingolipid degradation such as acid ceramidase), which leads to massive accumulation of lipids in the lysosome. Defective cholesterol trafficking subsequently reduces the amount of cytosolic cholesterol, which impairs AKT1 signaling, thereby further promoting autophagy. Prolonged overactivation of autophagy and lysosomal lipid overload synergistically induce lysosomal membrane permeabilization (LMP) and subsequent lysosomal cell death (LCD). Moreover, impairment of lysosomal function culminates is associated with a late stage autophagy block. Besides pro-death bulk autophagy, defective lysosomes are degraded by selective lysophagy to prevent LCD following lysosomal rupture, thereby promoting cell survival. (modified from Servier Medical Art, licensed under a Creative Common Attribution 3.0 Generic License. http://smart.servier.com/.)

6.14 Conclusion

In this study, the induction of autophagic cell death (ACD) and its underlying mechanisms were investigated in glioblastoma cells following treatment with various autophagy-inducing compounds.

The first part focused on a follow-up study on the natural compound and ACD inducer AT 101, which is currently investigated as an anticancer agent (Voss et al., 2010). Here, it was observed that AT 101 severely damaged mitochondria by prolonged opening of the mitochondrial permeability transition pore (mPTP), leading to mitochondrial depolarization

(Warnsmann et al., 2018). To prevent further cellular toxicity, damaged mitochondria were subsequently degraded by mitophagy. In addition, AT 101 enhanced the protein levels of HMOX1 and of selective mitophagy receptors BNIP3 and BNIP3L, thereby further promoting mitophagy. Accordingly, it is suggested that in AT 101-treated glioma cells, HMOX1 induction and mitochondrial damage synergize to induce hyperactivated, selective mitophagy and subsequent cell death in glioma cells.

HMOX1 and autophagy induction are generally considered as adaptive responses to cope with cellular stress, but their roles in cell survival or death are supposed to be dependent on the extent and the specific cellular context. The pro-death role of mitophagy upon treatment with AT 101 could be explained by a threshold effect similar to bulk autophagy, where too much degradation turns into a death-promoting process. Moreover, the massive loss of mitochondria might lead to a severe energy deficit of the cells, further limiting cellular survival. In future studies, it would be interesting to decipher the threshold of mitophagy that must be reached for the induction of irreversible cellular demise in different cancer types compared to non-transformed cells to enable predictions about cellular behavior.

In the second part of the study, the newly identified ACD inducers loperamide, pimozide and STF-62247 as well as the positive control imipramine + ticlopidine were extensively investigated according to ACD induction and the underlying signaling pathways (Shchors et al., 2015). Indeed, all four compounds showed the typical phenotype of ACD, including increased autophagic flux and cell death that was rescued by *ATG5* and *ATG7* knockout. Moreover, it was found that imipramine + ticlopidine, loperamide and pimozide inhibited the lysosomal enzyme acid sphingomyelinase (ASM) and strongly impaired lipid trafficking, leading to lysosomal lipid accumulation and lipotoxicity. These effects were accompanied by decreased AKT1 signaling, lysosomal membrane permeabilization and subsequent lysosomal cell death. Strikingly, this study demonstrated a dual role of autophagy in that context. On the one hand, inhibition of bulk autophagy by *ATG5* and *ATG7* KO extensively reduced LMP as well as cell death. On the other hand, clearance of damaged lysosomes by selective lysophagy promoted cell survival. Collectively, it is proposed that the synergistic effects of hyperactivated autophagy, lysosomal damage and consequent impairment of lysosomal degradative function at later time points triggers massive autophagic and lysosomal stress and finally culminates in cell demise.

The results of this study underscore that mechanistically separable types of ACD, namely a predominantly mitophagic vs. an autophagy-dependent lysosomal cell death exist. They also highlight the difficulties of a clear separation between different cell death forms. Referring to the recommendations of the Nomenclature Committee on Cell Death, the term “autophagy-dependent cell death/autophagic cell death” should be exclusively used when cell death relies on the autophagic machinery and does not favor the engagement of other regulated

cell death forms such as apoptosis, ferroptosis or necroptosis (Galluzzi et al., 2018). Indeed, all investigated ACD inducers in this study failed to induce apoptosis, ferroptosis or necroptosis, but closer investigation elucidated the participation of other cell death modalities. In case of AT 101, mitophagic cell death was accompanied by mitochondrial damage and presumably mPTP-driven necrosis. Moreover, the published ACD inducer imipramine + ticlopidine and two of three hit compounds identified in the ENZO Screen-Well™ autophagy library screen for ACD were shown to inhibit ASM, induce lysosomal lipid overload and trigger autophagy-dependent LMP and a lysosomal type of cell death, suggesting that lysosomal damage might be a key driver in many paradigms of ACD (Shchors et al., 2015; Zielke et al., 2018).

Owing to the devastating prognosis for patients with GBM, which is causally related to the apoptosis resistance and highly invasive nature of these tumors, it is of urgent need to identify new candidate drugs to bypass therapy resistance. In that context, ACD may represent an alternative or additive strategy to kill tumor cells (Wagenknecht et al., 1999; Jiang et al., 2003; Kögel et al., 2010; Wilson et al., 2014). Besides their effects as ACD inducers, the compounds investigated here possess additional cytotoxic effects that might be of interest for cancer therapy, even if tumor cells were not completely eliminated. Based on the notion that tumor cells reprogram their mitochondrial metabolism for cell proliferation, selective mitophagy as well as mitochondrial damage induced by AT 101 might reduce tumor growth (Ward and Thompson, 2012). Moreover, the high dependency of glioblastoma cells on cholesterol metabolism and the findings that various cancers possess upregulated lysosomal activity as well as destabilized lysosomes makes GBM potentially prone to impaired lipid transport and lysosomal lipotoxicity induced by imipramine + ticlopidine, loperamide and pimozide (Fehrenbacher et al., 2008; Perera et al., 2015; Villa et al., 2016; Kuzu et al., 2017; Domagala et al., 2018).

From the clinical point of view, it must be considered that AT 101 insufficiently crosses the blood-brain-barrier and that loperamide is not systemically bioavailable after oral administration and completely fails to cross the blood-brain-barrier (Kalla and Sud, 1990; Alyautdin et al., 1997). This restriction for GBM therapy might be overcome by using nanoparticles and p-glycoprotein inhibition (Ulbrich et al., 2011; Bauer et al., 2012). In contrast, antipsychotic drugs such as imipramine and pimozide enter the brain without difficulties, which would simplify their usage as repurposed drugs for brain tumor treatment. Of note, the putative benefits of antipsychotics for GBM therapy gained increasing attention in the recent years, because of their anti-neoplastic effects on human cancers and long history of clinical use (Faraz et al., 2016; Lee et al., 2016; Tan et al., 2018).

In future experimental studies, it would be of high interest to elucidate the anti-cancer effect of the ACD inducers investigated here *in vivo*, e.g. by using genetically engineered mouse

models or viral vector-mediated transduction mouse models. While conventional genetic approaches are limited by time and cost, viral-vector mediated approaches offer the ability to rapidly generate complex tumor models (Miyai et al., 2017). Moreover, to decipher the specific role of autophagy in that context, transgenic mice with systemically expressed GFP-LC3-RFP-LC3ΔG or mRFP-EGFP-LC3 could be used to monitor autophagy (Kuma et al., 2017). In addition, the usage of brain-specific, inducible knockout models of *ATG5* or *ATG7* compared to control mice might shed further light on the potential therapeutic relevance of autophagy inhibition (Kuma et al., 2017).

7 Summary

Autophagy, meaning “self-eating”, is an important cellular waste disposal mechanism. Thereby, damaged proteins, lipids and organelles are enclosed by autophagosomes and subsequently transported to the lysosomes for degradation into basic, cellular building blocks (Klionsky, 2008). Under basal conditions autophagy prevents the accumulation of defective and harmful material and generally promotes cell survival. However, in recent years several studies reported that hyperactivated autophagy, e.g. during developmental processes in lower eukaryotes, or during chemotherapeutic treatment of cancer cells, can also trigger cell death (Denton et al., 2009; Voss et al., 2010; Shchors et al., 2015; Dasari et al., 2017; Segala et al., 2017). This type of regulated cell death is called autophagic cell death (ACD) and is dependent on components of the autophagic machinery (Galluzzi et al., 2018). Collectively, the effects of autophagy on cell survival are highly dependent on the intensity of autophagy induction, the duration and the cellular context.

In recent years, ACD has been considered as an alternative cell death pathway for tumor therapy, especially for solid tumors with high apoptosis resistance such as glioblastoma (Fulda and Kögel, 2015). Glioblastoma (GBM) (WHO grade IV) is a very aggressive malignant primary brain tumor with a poor prognosis and a median survival time of ~ 15 months despite surgery and radiochemotherapy with TMZ (Thakkar et al., 2014). Interestingly, several anticancer agents such as AT 101, cannabinoids and the combination of imipramine + ticlopidine have been reported to induce ACD in GBM cells (Salazar et al., 2009; Voss et al., 2010; Shchors et al., 2015).

The aim of this project was to identify the underlying mechanisms of stress- and drug-induced ACD and its therapeutic potential for glioblastoma treatment. For detailed investigation of ACD, a CRISPR/Cas9-based approach was used to generate *ATG5* and *ATG7* knockouts as genetic models of autophagy deficiency in the glioma cell lines MZ-54 and U343. In a previous study of our lab, it was demonstrated that administration of AT 101 [(-)-gossypol], a natural compound from cotton seeds, triggers ACD in glioblastoma cells, which was accompanied by mitochondrial dysfunction and fragmentation, but no signs of apoptosis (Voss et al., 2010). Interestingly, mitochondrial fragmentation is known to be a prerequisite for mitophagy, which is the selective degradation of mitochondria by autophagy. Therefore, the first part of this study focused on investigating the potential role of mitophagy in AT 101-induced ACD.

In line with previous findings, AT 101 triggered mitochondrial membrane depolarization and cell death independent of BAX and BAK1. In addition, knockout of *ATG5* significantly diminished cell death induced by AT 101, supporting the notion that AT 101 triggers ACD in

glioma cells (Meyer et al., 2018). Interestingly, it was found that mitochondrial depolarization and cell death following AT 101-treatment were at least partly dependent on the opening of the mitochondrial permeability pore (mPTP).

A global proteomic analysis of AT 101-treated glioma cells revealed the robust decrease of mitochondrial protein clusters and upregulation of heme oxygenase-1 (HMOX1). To verify the induction of mitophagy by AT 101, several independent experiments were performed, including (1) western blot analysis of mitochondrial proteins, (2) flow cytometric measurement of MTG and (3) mito-mKeima as well as (4) qRT-PCR of mitochondrial versus nuclear DNA. Indeed, all experiments revealed the induction of mitophagy by AT 101, which could be reversed by genetic or pharmacologic inhibition of autophagy. Strikingly, analysis of selective mitophagy receptors involved in AT 101-induced mitophagy showed a strong increase of BNIP3 and BNIP3L, and siRNA-mediated knockdowns of both proteins were able to diminish cell death as well as mitophagy following AT 101 treatment. These data indicate that AT 101-induced mitophagy promotes cell death of glioblastoma cells. Nevertheless, inhibition of autophagy/mitophagy was not able to fully rescue cell death, suggesting that besides lethal mitophagy, the cells finally surrender to alternative types of cell death, mostly related to gross mitochondrial damage and mPTP-driven necrosis (Meyer et al., 2018).

Besides the function of HMOX1 in degrading pro-oxidant heme into carbon monoxide, biliverdin and iron, it has been described to regulate autophagy/mitophagy (Zukor et al., 2009; Constantin et al., 2012; Bansal et al., 2014). In that context, HMOX1-induced autophagy/mitophagy was proposed to play either a cytoprotective, or a cytotoxic role, which was dependent on the cellular model and the type of disease. According to these considerations, the potential role of HMOX1 in lethal mitophagy was investigated next. Of note, silencing of *HMOX1* significantly attenuated AT 101-dependent mitophagy and cell death. Taken together, these data demonstrate that AT 101-induced mitochondrial dysfunction and HMOX1 induction synergize to promote excessive mitophagy with a lethal outcome in glioma cells (Meyer et al., 2018).

To identify further compounds that can trigger ACD, a cell death screen of an autophagy library with MZ-54 WT versus *ATG5* and *ATG7* knockout cells was performed. The screen revealed three hit compounds: loperamide, pimozide and STF-62247 (Zielke et al., 2018). In subsequent experiments, the increase of the autophagic flux by these compounds was confirmed using two different LC3B-tandem plasmids. The established positive ACD control for these investigations was a combination of the antipsychotic imipramine and the anticoagulant ticlopidine. This combination has shown a remarkable induction of ACD in glioblastoma cells in a recent study (Shchors et al., 2015), which was confirmed in this thesis. Moreover, the induction of ACD by the above-named drugs was verified by flow-cytometry-based analysis of cell death of MZ-54 WT cells versus three different *ATG5* and

ATG7 knockouts (Zielke et al., 2018). Of note, imipramine + ticlopidine, STF-62247, loperamide and pimozide failed to induce mitochondrial dysfunction and mitophagy, indicating that these drugs induce a completely different mode of ACD. To decipher the molecular mechanisms behind ACD induced by imipramine + ticlopidine, STF-62247, loperamide and pimozide, a global proteomic analysis was performed. Interestingly, treatment with all four drugs revealed an increase of proteins related to cholesterol and lipid metabolic processes, with loperamide and pimozide showing the strongest effects. Cellular cholesterol stainings showed that treatment with the above-mentioned substances resulted in a massive accumulation of cholesterol in the lysosomes. These results indicate an inhibition of cellular lipid transport. Consistent with this hypothesis, imipramine, loperamide and pimozide are cationic amphiphilic substances that have been shown to act as functional inhibitors of acid sphingomyelinase (FIASMAs), an enzyme, which synthesizes the cleavage of sphingomyelin to ceramide and phosphorylcholine (Kornhuber et al., 2008; Kornhuber et al., 2011). Interestingly, disturbed function of the acid sphingomyelinase is a well-known feature of the lysosomal lipid storage disease Niemann-Pick type A and B (Schulze and Sandhoff, 2011). This inhibition of ASM by imipramine + ticlopidine, loperamide and pimozide could be confirmed in glioma cells in this thesis.

In the further course of this study, the connection between defective lipid transport and autophagy was closely investigated. On the one hand, it could be demonstrated that defective lipid transport promotes autophagy induction due to AKT1 inhibition. On the other hand, it has been reported that the accumulation of lipids in the lysosome has detrimental effects on lysosomal homeostasis and inhibits their degradative function (Schulze and Sandhoff, 2011; Lieberman et al., 2012). The targeted analysis of sphingolipids by a lipidomic approach revealed a massive increase in bioactive sphingolipids, especially ceramides, after treatment with loperamide and pimozide. The effects were not caused by an upregulation of the *de novo* synthesis, since the corresponding enzymes showed little or no expression changes. It should also be noted that the high ceramide levels cannot be explained by the functional inhibition of acid sphingomyelinase, since this rather leads to a reduction in ceramide synthesis. The fact that a large part of the sphingolipids measured (18 out of 23 in loperamide-treated cells and 16 out of 22 in pimozide-treated cells) was highly enriched after loperamide and pimozide treatment suggests that these effects are caused by fundamental inhibition of lysosomal degradation rather than by altered function of individual enzymes. Based on these results, it can be assumed that imipramine + ticlopidine, loperamide and pimozide increase the autophagic flux, but the impaired lipid transport culminates in lysosomal damage and subsequent blockade of the lysosomal degradation at later time points following drug treatment.

The massive accumulation of cholesterol, ceramides and other lipids is known to be associated with lysosomal stress, which can damage the lysosomal membrane (Boya and Kroemer, 2008; Petersen et al., 2013; Gabandé-Rodríguez et al., 2014). Indeed, it could be shown that loperamide and pimozide increase the level of lipid-ROS, resulting in the lysosomal membrane permeabilization (LMP) and subsequent lysosomal cell death. Lysosomal cell death is another non-apoptotic form of regulated cell death form that is caused by the leakage of lysosomal material into the cytosol can be inhibited by cathepsin inhibitors. Remarkably, the knockout of *ATG5* and *ATG7* strongly reduced imipramine + ticlopidine, loperamide, and pimozide-induced LMP. Since these knockout cell lines are also rescued from imipramine + ticlopidine, loperamide, and pimozide-induced cell death, it can be concluded that hyperactivated nonselective autophagy promotes lysosomal damage as well as subsequent cell death.

In contrast to the cell death-promoting effect of non-selective autophagy shown following treatment with the ACD inducers/FIASMAs here, it has recently been reported that lysophagy, the selective degradation of defective lysosomes, plays an important role in cell survival after severe lysosomal damage (Maejima et al., 2013; Papadopoulos et al., 2017). Consistent with these findings, the knockdown of *VCP* (valosin containing protein), which is an essential component of the lysophagy signaling pathway, increased loperamide and pimozide-induced cell death. These results illustrate the dual, contextual role of autophagy for cell survival.

In this study, two novel signaling pathways that induce autophagic cell death in glioma cells and may potentially be relevant for glioblastoma therapy were investigated in detail. First, it was demonstrated that AT 101, a compound that is currently investigated as an anticancer agent, induces mitochondrial damage and subsequent lethal mitophagy, in line with reports suggesting that excessive induction of mitophagy induces cell death in several other cancer cell models (Kim et al., 2007; Sentelle et al., 2012; Wang et al., 2014). Secondly, it was confirmed in this study that the substances loperamide, pimozide and STF-62247 cause ACD. In addition to the hyperactivation of bulk-autophagy, further experiments showed that loperamide and pimozide impaired lipid transport, resulting in lysosomal lipotoxicity, LMP and lysosomal cell death. This study also emphasizes the difficulties of a clear distinction between autophagic cell death and lysosomal cell death, which should be considered for the realistic definition of these cell death pathways. Of note, cancer cells often display an upregulation of lysosomal pathways, and especially GBM cells have a high demand of external cholesterol (Perera et al., 2015; Sun et al., 2016; Villa et al., 2016). Hence, targeting cholesterol trafficking and lysosomal stability in combination with ACD may constitute a promising approach for glioblastoma treatment. As the antipsychotic drug pimozide in

contrast to loperamide crosses the blood-brain-barrier without any difficulties and is already approved in the clinic, it might be of particular interest for glioblastoma therapy.

8 Zusammenfassung

Autophagie ist ein wichtiger Mechanismus zur Beseitigung zellulärer Abfallprodukte. Der Begriff wurde von Christian de Duve geprägt und setzt sich aus den griechischen Wörtern „auto“ und „phagein“ zusammen, was „sich selbst essen“ bedeutet (Klionsky, 2008). Dabei werden beschädigte Proteine, Lipide und Organellen von Autophagosomen eingeschlossen und anschließend zu den Lysosomen transportiert, um sie in die grundlegenden zellulären Bausteine zu zerlegen. Unter basalen Bedingungen verhindert Autophagie die Ansammlung von defektem, zytotoxischem Material, wie z.B. beschädigten Mitochondrien, und leistet somit einen essentiellen Beitrag zur zellulären Homöostase. Bei Nährstoffmangel werden durch Autophagie wichtige Grundbausteine bereitgestellt, die das Überleben der Zellen fördern. Im Gegensatz zu diesen positiven Auswirkungen der Autophagie auf das zelluläre Überleben haben allerdings mehrere Studien gezeigt, dass hyperaktivierte Autophagie, die z. B. während Entwicklungsprozessen niederer Eukaryonten oder bei chemotherapeutischer Behandlung von Krebszellen stattfindet, Zelltod-fördernd wirken kann (Galluzzi et al., 2018). Diese Form des Zelltods wird als autophagischer Zelltod bezeichnet und setzt voraus, dass der Zelluntergang von essentiellen Bestandteilen des Autophagie-Signalwegs abhängt, jedoch keine anderen Formen des programmierten Zelltods wie Apoptose, Ferroptose oder Nekroptose an seiner Verrichtung beteiligt sind (Galluzzi et al., 2018).

Diese Betrachtungen verdeutlichen, dass die zellulären Auswirkungen der Autophagie von dessen Intensität und Dauer sowie dem zellulären Kontext beeinflusst werden. In den letzten Jahren wurde Autophagie als alternativer Zelltodweg für die Tumortherapie näher in Betracht gezogen, insbesondere für solide Tumoren, die eine hohe Apoptose-Resistenz aufweisen, wie das Glioblastom (Fulda and Kögel, 2015). Das Glioblastom (GBM; WHO-Grad IV) ist ein sehr aggressiver, maligner, primärer Gehirntumor mit schlechter Prognose und einer medianen Überlebenszeit von ~ 15 Monaten trotz Operation und Radiochemotherapie mit Temozolomid (TMZ) (Thakkar et al., 2014). Daher besteht ein hohes Interesse diese Therapieresistenz durch alternative Zelltodmechanismen zu umgehen. Interessanterweise wurde in den vergangenen Jahren gezeigt, das verschiedene Substanzen, wie z.B. AT 101, Cannabinoide und die Kombination von Imipramin + Ticlopidin, einen autophagie-abhängigen Zelltod in GBM-Zellen induzieren (Salazar et al., 2009; Voss et al., 2010; Shchors et al., 2015).

Ziel dieses Projekts war es, die zugrundeliegenden Mechanismen des stress- und pharmakologisch-induzierten autophagischen Zelltodes und dessen therapeutisches Potenzial zur Umgehung der Apoptose-Resistenz bei Glioblastomen zu identifizieren. Für eine detaillierte Untersuchung des autophagischen Zelltodes wurde ein CRISPR/Cas9-

basierter Ansatz verwendet, um *ATG5*- und *ATG7*-depletierte Zelllinien als genetische Modelle für Autophagie-Inhibition in den GBM-Zelllinien MZ-54 und U343 zu generieren. In einer früheren Studie unseres Labors wurde gezeigt, dass AT 101 [(-)-Gossypol], eine natürliche Substanz aus Baumwollsamen, einen autophagischen Zelltod hervorruft (Voss et al., 2010). Dieser Zelltod ging mit mitochondrialer Fragmentierung und Dysfunktion einher, zeigte allerdings keine Anzeichen von Apoptose. Interessanterweise ist die mitochondriale Fragmentierung häufig ein Vorbote der Mitophagie, dem selektiven Abbau von Mitochondrien durch Autophagie. Daher wurde im ersten Teil dieser Doktorarbeit die potenzielle Rolle der Mitophagie beim AT 101-induzierten Zelltod untersucht.

In Übereinstimmung mit den früheren Befunden zu AT 101 konnte hier gezeigt werden, dass die Depletion von *ATG5* den AT 101-vermittelten Zelltod in MZ-54 und U343 GBM-Zellen signifikant verringert, was die Annahme unterstützt, dass AT 101 einen autophagischen Zelltod induziert. Zusätzlich zeigte diese Studie, dass die Behandlung mit AT 101 eine ausgeprägte mitochondriale Depolarisation zur Folge hat, die unter anderem durch die Öffnung der mitochondrialen Permeabilitätspore (mPTP) hervorgerufen wurde. Die globale Proteomanalyse AT 101-behandelter GBM-Zellen ergab eine robuste Abnahme mitochondrialer Proteincluster, was durch Western Blot Analysen bestätigt werden konnte, sowie die starke Zunahme des Enzyms Hämoxygenase-1 (HMOX1). Zudem konnte durch den Vergleich von MEF Wildtyp-Zellen und *Bax Bak1* Doppelknockout Zellen bestätigt werden, dass weder die Abnahme des mitochondrialen Membranpotentials, noch der mitochondrialen Proteine durch Inhibition der Apoptose beeinflusst werden.

Als nächstes wurde die Mitophagie-Induktion nach AT 101 Behandlung mit Hilfe dreier unabhängiger Ansätze gemessen: (1) der durchflusszytometrischen Messung von MTG und (2) mito-mKeima, sowie (3) der qRT-PCR von Mitochondrien- vs. Zellkern-DNA. Alle drei Verfahren wiesen übereinstimmend auf eine starke Induktion der Mitophagie durch AT 101 hin, die durch genetische oder pharmakologische Hemmung der Autophagie unter Verwendung *ATG5*-depletierter Zellen oder der Autophagie-Inhibitoren Wortmannin, Bafilomycin A_1 und Chloroquin wieder aufgehoben werden konnte (Meyer et al., 2018).

Um die Rolle der selektiven Mitophagie beim autophagischen Zelltod näher zu studieren, wurden als nächstes verschiedene Mitophagie-Rezeptoren untersucht. Die Analyse ergab einen bemerkenswerten Anstieg der Expression von BNIP3 und BNIP3L nach AT 101 Behandlung, und die siRNA-vermittelte Depletion beider Proteine konnte die AT 101-induzierte Mitophagie und den Zelltod signifikant verringern. Demnach lässt sich schlussfolgern, dass AT 101-induzierte, Rezeptor-abhängige Mitophagie den Zelltod von GBM-Zellen fördert (Meyer et al., 2018).

Neben der generellen Funktion von HMOX1 als abbauendes Enzym von oxidativen Häm-Gruppen zu Kohlenstoffmonoxid, Biliverdin und Eisen wurde kürzlich beschrieben, dass HMOX1 sowohl die mitochondriale Biogenese als auch Autophagie/Mitophagie reguliert (Zukor et al., 2009; Constantin et al., 2012; Bansal et al., 2014). In diesem Kontext konnte gezeigt werden, dass eine Induktion von Autophagie/Mitophagie durch HMOX1 je nach Zellmodell und pathologischem Kontext entweder mit zytoprotektiven oder zytotoxischen Effekten verbunden ist. Da in der Proteomanalyse von AT 101-behandelten GBM-Zellen eine starke Zunahme der HMOX1-Proteinmenge festgestellt werden konnte, wurden die potenziellen Effekte von HMOX1 auf die AT 101-induzierte Mitophagie und den Zelltod untersucht. Bemerkenswerterweise führte die siRNA-vermittelte Depletion von *HMOX1* zu einer signifikanten Verringerung der durch AT 101 ausgelösten Mitophagie und des Zelltodes. Zusammenfassend zeigen diese Daten, dass die AT 101-induzierte mitochondriale Dysfunktion und HMOX1-Aktivierung gemeinsam exzessive Mitophagie induzieren, was einen Mitophagie-abhängigen Zelltod zur Folge hat. Allerdings sollte hier angemerkt werden, dass die Inhibition der Mitophagie/Autophagie diesen Zelltod nicht vollständig verhindern konnte. Aufgrund der Experimente dieser Arbeit sowie vorangegangener Studien lassen sich die Beteiligung der Zelltod-Typen Apoptose, Ferroptose und Nekroptose weitestgehend ausschließen. Daher wird vermutet, dass die Zellen neben der letalen Mitophagie schließlich an einem alternativen Zelltod sterben, der höchstwahrscheinlich durch die ausgeprägte Schädigung der Mitochondrien und mPTP-gesteuerte Nekrose bedingt wird (Meyer et al., 2018).

Im zweiten Teil dieser Doktorarbeit lag der Fokus auf der Identifikation neuer Substanzen, die einen autophagischen Zelltod auslösen, sowie deren detaillierte Untersuchung in Bezug auf die zugrundeliegenden Zelltodmechanismen und Signalwege. Mittels eines Zelltodscreens der ENZO Screen-Well™ Autophagie Bibliothek in MZ-54 Wildtyp-Zellen vs. *ATG5*- und *ATG7*-depletierten Zellen wurden Loperamid, Pimozid und STF-62247 als autophagischen Zelltod-induzierende Substanzen identifiziert (Zielke et al., 2018). In nachfolgenden Experimenten wurde zunächst die Zunahme des autophagischen Fluxes durch diese Substanzen mit Hilfe zweier LC3B-Tandem-Plasmide quantifiziert. Als etablierte Positivkontrolle für autophagischen Zelltod diente eine Kombination aus dem Antipsychotikum Imipramin und dem Antikoagulans Ticlopidin, die in einer kürzlich publizierten Studie eine starke Induktion des autophagischen Zelltodes in GBM-Zellen hervorrief (Shchors et al., 2015), was sich in dieser Doktorarbeit bestätigen lies. Darüber hinaus wurde die Induktion des autophagischen Zelltodes durch durchflusszytometrische Analysen von MZ-54 Wildtyp-Zellen im Vergleich zu jeweils drei verschiedenen *ATG5*- und *ATG7*-depletierten Zelllinien verifiziert (Zielke et al., 2018).

Da nach Behandlung mit Imipramin + Ticlopidin, STF-62247, Loperamid und Pimozid im Gegensatz zu AT 101 keine Anzeichen von mitochondrialer Schädigung und Mitophagie erkennbar waren, wurde vermutet, dass andere Mechanismen an der Induktion und Exekution des autophagischen Zelltodes beteiligt sind. Um die molekularen Mechanismen hinter der zytotoxischen Wirkung von Imipramin + Ticlopidin, STF-62247, Loperamid und Pimozid zu entschlüsseln, wurde als nächstes eine globale Proteomanalyse durchgeführt. Hier fiel auf, dass die Behandlung mit allen vier Medikamenten eine signifikante Zunahme von Proteinclustern, die an Cholesterin- und Lipid-Stoffwechselprozessen beteiligt sind, induzierte, wobei Loperamid und Pimozid die stärksten Veränderungen hervorriefen. Durch Anfärben des zellulären Cholesterols wurde verdeutlicht, dass die Behandlung mit den oben genannten Substanzen eine massive Akkumulation von Cholesterol in den Lysosomen zur Folge hatte. Diese Ergebnisse weisen auf eine Hemmung des zellulären Lipidtransports hin. In Übereinstimmung mit dieser Hypothese handelt es sich bei Imipramin, Loperamid und Pimozid um kationische, amphiphile Subtanzen, die nachweislich die Funktion des lysosomalen Enzyms saure Sphingomyelinase inhibieren, welches die Spaltung von Sphingomyelin zu Ceramid und Phosphorylcholin synthetisiert (Kornhuber et al., 2008; Kornhuber et al., 2011). Eine gestörte Funktion der sauren Sphingomyelinase ist ein bekanntes Merkmal für die Lipidspeicherkrankheit Morbus Niemann-Pick Typ A und B, bei der das Enzym durch Genmutation stark beeinträchtigt ist (Schulze and Sandhoff, 2011). Die Inhibition der sauren Sphingomyelinase durch Imipramin + Ticlopidin, Loperamid und Pimozid in GBM-Zellen konnte in dieser Studie bestätigt werden.

Im weiteren Verlauf der Experimente wurde der Zusammenhang von defektem Lipidtransport und Autophagie näher untersucht. In Übereinstimmung mit früheren Studien konnte hier nachgewiesen werden, dass der defekte Lipidtransport zur Autophagieinduktion durch Hemmung von AKT1 beiträgt (Xu et al., 2010). Weiterhin war bereits bekannt, dass die lysosomale Ansammlung von Lipiden die Lysosomen schädigt und deren Abbaufunktion hemmt (Schulze and Sandhoff, 2011; Lieberman et al., 2012). Interessanterweise ergab die hier durchgeführte Lipidomanalyse einen massiven Anstieg der bioaktiven Sphingolipide, insbesondere der Ceramide, nach Behandlung mit Loperamid und Pimozid. Diese Effekte wurden nicht durch eine verstärkte *de novo* Synthese verursacht, da die entsprechenden Enzyme kaum Expressionsänderungen aufwiesen. Hier ist außerdem anzumerken, dass die hohen Ceramidspiegel nicht durch die funktionale Inhibition der sauren Sphingomyelinase erklärbar sind, da dies eher zu einer Reduktion der Ceramidsynthese führen sollte. Die Tatsache, dass ein Großteil der gemessenen Sphingolipide nach Loperamid- und Pimozid Behandlung stark angereichert war (18 von 23 gemessenen Sphingolipiden nach Loperamid- und 16 von 22 gemessenen Sphingolipiden nach Pimozid Behandlung), lässt vermuten, dass diese Effekte auf eine grundsätzliche Hemmung des lysosomalen Abbaus und weniger auf

die veränderte Funktion einzelner Enzyme zurückzuführen sind. Basierend auf diesen Ergebnissen wird angenommen, dass Imipramin + Ticlopidin, Loperamid und Pimozid einerseits den autophagischen Flux massiv erhöhen, der gestörte Lipidtransport die Lysosomen aber zunehmend schädigt, was im späteren Verlauf zu einer Blockade des lysosomalen Abbaus führt.

Die lysosomale Akkumulation von Cholesterol, Ceramiden und anderen Lipiden ist mit lysosomalem Stress assoziiert, wodurch eine Beschädigung der lysosomalen Membran hervorgerufen werden kann (Boya and Kroemer, 2008; Petersen et al., 2013; Gabandé-Rodríguez et al., 2014). Tatsächlich konnte hier gezeigt werden, dass Loperamid und Pimozid den Spiegel an Lipid-Reaktiven-Sauerstoffspezies erhöhen, was die Permeabilisierung der lysosomalen Membran und anschließend einen lysosomalen Zelltod zur Folge hatte. Der lysosomale Zelltod ist eine weitere, nicht-apoptotische, regulierte Zelltodform, die durch das Austreten des lysosomalen Materials ins Zytosol hervorgerufen wird und durch Cathepsininhibitoren gehemmt werden kann. Bemerkenswert war, dass *ATG5* und *ATG7*-depletierte Zellen im Vergleich zu Wildtyp-Zellen deine deutlich geringere Schädigung der lysosomalen Membran aufwiesen. Da die Depletion von *ATG5* und *ATG7* ebenfalls den durch Imipramin + Ticlopidin, Loperamid und Pimozid induzierten Zelltod verringert, lässt sich schlussfolgern, dass hyperaktivierte, unselektive Autophagie massiv zur Lysosomenschädigung und dem nachfolgenden Zelltod beitragen.

Im Gegensatz zu der hier gezeigten Zelltod-fördernden Wirkung von unselektiver Autophagie wurde kürzlich publiziert, dass Lysophagie, die selektive Degradation von defekten Lysosomen, für das Überleben der Zellen nach starker lysosomaler Schädigung eine wichtige Rolle spielt (Maejima et al., 2013; Papadopoulos et al., 2017). Tatsächlich konnten die Ergebnisse dieser Doktorarbeit bestätigen, dass die siRNA-vermittelte Depletion von *VCP* (valosin containing protein), welches ein essentieller Bestandteil des Lysophagie-Signalwegs ist, den durch Loperamid und Pimozid induzierten Zelltod verstärkt. Diese Ergebnisse verdeutlichen die duale, kontextbezogene Rolle der Autophagie für das Überleben der Zelle.

Zusammenfassend wurden in dieser Studie zwei neue Signalwege untersucht, die einen Autophagie-abhängigen Zelltod in GBM-Zellen induzieren und somit potenziell für die Glioblastomtherapie relevant sein könnten. Zunächst wurde gezeigt, dass AT 101, eine Substanz, die derzeit als Antikrebsmittel untersucht wird, die Öffnung der mPTP, eine massive Schädigung der Mitochondrien und schließlich letale Mitophagie auslöst. In Übereinstimmung mit diesen Ergebnissen konnte bereits in mehreren Krebszellmodellen die zelltodfördernde Wirkung von exzessiver Mitophagie nachgewiesen werden (Kim et al., 2007; Sentelle et al., 2012; Wang et al., 2014). Zweitens konnte in dieser Studie bestätigt werden, dass die Substanzen Loperamid, Pimozide und STF-62247 einen autophagischen

Zelltod hervorrufen. Neben der Hyperaktivierung der Autophagie zeigten nähere Untersuchungen, dass Loperamid und Pimozid eine Beeinträchtigung des Lipidtransports auslösen, was eine lysosomale Membranpermeabilisation und die Aktivierung eines lysosomalen Zelltodes zur Folge hatte. Die hier durchgeführten Experimente weisen außerdem darauf hin, dass eine eindeutige Abgrenzung des autophagischen Zelltodes zu anderen neu identifizierten Zelltodarten, wie dem lysosomalen Zelltod, sehr schwierig ist, was bei der realistischen Definition dieser Zelltodwege in Zukunft bedacht werden sollte. Da drei bereits publizierte, den autophagischen Zelltod-induzierende Substanzen, nämlich Imipramin + Ticlopidin, Loperamide und Pimozid (Zielke et al., 2018; Shchors et al., 2015), als funktionale Inhibitoren der sauren Sphingomelinase wirken und in dieser Studie starke lysosomale Lipotoxizität auslösten, könnte dies ein wichtiger, genereller Mechanismus beim Autophagie-abhängigen Zelltod sein.

Interessanterweise sind lysosomale Signalwege in Krebszellen häufig hochreguliert und tragen zur Tumor-Malignität bei (Perera et al., 2015; Sun et al., 2016). Zudem haben insbesondere Glioblastomzellen einen hohen Bedarf an Cholesterol (Villa et al., 2016). Deshalb könnte die durch Loperamid und Pimozid induzierte Beeinträchtigung des Cholesteroltransports sowie der lysosomalen Stabilität in Kombination mit der Induktion des autophagischen Zelltodes ein vielversprechender Ansatz für die Behandlung von Glioblastomen sein. Da das bereits in der Klinik zugelassene Antipsychotikum Pimozid im Gegensatz zu Loperamid die Blut-Hirn-Schranke problemlos überquert, ist diese Substanz möglicherweise für die Glioblastom-Therapie von besonderem Interesse.

9 Literature

Adrain C, Creagh EM, Martin SJ (2001) Apoptosis-associated release of Smac/DIABLO from mitochondria requires active caspases and is blocked by Bcl-2. EMBO J 20: 6627-6636.

Aits S, Jäättelä M (2013) Lysosomal cell death at a glance. J Cell Sci 126: 1905-1912.

Alers S, Löffler AS, Wesselborg S, Stork B (2012) Role of AMPK-mTOR-Ulk1/2 in the regulation of autophagy: cross talk, shortcuts, and feedbacks. Mol Cell Biol 32: 2-11.

Alessi DR, Andjelkovic M, Caudwell B, Cron P, Morrice N, Cohen P, Hemmings BA (1996) Mechanism of activation of protein kinase B by insulin and IGF-1. EMBO J 15: 6541-6551.

Allen GFG, Toth R, James J, Ganley IG (2013) Loss of iron triggers PINK1/Parkin-independent mitophagy. EMBO Rep 14: 1127-1135.

Alyautdin RN, Petrov VE, Langer K, Berthold A, Kharkevich DA, Kreuter J (1997) Delivery of loperamide across the blood-brain barrier with polysorbate 80-coated polybutylcyanoacrylate nanoparticles. Pharm Res 14: 325-328.

Amaya C, Fader CM, Colombo MI (2015) Autophagy and proteins involved in vesicular trafficking. FEBS Lett 589: 3343-3353.

Anding AL, Baehrecke EH (2017) Cleaning house: selective autophagy of organelles. Dev Cell 41: 10-22.

Arnandis T, Ferrer-Vicens I, García-Trevijano ER, Miralles VJ, García C, Torres L, Viña JR, Zaragozá R (2012) Calpains mediate epithelial-cell death during mammary gland involution: mitochondria and lysosomal destabilization. Cell Death Differ 19: 1536-1548.

Asai A, Miyagi Y, Sugiyama A, Gamanuma M, Hong SH, Takamoto S, Nomura K, Matsutani M, Takakura K, Kuchino Y (1994) Negative effects of wild-type p53 and s-Myc on cellular growth and tumorigenicity of glioma cells. Implication of the tumor suppressor genes for gene therapy. J Neurooncol 19: 259-268.

Ashburner M, Ball CA, Blake JA, Botstein D, Butler H, Cherry JM, Davis AP, Dolinski K, Dwight SS, Eppig JT, et al (2000) Gene ontology. Tool for the unification of biology. The Gene Ontology Consortium. Nat Genet 25: 25-29.

Ashrafi G, Schwarz TL (2013) The pathways of mitophagy for quality control and clearance of mitochondria. Cell Death Differ 20: 31-42.

Axe EL, Walker SA, Manifava M, Chandra P, Roderick HL, Habermann A, Griffiths G, Ktistakis NT (2008) Autophagosome formation from membrane compartments enriched in phosphatidylinositol 3-phosphate and dynamically connected to the endoplasmic reticulum. J Cell Biol 182: 685-701.

Bansal S, Biswas G, Avadhani NG (2014) Mitochondria-targeted heme oxygenase-1 induces oxidative stress and mitochondrial dysfunction in macrophages, kidney fibroblasts and in chronic alcohol hepatotoxicity. Redox Biol 2: 273-283.

Barani IJ, Larson DA (2015) Radiation therapy of glioblastoma. Cancer Treat Res 163: 49-73.

Bardou P, Mariette J, Escudié F, Djemiel C, Klopp C (2014) jvenn: an interactive Venn diagram viewer. BMC Bioinformatics 15: 293.

Bauer M, Zeitlinger M, Karch R, Matzneller P, Stanek J, Jäger W, Böhmdorfer M, Wadsak W, Mitterhauser M, Bankstahl JP, et al (2012) Pgp-mediated interaction between (*R*)-[^{11}C]verapamil and tariquidar at the human blood-brain barrier: a comparison with rat data. Clin Pharmacol Ther 91: 227-233.

Behrends C, Sowa ME, Gygi SP, Harper JW (2010) Network organization of the human autophagy system. Nature 466: 68-76.

Bernardi P (2013) The mitochondrial permeability transition pore: a mystery solved? Front Physiol 4: 95.

Bernardi P (2018) Why F-ATP synthase remains a strong candidate as the mitochondrial permeability transition pore. Front Physiol 9: 1543.

Bernardi P, Di Lisa F (2015) The mitochondrial permeability transition pore: molecular nature and role as a target in cardioprotection. J Mol Cell Cardiol 78: 100-106.

Bialik S, Dasari SK, Kimchi A (2018) Autophagy-dependent cell death - where, how and why a cell eats itself to death. J Cell Sci 131.

Blommaart EF, Krause U, Schellens JP, Vreeling-Sindelárová H, Meijer AJ (1997) The phosphatidylinositol 3-kinase inhibitors wortmannin and LY294002 inhibit autophagy in isolated rat hepatocytes. Eur J Biochem 243: 240-246.

Bonora M, Pinton P (2014) The mitochondrial permeability transition pore and cancer: molecular mechanisms involved in cell death. Front Oncol 4: 302.

Bordet T, Buisson B, Michaud M, Drouot C, Galéa P, Delaage P, Akentieva NP, Evers AS, Covey DF, Ostuni MA, et al (2007) Identification and characterization of cholest-4-en-3-one, oxime (TRO19622), a novel drug candidate for amyotrophic lateral sclerosis. J Pharmacol Exp Ther 322: 709-720.

Boya P, Kroemer G (2008) Lysosomal membrane permeabilization in cell death. Oncogene 27: 6434-6451.

Bradford MM (1976) A rapid and sensitive method for the quantitation of microgram quantities of protein utilizing the principle of protein-dye binding. Anal Biochem 72: 248-254.

Brand MD (2010) The sites and topology of mitochondrial superoxide production. Exp Gerontol 45: 466-472.

Burton GJ, Jauniaux E (2011) Oxidative stress. Best Pract Res Clin Obstet Gynaecol 25: 287-299.

Bustin SA (2000) Absolute quantification of mRNA using real-time reverse transcription polymerase chain reaction assays. J Mol Endocrinol 25: 169-193.

Capper D, Jones DTW, Sill M, Hovestadt V, Schrimpf D, Sturm D, Koelsche C, Sahm F, Chavez L, Reuss DE, et al (2018) DNA methylation-based classification of central nervous system tumours. Nature 555: 469-474.

Carchman EH, Rao J, Loughran PA, Rosengart MR, Zuckerbraun BS (2011) Heme oxygenase-1-mediated autophagy protects against hepatocyte cell death and hepatic injury from infection/sepsis in mice. Hepatology 53: 2053-2062.

Cea M, Cagnetta A, Fulciniti M, Tai Y-T, Hideshima T, Chauhan D, Roccaro A, Sacco A, Calimeri T, Cottini F, et al (2012) Targeting NAD^+ salvage pathway induces autophagy in multiple myeloma cells via mTORC1 and extracellular signal-regulated kinase (ERK1/2) inhibition. Blood 120: 3519-3529.

Chauhan S, Kumar S, Jain A, Ponpuak M, Mudd MH, Kimura T, Choi SW, Peters R, Mandell M, Bruun J-A, et al (2016) TRIMs and Galectins globally cooperate and TRIM16 and Galectin-3 co-direct autophagy in endomembrane damage homeostasis. Dev Cell 39: 13-27.

Chourasia AH, Boland ML, Macleod KF (2015) Mitophagy and cancer. Cancer Metab 3: 4.

Chu B-B, Liao Y-C, Qi W, Xie C, Du X, Wang J, Yang H, Miao H-H, Li B-L, Song B-L (2015) Cholesterol transport through lysosome-peroxisome membrane contacts. Cell 161: 291-306.

Chu CT, Ji J, Dagda RK, Jiang JF, Tyurina YY, Kapralov AA, Tyurin VA, Yanamala N, Shrivastava IH, Mohammadyani D, et al (2013) Cardiolipin externalization to the outer mitochondrial membrane acts as an elimination signal for mitophagy in neuronal cells. Nat Cell Biol 15: 1197-1205.

Church J, Fletcher EJ, Abdel-Hamid K, MacDonald JF (1994) Loperamide blocks high-voltage-activated calcium channels and N-methyl-D-aspartate-evoked responses in rat and mouse cultured hippocampal pyramidal neurons. Mol Pharmacol 45: 747-757.

Cianfanelli V, Fuoco C, Lorente M, Salazar M, Quondamatteo F, Gherardini PF, Zio D de, Nazio F, Antonioli M, D'Orazio M, et al (2015) AMBRA1 links autophagy to cell proliferation and tumorigenesis by promoting c-Myc dephosphorylation and degradation. Nat Cell Biol 17: 20-30.

Cleland MM, Norris KL, Karbowski M, Wang C, Suen D-F, Jiao S, George NM, Luo X, Li Z, Youle RJ (2011) Bcl-2 family interaction with the mitochondrial morphogenesis machinery. Cell Death Differ 18: 235-247.

Constantin M, Choi AJS, Cloonan SM, Ryter SW (2012) Therapeutic potential of heme oxygenase-1/carbon monoxide in lung disease. Int J Hypertens 2012: 859235.

Corcelle-Termeau E, Vindeløv SD, Hämälistö S, Mograbi B, Keldsbo A, Bräsen JH, Favaro E, Adam D, Szyniarowski P, Hofman P, et al (2016) Excess sphingomyelin disturbs ATG9A trafficking and autophagosome closure. Autophagy 12: 833-849.

Cornillon S, Foa C, Davoust J, Buonavista N, Gross JD, Golstein P (1994) Programmed cell death in *Dictyostelium*. J Cell Sci 107 (Pt 10): 2691-2704.

Czabotar PE, Lessene G, Strasser A, Adams JM (2014) Control of apoptosis by the BCL-2 protein family: implications for physiology and therapy. Nat Rev Mol Cell Biol 15: 49-63.

Dai H, Meng W, Kaufmann S (2016) BCL2 family, mitochondrial apoptosis, and beyond. Cancer Transl Med 2: 7.

Daido S, Kanzawa T, Yamamoto A, Takeuchi H, Kondo Y, Kondo S (2004) Pivotal role of the cell death factor BNIP3 in ceramide-induced autophagic cell death in malignant glioma cells. Cancer Res 64: 4286-4293.

Danial NN, Korsmeyer SJ (2004) Cell death: critical control points. Cell 116: 205-219.

Das G, Shravage BV, Baehrecke EH (2012) Regulation and function of autophagy during cell survival and cell death. Cold Spring Harb Perspect Biol 4.

Dasari SK, Bialik S, Levin-Zaidman S, Levin-Salomon V, Merrill AH, Futerman AH, Kimchi A (2017) Signalome-wide RNAi screen identifies GBA1 as a positive mediator of autophagic cell death. Cell Death Differ 24: 1288-1302.

Davis ME (2016) Glioblastoma: overview of disease and treatment. Clin J Oncol Nurs 20: S2-8.

de Duve C (1983) Lysosomes revisited. Eur J Biochem 137: 391-397.

Degenhardt K, Mathew R, Beaudoin B, Bray K, Anderson D, Chen G, Mukherjee C, Shi Y, Gélinas C, Fan Y, et al (2006) Autophagy promotes tumor cell survival and restricts necrosis, inflammation, and tumorigenesis. Cancer Cell 10: 51-64.

DeHaven-Hudkins DL, Burgos LC, Cassel JA, Daubert JD, DeHaven RN, Mansson E, Nagasaka H, Yu G, Yaksh T (1999) Loperamide (ADL 2-1294), an opioid antihyperalgesic agent with peripheral selectivity. J Pharmacol Exp Ther 289: 494-502.

Denton D, Shravage B, Simin R, Mills K, Berry DL, Baehrecke EH, Kumar S (2009) Autophagy, not apoptosis, is essential for midgut cell death in *Drosophila*. Curr Biol 19: 1741-1746.

Devereaux K, Dall'Armi C, Alcazar-Roman A, Ogasawara Y, Zhou X, Wang F, Yamamoto A, Camilli P de, Di Paolo G (2013) Regulation of mammalian autophagy by class II and III PI 3-kinases through PI3P synthesis. PLoS ONE 8: e76405.

Ding W-X, Yin X-M (2012) Mitophagy. Mechanisms, pathophysiological roles, and analysis. Biol Chem 393: 547-564.

Do R, Kiss RS, Gaudet D, Engert JC (2009) Squalene synthase. A critical enzyme in the cholesterol biosynthesis pathway. Clin Genet 75: 19-29.

Doench JG, Hartenian E, Graham DB, Tothova Z, Hegde M, Smith I, Sullender M, Ebert BL, Xavier RJ, Root DE (2014) Rational design of highly active sgRNAs for CRISPR-Cas9-mediated gene inactivation. Nat Biotechnol 32: 1262-1267.

Domagala A, Fidyt K, Bobrowicz M, Stachura J, Szczygiel K, Firczuk M (2018) Typical and atypical inducers of lysosomal cell death: a promising anticancer strategy. Int J Mol Sci 19.

Dooley HC, Razi M, Polson HEJ, Girardin SE, Wilson MI, Tooze SA (2014) WIPI2 links LC3 conjugation with PI3P, autophagosome formation, and pathogen clearance by recruiting Atg12-5-16L1. Mol Cell 55: 238-252.

Drake LE, Springer MZ, Poole LP, Kim CJ, Macleod KF (2017) Expanding perspectives on the significance of mitophagy in cancer. Semin Cancer Biol 47: 110-124.

Dunn WA, Cregg JM, Kiel JAKW, van der Klei IJ, Oku M, Sakai Y, Sibirny AA, Stasyk OV, Veenhuis M (2005) Pexophagy: the selective autophagy of peroxisomes. Autophagy 1: 75-83.

Elmaci I, Altinoz MA (2018) Targeting the cellular schizophrenia. Likely employment of the antipsychotic agent pimozide in treatment of refractory cancers and glioblastoma. Crit Rev Oncol Hematol 128: 96-109.

Endo H, Nito C, Kamada H, Nishi T, Chan PH (2006) Activation of the Akt/GSK3beta signaling pathway mediates survival of vulnerable hippocampal neurons after transient global cerebral ischemia in rats. J Cereb Blood Flow Metab 26: 1479-1489.

Faraz S, Pannullo S, Rosenblum M, Smith A, Wernicke AG (2016) Long-term survival in a patient with glioblastoma on antipsychotic therapy for schizophrenia: a case report and literature review. Ther Adv Med Oncol 8: 421-428.

Fass E, Shvets E, Degani I, Hirschberg K, Elazar Z (2006) Microtubules support production of starvation-induced autophagosomes but not their targeting and fusion with lysosomes. J Biol Chem 281: 36303-36316.

Fehrenbacher N, Bastholm L, Kirkegaard-Sørensen T, Rafn B, Bøttzauw T, Nielsen C, Weber E, Shirasawa S, Kallunki T, Jäättelä M (2008) Sensitization to the lysosomal cell death pathway by oncogene-induced down-regulation of lysosome-associated membrane proteins 1 and 2. Cancer Res 68: 6623-6633.

Feng Y, He D, Yao Z, Klionsky DJ (2014) The machinery of macroautophagy. Cell Res 24: 24-41.

Frank S, Gaume B, Bergmann-Leitner ES, Leitner WW, Robert EG, Catez F, Smith CL, Youle RJ (2001) The role of dynamin-related protein 1, a mediator of mitochondrial fission, in apoptosis. Dev Cell 1: 515-525.

Freedman SB, Patel S, Marwood R, Emms F, Seabrook GR, Knowles MR, McAllister G (1994) Expression and pharmacological characterization of the human D3 dopamine receptor. J Pharmacol Exp Ther 268: 417-426.

Friedman JR, Nunnari J (2014) Mitochondrial form and function. Nature 505: 335-343.

Fulda S, Kögel D (2015) Cell death by autophagy: emerging molecular mechanisms and implications for cancer therapy. Oncogene 34: 5105-5113.

Gabaldón T, Huynen MA (2004) Shaping the mitochondrial proteome. Biochim Biophys Acta 1659: 212-220.

Gabandé-Rodríguez E, Boya P, Labrador V, Dotti CG, Ledesma MD (2014) High sphingomyelin levels induce lysosomal damage and autophagy dysfunction in Niemann Pick disease type A. Cell Death Differ 21: 864-875.

Galluzzi L, Aaronson SA, Abrams J, Alnemri ES, Andrews DW, Baehrecke EH, Bazan NG, Blagosklonny MV, Blomgren K, Borner C, et al (2009) Guidelines for the use and interpretation of assays for monitoring cell death in higher eukaryotes. Cell Death Differ 16: 1093-1107.

Galluzzi L, Bravo-San Pedro JM, Kepp O, Kroemer G (2016) Regulated cell death and adaptive stress responses. Cell Mol Life Sci 73: 2405-2410.

Galluzzi L, Morselli E, Kepp O, Vitale I, Younes AB, Maiuri MC, Kroemer G (2012) Evaluation of rapamycin-induced cell death. Methods Mol Biol 821: 125-169.

Galluzzi L, Vitale I, Aaronson SA, Abrams JM, Adam D, Agostinis P, Alnemri ES, Altucci L, Amelio I, Andrews DW, et al (2018) Molecular mechanisms of cell death. Recommendations of the Nomenclature Committee on Cell Death 2018. Cell Death Differ 25: 486-541.

Garcia-Garcia A, Anandhan A, Burns M, Chen H, Zhou Y, Franco R (2013) Impairment of Atg5-dependent autophagic flux promotes paraquat- and MPP^+-induced apoptosis but not rotenone or 6-hydroxydopamine toxicity. Toxicol Sci 136: 166-182.

Garneau JE, Dupuis M-È, Villion M, Romero DA, Barrangou R, Boyaval P, Fremaux C, Horvath P, Magadán AH, Moineau S (2010) The CRISPR/Cas bacterial immune system cleaves bacteriophage and plasmid DNA. Nature 468: 67-71.

Georgakopoulos ND, Wells G, Campanella M (2017) The pharmacological regulation of cellular mitophagy. Nat Chem Biol 13: 136-146.

German JB, Smilowitz JT, Zivkovic AM (2006) Lipoproteins. When size really matters. Curr Opin Colloid Interface Sci 11: 171-183.

Ginet V, Puyal J, Rummel C, Aubry D, Breton C, Cloux A-J, Majjigapu SR, Sordat B, Vogel P, Bruzzone S, et al (2014) A critical role of autophagy in antileukemia/lymphoma effects of APO866, an inhibitor of NAD biosynthesis. Autophagy 10: 603-617.

Go G-W, Mani A (2012) Low-density lipoprotein receptor (LDLR) family orchestrates cholesterol homeostasis. Yale J Biol Med 85: 19-28.

Goberdhan DCI, Wilson C, Harris AL (2016) Amino acid sensing by mTORC1: intracellular transporters mark the spot. Cell Metab 23: 580-589.

Gondi CS, Rao JS (2013) Cathepsin B as a cancer target. Expert Opin Ther Targets 17: 281-291.

Gozuacik D, Kimchi A (2004) Autophagy as a cell death and tumor suppressor mechanism. Oncogene 23: 2891-2906.

Green DR, Fitzgerald P (2016) Just so stories about the evolution of apoptosis. Curr Biol 26: R620-R627.

Green DR, Levine B (2014) To be or not to be? How selective autophagy and cell death govern cell fate. Cell 157: 65-75.

Gulbins A, Schumacher F, Becker KA, Wilker B, Soddemann M, Boldrin F, Müller CP, Edwards MJ, Goodman M, Caldwell CC, et al (2018) Antidepressants act by inducing autophagy controlled by sphingomyelin-ceramide. Mol Psychiatry 23: 2324-2346.

Gupta M, Djalilvand A, Brat DJ (2005) Clarifying the diffuse gliomas. An update on the morphologic features and markers that discriminate oligodendroglioma from astrocytoma. Am J Clin Pathol 124: 755-768.

Gwinn DM, Shackelford DB, Egan DF, Mihaylova MM, Mery A, Vasquez DS, Turk BE, Shaw RJ (2008) AMPK phosphorylation of raptor mediates a metabolic checkpoint. Mol Cell 30: 214-226.

Hanna RA, Quinsay MN, Orogo AM, Giang K, Rikka S, Gustafsson ÅB (2012) Microtubule-associated protein 1 light chain 3 (LC3) interacts with Bnip3 protein to selectively remove endoplasmic reticulum and mitochondria via autophagy. J Biol Chem 287: 19094-19104.

Hardwick JM, Youle RJ (2009) SnapShot: BCL-2 proteins. Cell 138: 404, 404.e1.

Hawk MA, Gorsuch CL, Fagan P, Lee C, Kim SE, Hamann JC, Mason JA, Weigel KJ, Tsegaye MA, Shen L, et al (2018) RIPK1-mediated induction of mitophagy compromises the viability of extracellular-matrix-detached cells. Nat Cell Biol 20: 272-284.

He C, Klionsky DJ (2009) Regulation mechanisms and signaling pathways of autophagy. Annu Rev Genet 43: 67-93.

Heras-Sandoval D, Pérez-Rojas JM, Hernández-Damián J, Pedraza-Chaverri J (2014) The role of PI3K/AKT/mTOR pathway in the modulation of autophagy and the clearance of protein aggregates in neurodegeneration. Cell Signal 26: 2694-2701.

Hernández-Tiedra S, Fabriàs G, Dávila D, Salanueva ÍJ, Casas J, Montes LR, Antón Z, García-Taboada E, Salazar-Roa M, Lorente M, et al (2016) Dihydroceramide accumulation mediates cytotoxic autophagy of cancer cells via autolysosome destabilization. Autophagy 12: 2213-2229.

Hetschko H, Voss V, Senft C, Seifert V, Prehn JHM, Kögel D (2008) BH3 mimetics reactivate autophagic cell death in anoxia-resistant malignant glioma cells. Neoplasia 10: 873-885.

Hirota Y, Yamashita S-i, Kurihara Y, Jin X, Aihara M, Saigusa T, Kang D, Kanki T (2015) Mitophagy is primarily due to alternative autophagy and requires the MAPK1 and MAPK14 signaling pathways. Autophagy 11: 332-343.

Holland EC (2000) Glioblastoma multiforme. The terminator. Proc Natl Acad Sci U S A 97: 6242-6244.

Hsu PD, Scott DA, Weinstein JA, Ran FA, Konermann S, Agarwala V, Li Y, Fine EJ, Wu X, Shalem O, et al (2013) DNA targeting specificity of RNA-guided Cas9 nucleases. Nat Biotechnol 31: 827-832.

Huang C-Y, Kuo W-W, Ho T-J, Chiang S-F, Pai P-Y, Lin J-Y, Lin D-Y, Kuo C-H (2018) Rab9-dependent autophagy is required for the IGF-IIR triggering mitophagy to eliminate damaged mitochondria. J Cell Physiol 233: 7080-7091.

Hull TD, Boddu R, Guo L, Tisher CC, Traylor AM, Patel B, Joseph R, Prabhu SD, Suliman HB, Piantadosi CA, et al (2016) Heme oxygenase-1 regulates mitochondrial quality control in the heart. JCI Insight 1: e85817.

Inbal B, Bialik S, Sabanay I, Shani G, Kimchi A (2002) DAP kinase and DRP-1 mediate membrane blebbing and the formation of autophagic vesicles during programmed cell death. J Cell Biol 157: 455-468.

Itakura E, Kishi-Itakura C, Koyama-Honda I, Mizushima N (2012) Structures containing Atg9A and the ULK1 complex independently target depolarized mitochondria at initial stages of Parkin-mediated mitophagy. J Cell Sci 125: 1488-1499.

Izzo V, Bravo-San Pedro JM, Sica V, Kroemer G, Galluzzi L (2016) Mitochondrial permeability transition: new findings and persisting uncertainties. Trends Cell Biol 26: 655-667.

Jackson WT, Giddings TH, Taylor MP, Mulinyawe S, Rabinovitch M, Kopito RR, Kirkegaard K (2005) Subversion of cellular autophagosomal machinery by RNA viruses. PLoS Biol 3: e156.

Jandaghi P, Najafabadi HS, Bauer AS, Papadakis AI, Fassan M, Hall A, Monast A, von Knebel Doeberitz M, Neoptolemos JP, Costello E, et al (2016) Expression of DRD2 is increased in human pancreatic ductal adenocarcinoma and inhibitors slow tumor growth in mice. Gastroenterology 151: 1218-1231.

Jawhari S, Ratinaud M-H, Verdier M (2016) Glioblastoma, hypoxia and autophagy. A survival-prone 'ménage-à-trois'. Cell Death Dis 7: e2434.

Jiang T, Harder B, La Rojo de Vega M, Wong PK, Chapman E, Zhang DD (2015) p62 links autophagy and Nrf2 signaling. Free Radic Biol Med 88: 199-204.

Jiang Z, Zheng X, Rich KM (2003) Down-regulation of Bcl-2 and Bcl-xL expression with bispecific antisense treatment in glioblastoma cell lines induce cell death. J Neurochem 84: 273-281.

Jost PJ, Grabow S, Gray D, McKenzie MD, Nachbur U, Huang DCS, Bouillet P, Thomas HE, Borner C, Silke J, et al (2009) XIAP discriminates between type I and type II FAS-induced apoptosis. Nature 460: 1035-1039.

Kågedal K, Zhao M, Svensson I, Brunk UT (2001) Sphingosine-induced apoptosis is dependent on lysosomal proteases. Biochem J 359: 335-343.

Kaizuka T, Morishita H, Hama Y, Tsukamoto S, Matsui T, Toyota Y, Kodama A, Ishihara T, Mizushima T, Mizushima N (2016) An autophagic flux probe that releases an internal control. Mol Cell 64: 835-849.

Kalla NR, Sud S (1990) Distribution of gossypol. Acta Eur Fertil 21: 77-80.

Kanki T, Wang K, Cao Y, Baba M, Klionsky DJ (2009) Atg32 is a mitochondrial protein that confers selectivity during mitophagy. Dev Cell 17: 98-109.

Kanzawa T, Germano IM, Komata T, Ito H, Kondo Y, Kondo S (2004) Role of autophagy in temozolomide-induced cytotoxicity for malignant glioma cells. Cell Death Differ 11: 448-457.

Kanzawa T, Zhang L, Xiao L, Germano IM, Kondo Y, Kondo S (2005) Arsenic trioxide induces autophagic cell death in malignant glioma cells by upregulation of mitochondrial cell death protein BNIP3. Oncogene 24: 980-991.

Kast RE (2010) Glioblastoma chemotherapy adjunct via potent serotonin receptor-7 inhibition using currently marketed high-affinity antipsychotic medicines. Br J Pharmacol 161: 481-487.

Katayama H, Kogure T, Mizushima N, Yoshimori T, Miyawaki A (2011) A sensitive and quantitative technique for detecting autophagic events based on lysosomal delivery. Chem Biol 18: 1042-1052.

Katayama M, Kawaguchi T, Berger MS, Pieper RO (2007) DNA damaging agent-induced autophagy produces a cytoprotective adenosine triphosphate surge in malignant glioma cells. Cell Death Differ 14: 548-558.

Kaza N, Kohli L, Graham CD, Klocke BJ, Carroll SL, Roth KA (2014) BNIP3 regulates AT101 [(-)-gossypol] induced death in malignant peripheral nerve sheath tumor cells. PLoS ONE 9: e96733.

Kerr JF, Wyllie AH, Currie AR (1972) Apoptosis: a basic biological phenomenon with wide-ranging implications in tissue kinetics. Br J Cancer 26: 239-257.

Khaminets A, Behl C, Dikic I (2016) Ubiquitin-dependent and independent signals in selective autophagy. Trends Cell Biol 26: 6-16.

Kim EH, Sohn S, Kwon HJ, Kim SU, Kim M-J, Lee S-J, Choi KS (2007) Sodium selenite induces superoxide-mediated mitochondrial damage and subsequent autophagic cell death in malignant glioma cells. Cancer Res 67: 6314-6324.

Kim H, Rafiuddin-Shah M, Tu H-C, Jeffers JR, Zambetti GP, Hsieh JJ-D, Cheng EH-Y (2006) Hierarchical regulation of mitochondrion-dependent apoptosis by BCL-2 subfamilies. Nat Cell Biol 8: 1348-1358.

Kimura S, Noda T, Yoshimori T (2007) Dissection of the autophagosome maturation process by a novel reporter protein, tandem fluorescent-tagged LC3. Autophagy 3: 452-460.

Kirienko NV, Ausubel FM, Ruvkun G (2015) Mitophagy confers resistance to siderophore-mediated killing by *Pseudomonas aeruginosa*. Proc Natl Acad Sci U S A 112: 1821-1826.

Kirkegaard T, Jäättelä M (2009) Lysosomal involvement in cell death and cancer. Biochim Biophys Acta 1793: 746-754.

Kitada T, Asakawa S, Hattori N, Matsumine H, Yamamura Y, Minoshima S, Yokochi M, Mizuno Y, Shimizu N (1998) Mutations in the parkin gene cause autosomal recessive juvenile parkinsonism. Nature 392: 605-608.

Klionsky DJ (2008) Autophagy revisited: a conversation with Christian de Duve. Autophagy 4: 740-743.

Klionsky DJ, Abdelmohsen K, Abe A, Abedin MJ, Abeliovich H, Acevedo Arozena A, Adachi H, Adams CM, Adams PD, Adeli K, et al (2016) Guidelines for the use and interpretation of assays for monitoring autophagy (3rd edition). Autophagy 12: 1-222.

Klionsky DJ, Cuervo AM, Dunn WA, Levine B, van der Klei I, Seglen PO (2007) How shall I eat thee? Autophagy 3: 413-416.

Klutzny S, Lesche R, Keck M, Kaulfuss S, Schlicker A, Christian S, Sperl C, Neuhaus R, Mowat J, Steckel M, et al (2017) Functional inhibition of acid sphingomyelinase by Fluphenazine triggers hypoxia-specific tumor cell death. Cell Death Dis 8: e2709.

Kögel D, Fulda S, Mittelbronn M (2010) Therapeutic exploitation of apoptosis and autophagy for glioblastoma. Anticancer Agents Med Chem 10: 438-449.

Kölzer M, Werth N, Sandhoff K (2004) Interactions of acid sphingomyelinase and lipid bilayers in the presence of the tricyclic antidepressant desipramine. FEBS Lett 559: 96-98.

Komatsu M, Kageyama S, Ichimura Y (2012) p62/SQSTM1/A170: physiology and pathology. Pharmacol Res 66: 457-462.

Kondratskyi A, Kondratska K, Skryma R, Klionsky DJ, Prevarskaya N (2018) Ion channels in the regulation of autophagy. Autophagy 14: 3-21.

Kornhuber J, Muehlbacher M, Trapp S, Pechmann S, Friedl A, Reichel M, Mühle C, Terfloth L, Groemer TW, Spitzer GM, et al (2011) Identification of novel functional inhibitors of acid sphingomyelinase. PLoS ONE 6: e23852.

Kornhuber J, Tripal P, Reichel M, Mühle C, Rhein C, Muehlbacher M, Groemer TW, Gulbins E (2010) Functional inhibitors of acid sphingomyelinase (FIASMAs). A novel pharmacological group of drugs with broad clinical applications. Cell Physiol Biochem 26: 9-20.

Kornhuber J, Tripal P, Reichel M, Terfloth L, Bleich S, Wiltfang J, Gulbins E (2008) Identification of new functional inhibitors of acid sphingomyelinase using a structure-property-activity relation model. J Med Chem 51: 219-237.

Kosta A, Roisin-Bouffay C, Luciani M-F, Otto GP, Kessin RH, Golstein P (2004) Autophagy gene disruption reveals a non-vacuolar cell death pathway in *Dictyostelium*. J Biol Chem 279: 48404-48409.

Krex D, Klink B, Hartmann C, Deimling A von, Pietsch T, Simon M, Sabel M, Steinbach JP, Heese O, Reifenberger G, et al (2007) Long-term survival with glioblastoma multiforme. Brain 130: 2596-2606.

Kristiana I, Sharpe LJ, Catts VS, Lutze-Mann LH, Brown AJ (2010) Antipsychotic drugs upregulate lipogenic gene expression by disrupting intracellular trafficking of lipoprotein-derived cholesterol. Pharmacogenomics J 10: 396-407.

Kristiana I, Yang H, Brown AJ (2008) Different kinetics of cholesterol delivery to components of the cholesterol homeostatic machinery. Implications for cholesterol trafficking to the endoplasmic reticulum. Biochim Biophys Acta 1781: 724-730.

Kroemer G, Mariño G, Levine B (2010) Autophagy and the integrated stress response. Mol Cell 40: 280-293.

Kruiswijk F, Labuschagne CF, Vousden KH (2015) p53 in survival, death and metabolic health: a lifeguard with a licence to kill. Nat Rev Mol Cell Biol 16: 393-405.

Kuma A, Komatsu M, Mizushima N (2017) Autophagy-monitoring and autophagy-deficient mice. Autophagy 13: 1619-1628.

Kurz T, Terman A, Gustafsson B, Brunk UT (2008a) Lysosomes and oxidative stress in aging and apoptosis. Biochim Biophys Acta 1780: 1291-1303.

Kurz T, Terman A, Gustafsson B, Brunk UT (2008b) Lysosomes in iron metabolism, ageing and apoptosis. Histochem Cell Biol 129: 389-406.

Kuzu OF, Gowda R, Noory MA, Robertson GP (2017) Modulating cancer cell survival by targeting intracellular cholesterol transport. Br J Cancer 117: 513-524.

Kwon M-Y, Park E, Lee S-J, Chung SW (2015) Heme oxygenase-1 accelerates erastin-induced ferroptotic cell death. Oncotarget 6: 24393-24403.

Laemmli UK (1970) Cleavage of structural proteins during the assembly of the head of bacteriophage T4. Nature 227: 680-685.

Lam D, Levraud J-P, Luciani M-F, Golstein P (2007) Autophagic or necrotic cell death in the absence of caspase and bcl-2 family members. Biochem Biophys Res Commun 363: 536-541.

Lane N, Martin W (2010) The energetics of genome complexity. Nature 467: 929-934.

Lathia JD, Mack SC, Mulkearns-Hubert EE, Valentim CLL, Rich JN (2015) Cancer stem cells in glioblastoma. Genes Dev 29: 1203-1217.

Lau A, Wang X-J, Zhao F, Villeneuve NF, Wu T, Jiang T, Sun Z, White E, Zhang DD (2010) A noncanonical mechanism of Nrf2 activation by autophagy deficiency. Direct interaction between Keap1 and p62. Mol Cell Biol 30: 3275-3285.

Lau A, Zheng Y, Tao S, Wang H, Whitman SA, White E, Zhang DD (2013) Arsenic inhibits autophagic flux, activating the Nrf2-Keap1 pathway in a p62-dependent manner. Mol Cell Biol 33: 2436-2446.

Lazarou M, Jin SM, Kane LA, Youle RJ (2012) Role of PINK1 binding to the TOM complex and alternate intracellular membranes in recruitment and activation of the E3 ligase Parkin. Dev Cell 22: 320-333.

Lazarou M, Sliter DA, Kane LA, Sarraf SA, Wang C, Burman JL, Sideris DP, Fogel AI, Youle RJ (2015) The ubiquitin kinase PINK1 recruits autophagy receptors to induce mitophagy. Nature 524: 309-314.

Le Guerroué F, Eck F, Jung J, Starzetz T, Mittelbronn M, Kaulich M, Behrends C (2017) Autophagosomal content profiling reveals an LC3C-dependent piecemeal mitophagy pathway. Mol Cell 68: 786-796.e6.

Lee J-K, Nam D-H, Lee J (2016) Repurposing antipsychotics as glioblastoma therapeutics: potentials and challenges. Oncol Lett 11: 1281-1286.

Lemasters JJ (2005) Selective mitochondrial autophagy, or mitophagy, as a targeted defense against oxidative stress, mitochondrial dysfunction, and aging. Rejuvenation Res 8: 3-5.

Levine B (2005) Eating oneself and uninvited guests: autophagy-related pathways in cellular defense. Cell 120: 159-162.

Li J, Zhu S, Kozono D, Ng K, Futalan D, Shen Y, Akers JC, Steed T, Kushwaha D, Schlabach M, et al (2014) Genome-wide shRNA screen revealed integrated mitogenic signaling between dopamine receptor D2 (DRD2) and epidermal growth factor receptor (EGFR) in glioblastoma. Oncotarget 5: 882-893.

Li Y, Inoki K, Yeung R, Guan K-L (2002) Regulation of TSC2 by 14-3-3 binding. J Biol Chem 277: 44593-44596.

Lian J, Wu X, He F, Karnak D, Tang W, Meng Y, Xiang D, Ji M, Lawrence TS, Xu L (2011) A natural BH3 mimetic induces autophagy in apoptosis-resistant prostate cancer via modulating Bcl-2-Beclin1 interaction at endoplasmic reticulum. Cell Death Differ 18: 60-71.

Liberman EA, Topaly VP, Tsofina LM, Jasaitis AA, Skulachev VP (1969) Mechanism of coupling of oxidative phosphorylation and the membrane potential of mitochondria. Nature 222: 1076-1078.

Lieberman AP, Puertollano R, Raben N, Slaugenhaupt S, Walkley SU, Ballabio A (2012) Autophagy in lysosomal storage disorders. Autophagy 8: 719-730.

Lieberman F (2017) Glioblastoma update: molecular biology, diagnosis, treatment, response assessment, and translational clinical trials. F1000Res 6: 1892.

Lima S, Takabe K, Newton J, Saurabh K, Young MM, Leopoldino AM, Hait NC, Roberts JL, Wang H-G, Dent P, et al (2018) TP53 is required for BECN1- and ATG5-dependent cell death induced by sphingosine kinase 1 inhibition. Autophagy 14: 942-957.

Lin C-W, Jan M-S, Kuo J-HS (2014) Autophagy-related gene expression analysis of wild-type and atg5 gene knockout mouse embryonic fibroblast cells treated with polyethylenimine. Mol Pharm 11: 3002-3008.

Lin D-C, Xu L, Chen Y, Yan H, Hazawa M, Doan N, Said JW, Ding L-W, Liu L-Z, Yang H, et al (2015) Genomic and functional analysis of the E3 ligase PARK2 in glioma. Cancer Res 75: 1815-1827.

Liu L, Du Feng, Chen G, Chen M, Zheng Q, Song P, Ma Q, Zhu C, Wang R, Qi W, et al (2012) Mitochondrial outer-membrane protein FUNDC1 mediates hypoxia-induced mitophagy in mammalian cells. Nat Cell Biol 14: 177-185.

Liu Y-L, Yang P-M, Shun C-T, Wu M-S, Weng J-R, Chen C-C (2010) Autophagy potentiates the anti-cancer effects of the histone deacetylase inhibitors in hepatocellular carcinoma. Autophagy 6: 1057-1065.

Long X, Ortiz-Vega S, Lin Y, Avruch J (2005) Rheb binding to mammalian target of rapamycin (mTOR) is regulated by amino acid sufficiency. J Biol Chem 280: 23433-23436.

Louis DN, Perry A, Reifenberger G, Deimling A von, Figarella-Branger D, Cavenee WK, Ohgaki H, Wiestler OD, Kleihues P, Ellison DW (2016) The 2016 World Health Organization classification of tumors of the central nervous system. A summary. Acta Neuropathol 131: 803-820.

Lu M-D, Li L-Y, Li P-H, You T, Wang F-H, Sun W-J, Zheng Z-Q (2017) Gossypol induces cell death by activating apoptosis and autophagy in HT-29 cells. Mol Med Rep 16: 2128-2132.

Luo X, Budihardjo I, Zou H, Slaughter C, Wang X (1998) Bid, a Bcl2 interacting protein, mediates cytochrome c release from mitochondria in response to activation of cell surface death receptors. Cell 94: 481-490.

Madeo F, Fröhlich E, Fröhlich K-U (1997) A yeast mutant showing diagnostic markers of early and late apoptosis. J Cell Biol 139: 729-734.

Maejima I, Takahashi A, Omori H, Kimura T, Takabatake Y, Saitoh T, Yamamoto A, Hamasaki M, Noda T, Isaka Y, et al (2013) Autophagy sequesters damaged lysosomes to control lysosomal biogenesis and kidney injury. EMBO J 32: 2336-2347.

Manning BD, Cantley LC (2007) AKT/PKB signaling: navigating downstream. Cell 129: 1261-1274.

Mantovani A, Garlanda C, Allavena P (2010) Molecular pathways and targets in cancer-related inflammation. Ann Med 42: 161-170.

Mariño G, Niso-Santano M, Baehrecke EH, Kroemer G (2014) Self-consumption: the interplay of autophagy and apoptosis. Nat Rev Mol Cell Biol 15: 81-94.

Martinet W, Roth L, Meyer GRY de (2017) Standard immunohistochemical assays to assess autophagy in mammalian tissue. Cells 6.

Marzolo M-P, Bu G (2009) Lipoprotein receptors and cholesterol in APP trafficking and proteolytic processing, implications for Alzheimer's disease. Semin Cell Dev Biol 20: 191-200.

Mauthe M, Orhon I, Rocchi C, Zhou X, Luhr M, Hijlkema K-J, Coppes RP, Engedal N, Mari M, Reggiori F (2018) Chloroquine inhibits autophagic flux by decreasing autophagosome-lysosome fusion. Autophagy 14: 1435-1455.

Maxfield FR, Wüstner D (2012) Analysis of cholesterol trafficking with fluorescent probes. Methods Cell Biol 108: 367-393.

Maycotte P, Thorburn A (2011) Autophagy and cancer therapy. Cancer Biol Ther 11: 127-137.

McLelland G-L, Soubannier V, Chen CX, McBride HM, Fon EA (2014) Parkin and PINK1 function in a vesicular trafficking pathway regulating mitochondrial quality control. EMBO J 33: 282-295.

McMaster CR (2001) Lipid metabolism and vesicle trafficking. More than just greasing the transport machinery. Biochem Cell Biol 79: 681-692.

Meyer N, Zielke S, Michaelis JB, Linder B, Warnsmann V, Rakel S, Osiewacz HD, Fulda S, Mittelbronn M, Münch C, et al (2018) AT 101 induces early mitochondrial dysfunction and HMOX1 (heme oxygenase 1) to trigger mitophagic cell death in glioma cells. Autophagy 14: 1693-1709.

Meyer NM (2015) Investigating the role of mitochondrial dysfunction and mitophagy in cell death induced with the BH3 mimetic (-)-Gossypol. unpublished Master thesis (Frankfurt, Germany).

Milosch N, Tanriöver G, Kundu A, Rami A, François J-C, Baumkötter F, Weyer SW, Samanta A, Jäschke A, Brod F, et al (2014) Holo-APP and G-protein-mediated signaling are required for sAPPα-induced activation of the Akt survival pathway. Cell Death Dis 5: e1391.

Miyai M, Tomita H, Soeda A, Yano H, Iwama T, Hara A (2017) Current trends in mouse models of glioblastoma. J Neurooncol 135: 423-432.

Moreno-Gonzalez G, Vandenabeele P, Krysko DV (2016) Necroptosis: a novel cell death modality and its potential relevance for critical care medicine. Am J Respir Crit Care Med 194: 415-428.

Moretti L, Attia A, Kim KW, Lu B (2007) Crosstalk between Bak/Bax and mTOR signaling regulates radiation-induced autophagy. Autophagy 3: 142-144.

Mrschtik M, Ryan KM (2015) Lysosomal proteins in cell death and autophagy. FEBS J 282: 1858-1870.

Murphy MP (2009) How mitochondria produce reactive oxygen species. Biochem J 417: 1-13.

Nakao A, Murase N, Ho C, Toyokawa H, Billiar TR, Kanno S (2005) Biliverdin administration prevents the formation of intimal hyperplasia induced by vascular injury. Circulation 112: 587-591.

Nakatogawa H (2013) Two ubiquitin-like conjugation systems that mediate membrane formation during autophagy. Essays Biochem 55: 39-50.

Narendra D, Tanaka A, Suen D-F, Youle RJ (2008) Parkin is recruited selectively to impaired mitochondria and promotes their autophagy. J Cell Biol 183: 795-803.

Narendra DP, Jin SM, Tanaka A, Suen D-F, Gautier CA, Shen J, Cookson MR, Youle RJ (2010) PINK1 is selectively stabilized on impaired mitochondria to activate Parkin. PLoS Biol 8: e1000298.

Neuspiel M, Schauss AC, Braschi E, Zunino R, Rippstein P, Rachubinski RA, Andrade-Navarro MA, McBride HM (2008) Cargo-selected transport from the mitochondria to peroxisomes is mediated by vesicular carriers. Curr Biol 18: 102-108.

Nobukuni T, Joaquin M, Roccio M, Dann SG, Kim SY, Gulati P, Byfield MP, Backer JM, Natt F, Bos JL, et al (2005) Amino acids mediate mTOR/raptor signaling through activation of class 3 phosphatidylinositol 3OH-kinase. Proc Natl Acad Sci U S A 102: 14238-14243.

Noda T (2017) Autophagy in the context of the cellular membrane-trafficking system. The enigma of Atg9 vesicles. Biochem Soc Trans 45: 1323-1331.

Novak I, Kirkin V, McEwan DG, Zhang J, Wild P, Rozenknop A, Rogov V, Löhr F, Popovic D, Occhipinti A, et al (2010) Nix is a selective autophagy receptor for mitochondrial clearance. EMBO Rep 11: 45-51.

Nunnari J, Suomalainen A (2012) Mitochondria: in sickness and in health. Cell 148: 1145-1159.

Ohgaki H, Kleihues P (2007) Genetic pathways to primary and secondary glioblastoma. Am J Pathol 170: 1445-1453.

Ordoñez R, Fernández A, Prieto-Domínguez N, Martínez L, García-Ruiz C, Fernández-Checa JC, Mauriz JL, González-Gallego J (2015) Ceramide metabolism regulates autophagy and apoptotic cell death induced by melatonin in liver cancer cells. J Pineal Res 59: 178-189.

Otterbein LE, Bach FH, Alam J, Soares M, Tao Lu H, Wysk M, Davis RJ, Flavell RA, Choi AM (2000) Carbon monoxide has anti-inflammatory effects involving the mitogen-activated protein kinase pathway. Nat Med 6: 422-428.

Paolillo M, Boselli C, Schinelli S (2018) Glioblastoma under siege: an overview of current therapeutic strategies. Brain Sci 8.

Papadopoulos C, Kirchner P, Bug M, Grum D, Koerver L, Schulze N, Poehler R, Dressler A, Fengler S, Arhzaouy K, et al (2017) VCP/p97 cooperates with YOD1, UBXD1 and PLAA to drive clearance of ruptured lysosomes by autophagy. EMBO J 36: 135-150.

Papadopoulos C, Meyer H (2017) Detection and clearance of damaged lysosomes by the endo-lysosomal damage response and lysophagy. Curr Biol 27: R1330-R1341.

Park SJ, Shin JH, Kim ES, Jo YK, Kim JH, Hwang JJ, Kim JC, Cho D-H (2012) Mitochondrial fragmentation caused by phenanthroline promotes mitophagy. FEBS Lett 586: 4303-4310.

Pattingre S, Bauvy C, Codogno P (2003) Amino acids interfere with the ERK1/2-dependent control of macroautophagy by controlling the activation of Raf-1 in human colon cancer HT-29 cells. J Biol Chem 278: 16667-16674.

Perera RM, Stoykova S, Nicolay BN, Ross KN, Fitamant J, Boukhali M, Lengrand J, Deshpande V, Selig MK, Ferrone CR, et al (2015) Transcriptional control of autophagy-lysosome function drives pancreatic cancer metabolism. Nature 524: 361-365.

Petersen NHT, Olsen OD, Groth-Pedersen L, Ellegaard A-M, Bilgin M, Redmer S, Ostenfeld MS, Ulanet D, Dovmark TH, Lønborg A, et al (2013) Transformation-associated changes in sphingolipid metabolism sensitize cells to lysosomal cell death induced by inhibitors of acid sphingomyelinase. Cancer Cell 24: 379-393.

Petronilli V, Penzo D, Scorrano L, Bernardi P, Di Lisa F (2001) The mitochondrial permeability transition, release of cytochrome c and cell death. Correlation with the duration of pore openings in situ. J Biol Chem 276: 12030-12034.

Ran FA, Hsu PD, Wright J, Agarwala V, Scott DA, Zhang F (2013) Genome engineering using the CRISPR-Cas9 system. Nat Protoc 8: 2281-2308.

Rao S, Tortola L, Perlot T, Wirnsberger G, Novatchkova M, Nitsch R, Sykacek P, Frank L, Schramek D, Komnenovic V, et al (2014) A dual role for autophagy in a murine model of lung cancer. Nat Commun 5: 3056.

Rhainds D, Brissette L (2004) The role of scavenger receptor class B type I (SR-BI) in lipid trafficking. defining the rules for lipid traders. Int J Biochem Cell Biol 36: 39-77.

Roberts RF, Tang MY, Fon EA, Durcan TM (2016) Defending the mitochondria. The pathways of mitophagy and mitochondrial-derived vesicles. Int J Biochem Cell Biol 79: 427-436.

Rolland SG, Lu Y, David CN, Conradt B (2009) The BCL-2-like protein CED-9 of *C. elegans* promotes FZO-1/Mfn1,2- and EAT-3/Opa1-dependent mitochondrial fusion. J Cell Biol 186: 525-540.

Rubinsztein DC, Codogno P, Levine B (2012) Autophagy modulation as a potential therapeutic target for diverse diseases. Nat Rev Drug Discov 11: 709-730.

Ryter SW, Alam J, Choi AMK (2006) Heme oxygenase-1/carbon monoxide: from basic science to therapeutic applications. Physiol Rev 86: 583-650.

Salazar M, Carracedo A, Salanueva ÍJ, Hernández-Tiedra S, Lorente M, Egia A, Vázquez P, Blázquez C, Torres S, García S, et al (2009) Cannabinoid action induces autophagy-mediated cell death through stimulation of ER stress in human glioma cells. J. Clin. Invest. 119: 1359-1372.

Santos-Lozano A, Villamandos García D, Sanchis-Gomar F, Fiuza-Luces C, Pareja-Galeano H, Garatachea N, Nogales Gadea G, Lucia A (2015) Niemann-Pick disease treatment. A systematic review of clinical trials. Ann Transl Med 3: 360.

Sazanov LA (2015) A giant molecular proton pump: structure and mechanism of respiratory complex I. Nat Rev Mol Cell Biol 16: 375-388.

Scarlatti F, Bauvy C, Ventruti A, Sala G, Cluzeaud F, Vandewalle A, Ghidoni R, Codogno P (2004) Ceramide-mediated macroautophagy involves inhibition of protein kinase B and up-regulation of beclin 1. J Biol Chem 279: 18384-18391.

Schmittgen TD, Livak KJ (2008) Analyzing real-time PCR data by the comparative C_T method. Nat Protoc 3: 1101-1108.

Schulze H, Sandhoff K (2011) Lysosomal lipid storage diseases. Cold Spring Harb Perspect Biol 3.

Schwarten M, Mohrlüder J, Ma P, Stoldt M, Thielmann Y, Stangler T, Hersch N, Hoffmann B, Merkel R, Willbold D (2009) Nix directly binds to GABARAP: a possible crosstalk between apoptosis and autophagy. Autophagy 5: 690-698.

Schweers RL, Zhang J, Randall MS, Loyd MR, Li W, Dorsey FC, Kundu M, Opferman JT, Cleveland JL, Miller JL, et al (2007) NIX is required for programmed mitochondrial clearance during reticulocyte maturation. Proc Natl Acad Sci U S A 104: 19500-19505.

Segala G, David M, Medina P de, Poirot MC, Serhan N, Vergez F, Mougel A, Saland E, Carayon K, Leignadier J, et al (2017) Dendrogenin A drives LXR to trigger lethal autophagy in cancers. Nat Commun 8: 1903.

Sentelle RD, Senkal CE, Jiang W, Ponnusamy S, Gencer S, Selvam SP, Ramshesh VK, Peterson YK, Lemasters JJ, Szulc ZM, et al (2012) Ceramide targets autophagosomes to mitochondria and induces lethal mitophagy. Nat Chem Biol 8: 831-838.

Serrano-Puebla A, Boya P (2016) Lysosomal membrane permeabilization in cell death. New evidence and implications for health and disease. Ann N Y Acad Sci 1371: 30-44.

Serrano-Puebla A, Boya P (2018) Lysosomal membrane permeabilization as a cell death mechanism in cancer cells. Biochem Soc Trans 46: 207-215.

Sharpe LJ, Brown AJ (2013) Controlling cholesterol synthesis beyond 3-hydroxy-3-methylglutaryl-CoA reductase (HMGCR). J Biol Chem 288: 18707-18715.

Shchors K, Evan G (2007) Tumor angiogenesis. Cause or consequence of cancer? Cancer Res 67: 7059-7061.

Shchors K, Massaras A, Hanahan D (2015) Dual targeting of the autophagic regulatory circuitry in gliomas with repurposed drugs elicits cell-lethal autophagy and therapeutic benefit. Cancer Cell 28: 456-471.

Shroff A, Reddy KVR (2018) Autophagy gene ATG5 knockdown upregulates apoptotic cell death during *Candida albicans* infection in human vaginal epithelial cells. Am J Reprod Immunol 80: e13056.

Sinha S, Levine B (2008) The autophagy effector Beclin 1: a novel BH3-only protein. Oncogene 27 Suppl 1: S137-48.

Soderquist RS, Eastman A (2016) BCL2 inhibitors as anticancer drugs: a plethora of misleading BH3 mimetics. Mol Cancer Ther 15: 2011-2017.

Soubannier V, McLelland G-L, Zunino R, Braschi E, Rippstein P, Fon EA, McBride HM (2012) A vesicular transport pathway shuttles cargo from mitochondria to lysosomes. Curr Biol 22: 135-141.

Stupp R, Taillibert S, Kanner AA, Kesari S, Steinberg DM, Toms SA, Taylor LP, Lieberman F, Silvani A, Fink KL, et al (2015) Maintenance therapy with tumor-treating fields plus temozolomide vs temozolomide alone for glioblastoma: a randomized clinical trial. JAMA 314: 2535-2543.

Suliman HB, Keenan JE, Piantadosi CA (2017) Mitochondrial quality-control dysregulation in conditional HO-1$^{-/-}$ mice. JCI Insight 2: e89676.

Sun T, Jiang D, Zhang L, Su Q, Mao W, Jiang C (2016) Expression profile of cathepsins indicates the potential of cathepsins B and D as prognostic factors in breast cancer patients. Oncol Lett 11: 575-583.

Tan SK, Jermakowicz A, Mookhtiar AK, Nemeroff CB, Schürer SC, Ayad NG (2018) Drug repositioning in glioblastoma: a pathway perspective. Front Pharmacol 9.

Tanaka A, Cleland MM, Xu S, Narendra DP, Suen D-F, Karbowski M, Youle RJ (2010) Proteasome and p97 mediate mitophagy and degradation of mitofusins induced by Parkin. J Cell Biol 191: 1367-1380.

Thakkar JP, Dolecek TA, Horbinski C, Ostrom QT, Lightner DD, Barnholtz-Sloan JS, Villano JL (2014) Epidemiologic and molecular prognostic review of glioblastoma. Cancer Epidemiol Biomarkers Prev 23: 1985-1996.

The Gene Ontology Consortium (2017) Expansion of the Gene Ontology knowledgebase and resources. Nucleic Acids Res 45: D331-D338.

Thornberry NA, Lazebnik Y (1998) Caspases: enemies within. Science 281: 1312-1316.

Turcotte S, Chan DA, Sutphin PD, Hay MP, Denny WA, Giaccia AJ (2008) A molecule targeting VHL-deficient renal cell carcinoma that induces autophagy. Cancer Cell 14: 90-102.

Tyanova S, Temu T, Sinitcyn P, Carlson A, Hein MY, Geiger T, Mann M, Cox J (2016) The Perseus computational platform for comprehensive analysis of (prote)omics data. Nat Methods 13: 731-740.

Ugland H, Naderi S, Brech A, Collas P, Blomhoff HK (2011) cAMP induces autophagy via a novel pathway involving ERK, cyclin E and Beclin 1. Autophagy 7: 1199-1211.

Ulbrich K, Knobloch T, Kreuter J (2011) Targeting the insulin receptor: nanoparticles for drug delivery across the blood-brain barrier (BBB). J Drug Target 19: 125-132.

Urra H, Dufey E, Lisbona F, Rojas-Rivera D, Hetz C (2013) When ER stress reaches a dead end. Biochim Biophys Acta 1833: 3507-3517.

Valente EM, Abou-Sleiman PM, Caputo V, Muqit MMK, Harvey K, Gispert S, Ali Z, Del Turco D, Bentivoglio AR, Healy DG, et al (2004) Hereditary early-onset Parkinson's disease caused by mutations in PINK1. Science 304: 1158-1160.

Vara D, Salazar M, Olea-Herrero N, Guzmán M, Velasco G, Díaz-Laviada I (2011) Anti-tumoral action of cannabinoids on hepatocellular carcinoma: role of AMPK-dependent activation of autophagy. Cell Death Differ 18: 1099-1111.

Villa E, Marchetti S, Ricci J-E (2018) No Parkin zone: mitophagy without Parkin. Trends Cell Biol 28: 882-895.

Villa GR, Hulce JJ, Zanca C, Bi J, Ikegami S, Cahill GL, Gu Y, Lum KM, Masui K, Yang H, et al (2016) An LXR-cholesterol axis creates a metabolic co-dependency for brain cancers. Cancer Cell 30: 683-693.

Vögeli B, Engilberge S, Girard E, Riobé F, Maury O, Erb TJ, Shima S, Wagner T (2018) Archaeal acetoacetyl-CoA thiolase/HMG-CoA synthase complex channels the intermediate via a fused CoA-binding site. Proc Natl Acad Sci U S A 115: 3380-3385.

Voss V, Senft C, Lang V, Ronellenfitsch MW, Steinbach JP, Seifert V, Kögel D (2010) The pan-Bcl-2 inhibitor (-)-gossypol triggers autophagic cell death in malignant glioma. Mol Cancer Res 8: 1002-1016.

Wagenknecht B, Glaser T, Naumann U, Kügler S, Isenmann S, Bähr M, Korneluk R, Liston P, Weller M (1999) Expression and biological activity of X-linked inhibitor of apoptosis (XIAP) in human malignant glioma. Cell Death Differ 6: 370-376.

Wang J, Jin L, Li X, Deng H, Chen Y, Lian Q, Ge R, Deng H (2013) Gossypol induces apoptosis in ovarian cancer cells through oxidative stress. Mol Biosyst 9: 1489-1497.

Wang RC, Wei Y, An Z, Zou Z, Xiao G, Bhagat G, White M, Reichelt J, Levine B (2012) Akt-mediated regulation of autophagy and tumorigenesis through Beclin 1 phosphorylation. Science 338: 956-959.

Wang W-j, Wang Y, Chen H-z, Xing Y-z, Li F-w, Zhang Q, Zhou B, Zhang H-k, Zhang J, Bian X-l, et al (2014) Orphan nuclear receptor TR3 acts in autophagic cell death via mitochondrial signaling pathway. Nat Chem Biol 10: 133-140.

Wang Y, Rao PN (1984) Effect of gossypol on DNA synthesis and cell cycle progression of mammalian cells in vitro. Cancer Res 44: 35-38.

Wang Z, Wen L, Zhu F, Wang Y, Xie Q, Chen Z, Li Y (2017) Overexpression of ceramide synthase 1 increases C18-ceramide and leads to lethal autophagy in human glioma. Oncotarget 8: 104022-104036.

Ward PS, Thompson CB (2012) Metabolic reprogramming: a cancer hallmark even Warburg did not anticipate. Cancer Cell 21: 297-308.

Warnsmann V, Meyer N, Hamann A, Kögel D, Osiewacz HD (2018) A novel role of the mitochondrial permeability transition pore in (-)-gossypol-induced mitochondrial dysfunction. Mech Ageing Dev 170: 45-58.

Wasiak S, Zunino R, McBride HM (2007) Bax/Bak promote sumoylation of DRP1 and its stable association with mitochondria during apoptotic cell death. J Cell Biol 177: 439-450.

Wauson EM, Dbouk HA, Ghosh AB, Cobb MH (2014) G protein-coupled receptors and the regulation of autophagy. Trends Endocrinol Metab 25: 274-282.

Wei MC, Zong WX, Cheng EH, Lindsten T, Panoutsakopoulou V, Ross AJ, Roth KA, MacGregor GR, Thompson CB, Korsmeyer SJ (2001) Proapoptotic BAX and BAK. A requisite gateway to mitochondrial dysfunction and death. Science 292: 727-730.

Wei X, Duan W, Li Y, Zhang S, Xin X, Sun L, Gao M, Li Q, Wang D (2016) AT101 exerts a synergetic efficacy in gastric cancer patients with 5-FU based treatment through promoting apoptosis and autophagy. Oncotarget 7: 34430-34441.

Weyerhäuser P, Kantelhardt SR, Kim EL (2018) Re-purposing chloroquine for glioblastoma: potential merits and confounding variables. Front Oncol 8: 335.

Wiklund ED, Catts VS, Catts SV, Ng TF, Whitaker NJ, Brown AJ, Lutze-Mann LH (2010) Cytotoxic effects of antipsychotic drugs implicate cholesterol homeostasis as a novel chemotherapeutic target. Int J Cancer 126: 28-40.

Williams A, Sarkar S, Cuddon P, Ttofi EK, Saiki S, Siddiqi FH, Jahreiss L, Fleming A, Pask D, Goldsmith P, et al (2008) Novel targets for Huntington's disease in an mTOR-independent autophagy pathway. Nat Chem Biol 4: 295-305.

Williams RAM, Smith TK, Cull B, Mottram JC, Coombs GH (2012) ATG5 is essential for ATG8-dependent autophagy and mitochondrial homeostasis in *Leishmania major*. PLoS Pathog 8: e1002695.

Wilson TA, Karajannis MA, Harter DH (2014) Glioblastoma multiforme. State of the art and future therapeutics. Surg Neurol Int 5: 64.

Wyant GA, Abu-Remaileh M, Frenkel EM, Laqtom NN, Dharamdasani V, Lewis CA, Chan SH, Heinze I, Ori A, Sabatini DM (2018) NUFIP1 is a ribosome receptor for starvation-induced ribophagy. Science 360: 751-758.

Xiao B, Deng X, Zhou W, Tan E-K (2016) Flow cytometry-based assessment of mitophagy using MitoTracker. Front Cell Neurosci 10: 76.

Xu J, Dang Y, Ren YR, Liu JO (2010) Cholesterol trafficking is required for mTOR activation in endothelial cells. Proc Natl Acad Sci U S A 107: 4764-4769.

Yamamoto A, Tagawa Y, Yoshimori T, Moriyama Y, Masaki R, Tashiro Y (1998) Bafilomycin A_1 prevents maturation of autophagic vacuoles by inhibiting fusion between autophagosomes and lysosomes in rat hepatoma cell line, H-4-II-E cells. Cell Struct Funct 23: 33-42.

Yamane M, Moriya S, Kokuba H (2017) Visualization of ceramide channels in lysosomes following endogenous palmitoyl-ceramide accumulation as an initial step in the induction of necrosis. Biochem Biophys Rep 11: 174-181.

Yang W-E, Ho C-C, Yang S-F, Lin S-H, Yeh K-T, Lin C-W, Chen M-K (2016) Cathepsin B expression and the correlation with clinical aspects of oral squamous cell carcinoma. PLoS ONE 11: e0152165.

Yang WS, SriRamaratnam R, Welsch ME, Shimada K, Skouta R, Viswanathan VS, Cheah JH, Clemons PA, Shamji AF, Clish CB, et al (2014) Regulation of ferroptotic cancer cell death by GPX4. Cell 156: 317-331.

Yeo CWS, Ng FSL, Chai C, Tan JMM, Koh GRH, Chong YK, Koh LWH, Foong CSF, Sandanaraj E, Holbrook JD, et al (2012) Parkin pathway activation mitigates glioma cell proliferation and predicts patient survival. Cancer Res 72: 2543-2553.

Yoshida Y, Yasuda S, Fujita T, Hamasaki M, Murakami A, Kawawaki J, Iwai K, Saeki Y, Yoshimori T, Matsuda N, et al (2017) Ubiquitination of exposed glycoproteins by SCFFBXO27 directs damaged lysosomes for autophagy. Proc Natl Acad Sci U S A 114: 8574-8579.

Yoshimori T, Yamamoto A, Moriyama Y, Futai M, Tashiro Y (1991) Bafilomycin A_1, a specific inhibitor of vacuolar-type H^+-ATPase, inhibits acidification and protein degradation in lysosomes of cultured cells. J Biol Chem 266: 17707-17712.

Youle RJ, Narendra DP (2011) Mechanisms of mitophagy. Nat Rev Mol Cell Biol 12: 9-14.

Yu L, Chen Y, Tooze SA (2018) Autophagy pathway: cellular and molecular mechanisms. Autophagy 14: 207-215.

Yu L, McPhee CK, Zheng L, Mardones GA, Rong Y, Peng J, Mi N, Zhao Y, Liu Z, Wan F, et al (2010) Termination of autophagy and reformation of lysosomes regulated by mTOR. Nature 465: 942-946.

Zhang F, Yang J, Li H, Liu M, Zhang J, Zhao L, Wang L, LingHu R, Feng F, Gao X, et al (2016) Combating rituximab resistance by inducing ceramide/lysosome-involved cell death through initiation of CD20-TNFR1 co-localization. Oncoimmunology 5: e1143995.

Zhang H, Bosch-Marce M, Shimoda LA, Tan YS, Baek JH, Wesley JB, Gonzalez FJ, Semenza GL (2008) Mitochondrial autophagy is an HIF-1-dependent adaptive metabolic response to hypoxia. J Biol Chem 283: 10892-10903.

Zhang J (2013) Autophagy and mitophagy in cellular damage control. Redox Biol 1: 19-23.

Zhang J, Ney PA (2009) Role of BNIP3 and NIX in cell death, autophagy, and mitophagy. Cell Death Differ 16: 939-946.

Zhao M, Klionsky DJ (2011) AMPK-dependent phosphorylation of ULK1 induces autophagy. Cell Metab 13: 119-120.

Zhou W, Yuan J (2014) Necroptosis in health and diseases. Semin Cell Dev Biol 35: 14-23.

Zielke S, Meyer N, Mari M, Abou-El-Ardat K, Reggiori F, van Wijk SJL, Kögel D, Fulda S (2018) Loperamide, pimozide, and STF-62247 trigger autophagy-dependent cell death in glioblastoma cells. Cell Death Dis 9: 994.

Zorov DB, Juhaszova M, Sollott SJ (2014) Mitochondrial reactive oxygen species (ROS) and ROS-induced ROS release. Physiol Rev 94: 909-950.

Zukor H, Song W, Liberman A, Mui J, Vali H, Fillebeen C, Pantopoulos K, Wu T-D, Guerquin-Kern J-L, Schipper HM (2009) HO-1-mediated macroautophagy: a mechanism for unregulated iron deposition in aging and degenerating neural tissues. J Neurochem 109: 776-791.

10 Supplemental information

Table 10.1. Top 20 up- and downregulated proteins in U343 and U87MG cells measured by mass spectrometry.
(A-D) Top 20 downregulated (A, B) and upregulated (C, D) proteins in U343 cells (A, C) or U87MG cells (B, D) after treatment with 15 µM AT 101 for 48 h. Bold and underlined names are mitochondria-related.

A) Top 20 downregulated proteins in U343 cells

Log_2 AT 101/DMSO	Log p-value	Gene name
-5,34444	1,91208	MRPL14
-4,90578	1,5027	ITSN2
-4,50307	2,76529	HIST1H1E
-4,19465	2,14686	SDE2
-4,09133	2,75789	RAD18
-4,07443	3,35775	WDR59
-3,89727	2,443	MRPL47
-3,8902	2,66136	MRPL37
-3,8803	3,29278	ANLN
-3,85955	1,35402	TANGO6
-3,73098	1,6512	MRPL15
-3,71424	1,56607	PLK1
-3,69889	1,48761	TNRC6A
-3,68284	2,13336	MRPL24
-3,60828	1,50662	FDX1
-3,53978	2,1192	UBE2C
-3,48687	1,78953	KIAA0101
-3,45461	2,54696	UBE2S
-3,43106	1,5426	SOX2
-3,4146	1,59763	BCKDHA

B) Top 20 downregulated proteins in U87MG cells

Log_2 AT 101/Con	Log_{10} Intensity	Gene name
-1,4023593	8,179543174	TARS2
-1,3974856	8,704051802	ETFA
-1,3907677	7,922154325	TK1
-1,3828696	9,12671246	HADHA
-1,3554181	8,703669609	MCM2
-1,3283017	8,202719843	GYG1
-1,3273693	8,304845832	RRM1
-1,3178467	8,372901882	DUT
-1,2429722	8,534654236	ECHS1
-1,2353987	8,521222449	SQRDL
-1,2324207	9,037985939	DDX5
-1,2281823	8,552412674	ATP5L
-1,2097117	7,741722663	ELAC2
-1,1994105	6,545709055	FAM63A
-1,1839606	8,006553748	ACSL4

-1,1772793	8,374234952	HAT1
-1,1645299	8,226085406	OAT
-1,1523244	8,932580296	COX5A
-1,1508272	7,524941083	XRCC1
-1,1323747	8,643482286	KPNA2

C) Top 20 upregulated proteins in U343 cells

Log_2 AT 101/DMSO	Log p-value	Gene name
9.66906075	2.84814	RPLP1
6.094719025	2.60884	GDF15
5.060562059	3.06684	CADPS2
3.45192345	2.14945	SLC2A1
3.439411724	1.53515	TPP1
3.360855674	3.00751	GAMT
3.340163577	2.34884	PRDX4
3.285207629	3.52748	SQSTM1
3.256917059	1.51885	SRFS10
3.224938459	1.52734	SNRPE
3.195503431	2.03883	KDM3A
3.192073008	1.53797	PPAN
3.118200486	2.08018	MAN2C1
3.102015674	2.12905	TICAM2
3.003625013	2.54793	MTM1
2.925610458	1.43893	HLA-A
2.868579336	2.33814	unknown*
2.821304991	1.78468	PCK2
2.77633373	2.12202	CYCS
2.716006941	1.4862	SPHK2

*: this protein could not be determined based on the peptide profile measured.

D) Top 20 upregulated proteins in U87MG cells

Log_2 AT 101/Con	Log_{10} Intensity	Gene name
4.29570598	9.208064948	NDRG1
3.59978429	9.355318357	HMOX1
3.47548423	8.303124749	RRAD
3.44577679	7.360375644	IRS2
3.30852339	6.944591232	CDKN1A
3.14317396	7.842406397	SLC3A2
2.8614011	9.163408876	CLU
2.81069393	7.687729564	SQSTM1
2.63451109	9.15717561	SLC2A11
2.61562379	8.201629232	RPS27A
2.59229728	9.162116141	HSPA1A
2.50268311	9.898327445	FGF2
2.44989214	7.94379367	HK2

2.37841283	8.551563436	NAMPT
2.06155181	9.223978511	TXN
1.88626529	8.575322963	YBX1
1.77874345	8.380932657	APP
1.73159724	8.038957771	ASNS
1.72368625	9.004138588	GBE1
1.71949929	8.952763392	GARS

Table 10.2. Top 50 up- and downregulated proteins in MZ-54 cells measured by mass spectrometry.
(A-H) MZ-54 cells were exposed to 20 µM imipramine + 75 µM ticlopidine (A, B), 12.5 µM loperamide (C, D), 12.5 µM pimozide (E, F) or 40 µM STF-62247 (G, H) for 24 h. Tables display the top 50 downregulated (A, C, E, G) or upregulated (B, D, F, H) proteins.

A) Top 50 downregulated proteins upon imipramine + ticlopidine treatment.

Gene name	gene symbol	Log_2 IM+TIC/ DMSO	log p-value
Ribonucleoside-diphosphate reductase subunit M2	RRM2	-1,289	2,3611965
Sodium-coupled neutral amino acid transporter 4	SLC38A4	-1,010	2,02441253
Kinesin-like protein KIF11	KIF11	-0,880	2,03307681
Ubiquitin-conjugating enzyme E2 S	UBE2S	-0,836	2,49871698
WW domain-containing transcription regulator protein 1	WWTR1	-0,799	2,05075134
Fatty acid desaturase 3	FADS3	-0,711	2,30487951
Dual specificity protein kinase TTK	TTK	-0,684	2,03581372
Protein FAM127B;Protein FAM127A;Protein FAM127C	FAM127B;FAM127A; FAM127C	-0,626	2,11502223
Retrotransposon-derived protein PEG10	PEG10	-0,624	2,30491039
TRPM8 channel-associated factor 1	TCAF1	-0,589	2,17765924
Bifunctional heparan sulfate N-deacetylase/N-sulfotransferase 1;Heparan sulfate N-deacetylase 1;Heparan sulfate N-sulfotransferase 1	NDST1	-0,585	2,5786086
DnaJ homolog subfamily C member 1	DNAJC1	-0,572	2,4887167
Cdc42 effector protein 1	CDC42EP1	-0,562	2,03990323
Golgi apparatus protein 1	GLG1	-0,559	2,88347811
Cyclin-dependent kinase 6	CDK6	-0,491	2,25280968
Vesicle-associated membrane protein 7	VAMP7	-0,450	2,1701768
Obscurin-like protein 1	OBSL1	-0,399	2,72489659
Filamin-interacting protein FAM101A	FAM101A	-0,396	2,14146849
Oral cancer-overexpressed protein 1	ORAOV1	-0,379	2,31772974
Transgelin	TAGLN	-0,374	2,90667665
Phosducin-like protein	PDCL	-0,363	2,29555679
Calcium/calmodulin-dependent 3,5-cyclic nucleotide phosphodiesterase 1C	PDE1C	-0,352	2,54892159
Filamin-interacting protein FAM101B	FAM101B	-0,345	2,10935461
Prolyl 3-hydroxylase 2	LEPREL1	-0,342	2,84307457
CD99 antigen-like protein 2	CD99L2	-0,338	3,16223701
Ubiquitin carboxyl-terminal hydrolase 11	USP11	-0,337	3,00078989
Endothelial protein C receptor	PROCR	-0,335	2,52924055

Protein NEDD1	NEDD1	-0,327	2,47642014
NADH dehydrogenase [ubiquinone] 1 alpha subcomplex subunit 7	NDUFA7	-0,327	2,17463246
Zinc finger and BTB domain-containing protein 11	ZBTB11	-0,318	2,97408799
MORC family CW-type zinc finger protein 3	MORC3	-0,316	2,23776883
Death-associated protein kinase 3	DAPK3	-0,309	2,37196246
NADH dehydrogenase [ubiquinone] 1 alpha subcomplex subunit 9, mitochondrial	NDUFA9	-0,306	2,03607819
Geranylgeranyl transferase type-2 subunit beta	RABGGTB	-0,301	2,08934345
RNA polymerase II elongation factor ELL	ELL	-0,300	2,05819418
Ganglioside-induced differentiation-associated protein 2	GDAP2	-0,297	3,05240019
Signal recognition particle receptor subunit alpha	SRPR	-0,296	2,08275341
Phosphomannomutase 1	PMM1	-0,290	2,76647451
NADH dehydrogenase [ubiquinone] flavoprotein 1, mitochondrial	NDUFV1	-0,289	2,26783927
Trafficking protein particle complex subunit 5	TRAPPC5	-0,288	2,19769916
Transmembrane 9 superfamily member 2	TM9SF2	-0,287	2,26417825
Activity-dependent neuroprotector homeobox protein	ADNP	-0,282	2,13972356
NADH-ubiquinone oxidoreductase 75 kDa subunit, mitochondrial	NDUFS1	-0,268	3,11310598
Trans-Golgi network integral membrane protein 2	TGOLN2	-0,256	2,00331814
Ras-related protein Rab-30	RAB30	-0,256	2,38957584
NADH dehydrogenase [ubiquinone] 1 beta subcomplex subunit 6	NDUFB6	-0,254	2,22766561
Probable global transcription activator SNF2L1	SMARCA1	-0,250	2,64414057
Vacuolar fusion protein CCZ1 homolog;Vacuolar fusion protein CCZ1 homolog B	CCZ1;CCZ1B	-0,245	2,46777464
Beta-1,3-galactosyltransferase 6	B3GALT6	-0,239	2,26196483
Splicing factor 3B subunit 4	SF3B4	-0,238	2,38178411

B) Top 50 upregulated proteins upon imipramine + ticlopidine treatment.

Gene name	gene symbol	Log_2 IM+TIC/DMSO	LOP p-value
Abhydrolase domain-containing protein 2	ABHD2	2,161	3,778437359
Acyl-CoA desaturase	SCD	1,796	2,815007082
Transmembrane glycoprotein NMB	GPNMB	1,577	2,092840213
Testican-1	SPOCK1	1,497	2,504408068
Chromodomain-helicase-DNA-binding protein 9	CHD9	1,408	2,663783921
Exocyst complex component 3-like protein 4	EXOC3L4	1,368	2,510325638
Insulin-like growth factor-binding protein 7	IGFBP7	1,083	2,072359856
Angiopoietin-related protein 2	ANGPTL2	1,066	2,246531999
G-protein coupled receptor 56;GPR56 N-terminal fragment;GPR56 C-terminal fragment	GPR56	1,061	2,758395856

Rho-related GTP-binding protein RhoE	RND3	1,007	2,456177227
Metalloproteinase inhibitor 2	TIMP2	0,980	2,328195297
Heme oxygenase 1	HMOX1	0,961	3,628759298
Sodium/myo-inositol cotransporter	SLC5A3	0,945	3,324300937
Prenylated Rab acceptor protein 1	RABAC1	0,944	2,795639899
Syntaxin-3	STX3	0,896	2,151648994
Matrix metalloproteinase-14	MMP14	0,879	2,042044214
Integral membrane protein 2C;CT-BRI3	ITM2C	0,808	2,883315196
Cathepsin L1;Cathepsin L1 heavy chain;Cathepsin L1 light chain	CTSL	0,798	2,171419808
3-hydroxy-3-methylglutaryl-coenzyme A reductase	HMGCR	0,797	2,673342256
Scavenger receptor class B member 1	SCARB1	0,754	2,528060026
ORM1-like protein 3	ORMDL3	0,715	2,318160756
Integral membrane protein 2B;BRI2, membrane form;BRI2 intracellular domain;BRI2C, soluble form;Bri23 peptide	ITM2B	0,715	2,03300123
Serine incorporator 3	SERINC3	0,706	3,173203696
UDP-N-acetylhexosamine pyrophosphorylase-like protein 1	UAP1L1	0,705	3,852323814
Amyloid-like protein 2	APLP2	0,688	2,124372308
Pleckstrin homology domain-containing family M member 1	PLEKHM1	0,675	2,051564062
Protein 4.1	EPB41	0,669	2,147185899
Urotensin-2	UTS2	0,657	3,133657351
Ubiquitin-like protein 3	UBL3	0,618	2,35142126
Lactation elevated protein 1	LACE1	0,616	2,049865194
Sequestosome-1	SQSTM1	0,605	2,098330486
Collagen type IV alpha-3-binding protein	COL4A3BP	0,583	2,101875546
Ras-related protein Ral-A	RALA	0,561	2,653151721
Sterol regulatory element-binding protein 1;Processed sterol regulatory element-binding protein 1	SREBF1	0,548	2,179234345
Nuclear receptor coactivator 4	NCOA4	0,546	2,278554225
Peroxidasin homolog	PXDN	0,539	2,67889425
Platelet-derived growth factor receptor alpha	PDGFRA	0,515	2,106215918
Protein VAC14 homolog	VAC14	0,505	2,089544917
Oncostatin-M-specific receptor subunit beta	OSMR	0,499	3,009055548
Methylsterol monooxygenase 1	MSMO1	0,493	3,141939582
All-trans-retinol 13,14-reductase	RETSAT	0,490	2,194125091
78 kDa glucose-regulated protein	HSPA5	0,487	2,768261885
Trimeric intracellular cation channel type B	TMEM38B	0,481	2,922395266
Transmembrane protein 41B	TMEM41B	0,475	2,422168511
Heat shock 70 kDa protein 13	HSPA13	0,457	2,054292607
HCLS1-binding protein 3	HS1BP3	0,450	2,495316605
Syntenin-1	SDCBP	0,442	2,344253048
Tetraspanin-3	TSPAN3	0,435	2,013434533
Soluble scavenger receptor cysteine-rich domain-containing protein SSC5D	SSC5D	0,431	2,27022743
Attractin	ATRN	0,425	2,249834752

C) Top 50 downregulated proteins upon loperamide treatment.

Gene name	gene symbol	Log_2 LOP/DMSO	LOP p-value
Ribonucleoside-diphosphate reductase subunit M2	RRM2	-1,179	2,21181925
WW domain-containing transcription regulator protein 1	WWTR1	-1,139	2,86197551
Carbohydrate sulfotransferase 3	CHST3	-0,817	2,11581554
Tumor necrosis factor receptor superfamily member 11B	TNFRSF11B	-0,812	2,46029457
Keratin, type I cytoskeletal 18	KRT18	-0,779	2,60121225
Ubiquitin-conjugating enzyme E2 S	UBE2S	-0,712	2,34468109
Uncharacterized protein C1orf112	C1orf112	-0,602	3,92038092
Procollagen-lysine,2-oxoglutarate 5-dioxygenase 2	PLOD2	-0,587	2,0231587
Modulator of retrovirus infection homolog	MRI	-0,563	2,19864467
Zinc finger protein 644	ZNF644	-0,560	2,05077634
Ubiquitin carboxyl-terminal hydrolase 11	USP11	-0,513	2,30151743
Alpha-catulin	CTNNAL1	-0,511	2,08055874
Bax inhibitor 1	TMBIM6	-0,503	4,07915983
Vesicle-associated membrane protein 7	VAMP7	-0,485	2,19571346
Fatty acid desaturase 3	FADS3	-0,455	2,91667846
NADH dehydrogenase [ubiquinone] 1 alpha subcomplex subunit 7	NDUFA7	-0,447	3,31171638
Prolyl 3-hydroxylase 2	LEPREL1	-0,436	3,1527026
Cyclin-dependent kinase 6	CDK6	-0,434	2,45937517
NADH dehydrogenase [ubiquinone] flavoprotein 1, mitochondrial	NDUFV1	-0,409	2,34890365
Selenoprotein H	SELH	-0,398	2,18635579
Transgelin	TAGLN	-0,396	3,42829737
39S ribosomal protein L24, mitochondrial	MRPL24	-0,388	2,21178695
NF-kappa-B inhibitor-interacting Ras-like protein 2	NKIRAS2	-0,388	2,08571712
39S ribosomal protein L50, mitochondrial	MRPL50	-0,375	3,69161108
Helicase-like transcription factor	HLTF	-0,362	2,31135924
Pleckstrin homology-like domain family B member 1	PHLDB1	-0,355	3,05995982
Trans-Golgi network integral membrane protein 2	TGOLN2	-0,344	2,15114477
MORC family CW-type zinc finger protein 3	MORC3	-0,341	2,1317582
FERM domain-containing protein 4B	FRMD4B	-0,339	2,30917295
Serine/threonine-protein kinase SIK3	SIK3	-0,338	3,16894826
Sulfhydryl oxidase 2	QSOX2	-0,335	2,45895298
Phosducin-like protein	PDCL	-0,325	2,25223769
Serine/threonine-protein phosphatase 6 regulatory ankyrin repeat subunit C	ANKRD52	-0,321	2,18525136
Filamin-binding LIM protein 1	FBLIM1	-0,321	2,20995512
39S ribosomal protein L51, mitochondrial	MRPL51	-0,314	2,18493246
Calponin-2	CNN2	-0,314	2,59261195
DNA excision repair protein ERCC-1	ERCC1	-0,310	2,00605847
Calcium/calmodulin-dependent 3,5-cyclic	PDE1C	-0,309	2,40545636

nucleotide phosphodiesterase 1C			
Collagen alpha-1(XVIII) chain;Endostatin	COL18A1	-0,307	3,90811125
NADH-ubiquinone oxidoreductase 75 kDa subunit, mitochondrial	NDUFS1	-0,306	2,28163267
Heat shock factor protein 1	HSF1	-0,301	2,23711762
Phospholipid hydroperoxide glutathione peroxidase, mitochondrial	GPX4	-0,298	2,15440298
Selenoprotein K	SELK	-0,298	2,01374875
Zinc finger and BTB domain-containing protein 11	ZBTB11	-0,289	2,56301877
BRCA1-associated ATM activator 1	BRAT1	-0,288	2,31426382
Niban-like protein 1	FAM129B	-0,285	2,35922635
Protein NEDD1	NEDD1	-0,277	3,05535831
Nucleus accumbens-associated protein 2	NACC2	-0,273	2,11880985
Mediator of RNA polymerase II transcription subunit 10	MED10	-0,272	2,8431251
Histone deacetylase 2	HDAC2	-0,271	2,19059721

D) Top 50 upregulated proteins upon loperamide treatment.

Gene name	gene symbol	Log_2 LOP/DMSO	LOP p-value
Zinc finger protein 891	ZNF891	2,854	2,0341539
Acyl-CoA desaturase	SCD	2,757	3,78832659
Chromodomain-helicase-DNA-binding protein 9	CHD9	2,305	3,04766414
Putative uncharacterized protein CRYM-AS1	CRYM-AS1	2,252	2,42862935
Fatty acid-binding protein, heart	FABP3	1,769	2,01549087
Transmembrane glycoprotein NMB	GPNMB	1,717	2,26034974
3-hydroxy-3-methylglutaryl-coenzyme A reductase	HMGCR	1,706	3,54674516
Low-density lipoprotein receptor	LDLR	1,606	2,17352678
Apolipoprotein B-100;Apolipoprotein B-48	APOB	1,302	2,19820495
Transmembrane protein 59	TMEM59	1,297	2,20823541
Integral membrane protein 2C;CT-BRI3	ITM2C	1,282	3,01035196
Tax1-binding protein 1	TAX1BP1	1,206	2,27218025
Nuclear receptor coactivator 4	NCOA4	1,196	2,17929518
Scavenger receptor class B member 1	SCARB1	1,181	2,2254291
Next to BRCA1 gene 1 protein	NBR1	1,169	3,05614858
Protein prune homolog 2	PRUNE2	1,119	2,12059426
Squalene monooxygenase	SQLE	1,114	2,81035777
Amyloid-like protein 2	APLP2	1,111	2,31983324
Squalene synthase	FDFT1	1,092	3,07747284
Sequestosome-1	SQSTM1	1,077	2,58466728
Phosphatidate phosphatase LPIN1	LPIN1	1,068	2,05142995
Hydroxymethylglutaryl-CoA synthase, cytoplasmic	HMGCS1	1,031	2,33569417
Methylsterol monooxygenase 1	MSMO1	0,980	2,02864786
Anthrax toxin receptor 1	ANTXR1	0,976	2,08280822
Matrix metalloproteinase-14	MMP14	0,973	2,53709984
7-dehydrocholesterol reductase	DHCR7	0,958	3,72573849

Isopentenyl-diphosphate Delta-isomerase 1	IDI1	0,954	2,63489799
Mid1-interacting protein 1	MID1IP1	0,953	2,13589563
G-protein coupled receptor 56;GPR56 N-terminal fragment;GPR56 C-terminal fragment	GPR56	0,941	2,96074211
Integral membrane protein 2B;BRI2, membrane form;BRI2 intracellular domain;BRI2C, soluble form;Bri23 peptide	ITM2B	0,938	2,64702154
Synaptic vesicle glycoprotein 2A	SV2A	0,929	2,12625181
Amyloid beta A4 protein;N-APP;Soluble APP-alpha;Soluble APP-beta;C99;Beta-amyloid protein 42;Beta-amyloid protein 40;C83;P3(42);P3(40);C80;Gamma-secretase C-terminal fragment 59;Gamma-secretase C-terminal fragment 57;Gamma-secretase C-terminal fragment 50;C31	APP	0,920	2,60131474
Serine incorporator 3	SERINC3	0,918	3,06960542
Syntaxin-3	STX3	0,906	2,31810018
Inhibitor of nuclear factor kappa-B kinase subunit beta	IKBKB	0,903	2,08671907
N-acetylglucosamine-1-phosphodiester alpha-N-acetylglucosaminidase	NAGPA	0,902	2,21370642
Cell cycle progression protein 1	CCPG1	0,871	2,27385233
Protein 4.1	EPB41	0,844	2,33961379
TGF-beta receptor type-2	TGFBR2	0,833	2,44250148
Fatty acid desaturase 2	FADS2	0,813	2,32147623
Interleukin-6 receptor subunit beta	IL6ST	0,811	2,00057899
Oncostatin-M-specific receptor subunit beta	OSMR	0,806	2,84449004
Lanosterol synthase	LSS	0,799	2,35115196
Ubiquitin-like protein 3	UBL3	0,796	2,22272636
Discoidin domain-containing receptor 2	DDR2	0,780	2,29715782
Platelet-derived growth factor receptor alpha	PDGFRA	0,779	2,34463117
Synaptotagmin-11	SYT11	0,772	2,58187264
Chloride transport protein 6	CLCN6	0,760	2,11030396
Metalloproteinase inhibitor 2	TIMP2	0,727	2,53404966
Fatty acid synthase;[Acyl-carrier-protein] S-acetyltransferase;[Acyl-carrier-protein] S-malonyltransferase;3-oxoacyl-[acyl-carrier-protein] synthase;3-oxoacyl-[acyl-carrier-protein] reductase;3-hydroxyacyl-[acyl-carrier-protein] dehydratase;Enoyl-[acyl-carrier-protein] reductase;Oleoyl-[acyl-carrier-protein] hydrolase	FASN	0,702	2,12187478

E) Top 50 downregulated proteins upon pimozide treatment.

Gene name	gene symbol	Log_2 PIMO/DMSO	LOP p-value
Tumor necrosis factor receptor superfamily member 11B	TNFRSF11B	-1,309	2,26781653
Ribonucleoside-diphosphate reductase subunit M2	RRM2	-1,132	2,26312656
DnaJ homolog subfamily C member 1	DNAJC1	-1,054	3,79956335

Serine/threonine-protein kinase Chk1	CHEK1	-0,957	2,12424679
Carbohydrate sulfotransferase 3	CHST3	-0,932	2,68905821
LIM domain-containing protein 2	LIMD2	-0,803	2,20097068
WW domain-containing transcription regulator protein 1	WWTR1	-0,792	2,66415842
Disks large-associated protein 5	DLGAP5	-0,746	2,13422151
Bax inhibitor 1	TMBIM6	-0,715	2,75448864
Protein FAM127B;Protein FAM127A;Protein FAM127C	FAM127B;FAM127A; FAM127C	-0,713	2,16852462
Frizzled-2	FZD2	-0,686	2,06010051
Keratin, type I cytoskeletal 18	KRT18	-0,637	2,22812222
Nucleolar protein 4;Nucleolar protein 4-like	NOL4;NOL4L	-0,622	2,05023111
UbiA prenyltransferase domain-containing protein 1	UBIAD1	-0,609	2,22654438
Stromal membrane-associated protein 2	SMAP2	-0,590	3,07442233
Coiled-coil-helix-coiled-coil-helix domain-containing protein 2;Putative coiled-coil-helix-coiled-coil-helix domain-containing protein CHCHD2P9, mitochondrial	CHCHD2;CHCHD2P9	-0,533	2,11664306
Protein TANC2	TANC2	-0,531	2,91165348
TRPM8 channel-associated factor 1	TCAF1	-0,526	2,12059086
Neuron navigator 1	NAV1	-0,524	2,26380261
Vesicle-associated membrane protein 7	VAMP7	-0,510	2,42790899
Paired mesoderm homeobox protein 1	PRRX1	-0,477	2,42917135
Prolyl 3-hydroxylase 2	LEPREL1	-0,471	2,0979813
Mitotic spindle assembly checkpoint protein MAD2A	MAD2L1	-0,461	2,06120674
Trans-Golgi network integral membrane protein 2	TGOLN2	-0,447	2,24512144
Uncharacterized protein C12orf45	C12orf45	-0,422	2,04837229
Lysine-specific histone demethylase 1B	KDM1B	-0,416	2,13749556
Growth hormone-inducible transmembrane protein	GHITM	-0,405	2,03081944
Cyclin-dependent kinase 6	CDK6	-0,398	2,26499327
Fatty acid desaturase 3	FADS3	-0,391	2,09782303
Helicase-like transcription factor	HLTF	-0,389	2,09240165
Histone-lysine N-methyltransferase NSD2	WHSC1	-0,383	2,34978108
Leucine-rich repeat and WD repeat-containing protein 1	LRWD1	-0,373	3,09858464
Gamma-glutamyl hydrolase	GGH	-0,369	2,44664771
BRCA1-associated ATM activator 1	BRAT1	-0,368	2,39772148
Outer dense fiber protein 2	ODF2	-0,362	2,05873845
Phosphatidylinositol-binding clathrin assembly protein	PICALM	-0,353	2,0355803
Adenosine 3-phospho 5-phosphosulfate transporter 1	SLC35B2	-0,349	2,16743579
CD99 antigen-like protein 2	CD99L2	-0,347	3,30920214
NADH dehydrogenase [ubiquinone] iron-sulfur protein 6, mitochondrial	NDUFS6	-0,343	2,1488138
SPATS2-like protein	SPATS2L	-0,336	2,26402787
Transgelin	TAGLN	-0,332	2,35701284
Cytochrome c oxidase assembly protein COX15 homolog	COX15	-0,320	2,35712135

Activity-dependent neuroprotector homeobox protein	ADNP	-0,318	2,21742146
NADH dehydrogenase [ubiquinone] 1 alpha subcomplex subunit 9, mitochondrial	NDUFA9	-0,317	2,11432269
Protein NEDD1	NEDD1	-0,317	2,17180331
Receptor expression-enhancing protein 3	REEP3	-0,315	2,24695138
Cytochrome c oxidase subunit 7A-related protein, mitochondrial	COX7A2L	-0,311	2,33208949
Ubiquitin carboxyl-terminal hydrolase 11	USP11	-0,311	3,46870469
DNA polymerase epsilon subunit 3	POLE3	-0,303	3,04667855
RNA-binding protein 24;RNA-binding protein 38	RBM24;RBM38	-0,292	3,00598483

F) Top 50 upregulated proteins upon pimozide treatment.

Gene name	gene symbol	Log_2 PIMO/DMSO	LOP p-value
Zinc finger protein 891	ZNF891	3,162	2,12162232
Putative uncharacterized protein CRYM-AS1	CRYM-AS1	2,532	2,62803475
Chromodomain-helicase-DNA-binding protein 9	CHD9	2,076	2,83741429
GRAM domain-containing protein 4	GRAMD4	1,909	2,15002933
Acyl-CoA desaturase	SCD	1,800	4,02160757
Abhydrolase domain-containing protein 2	ABHD2	1,593	4,07380484
Low-density lipoprotein receptor	LDLR	1,569	2,34559188
Transmembrane glycoprotein NMB	GPNMB	1,504	3,5767909
Apolipoprotein B-100;Apolipoprotein B-48	APOB	1,496	2,42183057
Testican-1	SPOCK1	1,469	2,42865558
Rho-related GTP-binding protein RhoE	RND3	1,438	2,07545804
Protein NOV homolog	NOV	1,428	2,0634841
3-hydroxy-3-methylglutaryl-coenzyme A reductase	HMGCR	1,334	3,63800742
Nuclear receptor coactivator 4	NCOA4	1,330	3,30784408
Amyloid beta A4 protein;N-APP;Soluble APP-alpha;Soluble APP-beta;C99;Beta-amyloid protein 42;Beta-amyloid protein 40;C83;P3(42);P3(40);C80;Gamma-secretase C-terminal fragment 59;Gamma-secretase C-terminal fragment 57;Gamma-secretase C-terminal fragment 50;C31	APP	1,298	2,53675287
Amyloid-like protein 2	APLP2	1,270	2,39473069
Integral membrane protein 2C;CT-BRI3	ITM2C	1,267	5,08631554
Squalene synthase	FDFT1	1,256	2,39080111
Sequestosome-1	SQSTM1	1,253	2,73543724
Transmembrane protein 59	TMEM59	1,236	2,70074168
Next to BRCA1 gene 1 protein	NBR1	1,219	3,00591786
Tax1-binding protein 1	TAX1BP1	1,152	2,63039522
Heme oxygenase 1	HMOX1	1,133	2,92881362
Inhibitor of nuclear factor kappa-B kinase subunit beta	IKBKB	1,084	2,1950482
Scavenger receptor class B member 1	SCARB1	1,076	2,87894408
Matrix metalloproteinase-14	MMP14	1,067	2,36998206
Cell cycle progression protein 1	CCPG1	1,011	2,00276732

Interleukin-6 receptor subunit beta	IL6ST	1,010	4,04137366
Cathepsin L1;Cathepsin L1 heavy chain;Cathepsin L1 light chain	CTSL	0,998	2,00197925
Metalloproteinase inhibitor 2	TIMP2	0,979	3,47562328
Clusterin;Clusterin beta chain;Clusterin alpha chain	CLU	0,972	2,34040159
Dickkopf-related protein 3	DKK3	0,970	2,51434603
Very low-density lipoprotein receptor	VLDLR	0,967	3,14866066
Oncostatin-M-specific receptor subunit beta	OSMR	0,931	2,89027315
Hydroxymethylglutaryl-CoA synthase, cytoplasmic	HMGCS1	0,915	2,21290079
Synaptotagmin-11	SYT11	0,915	2,54580473
Syntaxin-3	STX3	0,899	2,65922064
Integral membrane protein 2B;BRI2, membrane form;BRI2 intracellular domain;BRI2C, soluble form;Bri23 peptide	ITM2B	0,897	2,78199854
Discoidin domain-containing receptor 2	DDR2	0,883	2,40386254
Anthrax toxin receptor 1	ANTXR1	0,876	2,67636677
Platelet-derived growth factor receptor alpha	PDGFRA	0,874	2,80161187
Prostate tumor-overexpressed gene 1 protein	PTOV1	0,873	2,62637539
Serine incorporator 3	SERINC3	0,872	2,40499339
Ceramide glucosyltransferase	UGCG	0,861	2,90127727
Lactation elevated protein 1	LACE1	0,797	2,29140891
Ferritin heavy chain;Ferritin heavy chain, N-terminally processed	FTH1	0,793	2,08871742
G-protein coupled receptor 56;GPR56 N-terminal fragment;GPR56 C-terminal fragment	GPR56	0,783	3,10413509
Urotensin-2	UTS2	0,780	3,32138063
Phosphatidate phosphatase LPIN1	LPIN1	0,780	2,13862765
Protein prune homolog 2	PRUNE2	0,771	2,19816877

G) Top 50 downregulated proteins upon STF-62247 treatment.

Gene name	gene symbol	Log_2 STF/DMSO	LOP p-value
Tropomyosin alpha-4 chain	TPM4	-2,267	2,0199801
Lymphoid-specific helicase	HELLS	-1,796	2,48445679
E3 ubiquitin-protein ligase UHRF1	UHRF1	-1,510	2,01736657
Ribonucleoside-diphosphate reductase subunit M2	RRM2	-1,266	2,13492723
Serine/threonine-protein kinase Chk1	CHEK1	-1,218	2,63680978
WW domain-containing transcription regulator protein 1	WWTR1	-1,172	3,02739013
Procollagen-lysine,2-oxoglutarate 5-dioxygenase 2	PLOD2	-0,971	2,36890316
Fatty acid desaturase 3	FADS3	-0,965	3,91307219
Alpha-catulin	CTNNAL1	-0,931	2,56904127
Fatty acid desaturase 2	FADS2	-0,787	3,0837994
DnaJ homolog subfamily C member 1	DNAJC1	-0,779	2,76479535
Retrotransposon-derived protein PEG10	PEG10	-0,752	2,30670449
Ubiquitin-conjugating enzyme E2 S	UBE2S	-0,732	2,26914104

Mitotic spindle assembly checkpoint protein MAD2A	MAD2L1	-0,695	2,43416756
Bax inhibitor 1	TMBIM6	-0,688	3,1731507
Ubiquitin-conjugating enzyme E2 H	UBE2H	-0,685	2,19228743
Uncharacterized protein C1orf112	C1orf112	-0,663	2,05739696
TRPM8 channel-associated factor 1	TCAF1	-0,661	2,17307396
MAP7 domain-containing protein 1	MAP7D1	-0,652	2,30959054
Oral cancer-overexpressed protein 1	ORAOV1	-0,630	3,50100421
Cell division cycle protein 123 homolog	CDC123	-0,615	2,19461943
Prolyl 3-hydroxylase 2	LEPREL1	-0,573	2,30876391
SPATS2-like protein	SPATS2L	-0,552	3,00330192
Cyclin-dependent kinase 6	CDK6	-0,539	2,28845752
Neuron navigator 1	NAV1	-0,511	2,14107753
DNA primase large subunit	PRIM2	-0,507	2,06939992
Frizzled-2	FZD2	-0,493	3,56725741
Calponin-2	CNN2	-0,491	2,25395298
Transgelin	TAGLN	-0,489	2,29360882
Geranylgeranyl transferase type-2 subunit beta	RABGGTB	-0,486	2,46058712
Ubiquitin-conjugating enzyme E2 E1;Ubiquitin-conjugating enzyme E2 E2	UBE2E1;UBE2E2	-0,479	2,06000419
Ribonuclease ZC3H12A;Probable ribonuclease ZC3H12B;Probable ribonuclease ZC3H12C	ZC3H12A;ZC3H12B; ZC3H12C	-0,475	2,4683144
EH domain-containing protein 2	EHD2	-0,465	2,191223
A-kinase anchor protein 17A	AKAP17A	-0,464	2,37632335
Phosducin-like protein	PDCL	-0,458	2,0736439
Tensin-2	TNS2	-0,456	2,25208292
CXXC-type zinc finger protein 5	CXXC5	-0,455	2,09747523
Calponin-3	CNN3	-0,443	3,16438598
DNA polymerase alpha catalytic subunit	POLA1	-0,438	2,00554208
Palmdelphin	PALMD	-0,437	2,72972006
Helicase-like transcription factor	HLTF	-0,421	2,49512894
Heat shock factor protein 1	HSF1	-0,417	2,2556045
Clathrin interactor 1	CLINT1	-0,415	2,15760778
PDZ and LIM domain protein 2	PDLIM2	-0,401	2,30912284
Fatty acid desaturase 1	FADS1	-0,401	2,60044029
PX domain-containing protein 1	PXDC1	-0,398	2,36635282
Fibronectin type III domain-containing protein 3B	FNDC3B	-0,393	2,40260025
Filamin-interacting protein FAM101A	FAM101A	-0,392	2,02202678
Calcium/calmodulin-dependent 3,5-cyclic nucleotide phosphodiesterase 1C	PDE1C	-0,382	2,5288331
Basic leucine zipper and W2 domain-containing protein 1	BZW1	-0,376	2,37511963

H) Top 50 upregulated proteins upon STF-62247 treatment.

Gene name	gene symbol	Log_2 STF/DMSO	LOP p-value
Transmembrane glycoprotein NMB	GPNMB	1,867	3,82996776
Testican-1	SPOCK1	1,787	2,88236636

Chromodomain-helicase-DNA-binding protein 9	CHD9	1,781	2,54312016
Granulins;Acrogranin;Paragranulin;Granulin-1;Granulin-2;Granulin-3;Granulin-4;Granulin-5;Granulin-6;Granulin-7	GRN	1,492	2,44453444
72 kDa type IV collagenase;PEX	MMP2	1,376	2,38788386
Niemann-Pick C1 protein	NPC1	1,342	2,19448915
Transmembrane protein 59	TMEM59	1,341	3,05027916
Heme oxygenase 1	HMOX1	1,329	2,81630593
Clusterin;Clusterin beta chain;Clusterin alpha chain	CLU	1,299	2,59488459
Serine incorporator 3	SERINC3	1,297	3,29930064
Integral membrane protein 2C;CT-BRI3	ITM2C	1,294	5,17386611
Amyloid-like protein 2	APLP2	1,230	2,1107791
MAM domain-containing protein 2	MAMDC2	1,223	2,18561785
Cathepsin L1;Cathepsin L1 heavy chain;Cathepsin L1 light chain	CTSL	1,222	2,06811068
ATP-binding cassette sub-family A member 1	ABCA1	1,219	2,64358509
Metalloproteinase inhibitor 2	TIMP2	1,187	2,49800768
Acyl-CoA desaturase	SCD	1,180	3,04727108
Amyloid beta A4 protein;N-APP;Soluble APP-alpha;Soluble APP-beta;C99;Beta-amyloid protein 42;Beta-amyloid protein 40;C83;P3(42);P3(40);C80;Gamma-secretase C-terminal fragment 59;Gamma-secretase C-terminal fragment 57;Gamma-secretase C-terminal fragment 50;C31	APP	1,158	2,4998608
Angiopoietin-related protein 2	ANGPTL2	1,135	3,33109836
Sodium/myo-inositol cotransporter	SLC5A3	1,120	2,68486551
Syntaxin-3	STX3	1,110	2,46228899
Nuclear receptor coactivator 4	NCOA4	1,109	3,55043926
Matrix metalloproteinase-14	MMP14	1,090	3,07881877
Next to BRCA1 gene 1 protein	NBR1	1,059	2,82564057
Galectin-3-binding protein	LGALS3BP	1,025	2,08491329
Integral membrane protein 2B;BRI2, membrane form;BRI2 intracellular domain;BRI2C, soluble form;Bri23 peptide	ITM2B	1,022	2,8918533
Glia-derived nexin	SERPINE2	0,996	2,24725393
Sulfhydryl oxidase 1	QSOX1	0,992	3,07678447
Disintegrin and metalloproteinase domain-containing protein 12	ADAM12	0,987	2,11957156
Sequestosome-1	SQSTM1	0,985	2,05821261
Ubiquitin-like protein 3	UBL3	0,971	2,74360978
G-protein coupled receptor 56;GPR56 N-terminal fragment;GPR56 C-terminal fragment	GPR56	0,954	2,52798162
Ceramide glucosyltransferase	UGCG	0,952	2,42574416
Abhydrolase domain-containing protein 2	ABHD2	0,935	2,89409057
Synaptotagmin-11	SYT11	0,902	2,73587407
Tax1-binding protein 1	TAX1BP1	0,895	2,68831737
Caprin-2	CAPRIN2	0,894	2,18998401
EGF-like repeat and discoidin I-like domain-containing protein 3	EDIL3	0,888	2,15313775

Dickkopf-related protein 3	DKK3	0,881	2,004561
Protein prune homolog 2	PRUNE2	0,850	2,28350273
Calcium-binding and coiled-coil domain-containing protein 1	CALCOCO1	0,797	2,43634251
Prenylated Rab acceptor protein 1	RABAC1	0,783	2,47140366
Scavenger receptor class B member 1	SCARB1	0,771	2,35904666
Rho-related GTP-binding protein RhoE	RND3	0,757	2,27102298
Sodium- and chloride-dependent taurine transporter	SLC6A6	0,756	2,1308424
Histone H1x	H1FX	0,752	2,11097192
Metalloproteinase inhibitor 1	TIMP1	0,731	2,11253208
Cell cycle progression protein 1	CCPG1	0,709	2,77562283
Neuropilin-2	NRP2	0,705	2,0705785
Glypican-4;Secreted glypican-4	GPC4	0,696	2,18475265

11 Appendix

11.1 Abbreviations

Table 11.1. Abbreviations.

α-TOC	α-tocopherol
ACD	autophagic cell death
ACN	acetonitrile
ADP	adenosine diphosphate
AIF	apoptosis-inducing factor
AKT1	AKT serine/threonine kinase 1
AMBRA1	autophagy and beclin 1 regulator 1
AMC	aminomethylcumarin
AMP	adenosine monophosphate
AMPKalpha	protein kinase AMP-activated catalytic subunit alpha
ANOVA	analysis of variance
ANT	adenine nucleotide translocator
APAF1	apoptotic peptidase activating factor 1
APLP2	amyloid beta precursor like protein 2
APOB	apolipoprotein B
APP	amyloid beta precursor protein
APS	ammonium persulfate
ASM	acid sphingomyelinase
ATG	autophagy-related gene
ATP	adenosine triphosphate
BAD	BCL2 associated agonist of cell death
BAF	bafilomycin A_1
BAG3	BCL2 associated athanogene 3
BAK1	BCL2 antagonist/killer 1
BAX	BCL2 associated X
BCL2	B-cell CLL/lymphoma 2
BCL2L1 (BCL-xL)	BCL2 like 1
BCL2L2 (BCLW)	BCL2 like 2
BECN1	beclin 1
BID	BH3 interacting domain death agonist
BNIP3	BCL2 interacting protein 3
BNIP3L (NIX)	BCL2 interacting protein 3 like
BOK	BCL2 related ovarian killer
BP	biological process
BSA	bovine serum albumin
cAMP	cyclic adenosine monophosphate

CC	cellular component
CCCP	carbonyl cyanide *m*-chlorophenyl hydrazone
CDKN2A	cyclin dependent kinase inhibitor 2A
cDNA	complementary DNA
Cer	ceramide
CERS	ceramide synthase
CHOL	cholesterol
CLU	clusterin
CNS	central nervous system
COX4I1 (COXIV)	cytochrome c oxidase subunit 4I1 pseudogene 1
CQ	chloroquine
CRISPR	clustered regularly interspaced short palindromic repeats
CSC	cancer stem cells
CTLA4	cytotoxic T-lymphocyte associated protein 4
CTSB	cathepsin B
CTSD	cathepsin D
CYPD	cyclophilin D
Da	dalton
DAPK1	death associated protein kinase 1
DAPK2 (DRP-1)	death associated protein kinase 2
DDA	dendrogenin A
DEGS1	delta 4-desaturase, sphingolipid 1
DFP	deferiprone
DIABLO	direct IAP-binding protein with low PI
DISC	death inducing signaling complex
DKO	double knockout
DMEM	Dulbecco's modified Eagle's medium
DMSO	dimethyl sulfoxide
DPBS	Dulbecco's Phosphate Buffered Saline
DRP	dynamin-related protein
DSB	double-strand break
DTT	Dithiothreitol
E. coli	*Escherichia coli*
EDTA	ethylenediaminetetraacetic acid
EGFR	epidermal growth factor receptor
EGTA	ethylene glycol-bis(β-aminoethyl ether)-N,N,N′,N′-tetraacetic acid
EIF2A	eukaryotic translation initiation factor 2A
EPAC	exchange protein directly activated by cAMP 1
ER	endoplasmatic reticulum
ERK1/2	extracellular signal-regulated protein kinases 1 and 2
ETC	electron transport chain
FADH2	flavin adenine dinucleotide

FAS	Fas cell surface death receptor
FBS	fetal bovine serum
FCCP	carbonyl cyanide-*4*-(trifluoromethoxy)phenylhydrazone
FDA	Food and Drug Administration
FDFT1	farnesyl-diphosphate farnesyltransferase 1
FIASMA	functional inhibitor of acid sphingomyelinase
FOXO3	forkhead box O3
FSC	forward scatter
FUNDC1	FUN14 domain containing 1
G418	geneticin disulfate
GABARAP	GABA receptor-associated protein
GAL3	galecin-3
GAPDH	glyceraldehyde-3-phosphate dehydrogenase
GBA1	glucosylceramidase beta
GBM	glioblastoma (multiforme)
GluCer	glucosylceramide
GO	gene ontology
GPCR	G protein–coupled receptors
GPX4	gluthatione peroxidase 4
GTP	guanosine triphosphate
HDAC	histone deacetylase
HDR	homology directed repair
HIF-1	hypoxia inducible factor 1
HMGCR	3-hydroxy-3-methylglutaryl-coenzyme A reductase
HMGCS1	hydroxymethylglutaryl-CoA synthase, cytoplasmic
HMOX1	heme oxygenase 1
HSP70 (HSPA1A)	heat shock protein family A [Hsp70] member 1A
HSPD1	heat shock protein family D [Hsp60] member 1
IDH1	isocitrate dehydrogenase 1 ($NADP^+$)
IGF1	insulin-like growth factor
IL-6	interleukin-6
IM	imipramine hydrochloride
IMM	inner mitochondrial membrane
IMS	intermembrane space
KCL	potassium chloride
KEAP1	kelch like ECH associated protein 1
KH_2PO_4	potassium phosphate monobasic
KO	knockout
LacCer	lactosylceramide
LAMP1	lysosomal associated membrane protein 1
LAMP2	lysosomal associated membrane protein 2
LC	liquid chromatography

LC3	microtubule associated protein 1 light chain 3
LC3B (MAP1LC3B)	microtubule associated protein 1 light chain 3 beta
LCD	lysosomal cell death
LDL	low density lipoprotein
LDLR	low density lipoprotein receptor
LGALS3	galectin-3
LIR	LC3 interaction region
LLOMe	Leu-Leu-O-methyl
LMP	lysosomal membrane permeabilization
LOP	loperamide hydrochloride
LPL	lipoprotein lipase
LXR	liver X receptor
Lys-C	lysyl endopeptidase
MAP2K1	mitogen-activated protein kinase kinase 1
MAP2K2	mitogen-activated protein kinase kinase 2
MAPK	mitogen-activated protein kinase
MCL1	myeloid cell leukemia 1
MEF	mouse embryonal fibroblasts
MFI	mean fluorescence intensity
MFN1/2	mitofusins 1/2
MGMT	O6-methylguanine methyltransferase
MLKL	mixed lineage kinase domain like pseudokinase
MOMP	mitochondrial outer-membrane permeabilization
mPTP	mitochondrial permeability transition pore
MS	mass spectrometry
MT-ND1	mitochondrially encoded NADH:ubiquinone oxidoreductase core subunit 1
MTG	MitoTracker Green FM
mTORC1	mammalian target of rapamycin complex 1
Na_2HPO_4	sodium phosphate dibasic
NaCl	sodium chloride
NADH	nicotinamide adenine dinucleotide
NaOH	sodium hydroxide
NBR1	neighbor of BRCA1 gene 1
NDP52 (CALCOCO2)	calcium binding and coiled-coil domain 2
NEC1	necrostatin-1
NFE2L2 (NRF2)	nuclear factor, erythroid 2 like 2
NFKB	NF-kappa-B
NHEJ	non-homologous end joining
NOR1 (OSCP1)	organic solute carrier partner 1
NOXA (PMAIP1)	phorbol-12-myristate-13-acetate-induced protein 1
NUR77 (NR4A1)	nuclear receptor subfamily 4 group A member 1
OCR	oxygen consumption rate

OMM	outer mitochondrial membrane
OPA1	optic atrophy 1 (mitochondrial dynamin like GTPase)
OPTN	optineurin
P. anserina	*Podospora anserina*
PAA	polyacrylamide
PAM	protospacer adjacent motif
Parkin	parkin RBR E3 ubiquitin protein ligase
PARL	presenilin associated rhomboid like
PBS	phosphate buffered saline
PBS-T	phosphate buffered saline + Tween
PCR	polymerase chain reaction
PD1 (PDCD1)	programmed cell death 1
PDL1 (CD274)	programmed cell death 1 ligand 1
PE	phosphatidylethanolamine
PEP A	pepstatin A
PI	propidium iodide
PI3K	phosphatidylinositol 3-kinase
PIMO	pimozide
PINK1	PTEN induced putative kinase 1
PIP3	phosphatidylinositol (3,4,5)-trisphosphate
PKA	Protein kinase A
PLC	phospholipase c
PMSF	phenylmethylsulfonylfluorid
PP2A (PTPA)	protein phosphatase 2 phosphatase activator
PS	phosphatidylserine
PTEN	phosphatase and tensin homolog
PUMA	p53-upregulated modulator of apoptosis
PX458	pSpCas9(BB)-2A-GFP
PX459	pSpCas9(BB)-2A-Puro
qRT-PCR	quantitative real-time polymerase chain reaction
RAF1	RAF proto-oncogene serine/threonine-protein kinase
RCD	regulated cell death
RIPK1	receptor interacting serine/threonine kinase 1
RIPK3	receptor interacting protein kinases 3
ROS	reactive oxygen species
RT	room temperature
S. pyogenes	*Streptococcus pyogenes*
S1P	sphingosine-1-phosphate
SAHA	suberoylanilide hydroxamic acid
SCARB1	scavenger receptor class B member 1
SDS	sodium dodecyl sulfate
SDS PAGE	sodium dodecyl sulfate polyacrylamide gel electrophoresis

sgRNA	single-guide RNAs
SILAC	stable isotope labelling with amino acids in cell culture
siRNA	small-interfering-RNA
SIRT1	silent information regulator T1
SK1-I	sphingosine kinase 1 inhibitor
SMAC	second mitochondria-derived activator of caspases
SPHK1	sphingosine kinase 1
SPMD1	sphingomyelin phosphodiesterase 1
SPTLC1	serine palmitoyltransferase long chain base subunit 1
SQSTM (p62)	sequestosome 1
SREBP	sterol regulatory element binding proteins
SSC	sideward scatter
STF	STF-62247
TBP	TATA-box binding protein
TBS-T	Tris buffered saline + Tween
TCA cycle	tricarbolic acid cycle
TEA	triethylamine
TEMED	tetramethyl-ethylenediamine
TEMED	tetramethyl-ethylenediamine
TFA	trifluoroacetic acid
THC	tetrahydrocannabinol
TIC	ticlopidine hydrochloride
Tm	melting temperature
TMRM	tetramethylrhodamine methyl ester
TMZ	temozolomide
TNF	tumor necrosis factor
TNFR1	tumor necrosis factor receptor 1
TOMM20	translocase of outer mitochondrial membrane 20
TP53	tumor protein p53
TRAIL	TNF-related apoptosis inducing ligand
TRIB3	tribbles pseudokinase 3
TRIM16	tripartite motif containing 16
Tris	tris(hydroxymethyl)aminomethane
TRO	olesoxime
TSC	tuberous sclerosis complex
TSPO	translocator protein
TUBA4A	tubulin alpha 4a
UBA domain	ubiquitin interaction domain
ULK1	unc-51 like autophagy activating kinase 1
UPR	unfolded protein response
V-ATPase	vacuolar type H^+-ATPase
VCP (p97)	valosin containing protein

VDAC	voltage dependent anion channel 1
VHL	von Hippel-Lindau
VMP1	vacuole membrane protein 1
versus	vs.
WHO	World Health Organization
WIPI2	WD repeat domain, phosphoinositide interacting 2
WM	wortmannin
XIAP	X-linked inhibitor of apoptosis

11.2 Figures

Figure 1.1: Regulation of the autophagic pathway. 6
Figure 1.2. Mitochondrial quality control mechanisms. 11
Figure 1.3. The mitochondrial respiratory chain. 13
Figure 1.4. Apoptotic pathways. 18
Figure 1.5. Lysosomal membrane permeabilization. 23
Figure 4.1. TMRM measurement by flow cytometry (BD Accuri C6). 49
Figure 4.2. Measurement of APC-annexin V and PI by flow cytometry (BD Accuri C6). 51
Figure 4.3. Assessment of autophagic flux with the pMRX-IP-GFP-LC3-RFP-LC3ΔG plasmid. 52
Figure 4.4. Procedure of CRISPR/Cas9 knockout generation. 54
Figure 4.5. CRISPR/Cas9 deletions of the human *ATG5* gene. 58
Figure 4.6. CRISPR/Cas9 deletions of the human *ATG7* gene. 59
Figure 5.1. AT 101 induces the autophagic flux. 67
Figure 5.2. AT 101 induces mitochondrial depolarization. 69
Figure 5.3. FCCP induces mitochondrial depolarization. 69
Figure 5.4. Effect of mPTP inhibition on AT 101-induced mitochondrial depolarization and cell death. 70
Figure 5.5. Proteome analysis of U87MG and U343 glioma cells treated with AT 101. 72
Figure 5.6. AT 101 induces mitophagy in U343 human glioma cells. 73
Figure 5.7. Effect of AT 101 on mitochondrial proteins. 74
Figure 5.8. Generation of CRISPR/Cas9 *ATG5* KOs. 75
Figure 5.9. *ATG5* KO blocks AT 101-induced autophagy. 76
Figure 5.10. *ATG5* KO prevents AT 101-induced decrease of mitochondrial protein abundance. 76
Figure 5.11. Early effects of AT 101 and FCCP on mitochondrial depolarization and mitochondrial mass. 78
Figure 5.12. AT 101-induced mitophagy is decreased by autophagy inhibition. 79
Figure 5.13. AT 101 induces uptake of mitochondria into lysosomes. 80
Figure 5.14. AT 101-induced reduction of mitochondrial mass is blocked by *ATG5* KO. 81
Figure 5.15. Effect of *ATG5* KO on AT 101- and STS-induced cell death. 83
Figure 5.16. AT 101 does not induce necroptotic cell death. 84
Figure 5.17. Investigation of mitophagy receptors. 85

Figure 5.18. SiRNA-mediated knockdown of *BNIP3* and *BNIP3L*. 86
Figure 5.19. Depletion of *BNIP3* and *BNIP3L* reduces AT 101-induced mitophagy. 86
Figure 5.20. Knockdown of *BNIP3* and *BNIP3L* diminishes cell death induced by AT 101. 87
Figure 5.21. Determination of *HMOX1* knockdown and AT 101-induced increase of HMOX1. 88
Figure 5.22. HMOX1 depletion rescues AT 101-induced mitophagy and cell death. 89
Figure 5.23. Assessment of ferroptosis induced by AT 101. 90
Figure 5.24. Generation of CRISPR/Cas9 *ATG7* KOs. 91
Figure 5.25. Imipramine + ticlopidine, STF-62247, loperamide and pimozide induce autophagic flux. 92
Figure 5.26. Autophagy inhibition rescues imipramine + ticlopidine-, STF-62247-, loperamide- and pimozide-induced cell death. 94
Figure 5.27. Effect of autophagy inhibition on staurosporine-induced cell death. 95
Figure 5.28. Monitoring of effector caspase activity induced by imipramine + ticlopidine, STF-62247, loperamide and pimozide. 96
Figure 5.29. Effect of autophagy depletion on stress response genes. 97
Figure 5.30. Imipramine + ticlopidine, STF-62247, loperamide and pimozide increase the autophagic flux in an *ATG5*- and *ATG7*-dependent manner. 98
Figure 5.31. Analysis of the autophagic flux by fluorescence microscopy of imipramine + ticlopidine-, STF-62247-, loperamide- and pimozide-treated cells. 101
Figure 5.32. Imipramine + ticlopidine, STF-62247, loperamide and pimozide induce autophagic flux. 102
Figure 5.33. Effect of imipramine + ticlopidine, STF-62247, loperamide and pimozide on SQSTM1 protein levels and phosphorylation of AMPKalpha and AKT1. 103
Figure 5.34. Inhibition of 5-HT7 receptor signaling induces autophagic cell death. 104
Figure 5.35. Assessment of cell death following treatment with endomorphin-1 and verapamil. 105
Figure 5.36. Proteomic analysis of MZ-54 glioma cells treated with imipramine + ticlopidine, STF-62247, loperamide and pimozide. 106
Figure 5.37. Proteomic analysis of MZ-54 glioma cells treated with imipramine + ticlopidine, STF-62247, loperamide and pimozide. 108
Figure 5.38. Accumulation of cholesterol in the lysosomes. 110
Figure 5.39. Effect of cholesterol on phospho-AKT1 and LC3B-switch. 111
Figure 5.40. Imipramine + ticlopidine, loperamide and pimozide reduce acid sphingomyelinase activity. 112
Figure 5.41. Lipidomics screen of MZ-54 cells treated with loperamide and pimozide. 113
Figure 5.42. Heat maps of the lipidomics screen of MZ-54 cells treated with loperamide and pimozide. 114
Figure 5.43. Investigation of *de novo* ceramide synthesis. 115
Figure 5.44. Loperamide and pimozide induce ROS accumulation. 117
Figure 5.45. Loperamide and pimozide induce lysosomal rupture. 118
Figure 5.46. *ATG5* and *ATG7* knockout reduces pmCherry-GAL3 puncta formation upon pimozide and loperamide treatment. 119
Figure 5.47. Quantification of pmCherry-GAL3 puncta per cell. 120

Figure 5.48. Assessment of lysosomal cathepsin B release into the cytosol upon treatment with imipramine + ticlopidine, loperamide and pimozide. 121
Figure 5.49. Determination of lysosomal cathepsin release into the cytosol by immunoblot analysis.122
Figure 5.50. Investigation of lysosomal cell death induced by loperamide, pimozide, imipramine + ticlopidine and STF-62247. 123
Figure 5.51. Assessment of lysosomal cell death induced by loperamide, pimozide, imipramine + ticlopidine and STF-62247 in *ATG5* and *ATG7* KO cells. 124
Figure 5.52. Loperamide and pimozide induce colocalization of LC3B and GAL3. 125
Figure 5.53. Determination of siRNA-mediated knockdown of *VCP*. 125
Figure 5.54. Knockdown of *VCP* impairs degradation of ruptured lysosomes after pimozide washout. 126
Figure 5.55. VCP depletion impairs degradation of ruptured lysosomes and promotes cell death.....127
Figure 6.1. Hypothetical model of AT 101-induced lethal mitophagy. 136
Figure 6.2. Hypothetic pathway of imipramine + ticlopidine-, loperamide- and pimozide-induced lipotoxicity, and the dual role of autophagy in cell survival and death. 145

11.3 Tables

Table 1.1. Major ongoing clinical trials of malignant gliomas (Paolillo et al., 2018). 4
Table 1.2. Regulated cell death models of mammalian cells (Galluzzi et al., 2018). 15
Table 3.1: Cell lines. 27
Table 3.2: Stable CRISPR/Cas9 knockout cell lines. 27
Table 3.3: Medium contents. 27
Table 3.4: Bacteria. 28
Table 3.5: Medium and agar for bacteria. 28
Table 3.6: Plasmids. 28
Table 3.7: Chemicals for the treatment of cells. 29
Table 3.8. Fluorophores used for flow cytometry experiments. 30
Table 3.9: List of all other chemicals, cell culture supplements and enzymes that were used for the experiments. 30
Table 3.10: Primary antibodies used for western blot. 33
Table 3.11: Secondary antibodies used for western blot. 34
Table 3.12: Primary antibodies for immunofluorescent staining. 34
Table 3.13: Secondary antibodies for immunofluorescent staining. 34
Table 3.14: Buffers and solutions for caspase 3-like activity measurement. 34
Table 3.15: Buffers for flow cytometry analysis. 35
Table 3.16. Buffers for protein analysis (western blot). 35
Table 3.17: Buffers for proteome analysis. 35
Table 3.18: Buffers for separation of cytosol and organelle fraction containing intact lysosomes. 36
Table 3.19: Buffers for cathepsin B assay. 36

Table 3.20: Commercial kits. 36
Table 3.21: siRNA oligonucleotides for transfection. 37
Table 3.22: PCR primer for detection of CRISPR/Cas9 knockouts. 37
Table 3.23: Oligonucleotides for CRISPR/Cas9 sgRNA generation. 38
Table 3.24: FAM-MGP primer for qRT-PCR. 38
Table 3.25: Laboratory equipment. 39
Table 3.26: Software 42
Table 4.1. Laser and emission filters for flow cytometry experiments. 52
Table 4.2. PCR program for colony-screen PCR. 55
Table 4.3. PCR program for detection of CRISPR/Cas9 knockout clones. 57
Table 4.4. Thermo cycler program for qRT-PCR. 60
Table 10.1. Top 20 up- and downregulated proteins in U343 and U87MG cells measured by mass spectrometry. 175
Table 10.2. Top 50 up- and downregulated proteins in MZ-54 cells measured by mass spectrometry. 177
Table 11.1. Abbreviations. 189